Durham University

Durham E-Theses

HIGHLY EMISSIVE CHIRAL LANTHANIDE(III) COMPLEXES FOR LABELLING AND IMAGING

FRAWLEY, ANDREW,TIMOTHY

How to cite:

FRAWLEY, ANDREW,TIMOTHY (2017). *HIGHLY EMISSIVE CHIRAL LANTHANIDE(III) COMPLEXES FOR LABELLING AND IMAGING*, Durham e-Theses.
http://etheses.dur.ac.uk/12423/

Use policy

The full-text may be used and/or reproduced, and given to third parties in any format or medium, without prior permission or charge, for personal research or study, educational, or not-for-profit purposes provided that:

- a full bibliographic reference is made to the original source
- a link is made to the metadata record in Durham E-Theses
- the full-text is not changed in any way

The full-text must not be sold in any format or medium without the formal permission of the copyright holders.

Please consult the full Durham E-Theses policy for further details.

Academic Support Office, The Palatine Centre, Durham University, Stockton Road, Durham, DH1 3LE
e-mail: e-theses.admin@durham.ac.uk Tel: +44 0191 334 6107
http://etheses.dur.ac.uk

Durham University

Department of Chemistry

HIGHLY EMISSIVE CHIRAL LANTHANIDE(III) COMPLEXES FOR LABELLING AND IMAGING

Andrew Timothy Frawley

A thesis submitted for the degree of Doctor of Philosophy

2017

Declaration

The work described herein was undertaken at the Department of Chemistry, Durham University between October 2014 and September 2017. All of the work is my own, except where specifically stated otherwise. No part has previously been submitted for a degree at this or any other university.

Statement of Copyright

The copyright of this thesis rests with the author. No quotation from it should be published without the author's prior written consent and information derived from it should be acknowledged.

Abstract

Sensitised lanthanide complexes based on macrocyclic chelating ligands have been used extensively to study biological function at a cellular level, due to their very bright and long-lived emission, sharp emission bands and high stability to photo-degradation. These photophysical properties, in addition to their excellent chiroptical behaviour, also make these complexes promising candidates for security labelling and as anti-counterfeiting tools.

Novel highly emissive chiral europium(III) complexes based on macrocyclic ligands have been synthesised and their photophysical properties studied. They possess high molar extinction coefficients and are amenable to excitation using commonly available light sources. These complexes have been resolved by chiral HPLC and the circularly polarised luminescence (CPL) spectra of their enantiomers recorded. They exhibit strong circularly polarised emission in response to excitation using near ultra-violet light, and are stable to thermally-activated racemisation.

A simple off-the-shelf camera set up has been developed which is capable of discriminating 'real' europium(III) emission from emission from a 'fake' marking, based on emission lifetime and wavelength. Additionally, chiroptical discrimination has been achieved using a custom built microscope incorporating a quarter-wave plate and linear polariser.

The solvent dependent emission behaviour of a series of C_3-symmetric lanthanide(III) complexes has been studied, demonstrating that the form of the total emission and CPL is extremely sensitive to minor changes in the outer solvation sphere of the complex.

Finally, macropinocytosis has been identified as the mechanism of cell uptake of this family of complexes in NIH-3T3 cells, and the internalisation and subsequent sub-cellular localisation has been shown to be dependent on complex chirality.

Acknowledgements

I would like to thank the following people for making this work possible:

My supervisor, Prof. David Parker, for giving me the opportunity to carry out this project and for his ideas, guidance and support over the last 4 years.

Special thanks must go to Dr. Robert Pal for his help with all things both living and optical, specifically cameras, microscopes and cells.

Thank you to the following members of the Chemistry Department for their assistance: Dr. Alan Kenwright, Dr. Juan Aguilar, Catherine Heffernan and Dr. Raquel Belda-Vidal for NMR spectroscopy; Dr. Jackie Mosely, Pete Stokes and Dr. Dave Parker for mass spectrometry; Dr. Aileen Congreve and Lenny Lauchlan for HPLC training and for letting me loose in the HPLC lab; Dr. Lars-Olof Pålsson for assistance with low temperature photophysical measurements; Annette Passmoor, Gary Southern and all the stores and technical team for keeping us supplied with equipment and chemicals; the lab attendants for the daily supply of tea and coffee, and specifically to Claire for gently encouraging me to tidy my desk every so often. Thanks also to Dr. Chris Ottley (Dept. of Earth Sciences) for ICP-MS analyses.

Thanks to all the Parker Group members, past and present. In particular I'd like to thank Steve, Brian, Kanthi, Cidalia, Nicola, Matthieu, Kevin, Alex, Martina, Emily, Katie, Sergey, Edward, Alice, Laura, Ryan and Hannah for sharing their knowledge and keeping me going over the years.

I would also like to acknowledge Durham University for the award of a Durham Doctoral Scholarship which has allowed me to pursue my postgraduate studies.

Thanks to all the leaders, parents and young people at 19th Durham Scout Group for providing plenty of fun and adventure (and distraction from chemistry). A special thank you to Siân, Will, Evelyn and Nicholas Greeves for being my 'Durham family' for the last 7 years. I really can't thank you enough for everything you've done.

Finally, the biggest thanks to Mum, Dad and Helen for their unwavering support in everything I do.

List of Abbreviations

α_1-AGP	alpha-1-acid glycoprotein
12-N_4	1,4,7,10-tetraazacyclododecane
9-N_3	1,4,7-triazacyclononane
A431	human epidermoid carcinoma cell line
AAT	alpha-1-antitrypsin
AC	alternating current
acac	acetylacetonate
ADP	adenosine diphosphate
AFM	atomic force microscopy
AMP	adenosine monophosphate
ATP	adenosine triphosphate
bda	2,2’-bipyridine-6,6’-dicarboxylate
BET	back energy transfer
BINAP	2,2'-bis(diphenylphosphino)-1,1'-binaphthyl
BINOL	1,1'-bi-2-naphthol
BODIPY	boron-dipyrromethene
BP	band pass
br	broad (NMR)
BSA	bovine serum albumin
CCD	charge-coupled device
CCDC	Cambridge Crystallographic Data Centre
CD	circular dichroism
CHO	Chinese hamster ovary
CIE	Commission internationale de l'éclairage (International Commission on Illumination)
CPEL	circularly polarised electroluminescence
CPL	circularly polarised luminescence
CSP	chiral stationary phase

CW	continuous wave
cyclen	1,4,7,10-tetraazacyclododecane
d, dd, ddd	doublet, doublet of doublets, etc. (NMR)
DC	direct current
DCM	dichloromethane
dfppy	difluorophenylpyridine
DFT	density functional theory
DMEM	Dulbecco's modified Eagle's medium
DMF	*N,N*-dimethylformamide
DMSO	dimethylsulfoxide
DOTA	1,4,7,10-tetraazacyclododecane-1,4,7,10-tetraacetic acid
dpa	dipicolinic acid, pyridine-2,6-dicarboxylic acid
dppf	1,1'-bis(diphenylphosphino)ferrocene
dpyb	1,3-dipyridylbenzene
DSLR	digital single lens reflex
DTPA	diethylenetriaminepentaacetic acid
ED	electric dipole
ee	enantiomeric excess
E_T^N	Reichardt's normalised solvent polarity
eq.	equivalents
ESI	electrospray ionisation
eT	electron transfer
ET	energy transfer
facam	3-trifluoroacetylcamphorate
FOV	field of view
FRET	Förster/fluorescence resonance energy transfer
FWHM	full width half maximum
GCMS	gas chromatography mass spectrometry
HEPES	4-(2-hydroxyethyl)-1-piperazineethanesulfonic acid
hfac	1,1,1,5,5,5-hexafluoroacetylacetonate

hfbc	3-heptafluorobutyrylcamphorate
HP-DO3A	10-(2-hydroxypropyl)-1,4,7,10-tetraazacyclododecane-1,4,7-triacetic acid
HPLC	high pressure/performance liquid chromatography
HRMS	high resolution mass spectrometry
IC	internal conversion
IC_{50}	half-maximal inhibitory concentration
ICP-MS	inductively coupled plasma mass spectrometry
ICT	internal charge transfer
IR	infra-red
ISC	intersystem crossing
iTTL	through the lens metering (camera flash unit)
LCMS	liquid chromatography mass spectrometry
LED	light emitting diode
Ln	lanthanide
LP	long pass
LSCM	laser scanning confocal microscopy
LTG	LysoTracker Green
m	multiplet (NMR)
m.p.	melting point
*m*CPBA	*meta*-chloroperbenzoic acid
MD	magnetic dipole
MOPS	3-(*N*-morpholino)propanesulfonic acid
MRI	magnetic resonance imaging
Ms	methanesulfonyl
MTG	MitoTracker Green
NIH-3T3	mouse skin fibroblast cell line
NMR	nuclear magnetic resonance
NOTA	1,4,7-triazacyclononane-1,4,7-triacetic acid
PBS	phosphate buffered saline

pda	1,10-phenanthroline-2,9-dicarboxylic acid
PEM	photoelastic modulator
PET	positron emission tomography
phen	phenanthroline
PhMoNa	phase modulated nanoscopy
PMMA	poly(methyl methacrylate)
PMT	photomultiplier tube
ppm	parts per million
ppy	phenylpyridine
PVC	poly(vinyl chloride)
Q	quencher
QR	quick response
QToF	quadrupole time of flight (mass spectrometry)
S	singlet (energy level)
s	singlet (NMR)
SEM	scanning electron microscopy
SOM	single organic molecule
T	triplet (energy level)
t	triplet (NMR)
TBAF	tetrabutylammonium fluoride
td	triplet of doublets (NMR)
TFE	2,2,2-trifluoroethanol
THF	tetrahydrofuran
TLC	thin layer chromatography
TQD	triple quadrupole (mass spectrometry)
TTA	2-thenoyltrifluoroacetonate
UPLC	ultra performance liquid chromatography
UV	ultra violet
YAG	yttrium aluminium garnet, $Y_3Al_5O_{12}$

Table of Contents

CHAPTER ONE : INTRODUCTION

1.1 Introduction to lanthanide luminescence

1.1.1 Overview

Luminescence is defined as the spontaneous emission of radiation from an electronically excited species. Luminescence can be categorised further depending on how the electronically excited species is formed, e.g. photoluminescence is the result of absorption of a photon, chemiluminescence is a result of a chemical reaction, triboluminescence arises from mechanical stress and electroluminescence occurs as a result of an electric current passing through a substance.

Photoluminescence can be described using a Jabłońksi diagram which shows the processes that can occur (Fig. 1.1).

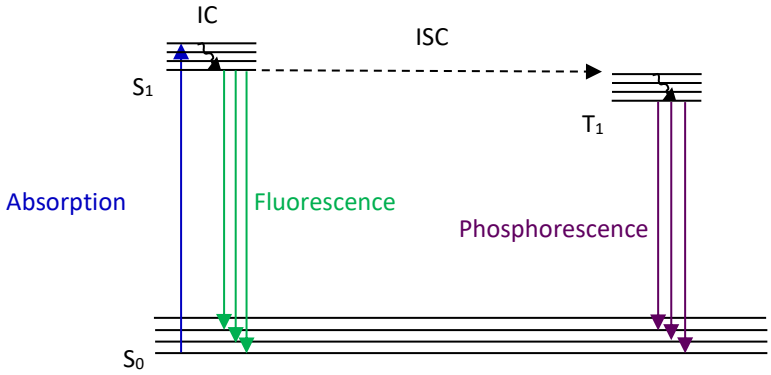

Figure 1.1 A Jabłońksi diagram showing the primary processes involved in photoluminescence.

Absorption of a photon excites the molecule from the singlet ground state (S_0) to higher vibrational levels of a singlet excited state (S_1). Very fast radiationless relaxation (timescale of 10^{-13} to 10^{-11} s) to the lowest vibrational level of S_1 occurs by internal conversion (IC), following Kasha's Rule.[1] From here, there are three possible pathways: (i) non-radiative decay back to S_0; (ii) decay to S_0 accompanied by emission of a photon (fluorescence, 10^{-9} to 10^{-7} s); or (iii) intersystem crossing (ISC) to a triplet excited state, T_1. From the T_1 state, a molecule can return to the S_0 state either by non-radiative pathways or by emission of a photon (phosphorescence, 10^{-4} s to hours e.g. in 'glow in the dark' products).

Trivalent lanthanide cations display peculiar photoluminescent properties which can be attributed to their electronic structure. Lanthanide(III) ions have partially filled 4*f* orbitals, and the arrangement of the electrons in these ions can be described using the Russell-Saunders coupling scheme by term symbols in the form, $^{2S+1}L_J$, where *S* denotes the spin quantum number of the ion and *L* is the total orbital angular momentum. Vector addition of *L* and *S* gives the possible values of *J,* the total angular momentum.

Several lanthanide(III) ions exhibit radiative decay from electronic excited states. Thus, Sm^{3+}, Eu^{3+}, Tb^{3+} and Dy^{3+} emit light in the visible region of the spectrum, while Nd^{3+}, Ho^{3+}, Er^{3+} and Yb^{3+} emit near infrared light, and Gd^{3+} emits UV light. Normally, the larger the energy gap between the emissive state and the ground state, the less likely non-radiative pathways are to occur. This means that visible and UV emitters tend to be more efficient than IR emitters. Eu^{3+} and Tb^{3+} are the most commonly used lanthanide ions for luminescence studies in the visible region. In this work, the focus has been on emissive europium(III) species.

The various electronic states of europium(III) can be characterised by their Russell-Saunders term symbols, and the splitting of energy levels caused by various factors can be broken down as shown in Fig. 1.2. For europium(III) luminescence spectroscopy, emission from the $^5D_0$ state is the most commonly studied. Emission from $^5D_1$, $^5D_2$ and higher levels is rarely observed, except in extended inorganic lattices.[2]

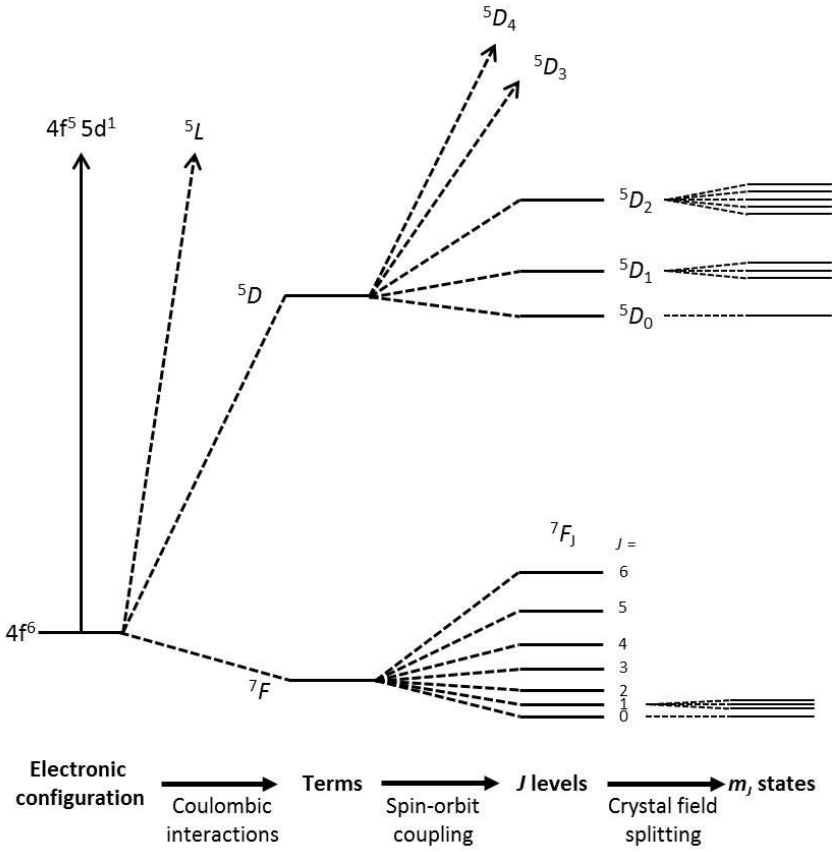

Figure 1.2 The contributions of various factors in the splitting of energy levels in Eu(III).

For the $4f^6$ electron configuration of Eu(III), the ground state term is ^7F. Spin-orbit coupling splits this term into 6 possible J levels (J = 0, 1, 2, 3, 4, 5, 6) which are separated from each other by energies of the order of 10^2-10^3 cm^{-1}. Each of these J states can be split by crystal field effects into $2J+1$ m_J or Stark states. In lanthanides, because the 4*f* orbitals are well shielded by the 5*s* and 5*p* orbitals, the effect of crystal field is small, meaning the separation of the m_J states is of the order of a few hundred wavenumbers. This small crystal field splitting (compared to the spin-orbit coupling) gives rise to transitions whose barycentres are largely independent of ligand environment. It is normally assumed that only the intensity and fine structure of transitions are affected by the environment.

Transitions from the $^5D_0$ excited state to various ^7F_J levels are characterised by the dipolar nature of the transition. Intraconfigurational (*s-s*, *p-p*, *d-d* and *f-f*) transitions are formally forbidden by the Laporte selection rule as they do not involve a change in parity, so electric dipole (ED) transitions cannot occur. However, in non-centrosymmetric environments, *f-f* transitions can occur via an induced electric

dipole mechanism. Magnetic dipole (MD) transitions are allowed by the Laporte selection rule but they are inherently weaker than electric dipole transitions. The selection rules for induced electric dipole and magnetic dipole transitions are summarised in Table 1.1.

Table 1.1 Selection rules for intraconfigurational *f-f* transitions.

	Selection rules		
Transition type	***S***	***L***	***J***
Induced electric dipole	$\Delta S = 0$	$\lvert\Delta L\rvert \leq 6$; if $L = 0$ or $L' = 0$, $\lvert\Delta L\rvert = 2, 4, 6$	$\lvert\Delta J\rvert \leq 6$; if $J = 0$ or $J' = 0$, $\lvert\Delta J\rvert = 2, 4, 6$
Magnetic dipole	$\Delta S = 0$	$\Delta L = 0$	$\lvert\Delta J\rvert \leq 1$ except $0 \leftrightarrow 0$

These strict selection rules for ΔS, ΔL and ΔJ rely on S, L, and J being good quantum numbers. However, for the moderately heavy lanthanides, this assumption begins to break down, meaning these strict selection rules can be relaxed slightly. In particular, it should be noted that all transitions involving a change in spin are formally forbidden. Since most of the transitions involved in lanthanide luminescence involve changes in spin, it is clear that these selection rules do not always hold. The selection rules for the orbit quantum number, L, are also relaxed. The outcome of these rules in the instance of transitions from the $^5D_0$ state of europium(III) is as follows. The $^5D_0 \rightarrow {}^7F_0$ ($\Delta J = 0$) transition is an allowed induced ED transition, while $^5D_0 \rightarrow {}^7F_1$ ($\Delta J = 1$) is forbidden by the selection rules for ΔJ for induced ED as $J' = 0$ (therefore only $\lvert\Delta J\rvert = 2, 4, 6$ are allowed). It is, however, an allowed MD transition. The $^5D_0 \rightarrow {}^7F_{2,4,6}$ ($\Delta J = 2, 4, 6$) transitions are induced ED allowed although $\Delta J = 6$ is rarely observed as it far into the red/near-IR region of the spectrum where conventional photomultiplier tube detectors are less sensitive. The $^5D_0 \rightarrow {}^7F_{3,5}$ ($\Delta J = 3, 5$) transitions are formally forbidden by all the selection rules. However, they can be very weakly allowed due to J-mixing, where wavefunctions of other J levels close in energy can mix, relaxing the ΔJ selection rules.

1.1.2 Emission lifetime

Long luminescent lifetimes are often observed for lanthanides because *f-f* transitions are formally forbidden and usually involve a change of spin. For the commonly used emissive lanthanides, this leads to lifetimes of the order of microseconds for samarium and dysprosium and milliseconds for europium and terbium. These lifetimes are several orders of magnitude longer than the nanosecond lifetimes of organic fluorophores, which introduces the possibility of time-gated detection (see Fig. 1.3). This allows emission from long-lived species to be measured without competing interference from short-lived emitting compounds. Time-gated fluorescence microscopy, for example, has proved to be useful in live cell imaging using lanthanide stains, as background fluorescence from endogenous biomolecules can be eliminated from the measurement.

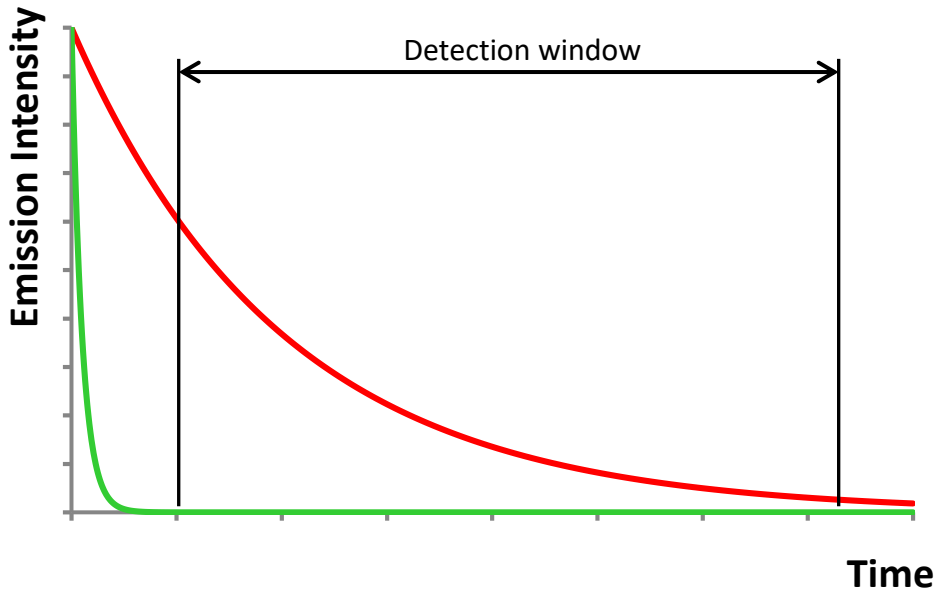

Figure 1.3 Schematic representation of time-gated detection: long-lived lanthanide luminescence (*red*) is detected after a short delay, allowing the short-lived organic fluorescence (*green*) to decay.

Emission from a single species decays following a first order rate profile such as in Eqn. 1.1.

$$I_t = I_0 e^{\frac{-t}{\tau}} \qquad \textbf{(1.1)}$$

where I_t and I_0 are the emission intensities at time, t, and at $t = 0$, respectively, and τ is the measured emission lifetime, which is the inverse of the observed rate

constant, k, for depopulation of the emissive state. As such, lifetimes can be obtained by measuring emission intensity at various time points after excitation. A plot of $\ln(I_t)$ against t has a gradient of $-1/\tau$.

1.1.3 Excitation of lanthanides

A further side-effect of forbidden *f-f* transitions is that transitions from lanthanide ground states to their excited states are very weakly absorbing, i.e. they have very low molar extinction coefficients (often <1 mol^{-1} dm^3 cm^{-1}). As a result, efficient direct excitation of lanthanide ions can only be achieved using lasers. This drawback can be overcome by the use of sensitising chromophores which excite the lanthanide via the antenna effect. The process involves absorption of incident photons by an antenna chromophore, followed by transfer of the energy onto the lanthanide ion. From the lanthanide excited state, photons can be emitted (see Fig. 1.4). This can result in large pseudo-Stokes' shifts compared to organic systems where absorption and emission bands often overlap.

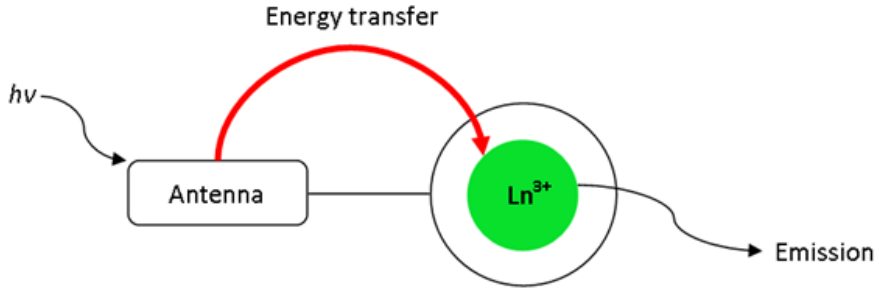

Figure 1.4 An illustration of the antenna effect in sensitised lanthanide photoluminescence.

The energy transfer step is classically explained either by the Förster or Dexter mechanisms. The Förster mechanism is a highly distance-dependent (r^{-6}) process involving non-radiative energy transfer through dipole-dipole coupling between the donor and acceptor,[3] while the Dexter mechanism is a short range electron transfer between the donor and acceptor.[4]

The Jabłońksi diagram in Fig. 1.1 can be extended to account for these processes (see Fig. 1.5). Here, the sensitising chromophore absorbs a photon before intersystem crossing to the triplet excited state T_1. From here, energy transfer to

the excited state of the lanthanide ion occurs, before lanthanide-centred emission returns the system to its ground state.

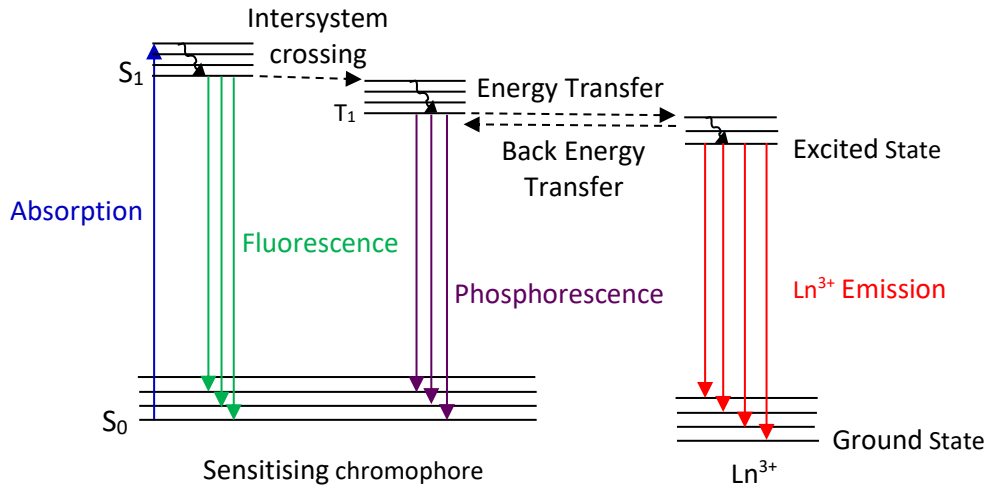

Figure 1.5 A Jabłoński diagram showing the pathways involved in sensitised emission of lanthanides.

There are several conditions that should be optimised to ensure efficient energy transfer to the lanthanide ion. The energy gap between S_1 and T_1 should be small to allow efficient intersystem crossing. If the energy gap is too large, chromophore fluorescence occurs more readily than intersystem crossing. Additionally, the T_1 state should be at least 1700 cm^{-1} higher in energy than the lanthanide excited state to minimise thermally-activated back energy transfer and chromophore phosphorescence.[5]

An alternative mechanism for sensitisation has also been proposed, involving an internal charge transfer (ICT) excited state.[6] This mechanism has been observed in systems where sensitising chromophores have large charge separation. Such ICT transitions often exhibit sensitivity to temperature and solvent polarity, and can occur in conjunction with the triplet-facilitated route described in Fig. 1.5.

1.1.4 Quenching processes

There are various pathways by which sensitised lanthanide emission can be quenched, the most important of which are summarised in Scheme 1.1. All of these processes will reduce the luminescence quantum yield of the species. After absorption of a photon, the chromophore singlet excited state can re-emit the

photon as fluorescence, be quenched by electron transfer (eT) or by collisional quenching (by a quencher, Q). The chromophore triplet excited state can phosphoresce or be quenched by molecular oxygen (which has a triplet ground state). The lanthanide excited state can be quenched by electron transfer, energy transfer (ET) to another species, back energy transfer (BET) to the chromophore or by vibrational energy transfer to proximal X-H oscillators (where X = C, N, O). For Eu(III) and Tb(III), inner sphere water molecules and secondary amine groups are particularly efficient quenching species as the lanthanide excited states are of similar energy to higher vibrational levels of the O-H and N-H oscillators.

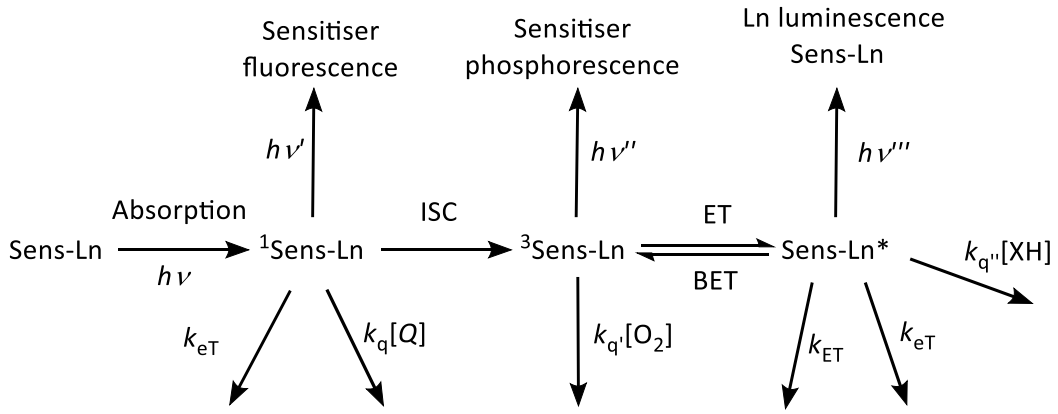

Scheme 1.1 Various quenching processes possible during sensitised lanthanide emission. Redrawn from Ref. [7].

1.1.5 Photoluminescence quantum yield and brightness

In order for a species to be useful in chiroptical or biological applications, it must possess a high photoluminescence quantum yield, Φ. In the case of sensitised lanthanide complexes, the quantum yield can be expressed as follows:

$$\Phi = \eta_{\mathrm{ISC}}\eta_{\mathrm{ET}}\Phi^{\mathrm{Ln}} \qquad (\mathbf{1.2})$$

where η_{ISC} is the efficiency of intersystem crossing from the chromophore singlet to the triplet excited state, η_{ET} is the efficiency of energy transfer from the chromophore triplet state to the lanthanide excited state and Φ^{Ln} is the intrinsic quantum yield of the lanthanide ion. This parameter can be regarded as the ratio of the radiative rate constant, k_r, to the sum of all possible rate constants for deactivation such that:

$$\Phi^{\mathrm{Ln}} = \frac{k_r}{k_r + k_{nr}} \quad (\mathbf{1.3})$$

In addition to high quantum yields, complexes should also possess large molar extinction coefficients for absorption. The molar extinction coefficient, ε, is an intrinsic property of a molecule and describes how strongly a species absorbs light at a given wavelength. It can be related to concentration, *c*, and experimentally measured absorbance, *A*, by the Beer-Lambert Law, where l is the pathlength of the light travelling through the sample.

$$A(\lambda) = \varepsilon(\lambda)cl \quad (\mathbf{1.4})$$

The photoluminescence quantum yield and molar extinction coefficient of an emissive complex can be used to calculate a brightness parameter, *B*, as in equation 1.5.

$$B(\lambda) = \varepsilon(\lambda)\phi \quad (\mathbf{1.5})$$

Here, the brightness corresponds to the product of the molar extinction coefficient at the wavelength of the absorption maximum and the quantum yield when excited at this wavelength. From this equation, it can be seen that practical probes for fluorescence imaging require both high quantum yields and large molar extinction coefficients.

1.1.6 Ligands for Ln(III) complexes

As discussed previously, the highly contracted nature of the 4f orbitals means that interactions between Ln(III) ions and their ligands are mostly electrostatic in nature. Ln(III) ions usually prefer to be 8- or 9-coordinate in solution. In lanthanide coordination chemistry, the ligand can be used to control thermodynamic and kinetic stability, solubility, responsiveness to the environment and photophysical properties.

In most of the applications of lanthanide coordination chemistry, stability towards lanthanide ion dissociation is a key requirement. Much of the development of ligands for lanthanide(III) ions has stemmed from their use in Gd^{3+} contrast agents for Magnetic Resonance Imaging (MRI). All of the currently approved Gd^{3+} contrast agents use complexes with chelating or macrocyclic ligands such as DTPA (Magnevist), DOTA (Dotarem) and HP-DO3A (ProHance) (see Fig. 1.6).[8] The nature of these ligands provides favourable binding due to the chelate effect and those with macrocycles further increase the stability by reducing the entropic penalty caused by ligand rearrangement upon metal binding. This can be observed by comparing the binding constants of $[Gd(DTPA)]^{2-}$ and $[Gd(DOTA)]^{-}$ (log K = 22.3 and 24.7, respectively).[9]

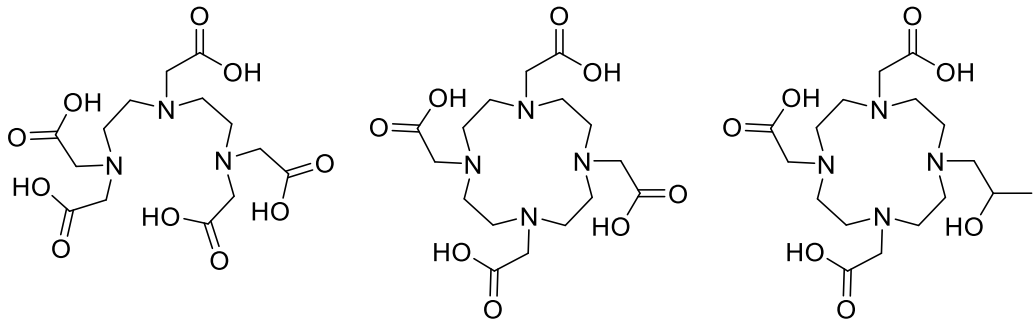

Figure 1.6 *From left to right*: H_5DTPA, H_4DOTA and H_3-HP-DO3A ligands for Gd^{3+}-based MRI contrast agents.

Whilst the macrocyclic ligands above are based on a cyclen core (1,4,7,10-tetraazacyclododecane, 12-N_4), it also possible to use 1,4,7-triazacyclononane (9-N_3) as the central macrocycle. The simple 9-N_3 analogue of DOTA (NOTA) is not a suitable ligand for lanthanide ion coordination as it only provides 6 donor atoms. However, NOTA has found use in other applications such as positron emission tomography (PET), where it has been used as a ligand in very stable C_3 symmetric complexes (log K = 31) of Ga^{3+}.[10] The carboxylate donor arms have also been replaced with phosphinate groups (Fig. 1.7), which confer various advantages over the carboxylate analogues. Firstly, the lower pK_a of the phosphinate groups (1.4 vs. 3.1 for the carboxylates) render them more stable to metal dissociation under acidic conditions.[11] Secondly, introduction of a pentavalent phosphorus(V) atom

allows for further functionalisation of the ligand and extra control of properties such as solubility.

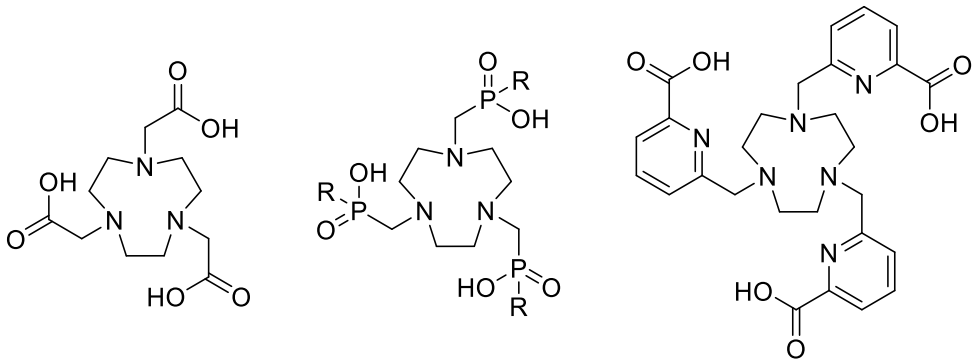

Figure 1.7 *From left to right*: 1,4,7- triazacyclononane-N,N',N''- triacetic acid (NOTA); the triphosphinic acid derivative of 9-N_3; and the tris-picolinic acid derivative of 9-N_3.

In order to make these 9-N_3 based ligands suitable for lanthanide coordination, extra donor atoms must be introduced. This can be achieved using the tris-picolinic acid derivative of 9-N_3. Addition of the pyridine ring allows the ligand to be used as a sensitising group in addition to its coordination behaviour. It can also provide the basis for functionalisation of the complex. Another example of a ligand that provides both chelating coordination and sensitisation is the tris-bipyridine cryptand shown in Figure 1.8. This ligand provides a cage in which the metal ion sits, however these complexes suffer from low aqueous solubility and low quantum yields due to the presence of bound solvent molecules, despite having reasonably high molar extinction coefficients (in the region of 18 000 mol^{-1} dm^3 cm^{-1}).[12]

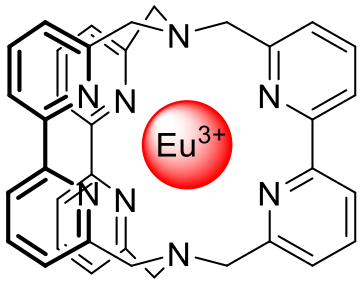

Figure 1.8 The europium complex of the tris-bipyridine macrobicyclic cryptand ligand.

A huge variety of chromophoric moieties has been used to sensitise lanthanide ions, although it ought to be noted that some chromophores cannot be used to sensitise multiple lanthanides. As discussed in Section 1.1.3, the chromophore excited state should lie at least 1700 cm^{-1} above the lanthanide emissive state in

order to efficiently sensitise the metal. In the cases of the most emissive lanthanides, the Eu(III) $^5D_0$ state has an energy of around 17 200 cm^{-1}, compared to 20 500 cm^{-1} for the $^5D_4$ state of Tb(III). As a result, some chromophores are better tuned to sensitise certain lanthanide ions.

Examples of sensitising groups that have been utilised in lanthanide(III) complexes include pyrenes and 8-hydroxyquinolinates (for near-IR emitting Er(III), Nd(III) and Yb(III));[13,14] 1-hydroxypyridin-2-one (1,2-HOPO) for Eu(III);[15] and 2-hydroxyisophthalamide (IAM) for Eu(III), Tb(III), Dy(III) and Sm(III).[16]

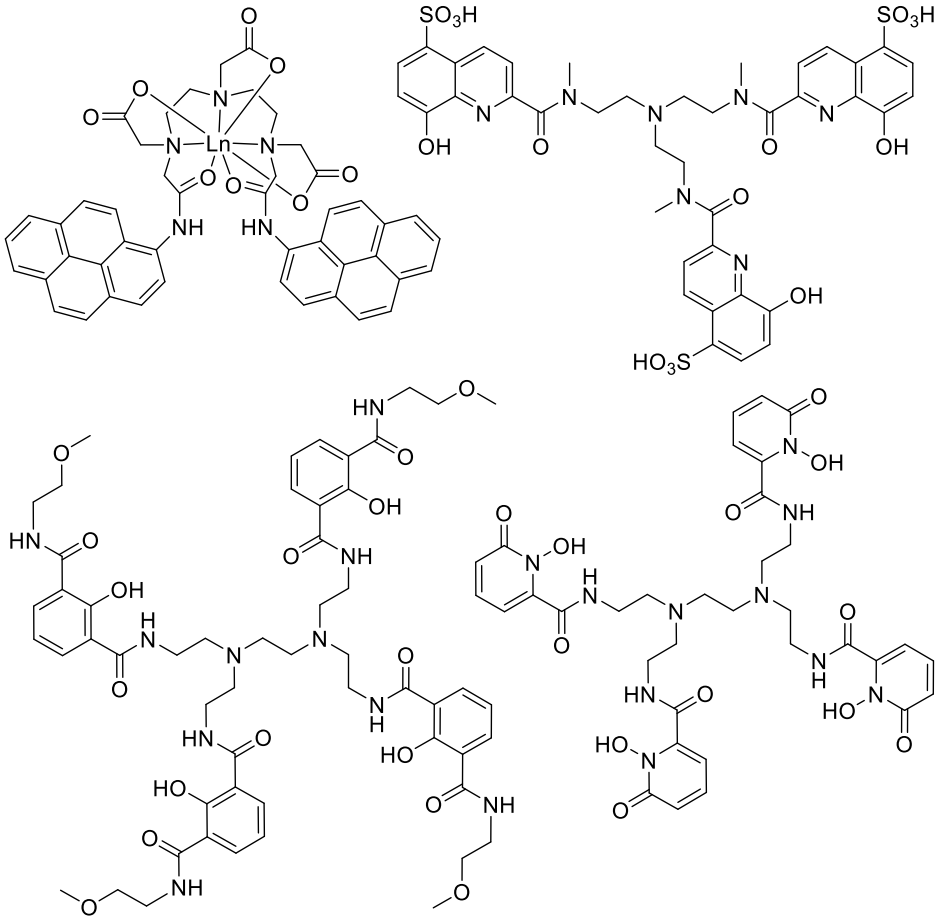

Figure 1.9 *Clockwise from top left*: DO3A appended with pyrene groups (Ln = Er(III), Nd(III) or Yb(III)); 8-hydroxyquinolinate sensitisers attached to a tripodal chelating platform; a tripodal ligand bearing 1,2-HOPO groups; and a similar ligand with 2-IAM sensitisers.

Some further examples of complexes bearing pendant chromophore arms are shown in Figure 1.10. Each of these examples and their derivatives possess absorption maxima in the range 330-410 nm, making them suitable for *in cellulo* imaging (excitation at these wavelengths avoids co-excitation of endogenous

fluorescent biological molecules). Tetraazatriphenylene based chromophores (Fig. 1.10, *left*) exhibit fast intersystem crossing and have suitable triplet excited energy (24 000 cm^{-1}) for sensitisation of both terbium(III) and europium(III).[17] Acridone groups (Fig. 1.10, *centre*) have also been investigated as pendant chromophores. They showed promising absorption characteristics (λ_{max} 410 nm, ε_{H2O} 5300 mol^{-1} dm^3 cm^{-1}),[18,19] but the highly solvent-dependent π-π^* singlet excited state is significantly lower in energy in polar solvents (such as water, alcohols) than in non-polar media. As a result, in polar media the rate of ligand fluorescence is greatly increased compared to the rate of intersystem crossing, meaning this chromophore is not usually suitable for use *in cellulo*. Extensive use has been made of azaxanthones and their sulphur analogues, azathioxanthones (Fig. 1.10, *right*). These systems have triplet excited state energies between 23 500 and 25 000 cm^{-1}, and a low ligand fluorescence quantum yield making them suitable for sensitising both europium(III) and terbium(III). Unlike the acridone group, the pyridine nitrogen binds to the metal centre. Substitution of oxygen for sulphur shifts the absorption maximum from 335 to 375 nm, although the sulphur analogue does have increased ligand fluorescence.[20] Complexes bearing aza(thio)xanthone and tetraazatriphenylene sensitisers have been used in live cell stains for the mitochondria[21] and lysosomes,[22] as well as probes for bicarbonate,[23] citrate,[24] lactate,[24] and pH.[25] The large size of these chromophores means that a maximum of two sensitisers can be appended to a 12-N_4 macrocycle.

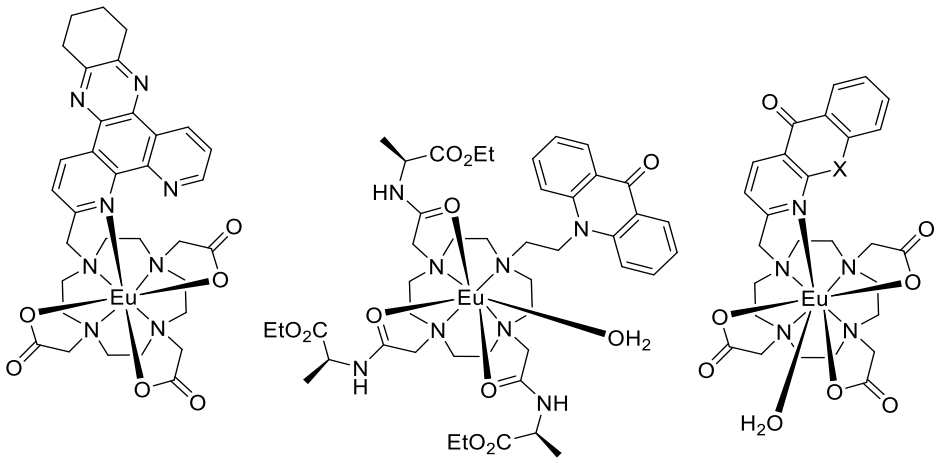

Figure 1.10 A selection of europium(III) complexes bearing pendant chromophore arms. *From left to right*: tetraazatriphenylene, acridone, azaxanthone (X = O) or azathioxanthone (X = S).

The various chromophores discussed above are all believed to use excited states corresponding to *n*-π^* or π-π^* transitions to sensitise lanthanide luminescence, which limits their molar extinction coefficients, and hence the complex brightness. An alternative class of chromophores have been shown to utilise an internal charge transfer (ICT) excited state. These chromophores possess pyridylarylalkynyl structures with electron rich aryl groups and electron deficient pyridine groups, separated by a conjugated alkyne linker (see Fig. 1.11). This creates a large charge separation along the chromophore, resulting in a broad ICT absorption band. Chromophores of this type were first used in lanthanide coordination chemistry in the early 1990s, incorporated into chelating aminopolycarboxylate ligands,[26] and have also been attached to 9-N_3 as pendant chromophore arms (see Fig 1.11, *right*).[27] The europium(III) complex of this macrocyclic ligand exhibited a molar extinction coefficient of 48 400 M^{-1} cm^{-1} and a luminescence quantum yield of 22% in aqueous solution.[28] However, the absorption maximum of 315 nm is somewhat too short for biological application (as discussed above). The complex was not able to efficiently sensitise terbium(III). This can be attributed to the fact that the ligand excited state is too low-lying, facilitating back energy transfer from the terbium(III) ion.

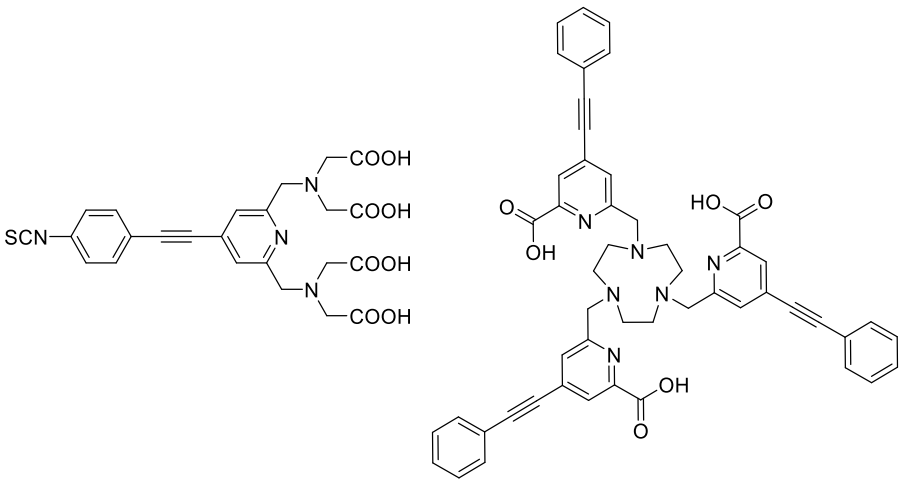

Figure 1.11 Early examples of pyridylarylalkynyl chromophores for europium(III) complexes.[26,27]

The advantage of these systems is that the absorption maximum can be tuned by the addition of electron donating groups to the aryl group of the chromophore. The

more electron-rich the aryl group becomes, the more the absorption maximum is shifted to longer wavelengths. Some examples are shown in Fig. 1.12.

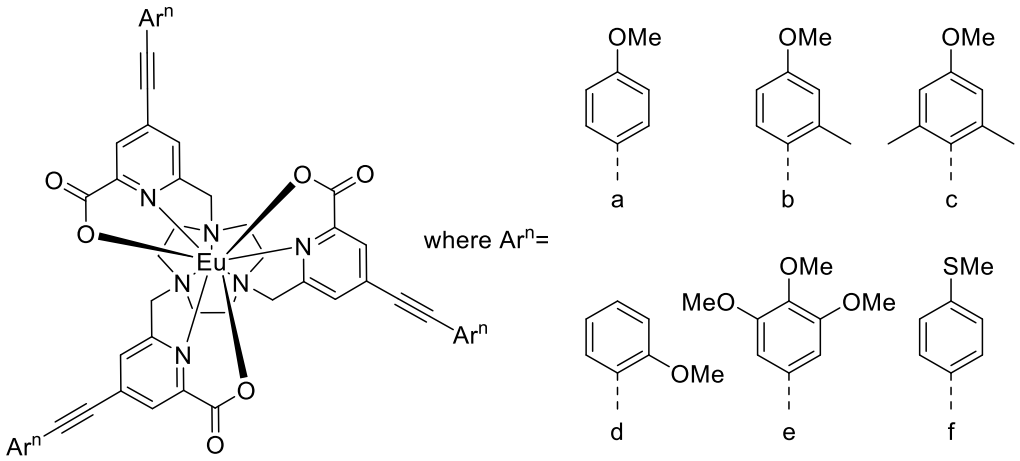

Figure 1.12 Examples of various Eu(III) complexes, **[Eu.Lc^{n}]**, containing different aryl substituents on the pyridylarylalkynyl chromophores. The photophysical properties of the Eu(III) complexes are shown in Table 1.2.[29]

Table 1.2 Photophysical properties for selected Eu(III) complexes bearing pyridylarylalkynyl chromophores. All measurements made in MeOH solution.[29]

Complex	λ_{max} / nm	ε / M^{-1} cm^{-1}	Φ / %	τ / ms
[Eu.Lc^{a}]	339	58 000	42	0.99
[Eu.Lc^{b}]	345	60 000	55	0.97
[Eu.Lc^{c}]	351	60 000	45	0.90
[Eu.Lc^{d}]	339	60 000	41	1.01
[Eu.Lc^{e}]	341	60 000	8	0.49
[Eu.Lc^{f}]	349	60 000	32	0.85

n.b. the units given in Ref [29] for the extinction coefficient, *ε*, are incorrect.

It is clear to see that addition of electron-donating groups in the conjugated *ortho* and *para* positions (relative to the alkyne group) causes a bathochromic shift in the absorption maxima but addition of alkoxy groups in the non-conjugated *meta* positions does little to affect the absorption properties (c.f. **[Eu.Lc^{a}]** and **[Eu.Lc^{e}]**). In every case, no ligand fluorescence was observed, suggesting highly efficient energy transfer to the lanthanide excited state. Each complex was highly emissive, with the exception of **[Eu.Lc^{e}]** which has a much lower quantum yield and shorter lifetime. It is possible that this is due to competition from alternative non-radiative

deactivation pathways that are present in this complex. It should be noted that the absorption bands for these derivatives are very broad and structureless, consistent with internal charge transfer character in the excited state. This behaviour is in contrast to the unsubstituted example in Fig. 1.11 which shows a structured absorption band corresponding to predominately π-π* character.[29]

The carboxylate donor groups can also be exchanged for phosphinate groups. As discussed earlier in this section, substitution of carboxylates by phosphinates confers several advantages, such as better stability towards metal dissociation, better control of solubility and opportunity for further functionalisation of the ligand. The methyl and phenyl phosphinate analogues of **[Eu.Lc^a]** (**[Eu.Lmp^a]** and **[Eu.Lpp^a]**, respectively) have been studied to determine what effect the change in donor groups has on the photophysical properties of the complex. DFT-optimised structures for the three yttrium(III) analogues showed little change in the overall calculated structure on changing from carboxylate to phosphinate groups (see Fig. 1.13),[29] and the DFT structure for **[Y.Lpp^a]** was consistent with the experimental X-ray structure for **[Eu.Lpp^a]**.[30] In the crystal structure, **[Eu.Lpp^a]** exists with a slightly distorted tri-capped trigonal prismatic coordination polyhedron with pseudo-C_3 symmetry. In solution, the complex exhibits only one ^{31}P NMR resonance and the ^{1}H NMR spectrum is consistent with time-averaged C_3 symmetry.

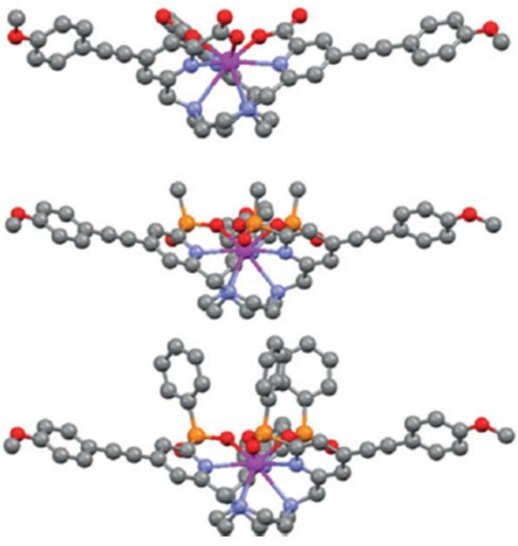

Figure 1.13 DFT-optimised structures of (*top* to *bottom*) **[Y.Lc^a]**, **[Y.Lmp^a]** and **[Y.Lpp^a]** showing increased shielding effect in the phosphinate complexes. Adapted with permission from Ref. [29]. Copyright (2014) Wiley-VCH Verlag GmbH & Co. KGaA, Weinheim.

The photophysical properties are displayed in Fig. 1.14 and Table 1.3. The red shift in the absorption maximum for **[Eu.Lc^a]** compared to the phosphinate complexes can be explained by the geometry of the complex. The tetrahedral geometry at the phosphorus atoms produced a more constrained chelate than the carboxylate. This, combined with the longer P-O bond compared to C-O, mean that the N_{py}-Ln bond length is slightly longer in the phosphinates than in the carboxylates. As a result, there is stronger coordination in the carboxylate complex with the Lewis acidic metal centre making the pyridine more electron deficient, and hence the chromophore has a larger charge separation leading to a longer wavelength absorption band.

Table 1.3 Photophysical properties for the carboxylate complex **[Eu.Lc^a]** and its, methyl phosphinate and phenyl phosphinate analogues. All measurements made in MeOH solution.[29]

Complex	λ_{max} / nm	ε / M^{-1} cm^{-1}	Φ / %	τ / ms
[Eu.Lc^a]	339	58 000	42	0.99
[Eu.Lmp^a]	331	58 000	43	1.18
[Eu.Lpp^a]	332	58 000	52	1.30

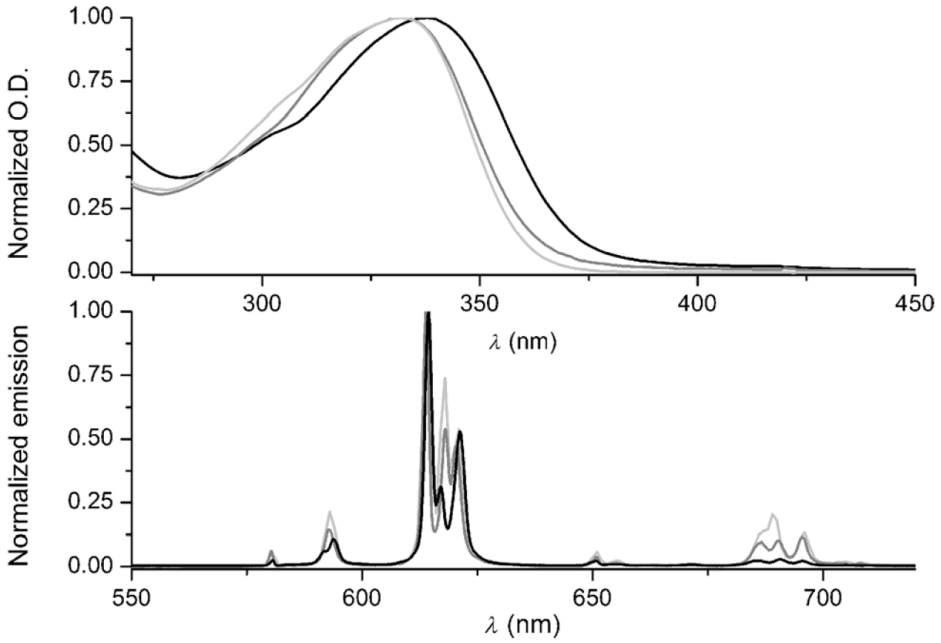

Figure 1.14 Absorption (*top*) and emission spectra (*bottom*) for **[Eu.Lc^a]** (*black*), **[Eu.Lmp^a]** (*dark grey*) and **[Eu.Lpp^a]** (*light grey*). Spectra were recorded in methanol at room temperature. Reprinted with permission from Ref. [29]. Copyright (2014) Wiley-VCH Verlag GmbH & Co. KGaA, Weinheim.

On changing from the carboxylate donor groups to the methyl and phenyl phosphinate groups, the emission lifetime also increases. This behaviour can be attributed to the increased shielding effect of the phosphinate moieties (see Fig. 1.13). The phosphinate substituents are positioned on the top face of the complex, thereby shielding it from solvent molecules.[‡] The quenching of the europium(III) excited state caused by O-H oscillations in the solvent is therefore reduced. For **[Eu.Lmp^a]**, the high quantum yield is retained in water (39%) with only a small drop in emission lifetime (1.01 ms).[29]

1.2 Introduction to circularly polarised luminescence

Circularly polarised luminescence (CPL) is a phenomenon that was first observed in 1948 by Samojlov whilst studying emission from single crystals of sodium uranyl acetate at low temperature.[31] In the late 1960s and early 1970s, CPL was observed in solution by Emeis and Oosterhoff, from chiral organic molecules and from the *Δ* and *Λ* enantiomers of $[Cr(en)_3]^{3+}$.[32,33] In 1974, the first results of CPL from lanthanide complexes were reported by Luk and Richardson.[34] These experiments concerned emission from complexes of Tb(III) with malic and aspartic acid ligands. Luk and Richardson observed that the form of the CPL was very sensitive to the ligand structure and that the complex fine structure in the total emission spectra of the terbium ion could be resolved using the CPL spectra. Much of the theoretical background to CPL was developed by Riehl and Richardson during the 1970s and 1980s.[35,36]

1.2.1 Theoretical background

Polarised light is classically described as an electromagnetic wave comprising a magnetic field vector and an electric field vector which are perpendicular to each other. Conventionally, the polarisation of the wave is determined by the direction of the electric field vector.

[‡] It should be noted that in pre-2015 publications, the phosphinate substituents were drawn as dashed, i.e. below the plane, when the complex was viewed from the top face. This is incorrect, as the substituents are orientated above the open face of the complex (see Fig. 1.13).

The electric field vector can be regarded as the superposition of two perpendicular components with equal frequency. When these two perpendicular components have identical amplitude, but are exactly a quarter wavelength phase shifted from one another, it results in a wave where the total electric field vector describes a helical wave as a function of time (see Fig. 1.15).

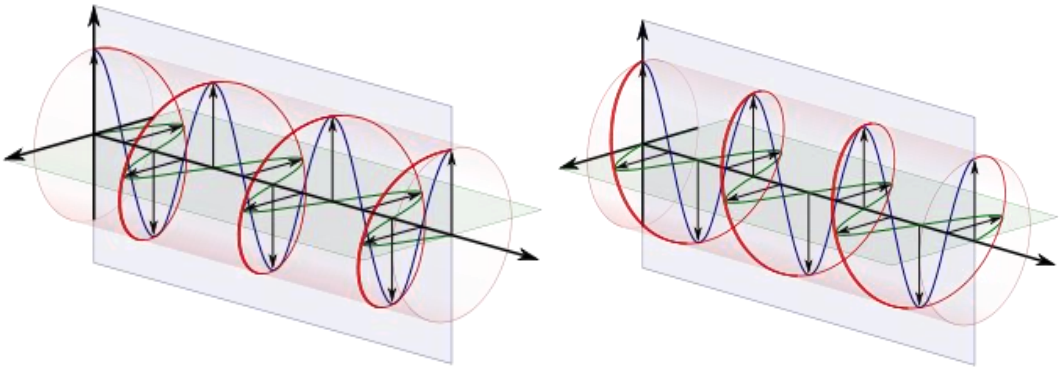

Figure 1.15 Left and right handed circularly polarised light; perpendicular components are in blue and green and the resulting electric field vector is shown in red.

Transformation between linearly and circularly polarised light can be achieved by passing the light through a quarter-wave plate at an angle of 45° to the optical axis. When linearly polarised light passes through the quarter-wave plate, one component is retarded by a quarter wavelength due to the birefringence of the quarter-wave plate, resulting in circularly polarised light.

Circularly polarised luminescence spectroscopy measures the differential emission of left- and right-handed circularly polarised light by a chiral species. It can be treated as a complementary tool to circular dichroism (CD) spectroscopy. In CD, it is the difference in absorption between left- and right-handed circularly polarised light that is measured, giving information about the ground state of the molecule. CPL spectroscopy measures the difference in emission intensity of left- and right-handed circularly polarised light after excitation with unpolarised light, and so explores the properties of the molecular excited state (see Eqn. 1.6).

$$\Delta I(\lambda) = I_L(\lambda) - I_R(\lambda) \qquad \textbf{(1.6)}$$

where I_L and I_R are the intensities of left- and right-handed CPL, respectively. Absolute measurements of emission intensity vary from instrument to instrument

and so can be difficult to compare. Instead, the magnitude of the CPL at a given wavelength can be calculated by comparison to the total emission (I_L + I_R), by defining an emission dissymmetry factor, g_{em}:

$$g_{\mathrm{em}}(\lambda) = \frac{2\Delta I(\lambda)}{I_{\mathrm{L}}(\lambda) + I_{\mathrm{R}}(\lambda)} \tag{1.7}$$

It can be seen from this definition that the maximum possible value for g_{lum} is ± 2, i.e. all emission at a given wavelength is polarised in one direction.

For a transition $i \longrightarrow j$, the emission dissymmetry factor, g_{em}, can also be written as

$$g_{\mathrm{em}} = \frac{4R_{ij}}{D_{ij}} \tag{1.8}$$

where R_{ij} is the rotatory strength of the transition $i \longrightarrow j$, and D_{ij} is the dipole strength of the transition $i \longrightarrow j$. These terms can also be expressed as functions of the magnetic transition dipole vector, $\mathbf{m}_{ij}$, and the electric transition dipole vector, $\boldsymbol{\mu}_{ij}$:

$$R_{ij} = \left|\boldsymbol{\mu}_{ij}\right| \cdot \left|\mathbf{m}_{ij}\right| \cos\theta_{\boldsymbol{\mu},\mathbf{m}} \tag{1.9}$$

$$D_{ij} = \left|\boldsymbol{\mu}_{ij}\right|^2 + \left|\mathbf{m}_{ij}\right|^2 \tag{1.10}$$

where $\theta_{\boldsymbol{\mu},\mathbf{m}}$ is the angle between the magnetic and electric transition dipole vectors. As a result, g_{em} can be rewritten as:

$$g_{\mathrm{em}} = 4\frac{\left|\boldsymbol{\mu}_{ij}\right| \cdot \left|\mathbf{m}_{ij}\right|}{\left|\boldsymbol{\mu}_{ij}\right|^2 + \left|\mathbf{m}_{ij}\right|^2}\cos\theta_{\boldsymbol{\mu},\mathbf{m}} \tag{1.11}$$

Typically the magnetic transition dipole is much smaller than the electric transition dipole, so equation 1.6 can be simplified to:

$$g_{\mathrm{em}} = 4\frac{\left|\mathbf{m}_{ij}\right|}{\left|\boldsymbol{\mu}_{ij}\right|}\cos\theta_{\boldsymbol{\mu},\mathbf{m}} \tag{1.12}$$

From this expression, it follows that the largest g_{em} values occur in magnetic dipole allowed transitions with small electric dipole character. It can also be seen that a value of zero is returned when the electric and magnetic dipole transition moments are orthogonal (i.e. $\theta_{\mu,m}$ = 90°) and is a maximum when $\theta_{\mu,m}$ = 0°, 180°. In the case of europium(III), it is the ΔJ = 1 transition that is magnetic dipole allowed, so it is in this emission manifold that we would normally expect to see the largest values for the emission dissymmetry factor.

CPL can be considered as a complementary technique to circular dichroism (CD). Whilst CD examines the chirality of the absorbing state, CPL can probe the emitting state of a transition. However, CPL can be particularly useful in lanthanide spectroscopy as it can be used to probe excited states that are difficult to access via absorption spectroscopy.

1.2.2 Instrumentation for the detection of CPL

Until the first commercial CPL spectrometer entered the market in recent years, the majority of CPL spectrometers were 'home-built'. In general, the spectrometer setup is modular (see Fig. 1.16), and home-built spectrometers tend to contain several common features. In several instances, spectra have been compared between different spectrometers and have been found to be broadly equivalent. Typically, excitation light is passed through a monochromator, allowing selection of the absorption maximum of the complex of interest. The sample is excited and the emitted light is collected at 90°. The emitted light first passes through a photoelastic modulator (PEM) and then a linear polariser. The PEM is made of an isotropically optically transparent material (e.g. quartz) which becomes birefringent on application of physical stress. It can behave as an oscillating quarter-wave plate at a frequency of 50 kHz when powered by an AC signal. In a cycle of the PEM, the left- and right-handed components of the circularly polarised light are alternately converted into the appropriate linearly polarised light which is selected by a linear polariser. The linearly polarised light is then passed through a scanning monochromator before detection. Two different methods of detection have been employed in home-built spectrometers. The first method (which is used in the

Durham spectrometer) was first reported by Steinberg and Gafni and comprises a photomultiplier tube (PMT) that collects the emitted photons. A lock-in amplifier operates in phase with the PEM cycle and extracts the left and right polarised components of the PMT output to an AC (CPL) and DC (total emission) signal.[37] The second method employs a photon gate coupled to the PEM. By synchronising the gate with the PEM signal, photons are directed into two different photon counters for detection.[38] The latter system was shown to be superior to the lock-in amplifier system for the detection of very small CPL signals. In the case of the Durham instrument, a red correction is embedded in the detection algorithm. A red correction is required because at longer wavelengths (such as in the red region of the visible spectrum), the photon energy is lower and therefore the probability of generating an electric current in the detector is reduced as it requires promotion of an electron across the band gap of the semiconducting material.

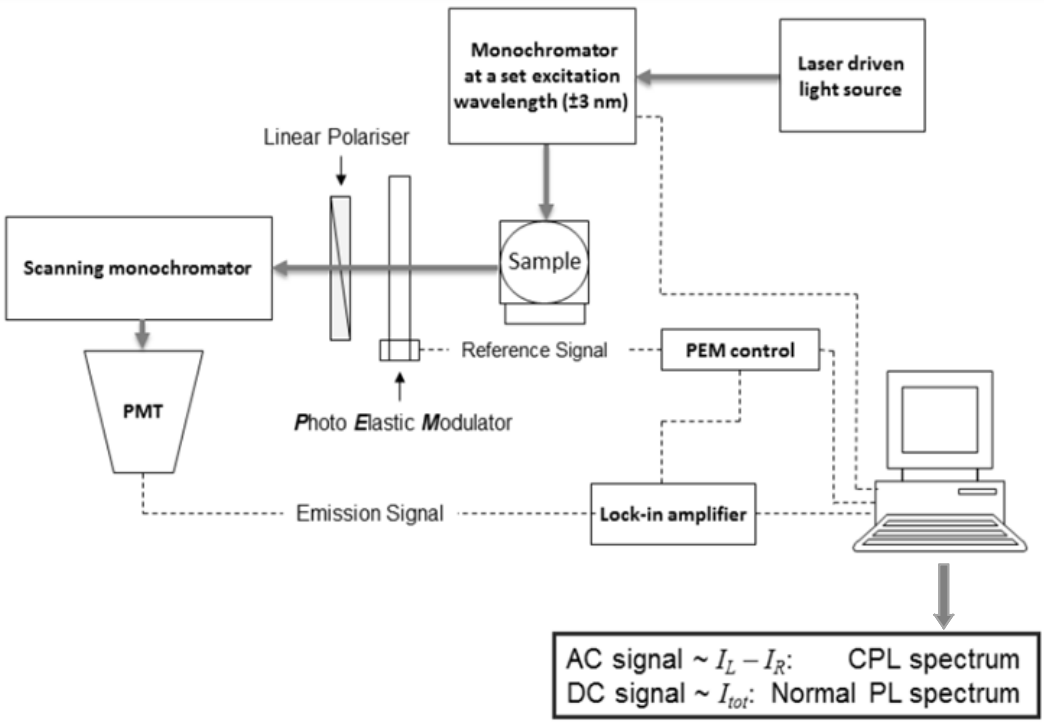

Figure 1.16 A schematic diagram of the Durham CPL spectrometer.[39]

1.3 CPL-active organic and transition metal systems

There are many examples of CPL-active systems in the literature, varying from single organic molecules to metal complexes and aggregated polymers. Each class of system has advantages and disadvantages for various applications, which will be discussed in the following sections.

1.3.1 Single Organic Molecule (SOM) systems

Examples of single organic molecules (SOMs) that emit circularly polarised luminescence have been observed from the early work of Emeis and Oosterhoff. They examined simple chiral ketones such as the bicyclic (+)-(*S,S*)-*trans*-β-hydrindanone (Fig. 1.17, *left*), which exhibited CPL in the ultraviolet region upon UV excitation of the carbonyl (g_{em} = 3.5 × 10^{-2} at 361 nm).[32] It ought to be noted that the luminescent-active carbonyl is itself planar (and hence inherently achiral), but that the nature of its electronic transition is influenced by the chirality of the structure in which it resides.

Since this observation, several other CPL-active ketones have been examined, mainly in molecules containing conformationally restricted polycyclic structures. Some examples based on norbornane and adamantane are shown in Fig. 1.17. All of these molecules exhibit g_{em} values within the 10^{-3}-10^{-2} range, but suffer from very low quantum yields (on the order of 10^{-5}).[40–42] Their small Stokes' shifts and UV-emission limits their practical use.

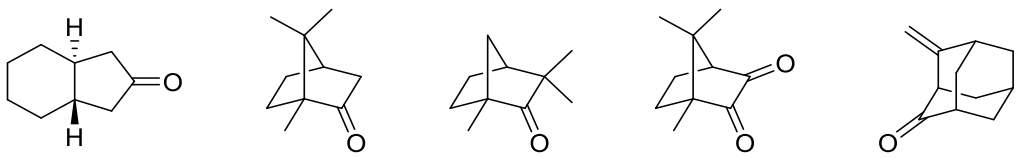

Figure 1.17 A selection of CPL-active chiral ketones; from left to right: (+)-(*S,S*)-*trans*-β-hydrindanone, (1*R*)-camphor, (1*R*)-fenchone, (1*R*)-camphorquinone and (1*S,* 3*R*)-4-methyleneadamantan-2-one.

In order to bring the emission wavelengths into the visible region of the spectrum, extended π-conjugated systems have also been developed. Among the most commonly used structures are BODIPY dyes (BODIPY = difluoro*bo*ron-*dipy*rromethene). BODIPY-based dyes are already used extensively in cellular

imaging but are usually achiral in nature.[43] Addition of chiral substituents to the BODIPY core has resulted in several examples of CPL-active BODIPY dyes. Addition of the dihydropyrrolone groups (Fig. 1.18, *left*) gave a BODIPY compound with a quantum yield of 48% and a g_{em} value of 0.94 × 10^{-3} at 546 nm (CH_2Cl_2). Interestingly, the excitation is thought to be via the dihydropyrrolone moieties, implying that there is an energy transfer occurring between the dihydropyrrolone groups and the BODIPY core.[44] Replacing the BF_2 bridge of the BODIPY core with the two enantiomers of an axially chiral 1,1'-bi-2-naphthol (BINOL) group gives two enantiomeric complexes which exhibit mirror imaged CPL (Fig. 1.18, *right*). Here, as with the chiral ketones earlier, the achiral BODIPY core is the chromophore and the chiral BINOL group perturbs the otherwise achiral environment. This compound exhibited very similar photophysical properties to the dihydropyrrolone-appended BODIPY (g_{em} = +0.7 × 10^{-3} (*R*), -0.8 × 10^{-3} (*S*) at 570 nm, Φ = 46%, $CHCl_3$). It can be seen in Figure 1.18 that the CPL signal is very weak and there is substantial noise in the data. The solid lines through the data are acquired by using the lineshape of the total emission band, overlaid onto the CPL data, and are therefore not true fits of the data. Here the BODIPY is excited directly, resulting in a small Stokes' shift (ca. 20 nm).[45]

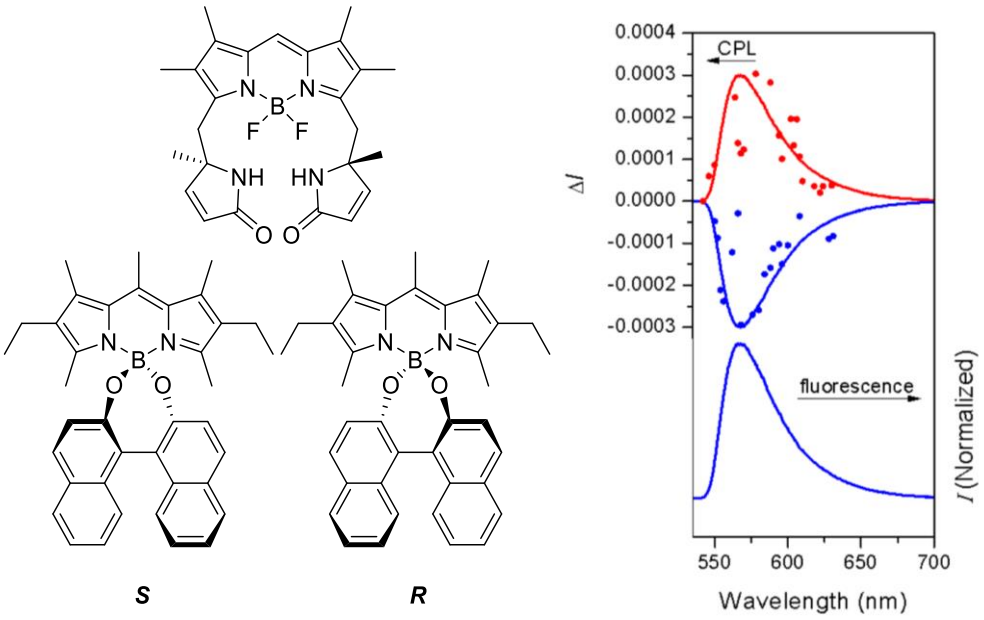

Figure 1.18 *Left*: examples of chiral BODIPY dyes bearing dihydropyrrolone (*top*) and 1,1'-bi-2-naphthol (BINOL) (*bottom*) substituents. *Right*: the total emission and CPL spectra for the *S* (*blue*) and *R* (*red*) enantiomers of the BINOL *O*-BODIPYs. Reproduced with permission from Ref. [45]. Copyright (2014) American Chemical Society.

In addition to the examples shown in Fig. 1.18, BODIPY monomers have been oxidatively coupled to produce dimers which contain an axis of chirality due to restricted rotation around a C-C single bond, in contrast to the previous examples where addition of a chiral substituent confers chirality to the BODIPY (see Fig. 1.19 for one example).[46] This compound exists as two enantiomers which can be assigned as a*R* and a*S*, and can be separated by chiral HPLC. The resolved enantiomers display mirror imaged CPL and CD spectra, with a Stokes' shift of 95 nm which is larger than most BODIPY dyes. The g_{em} values are $\pm 3.8 \times 10^{-3}$ at 655 nm in dichloromethane,[47] which is at the higher end of the range reported for single non-aggregated organic molecules.

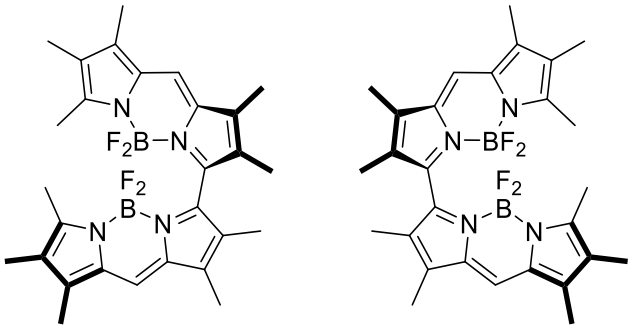

a*R* a*S*

Figure 1.19 A pair of axially chiral BODIPY dimer enantiomers.

Another class of organic compounds shown to exhibit CPL are helicenes and heterohelicenes. These molecules comprise *ortho*-fused aromatic rings which are sterically constrained to exist as helices, i.e. they are distorted from the expected planar conformation. As a result, they possess inherent chirality which is dependent on the direction of the helical twist. Recent examples of CPL-active helicenes include the work of the group of Tanaka in Tokyo (see Fig. 1.20). By following synthetic pathways involving achiral starting materials and the use of chiral metal complexes as catalysts, they have created enantioenriched helicenes (>90% ee) with a fluorene core, which exhibit CPL in the visible region of the spectrum. They possess g_{em} values around -3×10^{-2} upon irradiation with UV light, and quantum yields around 30%.[48]

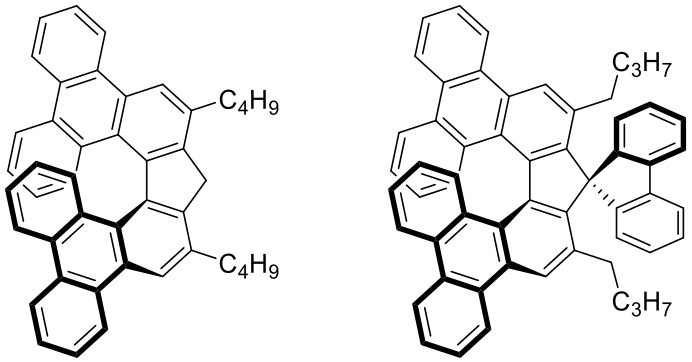

Figure 1.20 CPL-active helicenes with fluorene and spiro-fluorene cores.

These g_{em} values are an order of magnitude higher than have been reported for other helicenes that do not bear the fluorene core. However, the quantum yield is lower than has been observed for the BODIPY systems discussed previously, perhaps due to the distortion of the extended π-conjugation in the helicenes.

Using further enantioselective synthetic routes, Tanaka's group has also investigated 'S-shaped' double helicenes which showed enhanced CPL activity compared to the parent single helicenes. For example, the double azahelicene in Figure 1.21 has a g_{em} value more than 10 times higher than its parent single helicene (-1.1×10^{-2} vs. $< 1 \times 10^{-3}$ (below the limit of detection)).[49]

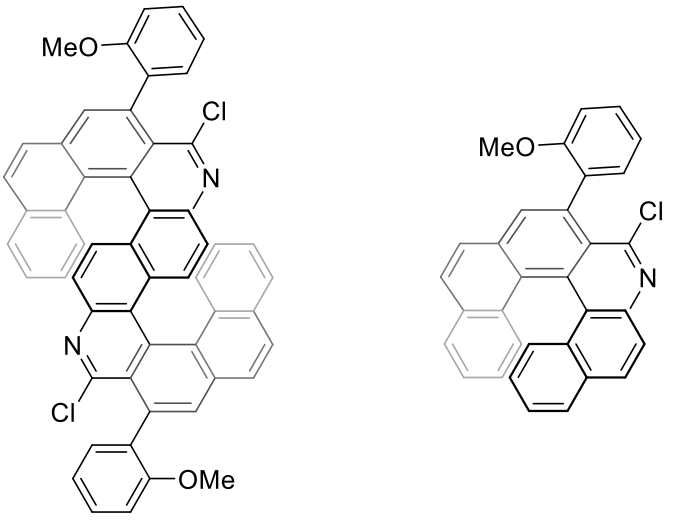

Figure 1.21 The *M*-double azahelicene (*left*) and its parent single helicene (*right*).

A very recent example of a CPL-active azahelicene utilises rigid linkers between helicene monomers to create a figure-of-eight shaped azahelicene dimer (see Fig.

1.22). Rather than enantioselective synthesis, resolution of the diethynyl helicene monomer is achieved by chiral HPLC before oxidative 'Eglinton type' Cu(II)-catalysed homocoupling forms the twisted dimer. The rigid structure limits non-radiative decay pathways, resulting in the dimer having a quantum yield of 55% with a g_{em} value of 8.5 × 10^{-3} at 588 nm. However, the extended π-conjugation shifts the absorption maximum to 536 nm, resulting in a small Stokes' shift.[50]

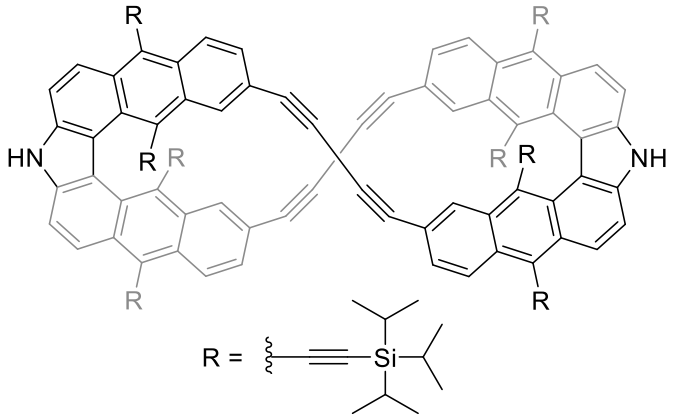

Figure 1.22 The structure of the figure-of-eight shaped azahelicene dimer.

Other recent examples of CPL-active heterohelicenes include the use of silicon,[51] boron,[52] and platinum[53] in the structures.

In summary, CPL-active single organic molecules offer high quantum yields which can, to some extent, make up for the low g_{em} values they exhibit. Weak CPL can be attributed to the primarily electric dipole nature of the transitions involved, which is an inherent limitation in these systems. Their solubility in organic solvents means they can be handled easily and are less prone to aggregation, which is beneficial in applications such as display devices.

1.3.2 Supramolecular aggregates

Species which aggregate in solution have been explored as a method of increasing emission dissymmetry factors in organic systems. Since the photophysical properties of organic molecules can often be controlled by self-assembly, extended planar aromatic systems offer the potential for highly circularly polarised emission. Often, aggregated assemblies amplify the small emission dissymmetry observed in

the monomeric units. Excimer-like properties have been observed in π-stacked chromophores such as the perylene bisimide shown in Figure 1.23. The two perylene units are attached to a cyclohexane ring which confers chirality to the molecule. In dilute solutions (10^{-5} M in chloroform) emission from both the monomeric and excimer forms are visible. The observed CPL is an order of magnitude stronger from the excimer state and is of opposite handedness to the monomer.[54]

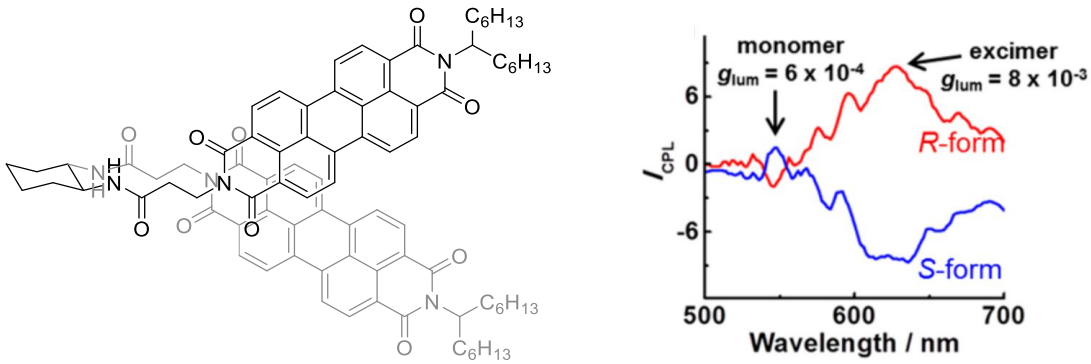

Figure 1.23 The structure of the *S*-form of the perylene bisimide (*left*) and the CPL spectra of the two enantiomers at a concentration of 1 × 10^{-5} M in $CHCl_3$ (*right*). Adapted with permission from Ref. [55] Copyright (2015) American Chemical Society.

In methylcyclohexane solution, self-assembly of the molecules into extended helical fibres could be observed by SEM and AFM, the helicity of which depended on the chirality in the cyclohexane core. The CPL of the aggregated fibres was observed to possess much higher emission dissymmetry than the monomer or excimer CPL and showed a change of sign compared to the excimer (see Fig. 1.24). The fibres formed from the opposite enantiomer of the monomer exhibited mirror imaged CPL.

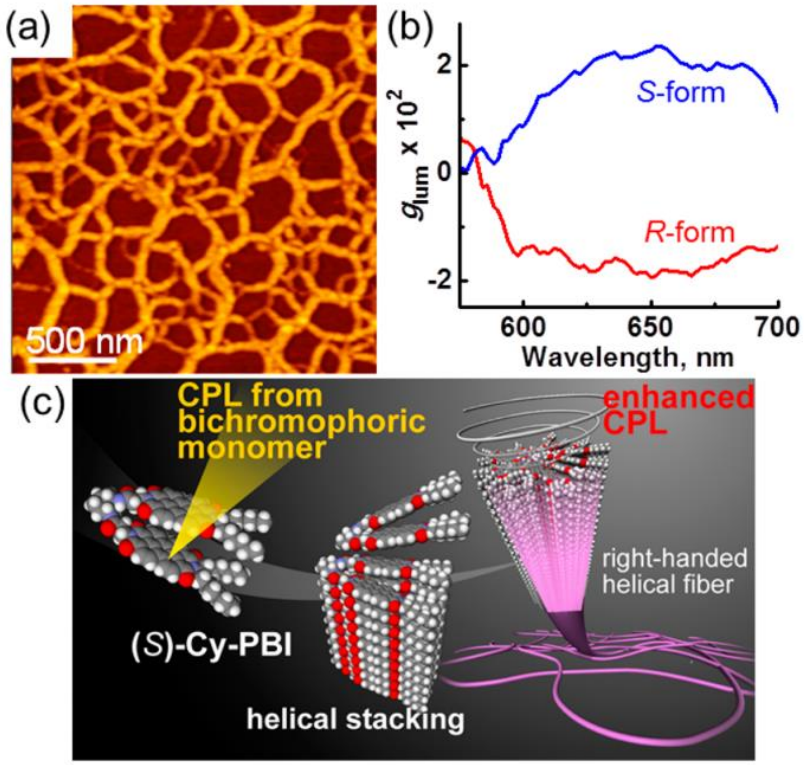

Figure 1.24 (*a*) An AFM image showing the network of fibres formed from aggregation of the chiral cyclohexyl perylene bisimides, (*b*) a g_{lum} vs wavelength plot for the aggregated fibres and (*c*) a schematic representation of the self-assembly process. Reprinted with permission from Ref. [55]. Copyright (2015) American Chemical Society.

Whilst self-assembled structures may provide larger g_{em} values, there are significant drawbacks to their use in CPL studies. It is often difficult to be certain of the speciation of these compounds as it is very dependent on solvent and concentration. Additionally, extended aggregated structures often suffer from low emission efficiency and can be very difficult to process, which limits their applicability in several applications, such as security printing, display devices and biosensing.

1.3.3 Transition metal complexes

In addition to the incorporation of a platinum ion into the backbone of the inherently chiral helicene discussed above, chiral transition metal complexes have also been investigated as CPL-emissive species. They have potential applications in 3D display screens and optical storage devices. Synthesised by various methods including enantioselective synthesis, use of enantiopure ligands, and chiral resolution of racemic products, a number of CPL-active transition metal complexes have been studied. Many are based on the numerous examples of emissive

transition metal complexes of Ru(II), Os(II) and Ir(III) developed for use in display devices. Transition metal complexes have the advantage that emission wavelength can be tuned by systematic ligand design, and complexes often possess high phosphorescence efficiency. However, some chelate complexes of transition metals have exhibited photo-induced racemisation.[56–60] Examples of complexes containing achiral ligands include the iridium(III) complexes shown in Figure 1.25. These complexes are synthesised as racemates and resolved by chiral supercritical fluid chromatography. The homoleptic fluorinated complex emits CPL in the blue-green region of the spectrum with a g_{em} value of $+1.99 \times 10^{-3}$ at 495 nm for the *Λ*-enantiomer while the heteroleptic acac complex has slightly less polarised emission ($g_{em} = +1.72 \times 10^{-3}$ at 515 nm). Both complexes have quantum yields in the region of 30%.[61] Recently, similarly designed Ir(III) complexes with achiral ligands have been investigated in terms of their circularly polarised electroluminescence (CPEL), displaying similar profiles to CP photoluminescence spectra. Again, emission dissymmetry factors are of the order of 10^{-3}.[62]

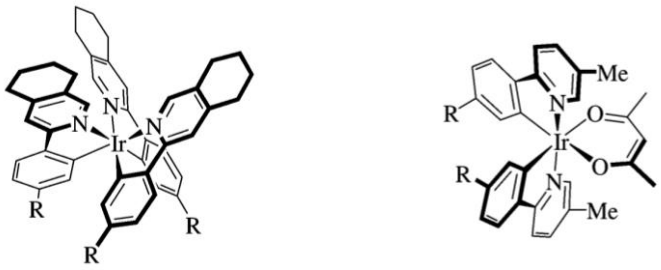

Figure 1.25 The structures of the *Λ* enantiomers of a homoleptic (*left*) and a heteroleptic (*right*) Ir(III) complex (R = fluorine). Adapted with permission from Ref. [61] Copyright (2008) American Chemical Society.

Other examples have incorporated chiral ligands to create CPL-active transition metal complexes. Many of these examples feature pinene units in the ligand structure. Cage-like structures containing pinene-appended bipyridine ligands have been shown to form helical complexes with Ru(II) and Zn(II). The enantiomers of each complex emitted mirror imaged CPL, with g_{em} values of $\pm 5.4 \times 10^{-4}$ and $\pm 2.4 \times 10^{-3}$ for the Ru(II) and Zn(II) complexes, respectively (see Fig. 1.26).[63] Interestingly, since Zn(II) has a d^{10} electron configuration, the emission in this complex is assumed not to involve metal orbitals and is purely a triplet ligand centred emissive state, in contrast to the Ru(II) analogue.

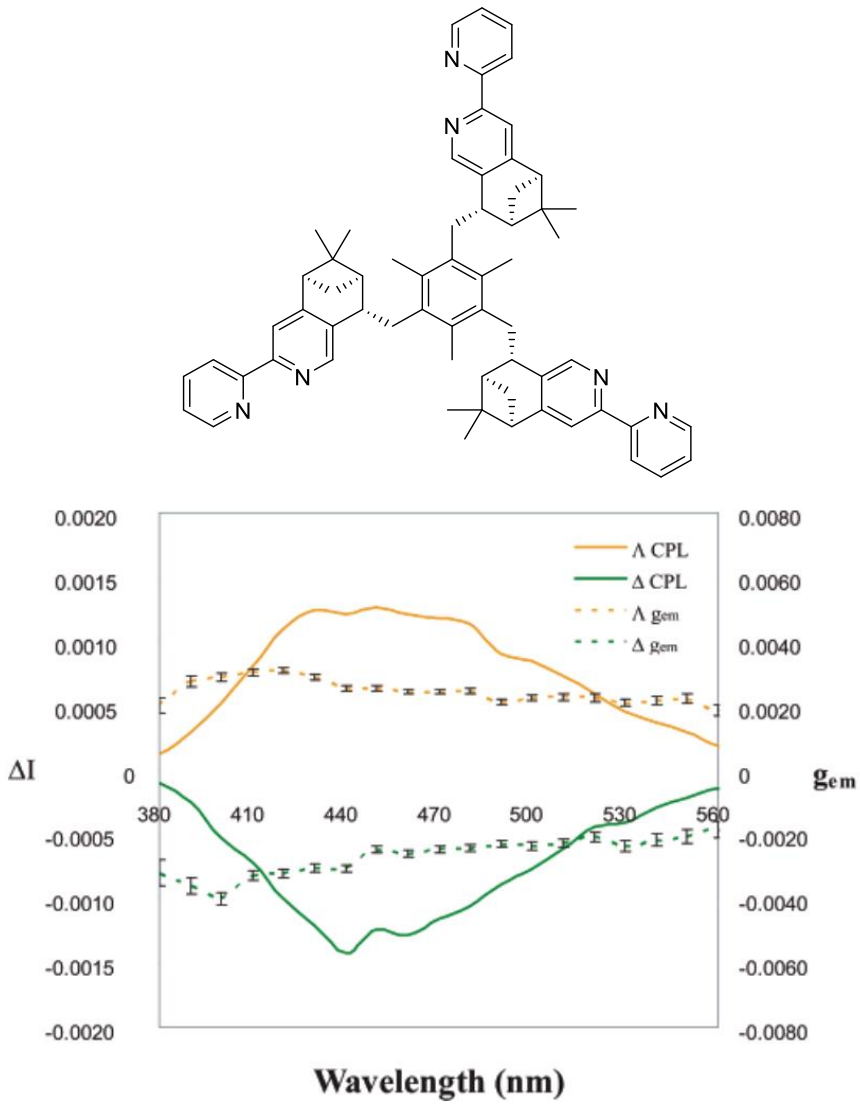

Figure 1.26 The (-)-pinene substituted bipyridine ligand which forms the *Δ*-helical Ru(II) and Zn(II) cage complexes (*top*); and the CPL and g_{em} spectra for the two enantiomers of the Zn(II) cage complex (*bottom*). Reprinted with permission from Ref. [63]. Copyright (2007) American Chemical Society.

Recently, a pinene-based cyclometallated platinum complex has been shown to reversibly switch on CPL signal in response to temperature. In methanol solution, the complex exhibits no CPL, but in aqueous solution a CPL signal is observed at room temperature. On heating to 353 K, the CPL signal is lost, but recovers on cooling.[64] It has been proposed that in aqueous solution helical aggregation occurs, controlled by the remote chirality of the pinene. At increased temperatures, the aggregates decompose, returning to CPL-inactive monomers.

In summary, whilst the photophysical properties of transition metal complexes can be tuned by rational ligand design, their small emission dissymmetry factors still make their practical use a challenge.

1.4 Chiral lanthanide complexes

As described in Section 1.2.1, large g_{em} values are expected to occur in transitions with large magnetic dipole character and only small electric dipole contribution. Compared to the organic and transition metal complexes discussed previously, lanthanide complexes can offer unparalleled access to large emission dissymmetry factors, due to their magnetic dipole allowed transitions. This section will discuss various approaches to CPL-active lanthanide complexes with reference to the molecular design, before describing some examples of the use of CPL to probe various biological analytes.

1.4.1 Design and control of chirality

There are several approaches that have been utilised to synthesise chiral lanthanide complexes. They can be broadly categorised as follows: (a) complexes that use enantiopure ligands to favourably form one enantiomer of complex over the other; (b) dynamically racemic complexes; (c) complexes that are formed as racemic mixtures and are separated into their enantiomers by methods such as chiral HPLC or co-crystallisation.

Arguably the easiest method of creating a chiral complex is to use chiral ligands. Examples of this strategy have already been discussed for transition metal complex in Section 1.3.3. In addition to the use of chelating and macrocyclic ligands, discussed in Section 1.1.6, β-diketonates have been shown to be effective ligands for lanthanide(III) ions due to the oxophilic nature of the metal ions and the ease of control of absorption characteristics, with relatively simple structural modifications.[65] Typical lanthanide(III) complexes of β-diketonate ligands can either possess three β-diketonate ligands, forming a neutral 6-coordinate complex, leaving the remaining coordination sites for solvent molecules, or can comprise or four ligands creating an anionic 8-coordinate complex. Examples of β-diketonates used

in lanthanide(III) complexes include hexafluoroacetylacetonate (hfac), thenoyltrifluoroacetonate (TTA), and trifluoromethylcamphorate (facam) (see Fig. 1.27). In fact, commercially available [Eu(facam)$_3$] in DMSO solution has been used as a standard for CPL spectrometers,[36] although its sensitivity to water has led to suggestions it should be replaced by alternatives. Furthermore, combining chiral ancillary ligands with achiral and chiral β-diketonates can modify the CPL of the complexes in solution. Examples include axially chiral BINAP-type ligands, and point chiral 'PyBox' ligands where chiral oxazoline groups are attached to a pyridine, making a tridentate neutral donor.[66–68]

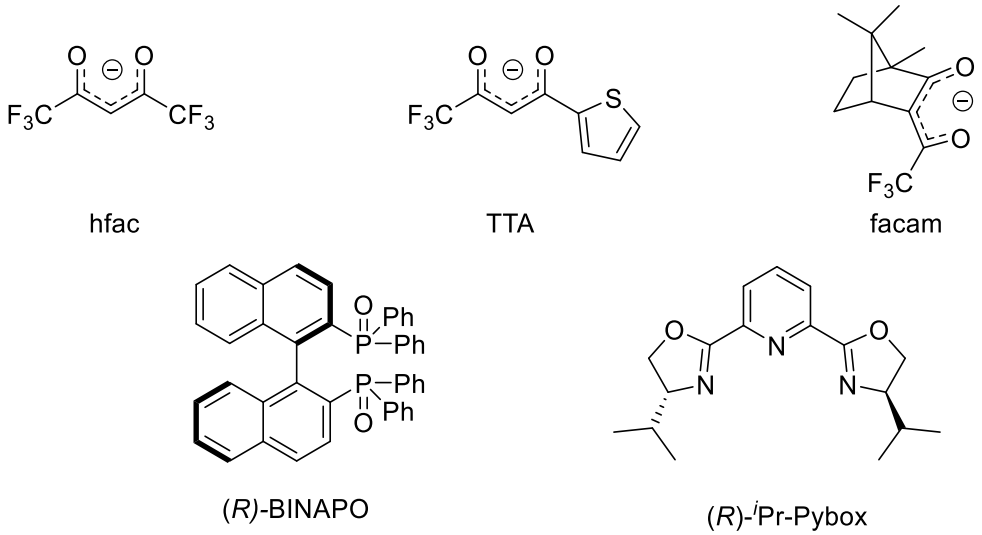

Figure 1.27 *Top*: examples of β-diketonate ligands used in Ln(III) coordination chemistry; *bottom*: chiral ancillary ligands used in CPL-active lanthanide complexes.

The largest reported emission dissymmetry factor has been from a complex containing chiral β-diketonate ligands. The Cs[Eu((+)-hfbc)$_4$] complex (where hfbc = heptafluorobutyrylcamphorate) showed a g_{em} value of +1.38 at 595 nm (see Fig. 1.28).[69] This ligand was also successful in producing highly circularly polarised emission from the samarium(III) complex (g_{em} values as large as -1.15 at 553 nm).[70] The analogous complexes with other Group 1 metals did not reveal such extraordinary emission dissymmetry and demonstrated multiple species in solution, whereas only one species was observed for the Cs^+ analogue.[71]

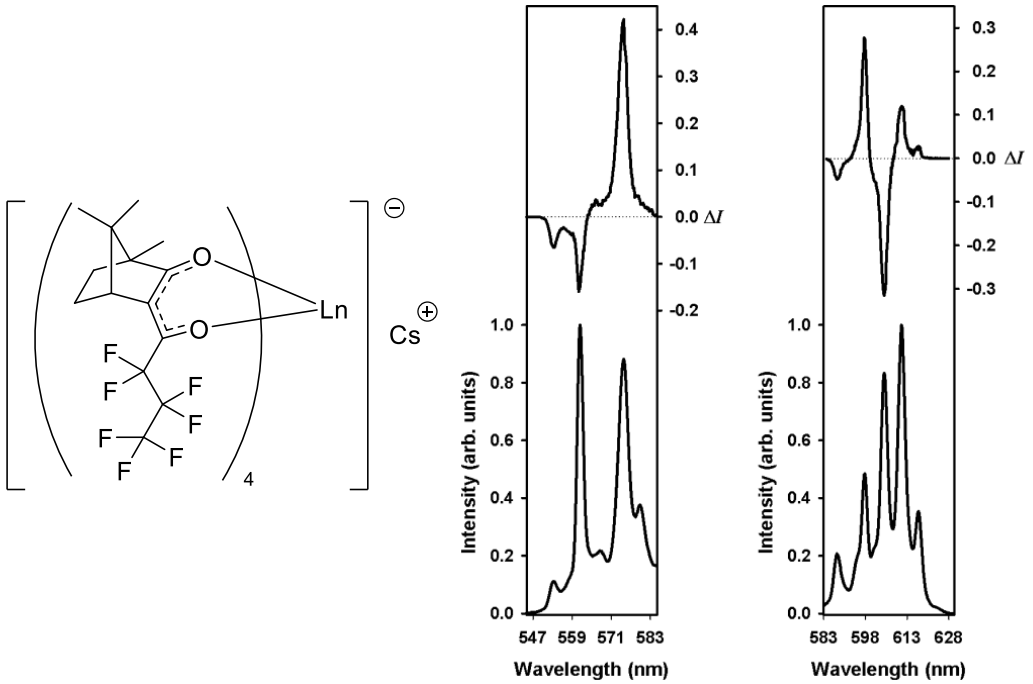

Figure 1.28 The structure of Cs[Ln((+)-hfbc)$_4$] (*left*) and the CPL spectra of Cs[Sm((+)-hfbc)$_4$] in the $^4G_{4/2}\rightarrow{}^6H_{5/2}$ and $^4G_{4/2}\rightarrow{}^6H_{7/2}$ transitions (*right*, $CHCl_3$, 295 K, λ_{exc} 338 nm) Reprinted with permission from Ref. [70]. Copyright (2011) American Chemical Society.

To rationalise the extraordinarily large emission dissymmetry observed in Cs[Eu((+)-hfbc)$_4$], it is necessary to consider the factors affecting the strength of CPL signals. As discussed in Section 1.2.1, the g_{em} value is dependent on the relative strength of the magnetic and electric dipole transition vectors, and the angle between them. In 8- or 9-coordinate C_4-symmetric environments (i.e. square prismatic and (twisted) square antiprismatic), the angle between the electric and magnetic dipole transitions is dependent on the twist angle between the two ligand planes, i.e. the atoms of the first coordination sphere.[72] If this angle, α, is 0° or 45° (corresponding to cubic or perfect square antiprismatic environments, respectively), then the first coordination environment is locally achiral. In these systems, CPL strength should follow a $\sin 2\alpha \cos 2\alpha$ relationship. As a result, largest CPL strengths are expected where the twist angle is ±22.5°. In the case of Cs[Yb((+)-hfbc)$_4$], which adopts a similar axially symmetric twisted square antiprismatic structure in solution, the twist angle was found to be -41.4° meaning the first coordination sphere is almost perfectly achiral (see Fig. 1.29).[71] Clearly, this so-called static coupling mechanism cannot account for the large g_{em} values observed in this system. Instead, a dynamic coupling mechanism must be considered,

involving the metal-centred magnetic dipole transition and the nearby electric dipole transitions in the diketonate ligands. In this system, the electric quadrupole generated by the metal-centred transition induces electric dipoles centred on the ligands. If the angle of the ligand-centred electric dipoles is skewed compared to the molecular symmetry axis, this can break the symmetry of the inner coordination environment. In the case of Cs[Yb((+)-hfbc)$_4$], the ligand-centred electric dipole is along the line between the two oxygen atoms of the diketonate which is tilted at an angle of -27.5° with respect to the symmetry axis. When the magnetic dipole transition of ΔJ = 1 is active, the induced electric dipoles couple constructively to add rotational strength to the transition, making its emission highly circularly polarised.[65]

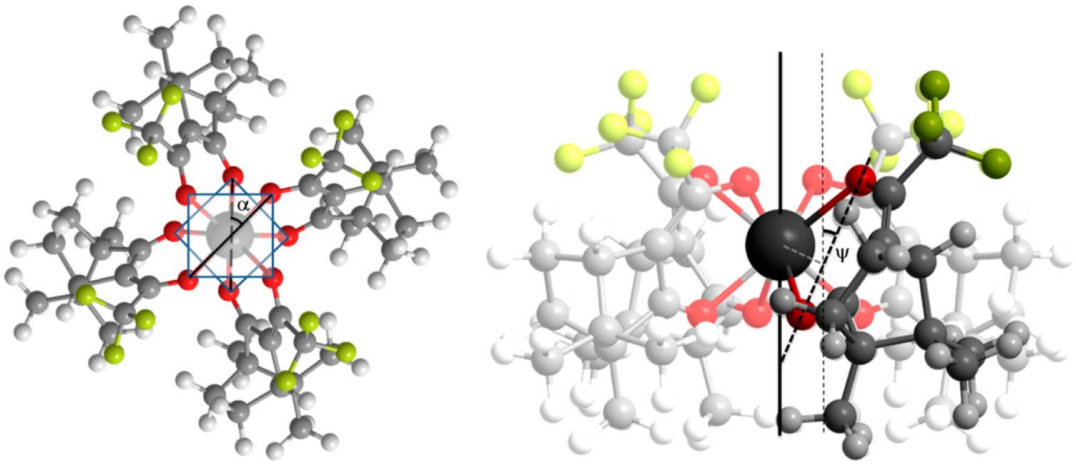

Figure 1.29 Solution state ($CHCl_3$) structure of Cs[Yb((+)-hfbc)$_4$] along (*left*) and perpendicular (*right*) to the C_4 symmetry axis. The angle, α, denotes the twist angle of the twisted square antiprism geometry while ψ denotes the tilt angle of the ligand-centred electric dipole relative to the symmetry axis. For ease of calculation, CF_3 groups were used in place of C_3H_7 chains. Reprinted with permission from Ref. [71]. Copyright (2012) American Chemical Society.

As discussed in Section 1.1.6, picolinate-based ligands are suitable for lanthanide(III) coordination. Examples of chiral dipicolinate derivatives have been used to form helical complexes of the form [ML_3]. This approach is exemplified by the work of Muller *et al.* who have used chiral dipicolinamides to form enantiomeric complexes with strong CPL activity. The two enantiomers of *N,N*'-bis(1-phenylethyl)-2,6-pyridinedicarboxamide were observed to self-assemble with Eu^{3+} ions with the (*R,R*) and (*S,S*) enantiomers forming the *Λ* and *Δ* complexes, respectively (see Fig. 1.30). Unfortunately, the complexes exhibit low luminescence

quantum yields, but their simple synthesis and strong CPL has led to the suggestion of their use as CPL calibration standards in the place of [Eu(facam)$_3$].[73]

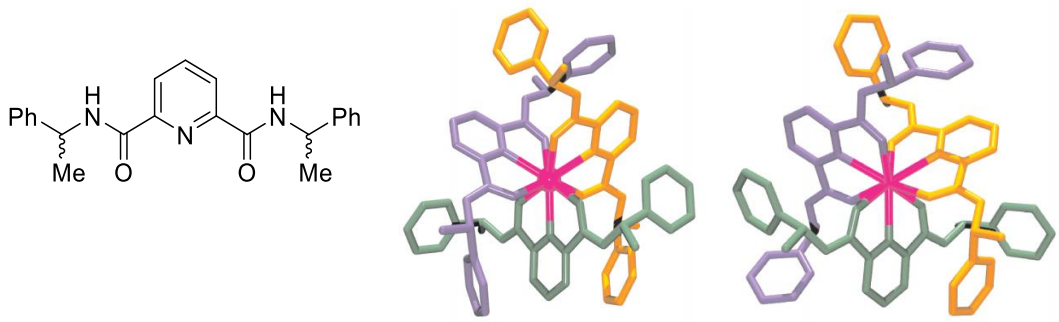

Figure 1.30 The structure of the *N,N'*-bis(1-phenylethyl)-2,6-pyridinedicarboxamide ligand (*left*) and schematic structures of the *Λ*-(centre) and *Δ*-(*right*) ML_3 helical complexes formed from (*R,R*) and (*S,S*) chiral dipicolinamides, respectively. Adapted with permission from Ref. [74]. Copyright (2011) American Chemical Society.

Combining the chiral aspects of these examples with the proven stability of the macrocyclic and chelating structures discussed earlier, offers the potential to create extremely stable chiral lanthanide(III) complexes. The increased rigidity of these complexes can also enhance their chiroptical behaviour. Numerous examples exist of macrocyclic ligands with remote chiral centres that are able to control the chirality of the resulting complexes. For example, amide donor groups with remote chiral centres have been shown to favour the formation of one complex helicity (either *Δ* or *Λ*) both in 9-N_3,[75] and 12-N_4 systems[76] (see Fig. 1.31). Briefly, helicity of the arms of a chelating complex can be described as either *Δ* or *Λ*, corresponding to a clockwise or anticlockwise arrangement, respectively. The torsion angle in the macrocyclic ring can be described by *δ* or *λ* depending on whether the angle is positive or negative. A more detailed explanation of the chirality in these aza-macrocyclic complexes is included in Chapter 2. In the case of the triazacyclononane example, the ratio of isomers was 15:1 for the europium(III) complex.[75] A similar approach has also been demonstrated where α-substituents on the carboxylate donor arms of DOTA type ligands can lock the conformation of the complex by providing a steric barrier to arm rotation.[77]

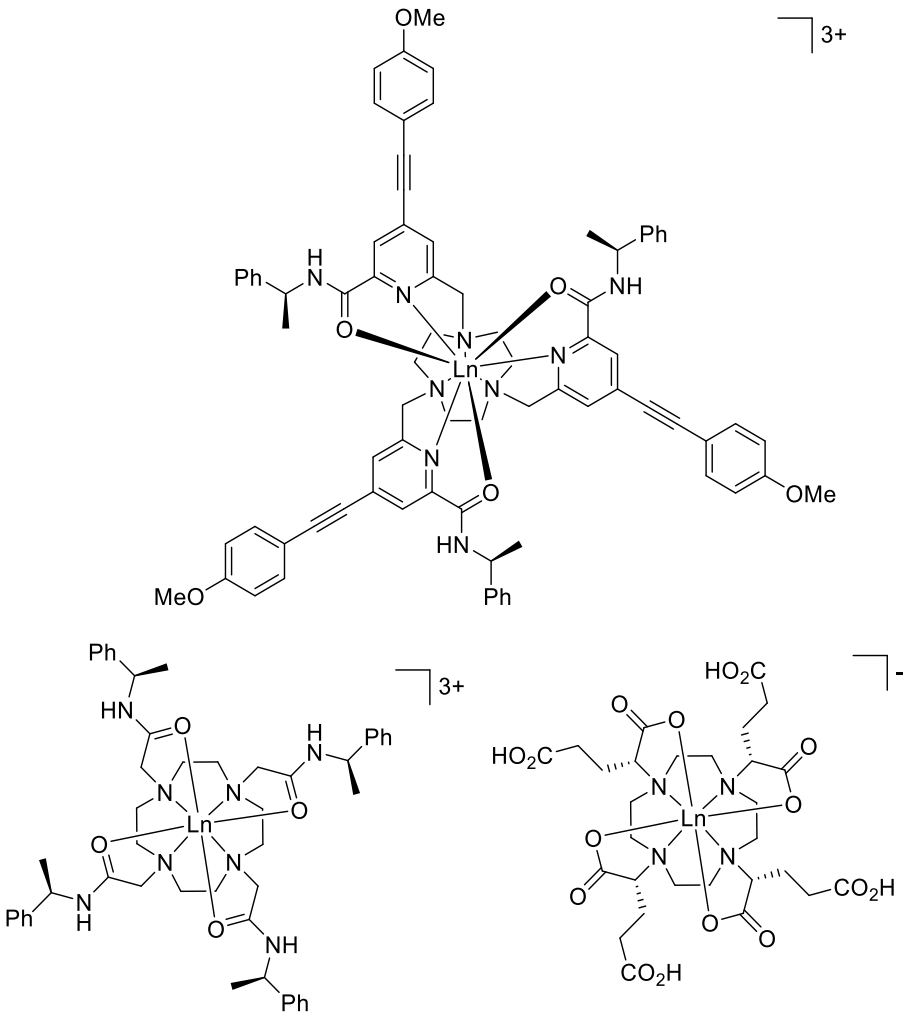

Figure 1.31 Representative examples of lanthanide(III) complexes where the inclusion of a chiral centre on a donor arm can control the helicity of the complexes.

Alternatively, *C*-substituted macrocycles such as those shown in Fig. 1.32 have also demonstrated the ability to preferentially induce the formation of one complex stereoisomer. Addition of chiral centres to the macrocyclic framework can provide an insurmountable barrier to the ring inversion process which is required for interconversion. Addition of four methyl substituents onto a DOTA framework yields a ligand whose ytterbium(III) complex ((*SSSS*)-[Yb[Me_4DOTA]$^-$) exists as two isomers in solution. These were identified to be the *Λ*-(*λλλλ*) and *Δ*-(*λλλλ*) isomers which are present in a 1:0.095 ratio, with the methyl substituents occupying equatorial positions.[78,79] This clearly demonstrates that the addition of the methyl groups locks the macrocyclic ring into one conformation (*S*-methyl group gives *λ*-macrocycle) and that this, in turn, favours one orientation of the acetate arms. In

triazacyclononane systems, addition of single substituents to the macrocycle has been shown to favour formation of one enantiomer of complex in high enantiomeric excess. Recently, the addition of an isopropyl substituent to the core of a tris-pyridylphosphinate ligand produced a single enantiomer of complex in >96% ee. By studying the CPL sign and form of the complexes and comparing to similar systems of known configuration it was found that an *S*-configuration at the chiral centre gave the *Λ*-complex while the *R*-configuration gave the corresponding *Δ*-complex.[39] A similar example using an (*S*)-lysine derived macrocycle has permitted conjugation of the complex to biomolecules known to bind to cell membrane receptors. This, in combination with the anionic nature of the complex due to the phenylsulfonate groups, has allowed this complex to be used in time-resolved FRET bioassays.[80,81]

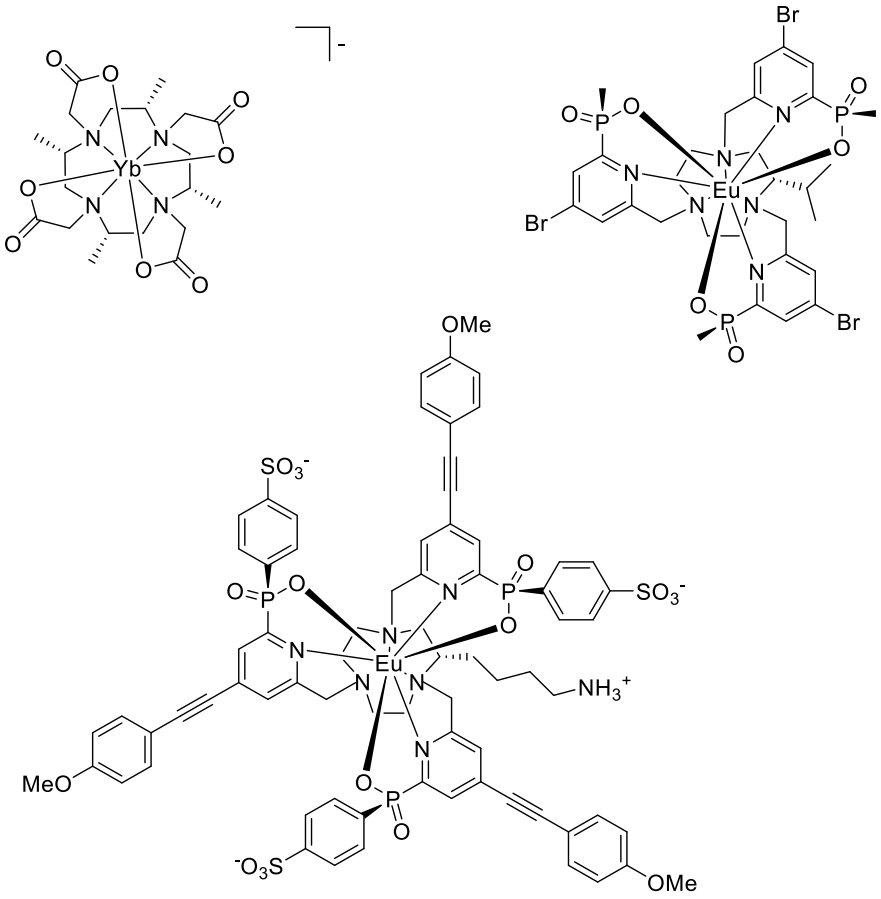

Figure 1.32 Examples of complexes where *C*-substitution of the macrocycle leads to preferential formation of one stereoisomer in the complex.

This approach requires that the chirality in the macrocycle is introduced early in the synthesis, often through the use of amino acid precursors. One such synthetic example is shown in Scheme 1.2.[80,81] Care must be taken throughout the synthesis to avoid the possibility of racemisation of the chiral centre, which can limit the conditions used. This method is obviously extremely labour intensive, as each macrocycle must be synthesised from acyclic precursors.

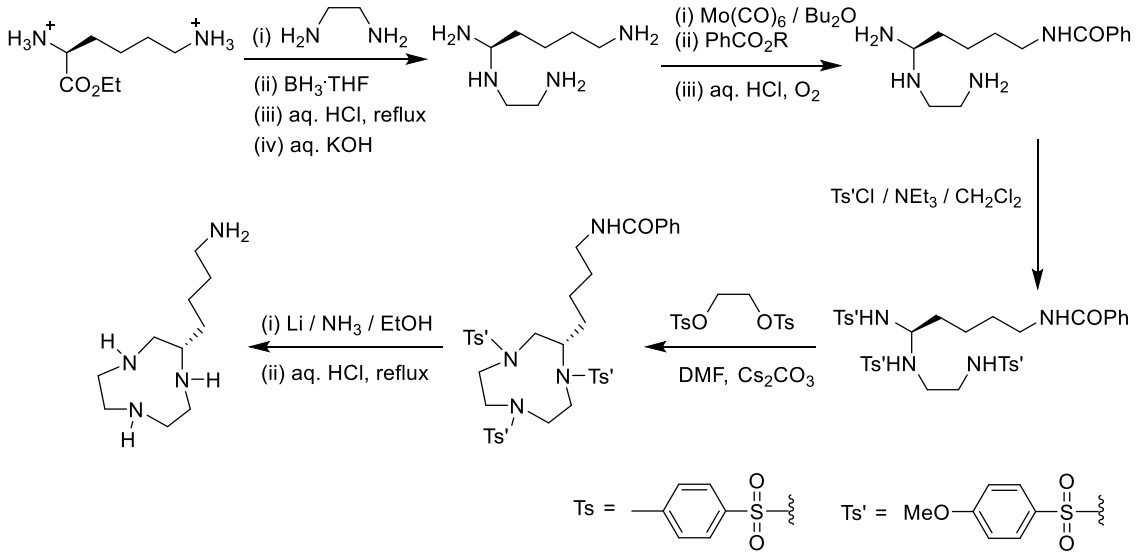

Scheme 1.2 A synthetic route to a C-substituted macrocycle.

The examples described so far all utilise chirality in the ligands to direct the formation of their corresponding complexes. However, it is also possible to form chiral complexes from achiral ligands that rapidly interconvert between stereoisomers. These are known as dynamically racemic complexes. Since they exist as a racemic mixture, they show no chiroptical properties such as CPL and CD. On interaction with another chiral species, CPL can be induced either by affecting the position of the equilibrium between the two enantiomers, or by changing the coordination environment.

Early examples of dynamically racemic lanthanide complexes focussed on D_3 symmetric complexes such as $[Eu(dpa)_3]^{3-}$, which exist as a rapidly interconverting mixture of Δ and Λ enantiomers (see Scheme 1.3). On addition of chiral additives, the equilibrium shifts in favour of one enantiomer which is stabilised due to more favourable diastereomeric interactions with the chiral additive. This phenomenon is termed the *Pfeiffer effect*, named after Paul Pfeiffer who observed this effect on

the induced optical rotation of dynamically racemic $[Zn(phen)_3]^{2+}$ complexes, on addition of camphorsulfonic acid.[82] Examples of CPL chiral additives studied include amino acids,[83] sugars,[84] and carboxylic acids.[85] It is important to note that this effect must be distinguished from the similar response that might be generated by displacing one of the achiral ligands with the chiral additive i.e. a constitutional change in the complex. When analysing the effect of adding a chiral species to a dynamically racemic complex, it is important to consider all the non-covalent interactions that are taking place (Coulombic, π-stacking, hydrophobic etc.), not just the configuration of the chiral additive. Recent work has shown that the effect is primarily caused by interaction of the complex with the outer-sphere hydrogen bonding network.[86] Further examples of dynamically racemic complexes will be discussed in the context of sensing biological analytes in Section 1.4.2, along with examples of achiral complexes which become chiral on the binding of a chiral analyte.

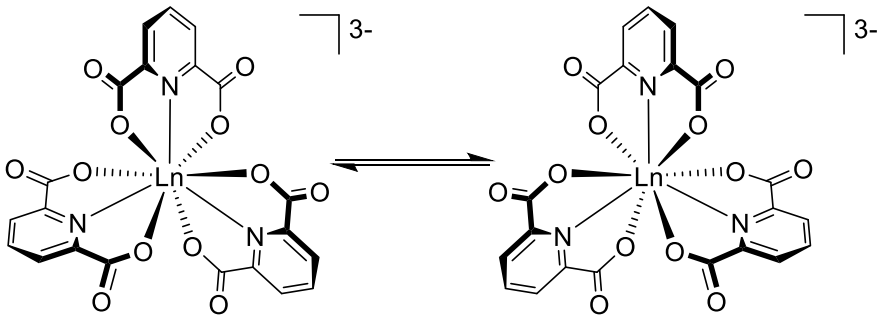

Δ-$[Ln(dpa)_3]^{3-}$ *Λ*-$[Ln(dpa)_3]^{3-}$

Scheme 1.3 The equilibrium between the *Δ* and *Λ* enantiomers of $[Ln(dpa)_3]^{3+}$ complexes; interconversion involves a dissociative ligand exchange mechanism.

1.4.2 Ln(III) complexes as CPL probes for biological analytes

Chiral lanthanide(III) complexes have been used as probes for various biological analytes such as proteins, DNA and oxyanions. Structurally well-defined chiral lanthanide complexes are practical probes in solution for a number of reasons. Binding events can be monitored by changes in emission, chiroptical behaviour and also by NMR. Specifically, changes in the coordination environment upon binding can lead to changes in total emission or CPL spectral form, and displacement of bound water molecules can bring about changes in emission lifetime by removing

proximal O-H oscillators. The ratio of changes between the hypersensitive $\Delta J = 2$ transition and other transitions (often $\Delta J = 1$) can be used as a ratiometric reporting mechanism, which removes the requirement to have a known concentration of probe complex.

A notable example of the modulation of a CPL signal on binding a chiral analyte can be seen in the work of Parker *et al*. Terbium(III) and europium(III) complexes based on 12-N_4 and bearing a tetraazatriphenylene chromophore were shown to bind to bovine serum albumin (BSA) with a significant change in the form of the CPL (see Fig. 1.33).[87] The (*SSS*)-*Δ*-isomers of the complexes were observed to bind to BSA with an apparent 1:1 binding constant of log $K = 5.1$. However, the enantiomeric (*RRR*)-*Λ* complex was shown to behave differently, with various low affinity adducts forming at different concentrations. This difference in response was confirmed by CPL spectroscopy which showed negligible change in form for the (*RRR*)-*Λ* enantiomer, but a significant reduction in CPL intensity, accompanied by a change in CPL sign and form, was observed for the (*SSS*)-*Δ* enantiomer.[87] This change in CPL sign signifies a change in complex helicity in the protein-bound form of the complex.[88]

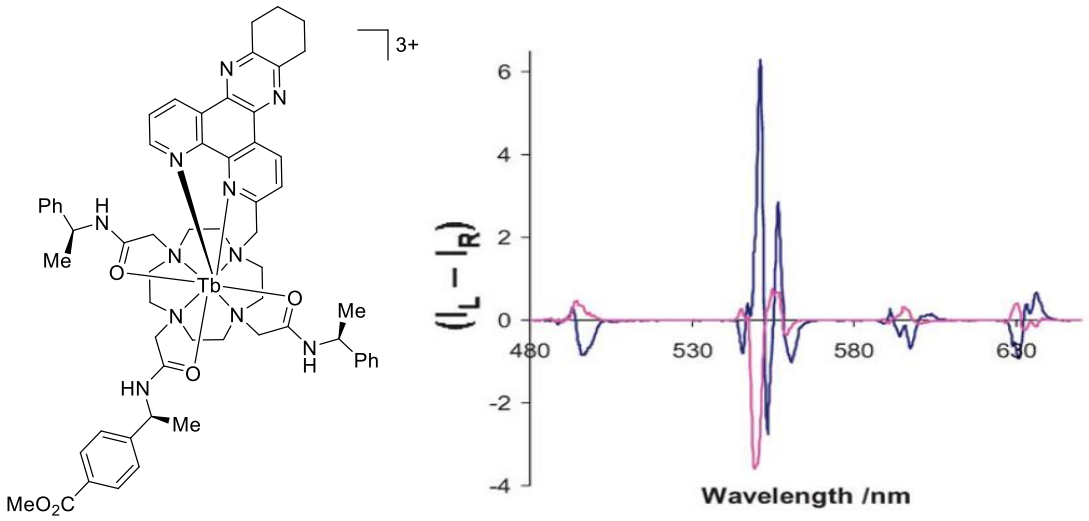

Figure 1.33 The (*SSS*)-*Δ* enantiomer (*left*) and its CPL spectrum in the absence (*blue*) and presence (*pink*) of 2 equivalents of bovine serum albumin (295 K, D_2O, λ_{exc} 348 nm). Reproduced from Ref. [87] with permission from The Royal Society of Chemistry.

Similarly, changes in CPL form have been used to measure bicarbonate (HCO_3^-) concentration.[89] A europium(III) 12-N_4 complex with chiral amide arms and an azaxanthone sensitising group showed significant changes in CPL form on binding bicarbonate (see Fig. 1.34). In contrast to the previous example, it is not likely that a change in complex helicity is responsible for this modulation, but that displacement of the bound water molecules changes the form of the CPL in the $\Delta J = 1$ and $\Delta J = 2$ transitions. Further evidence for this is a change in form of $\Delta J = 1$ in the total emission spectrum, and a large increase in intensity in $\Delta J = 2$, consistent with a change in axial ligand polarisability.

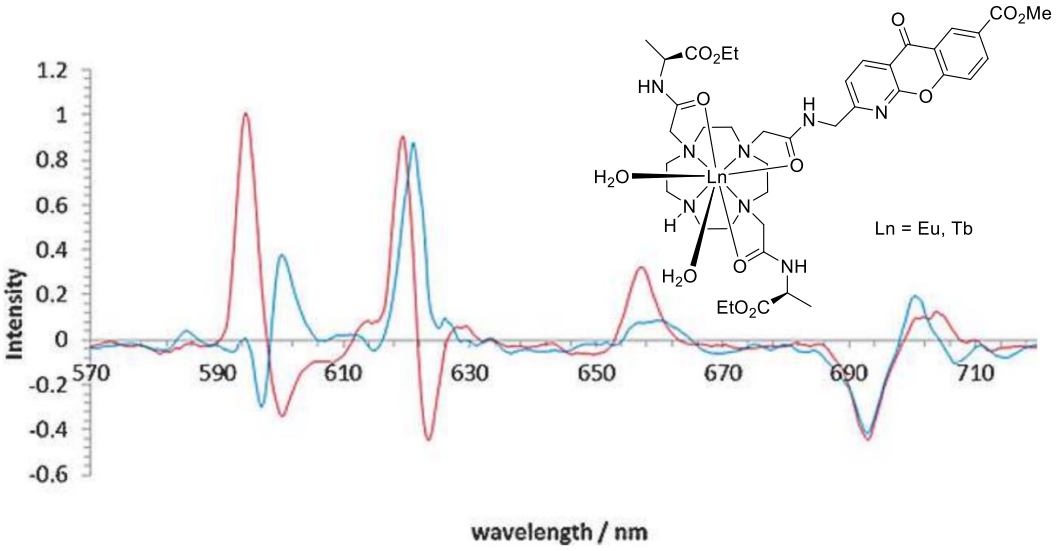

Figure 1.34 The CPL spectra of the europium(III) complex in the absence (*red*) and presence (*blue*) of 30 mM sodium bicarbonate (295 K, pH 7.40, 0.1 M NaCl). Reprinted with permission from Ref. [89]. Copyright (2012) Wiley-VCH Verlag GmbH & Co. KGaA, Weinheim.

Addition of a weakly bound sulfonamide arm to this complex renders it sensitive to pH.[90] At low pH, the sulfonamide nitrogen is protonated and is not bound to the metal centre. As pH increases, the nitrogen is deprotonated and binds to the metal, displacing a water molecule (see Fig. 1.35). The response can be monitored by observing changes in total emission, lifetime and also by CPL. When the sulfonamide binds to the metal, the complex becomes more rigid which in turn increases the magnitude of the emission dissymmetry. From the g_{em} data, a pK_a for the complex was found to be 5.65 ± 0.04. After calibration *in vitro,* the complex was then used to measure pH *in cellulo* where it localised to the lysosomes of NIH-3T3 (mouse skin fibroblast) cells.

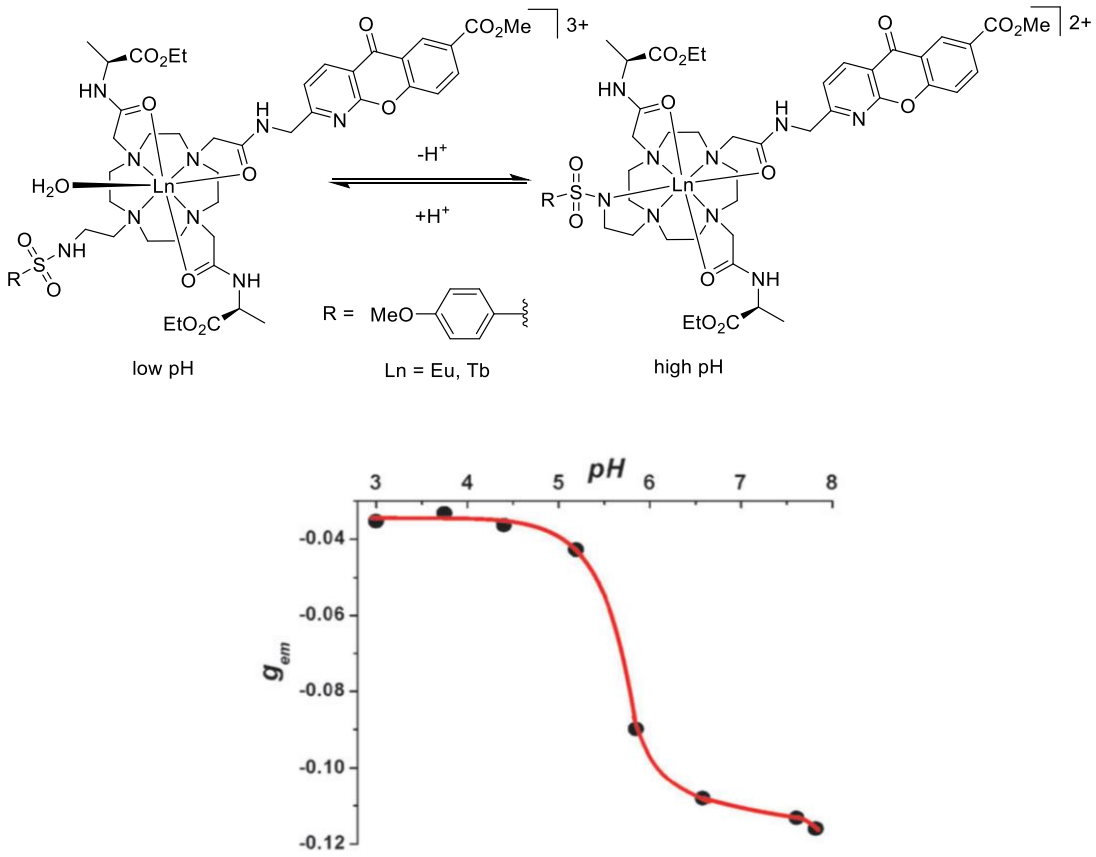

Figure 1.35 The mechanism of sulfonamide pH-responsiveness and the resulting variation in g_{em} value at 632 nm for the Eu(III) complex (295, K, 0.1 M NaCl). Reproduced from Ref. [90] with permission from The Royal Society of Chemistry.

A final example of the use of chiral lanthanide complexes for biological sensing involves the detection of phosphorus(V) oxyanions. These anions are an important class of biological molecule. Phosphorylated peptides and proteins are involved in cell signalling, proliferation and development, while phosphorylated sugars such as ATP, ADP and AMP are crucial in cellular respiration and signalling. As such, the ability to observe them with high spatial resolution in real time is highly desirable. CPL signals characteristic of the type of phosphate could be observed upon binding to a chiral europium(III) complex (see Fig. 1.36). Different forms of CPL were observed in ΔJ = 1 for HPO_4^-, glucose-6-phosphate $(Glc\text{-}6\text{-}P)^{2-}$ and *O*-phosphotyrosine $(O\text{-}P\text{-}Tyr)^{2-}$.[91]

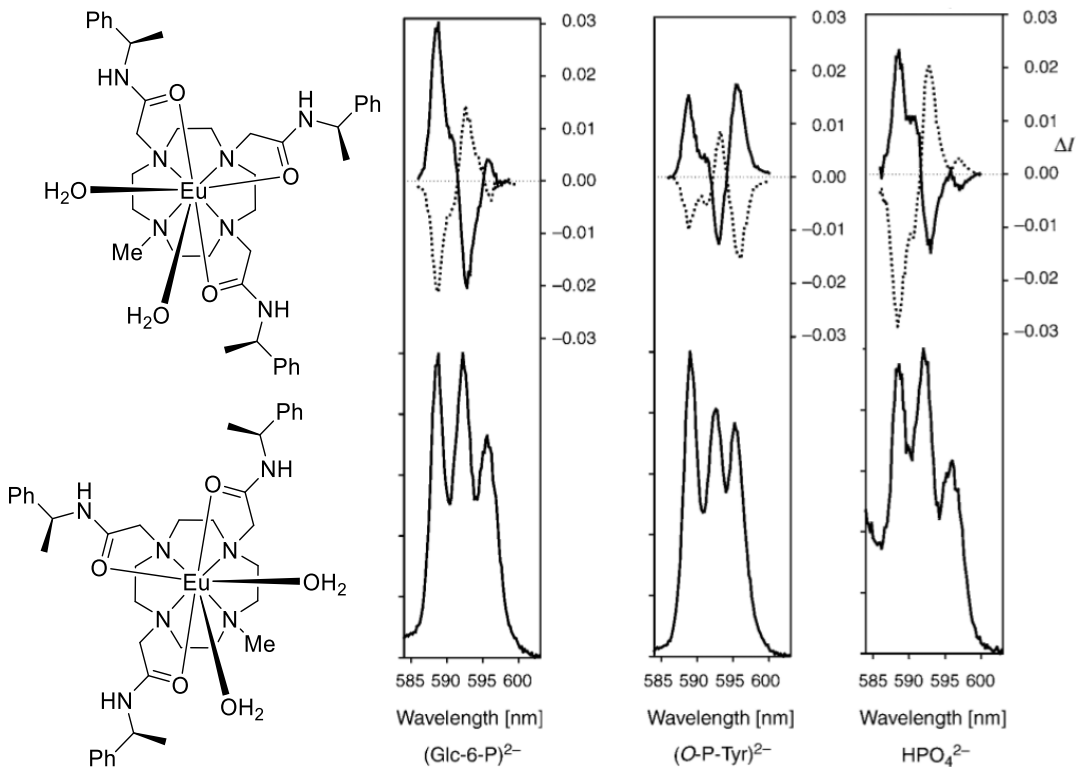

Figure 1.36 *Left*: the structures of the (*RRR*)-*Λ* enantiomer (*top*) and the (*SSS*)-*Δ* enantiomer (*bottom*). *Right*: the CPL (*top*) and total emission (*bottom*) of the complexes in the presence of 10 equivalents of phosphate anion (293 K, 0.1 M MOPS, pH 7.4). Adapted from Ref. [91] with permission from John Wiley and Sons. Copyright 2005.

There are several recent examples of dynamically racemic complexes that are capable of sensing biological molecules. One example uses a C_2-symmetric 12-N_4 complex which reversibly binds to α_1-acid glycoprotein (α_1-AGP), an acute phase protein involved in inflammatory response. The complex has two identical pendant azaxanthone chromophores and exists in solution as rapidly converting *Δ* and *Λ* enantiomers. As expected, no CPL or CD signal was observed for the complex in aqueous solution. However, on the addition of α_1-AGP, significant modulation of the total emission spectrum and a large induced CPL signal were observed with g_{em} = -0.23 at 598 nm (see Fig. 1.37). The ratio of the total emission intensities of ΔJ = 1 and ΔJ = 2, and the g_{em} values in these bands could be plotted as a function of added protein, allowing a calibration curve to be established.[92]

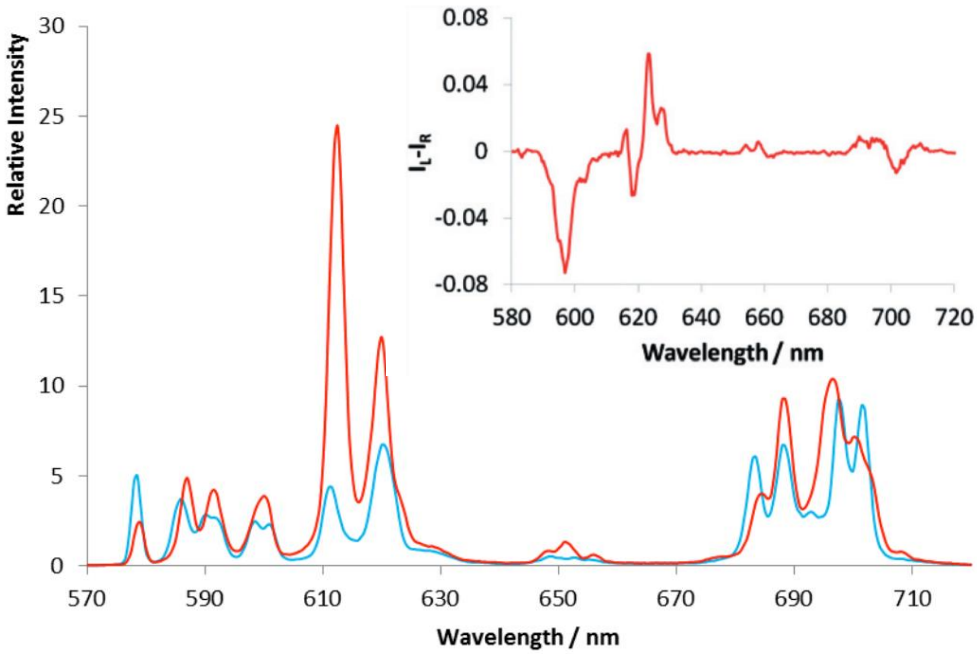

Figure 1.37 The total emission spectrum before (*blue*) and after (*red*) the addition of 50 μM α_1-AGP. *Inset*: the induced CPL spectrum after the addition of 50 μM α_1-AGP (20 μM complex, 295 K, 0.1 M NaCl, pH 7.4). Adapted from Ref. [92] with permission from The Royal Society of Chemistry.

The changes in photophysical properties were studied in detail in an attempt to elucidate the mode of binding between the complex and α_1-AGP. Firstly, on binding to the protein, measurement of the hydration state showed the bound water molecule was lost in the protein-bound form. The large increase in intensity of the ΔJ = 2 manifold suggests a change in axial ligand polarisability, consistent with displacement of the water by a proximal amino acid carboxylate side chain. The CD spectrum of the protein-bound complex showed two partially resolved bands, consistent with the two azaxanthone chromophores occupying different environments. As such, a binding mode was proposed (see Scheme 1.4) where one azaxanthone becomes uncoordinated and sits within the hydrophobic drug binding pocket of the protein, and the bound axial water is displaced by the carboxylate side chain of a proximal glutamate residue. Indeed, incremental addition of chlorpromazine (a drug known to bind in the hydrophobic pocket of α_1-AGP) led to a gradual decrease in the magnitude of the induced CD signal, suggesting the complex and chlorpromazine were competing for the binding site. The same complex was also shown to bind to α_1-antitrypsin (AAT) albeit with a lower binding constant.

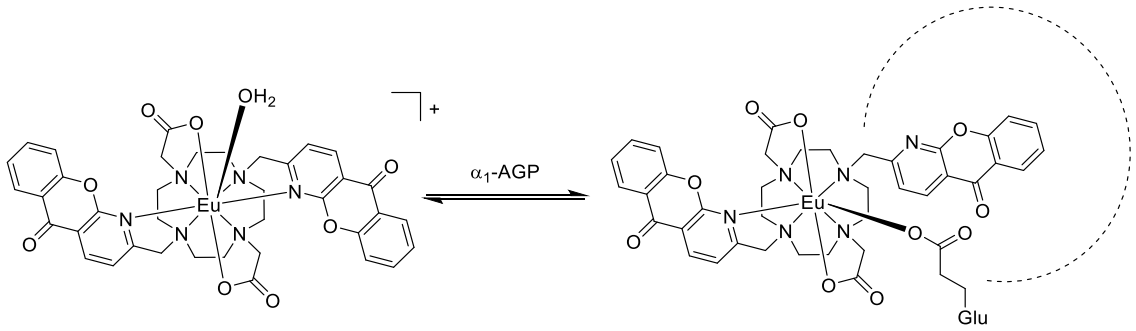

Scheme 1.4 The proposed binding mode to α_1-AGP with one azaxanthone chromophore situated in the hydrophobic binding pocket and the proximal glutamate carboxylic acid occupying an axial coordination site.

Recently, dynamically racemic complexes bearing pyridylarylalkynyl chromophores have exhibited induced CPL signals on binding to various phosphorylated amino acids,[93] and to sialic acid,[94] an amino sugar overexpressed in tumours. The complexes are based on 9-N_3 and have two identical chromophore arms. The third ring nitrogen is substituted with aromatic groups chosen to aid the binding of specific target biomolecules (see Fig. 1.38). Despite the complexes only being seven coordinate, there is no bound solvent molecule, most likely due to the steric bulk of the *N*-benzyl group. Sialic acid contains a 1,2-diol functional group which has been shown to reversibly form five-membered cyclic boronate esters with aromatic boronic acids. This motif has been used extensively in the design of various sensors for sugars.[95–97] Therefore, it was envisaged that the addition of an aromatic boronic acid would elicit binding to sialic acid, which in turn would establish a chiral environment around the complex, thereby inducing CPL. A similar principle was employed for the detection of phosphorylated amino acids. Addition of an *N*-methylammonium group on the benzyl substituent would provide a hydrogen bond donor which could stabilise the binding of an anionic phosphate to the metal centre.

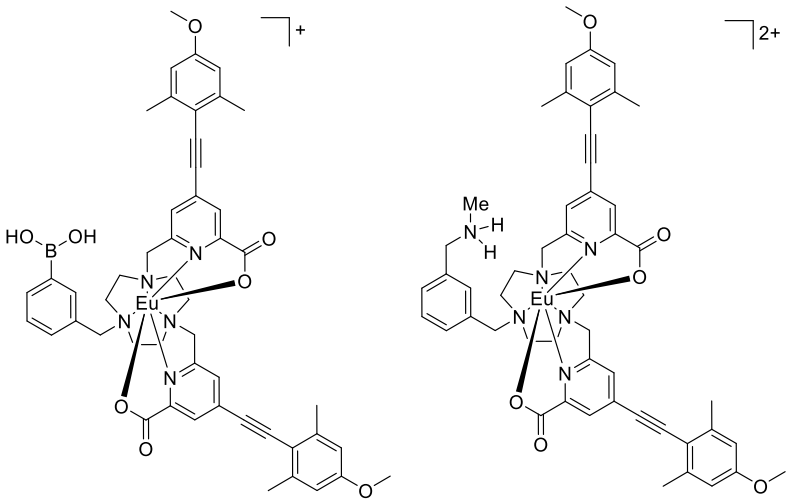

Figure 1.38 Dynamically racemic complexes for the detection of sialic acid (*left*) and phosphorylated amino acids (*right*).

On addition of sialic acid to the boronic acid complex in methanol solution, induced CPL was observed (Fig. 1.39), accompanied by a change in the total emission spectrum, indicating binding of sialic acid. Interestingly, a higher affinity was observed for this complex than for the analogous complex without the benzylboronic acid. This indicates that the boronic acid does indeed aid in the binding. However, no binding could be observed in water, likely due to the much higher hydration energy of sialic acid in water.

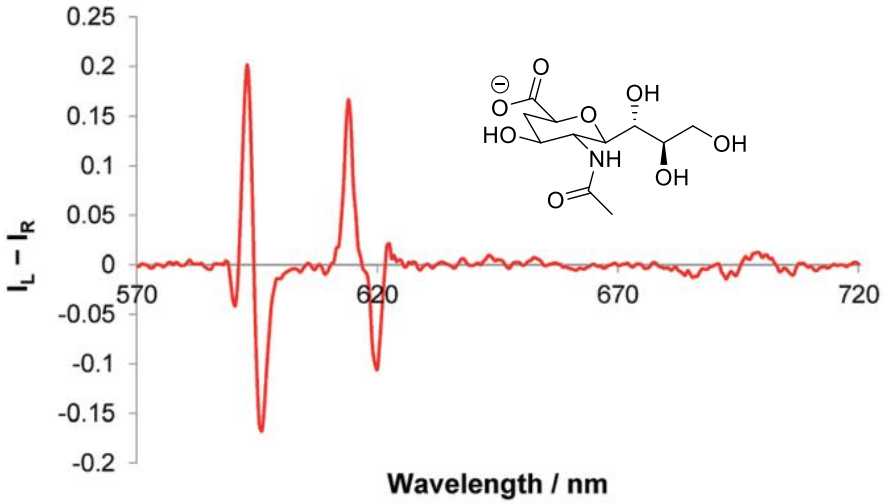

Figure 1.39 The induced CPL spectrum following addition of 10 equivalents of sialic acid (*inset*) (5 µM complex, λ_{exc} 356 nm, MeOH).[94]

In the case of sensing phosphorylated amino acids, addition of *O*-phosphoserine and *O*-phosphothreonine induced a CPL signal from the dynamically racemic probe

(see Fig. 1.40). Whilst the form of the induced CPL spectra were very similar, the g_{em} values differed, with the threonine adduct exhibiting larger emission dissymmetry factors than with serine. It was hypothesised that this was due to the extra methyl group in the side chain of threonine generating a more rigid adduct with the complex. Addition of *O*-phosphotyrosine did not elicit a CPL response, which was attributed to its chiral centre being more remote.[93] Hexapeptides incorporating these phosphorylated residues were also studied, and compared to the non-phosphorylated versions. No binding was observed with the non-phosphorylated peptides, confirming that the interaction is via the phosphate group. Interestingly, the forms of the induced CPL spectra were not the same as in the spectra after the addition of the single amino acids. This suggests that the chiral environment of the whole peptide is contributing to the form of the induced CPL.

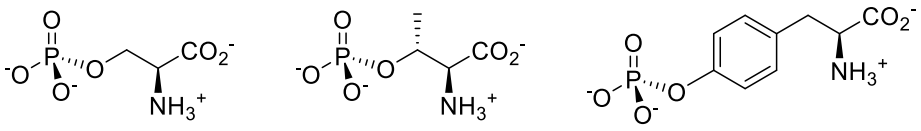

O-P-Ser *O*-P-Thr *O*-P-Tyr

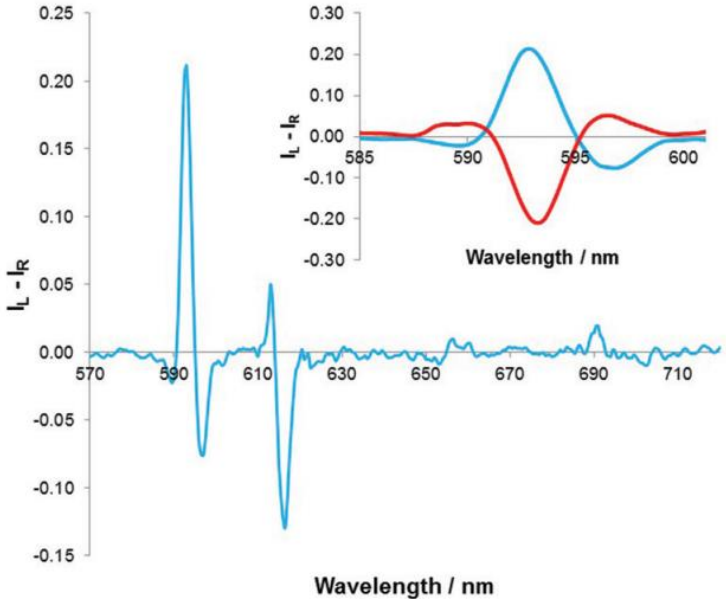

Figure 1.40 *Top*: the structures of phosphorylated serine, threonine and tyrosine. *Bottom*: the induced CPL spectrum after addition of 10 equivalents of natural *O*-P-Ser and an expansion of the $\Delta J = 1$ region after addition of both enantiomers of *O*-P-Ser (λ_{exc} 352 nm, 1:1 MeOH:H_2O, 10 mM HEPES, 5 µM complex, pH 7.4).[93]

In addition to dynamically racemic complexes, inherently achiral complexes can also be used as induced CPL sensors. The work of Iwamura involves the use of achiral 8-coordinate Eu(III) complexes based on 2,2'-bipyridine-6,6'-dicarboxylate (bda) to sense chiral amino acids by induced CPL.[98] The complex $[Eu(bda)_2]^-$ displays intense emission from europium under UV irradiation, but no CPL signal, as expected for an achiral complex. On addition of both enantiomers of 2-pyrrolidone-5-carboxylic acid, equal and opposite induced CPL was observed (see Fig. 1.41). The binding mode was proposed to involve direct coordination of the deprotonated carboxylate to the metal centre without displacement of a chromophore. A 10% drop in the emission intensity of the ΔJ = 2 transition also suggests a change in coordination environment occurs on binding. The appearance of the induced CPL could be plotted as a function of concentration of added amino acid to plot a calibration curve. However, it ought to be noted that these titrations are using approximately 10000-fold excess of amino acid relative to Eu(III) complex, which makes their practical utility somewhat limited.

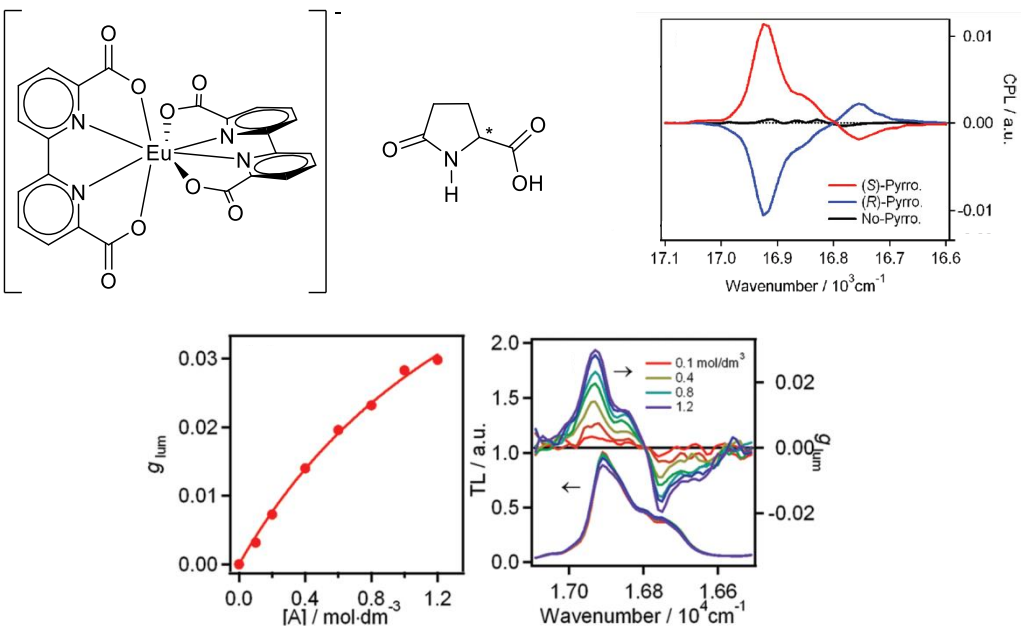

Figure 1.41 *Top*: the structures of $[Eu(bda)_2]^-$ and 2-pyrrolidone-5-carboxylic acid, and the induced CPL signal in the ΔJ = 1 transition on addition of *R*- and *S*-pyrrolidone-5-carboxylic acid (0.1 mM complex, 1 M amino acid). *Bottom*: the g_{em} value at 592 nm, CPL signal and total emission in ΔJ = 1 as a function of added S-2-pyrrolidone-5-carboxylic acid. Adapted with permission from Ref. [98]. Copyright (2012) American Chemical Society.

This work was then developed for other amino acids using 1,10-phenanthroline-2,9-dicarboxylic acid (pda) as the ligand.[99] Unlike for $[Eu(bda)_2]^-$, $[Eu(pda)_2]^-$ was found to exist as several species in aqueous solution, as shown by multiple $\Delta J = 0$ transitions in the total emission spectrum, although a single exponential decay in the lifetime measurement suggests these structures are in fast equilibrium on the timescale of the lifetime measurement (ca. 1 ms). Relatively strong induced CPL was observed on the addition of histidine and arginine, whilst little or no induced CPL was observed for ornithine, alanine, isoleucine, threonine, phenylalanine, proline, lysine, glutamine or leucine under the same conditions. Interestingly, the induced CPL was similar in form for histidine and arginine but was found to be pH dependent. The induced CPL could only be observed for histidine in acidic solution and arginine in neutral solution, implying that the binding of these amino acids is dependent on their protonation state. The concentration dependence of the induced CPL in response to arginine and histidine was studied (see Fig. 1.42). The data for arginine binding showed a sigmoidal profile and did not fit a 1:1 binding model, but the data did fit a 1:2 binding model (2 amino acids per metal centre). In contrast, the data for histidine binding was significantly more complex. 1:1 and 1:2 binding models failed to represent the data well, although a 1:3 model did seem more successful. In the context of coordination at the lanthanide centre, a 1:3 binding mode without loss of a pda ligand would make the metal centre 11-coordinate, which is not possible. If the 1:3 binding mode is indeed the case, partial dissociation of a pda ligand must occur, to satisfy the coordination requirements of the metal. Another important observation is that as the concentration of added histidine is increased, the CPL signal changes sign. This indicates that different adducts are present at different concentrations, and have significantly different chiral coordination environments. The complexity of the speciation behaviour and the weakness of amino acid binding limits considerably the impact and significance of this work.

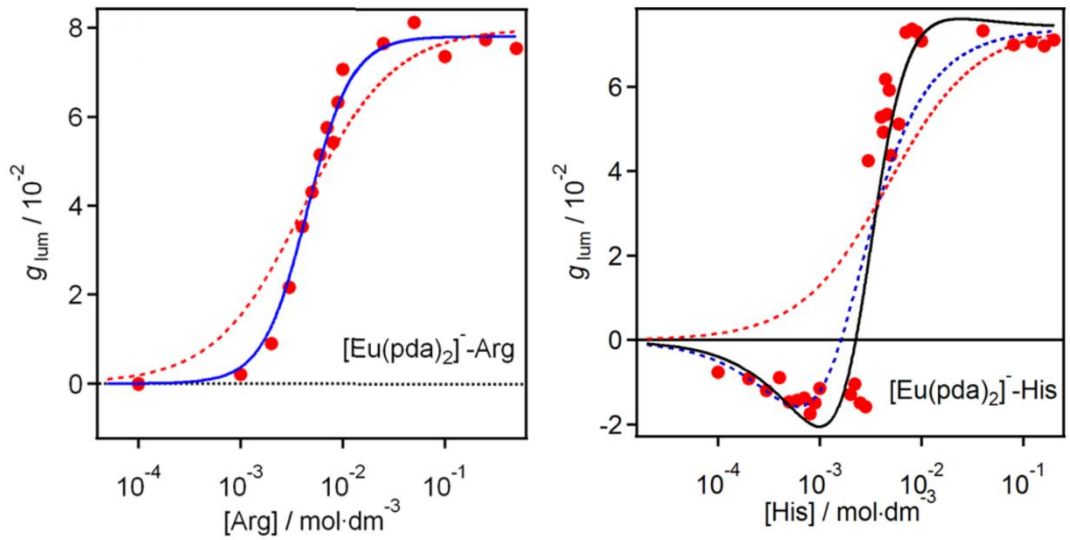

Figure 1.42 The variation of g_{em} as a function of added amino acid concentration for arginine at pH 7 (*left*) and histidine at pH 3 (*right*) (λ_{exc} 310 nm, λ_{em} 592 nm, 0.1 mM complex). The red, blue and black lines correspond to 1:1, 1:2 and 1:3 binding models, respectively. Adapted with permission from Ref. [99]. Copyright (2014) American Chemical Society.

1.5 Cell imaging with lanthanide complexes

Lanthanide complexes have extensively been shown to be of use as cellular stains for live cell imaging. The design considerations for emissive cellular stains will be discussed, followed by some examples of localisation profiles for various classes of complex. Finally, efforts to understand the cell uptake mechanisms of these complexes will be discussed.

1.5.1 Design considerations

For lanthanide complexes to be useful as emissive cellular stains for living cells, they must possess a number of properties. Firstly, the complexes must be capable of crossing the phospholipid cell membrane quickly and preferably irreversibly (although egress over time periods much longer than the period of measurement is acceptable). Secondly, the presence of the complex must not perturb cell homeostasis, otherwise it becomes impossible to probe normal cellular processes.

Following on from this requirement, the stain must be non-toxic at the concentration required for imaging (i.e. cell viability or division must not be compromised). The toxicity of a compound is often described by an IC_{50} value which

is the concentration of substance at which 50% of the cell sample is non-viable. The complexes should be stable both to chemical reaction and metal dissociation *in cellulo*, and should also be resistant to photobleaching and photofading to allow repeated measurements over a long period of time.

The photophysical properties of a complex must also be suitable for *in cellulo* imaging. Excitation should be possible using accessible wavelengths using lasers or LEDs. Commonly used light sources include nitrogen lasers (337 nm), Nd:YAG lasers (third harmonic at 355 nm), UV-LEDs (365 nm) and violet laser diodes based on GaN (405 nm). The advantage of using these long UV wavelength sources is two-fold. Firstly, most endogenous biological molecules are not excited in this region of the spectrum which reduces background interference. Secondly, these wavelengths are less harmful to the biological sample than shorter wavelength UV light (such as 254 nm from mercury lamps) which causes DNA and RNA damage.

Complexes should be highly absorbing (i.e. large extinction coefficients) and have large photoluminescence quantum yields, which maximises the brightness of the complex (see Section 1.1.5). Highly absorbing complexes allow the excitation sources to be used at lower power and in pulsed mode, which limits photodegradation and cell damage. Higher brightness also means smaller doses can be used, which minimises the possibility of disrupting cell homeostasis. Finally, long emission lifetimes permit time-resolved image acquisition, thereby increasing the signal to noise ratio (see Section 1.1.2).

1.5.2 Examples of sub-cellular localisation profiles

Broadly, 4 main sub-cellular localisation profiles have been observed for emissive europium(III) and terbium(III) complexes. These can be described by predominant localisation in the lysosomes, mitochondria, endoplasmic reticulum and nucleoli. Efforts to understand the structure-localisation correlation require various examples of structural modifications to be made and the localisation profiles compared.

Examples of complexes exhibiting lysosomal localisation are shown in Figure 1.43. These comprise 12-N_4 complexes bearing azaxanthone and tetraazatriphenylene chromophores,[22] as well as 9-N_3 complexes with pyridylarylalkynyl chromophores.[100] Complexes that enter cells via endocytotic pathways often show lysosomal staining, as endosomes mature into lysosomes over time. Additionally, complexes which the cell identifies as 'foreign' are often transported to the lysosomes.

Lysosomes are acidic vesicles used by the cell to degrade unwanted substances. The lysosomally-localised complexes have a wide variation in structure with no obvious common features. The selection comprises different chromophores, different donor groups (carboxylates, amides and phosphinates), different linkers between the macrocycle and chromophore (simple methylene bridges and pyrazole ring) and different charges (cationic, neutral and anionic). Among the triazacyclononane-based complexes, attempts to direct nuclear localisation by the addition of a Cys-Gly-Pro-$(Lys)_3$-Arg-Lys-Val nuclear localisation peptide were not successful, with the complex still localising to the lysosomes. Indeed, this complex was shown to be toxic with an IC_{50} of 1 μM compared to >100 μM for the other 9-N_3 complexes studied.[100]

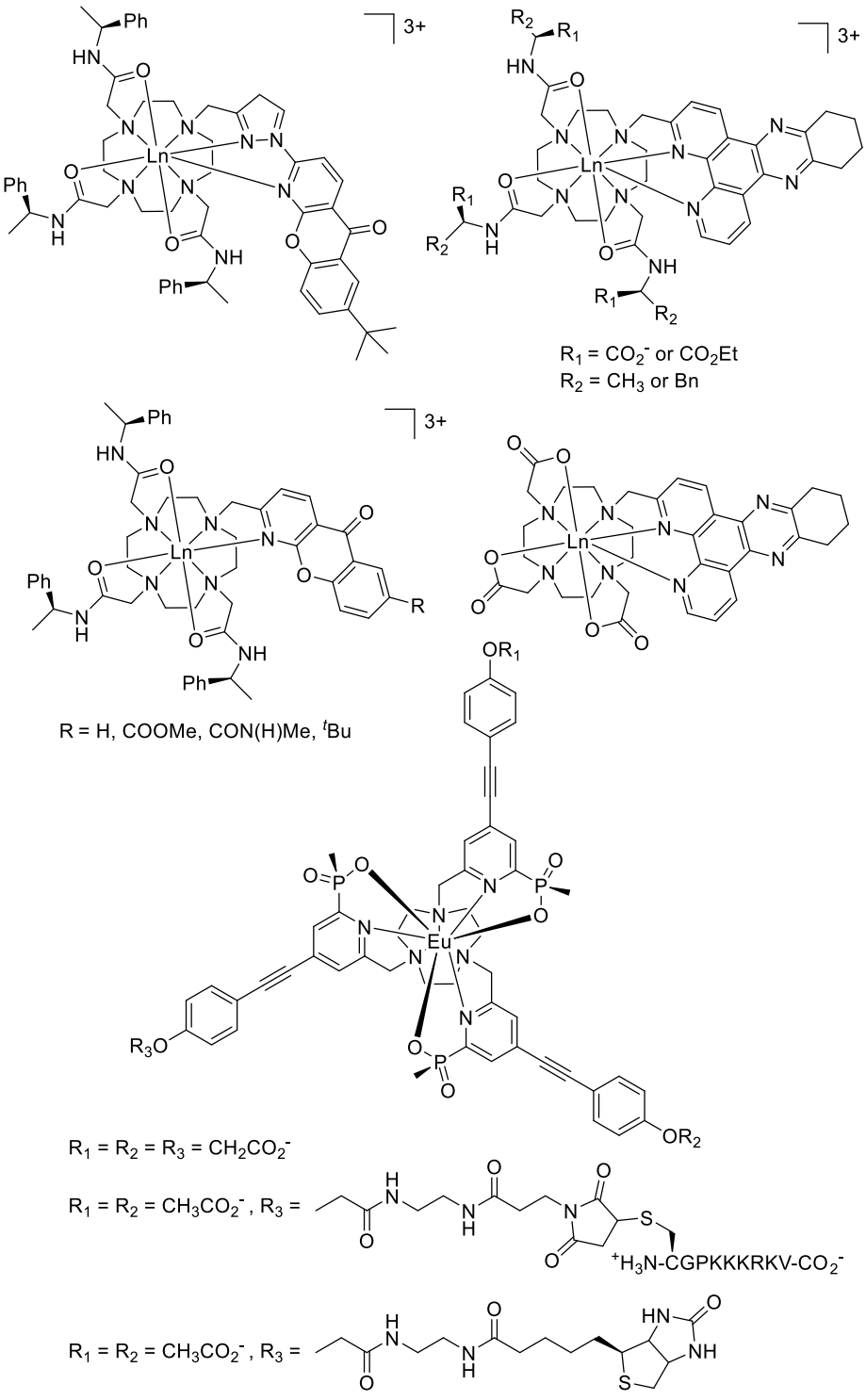

Figure 1.43 Examples of complexes exhibiting lysosomal localisation.[22,100]

The second class of complexes localises in the mitochondria. The mitochondria are the centre of aerobic respiration within the cell, and generate ATP which is an essential compound in many cellular processes. Again, large structural variation is observed among the mitochondrial-localising complexes (see Fig. 1.44). Fast uptake

of the glucamide-appended complex was observed in NIH-3T3 (mouse skin fibroblast) and CHO (Chinese hamster ovary) cells and mitochondrial localisation was confirmed by co-staining with MitoTracker Green. The cells could be imaged periodically over 48 hours with no reduction in cell proliferation. The localisation profile has been attributed to the amphipathic nature of the complex and the peripheral glucamides may inhibit degradation by normal cellular processes. Phosphorylation of the hydroxyl groups has been tentatively suggested to aid the mitochondrial localisation. In the anionic complex with one peripheral carboxylate group (see Fig. 1.44), mitochondrial localisation was also observed, in contrast to the analogous complex with three identical peripheral carboxylates which localised in the lysosomes. This result rules out the possibility that simply the nature of the head group controls the localisation of these triazacyclononane complexes. This complex was observed to move to the endoplasmic reticulum after approximately 8 hours. Addition of a peripheral poly-arginine peptide also directs localisation to the mitochondria followed by the endoplasmic reticulum after extended time periods.[100]

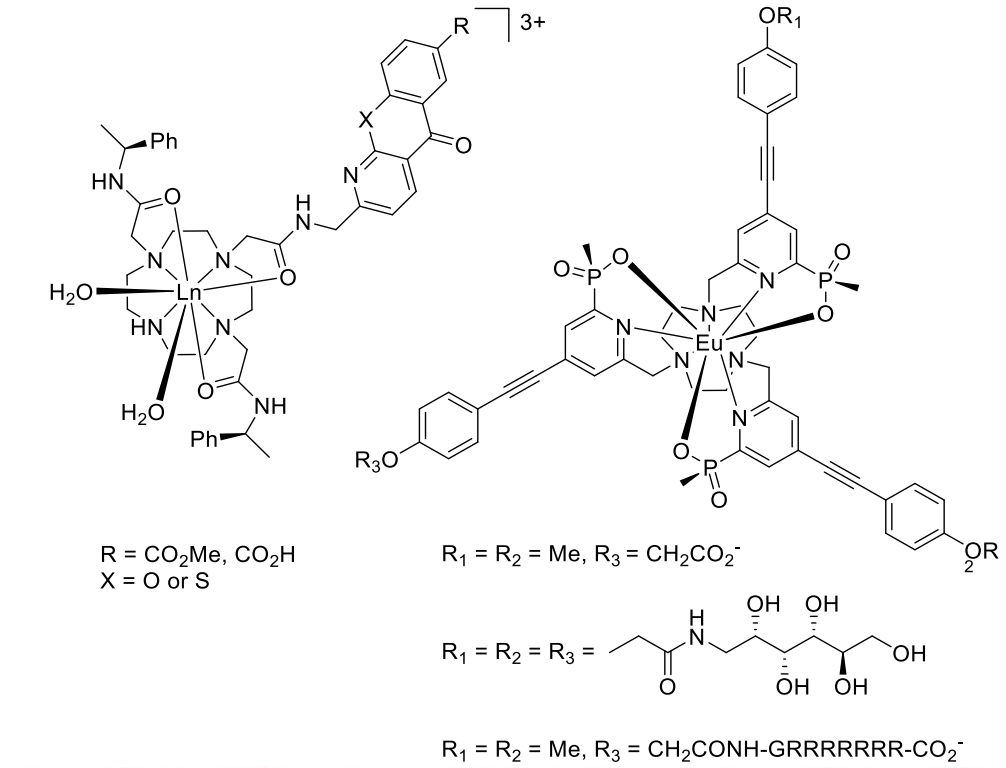

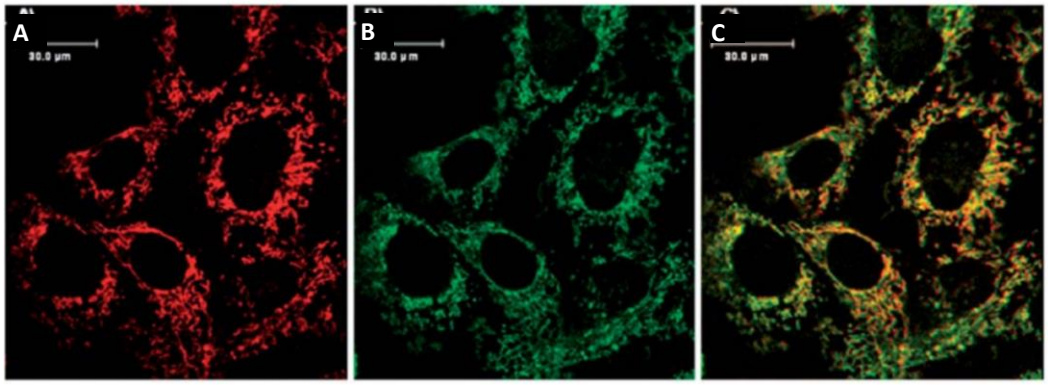

Figure 1.44 *Top*: examples of mitochondrial localising complexes. *Bottom*: LSCM images showing (*a*) mitochondrial localisation of the tris-glucamide complex in NIH-3T3 cells (1 h, 18 μM, λ_{exc} 355 nm, λ_{em} 605-720 nm); (*b*) MitoTracker Green (λ_{exc} 488 nm, λ_{em} 500-530 nm); and (*c*) RGB merged image showing co-localisation (*P* = 0.95). Reproduced from Ref. [100] with permission from The Royal Society of Chemistry.

Nucleolar staining has been observed from complexes based on 12-N_4 macrocycles. All the examples in Figure 1.45 contain the azathioxanthone chromophore but vary in the donor arm structure and linker group. The nucleolus is a sub-nuclear organelle involved in ribosome assembly. Cell uptake studies at various concentrations of complex and a range of incubation times have suggested that trafficking to the nucleolus occurs when the cell is under stress, which is linked to increased membrane permeability.[22] Indeed, by deliberately increasing membrane permeability by the addition of surfactants, several complexes which previously

localised in the mitochondria or lysosomes were observed to accumulate in the nucleoli.

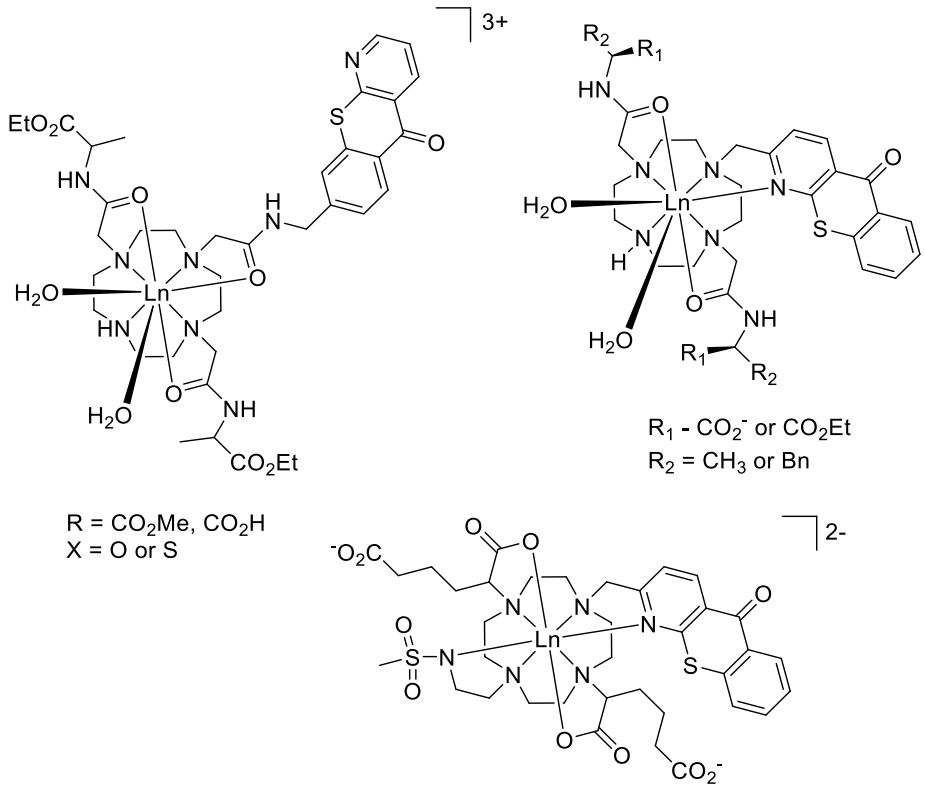

Figure 1.45 Examples of complexes that have been observed to localise in the nucleoli.[22]

1.5.3 Cell uptake mechanisms

A comprehensive understanding of the cell uptake mechanism of a probe is required if it is to be used *in cellulo*. It allows the rational design of probes and can provide insight into the causes of certain sub-cellular localisation profiles. Broadly, cell uptake mechanisms can be classified as either active or passive. Passive transport occurs along concentration gradients and includes osmosis and diffusion, while active transport requires an energy input. Active transport can further be categorised as primary, secondary or vesicular. Primary and secondary active transport are used to move small molecules and ions across membranes. However, lanthanide complexes for *in cellulo* imaging are too large to be taken up by primary or secondary active transport, and hence are taken in via vesicular pathways. Vesicular transport utilises fluid-filled vesicles formed from phospholipid membranes to transport species into (endocytosis) and out of (exocytosis) the cells.

There are a number of different types of vesicular endocytosis, which vary in the formation mechanism for the vesicle. Phagocytosis involves the cell membrane extending to engulf a solid particle before taking it into the cell to be digested. This process occurs in the destruction of dead cells and in the immune response for the removal of pathogens, for example. A second class of endocytotic pathways involve the invagination of the cell membrane in response to a substrate binding to a cell surface receptor to form a vesicle containing extracellular fluid (and any solute) which subsequently buds off the membrane.[101] This process is known receptor-mediated endocytosis, and is characterised by the way in which the invaginations form. Clathrin- and caveolae-mediated endocytosis are the two most common forms. In receptor-rich regions of the membrane, pits develop that are coated with protein (clathrin or caveolin). These proteins transform the pit into a vesicle by closing the top of the pit and inducing fission to form a clathrin- or caveolin-coated vesicle. Once separated from the inside of the cell membrane the coating is removed and the vesicle fuses with the appropriate organelle to release its contents.

In contrast to these receptor-mediated mechanisms, macropinocytosis does not involve the formation of coated vesicles. In macropinocytosis, the cell membrane responds to stimulation by forming ruffles which can close to form large, irregularly shaped vesicles called macropinosomes.[102] These membrane-bound vesicles can then fuse with other organelles to transport their contents. Macropinosomes are also thought to be leaky compared to other endocytotic vesicles, meaning that their contents can reach the cytoplasm before transport to various sub-cellular organelles.

Extensive studies have been carried out on 12-N_4 complexes of Eu(III) and Tb(III) to elucidate the mechanisms of cell uptake.[22] By incubating cells with complex in the presence of various known promoters and inhibitors of different endocytotic pathways, and subsequently measuring the intracellular complex concentration by ICP-MS, it is possible to find out which pathways are responsible for uptake. The promoters and inhibitors studied included sucrose and chlorpromazine (inhibitors of clathrin-mediated endocytosis),[103,104] filipin (inhibitor of caveolar

formation),[105,106] wortmannin and amiloride (inhibitors of macropinocytosis),[107–109] fatty acid glycerols and phorbol esters (stimulators of macropinocytosis),[110,111] and monensin and chloroquine (inhibitors of maturation and acidification of endosomes to form lysosomes).[112,113] Additionally, experiments were carried out at low temperature (4 °C) which inhibits all energy-dependent processes,[114] and with poly-L-lysine which disrupts the association of cell membranes.[115] A summary of the cell uptake mechanisms and their promoters and inhibitors is shown in Figure 1.46.

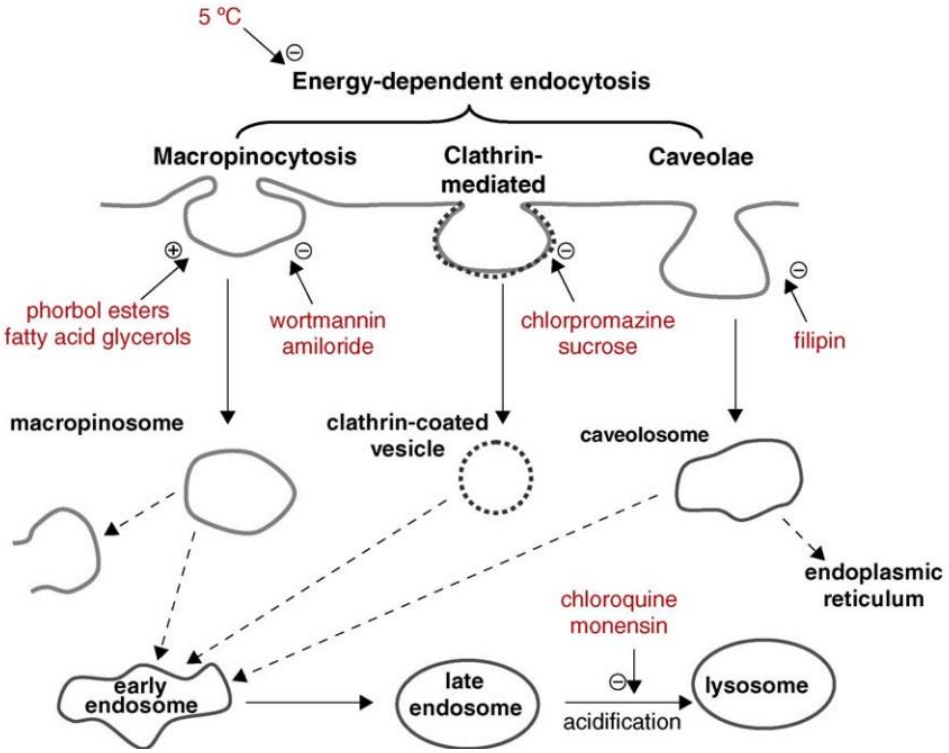

Figure 1.46 A schematic illustration of three possible endocytotic pathways for the uptake of lanthanide complexes, and the maturation of endosome to lysosomes. In red are known activators (denoted with a +) and inhibitors (-) of each process. Reprinted from Ref. [116] Copyright (2009) with permission from Elsevier.

Cell uptake experiments were conducted with a range of complexes which all have different localisation profiles, bearing various chromophores (tetraazatriphenylene, azaxanthone, azathioxanthone), various charges (neutral and cationic), various linker groups between the macrocycle and chromophore, and different counteranions (chloride, nitrate, acetate and triflate).[22,117] In every case, the observed uptake was consistent with macropinocytosis being the mechanism of cell uptake. The results are summarised graphically in Figure 1.47. Internalised cell concentration was reduced in the presence of wortmannin and amiloride, the

macropinocytosis inhibitors, and enhanced with the addition of a fatty acid glycerol and a phorbol ester which are known activators of macropinocytosis. None of the other treatments caused a significant effect on the cell uptake, except the low temperature study which confirmed that the uptake is energy-driven. The identification of macropinocytosis as the mechanism of uptake was supported by a co-localisation study which showed that a fluorescein-labelled dextran conjugate known to stain the macropinosomes. At early time points (up to 20 minutes), this stain was observed to co-localise with the Tb(III) and Eu(III) complexes.

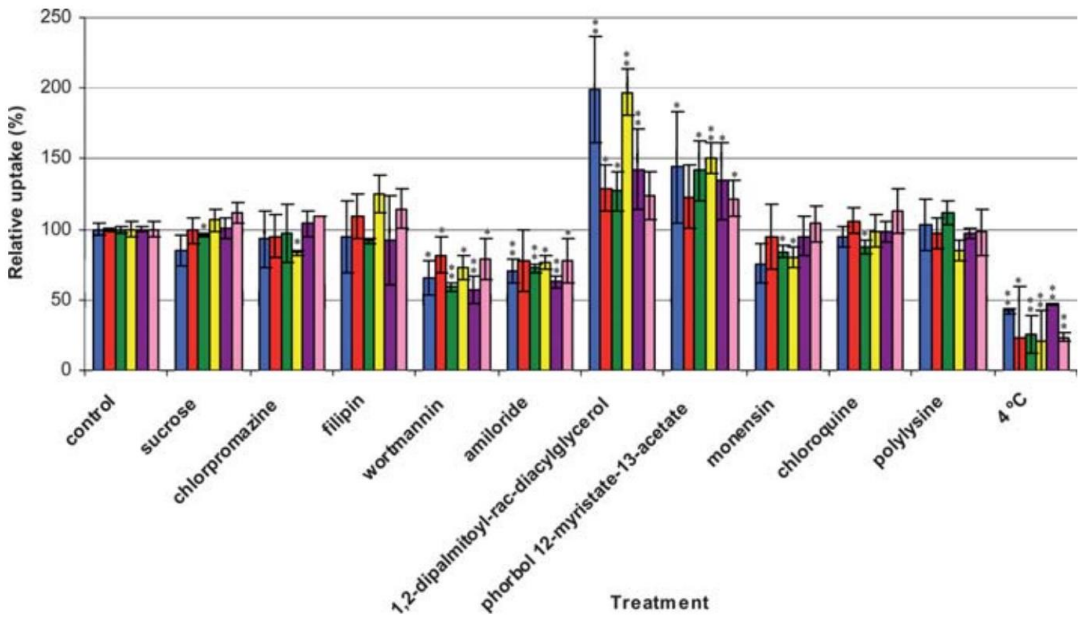

Figure 1.47 Relative uptake of various 12-N_4 complexes of Eu(III) and Tb(III) in the presence of inhibitors and activators of macropinocytosis, clathrin-mediated and caveolar-mediated endocytosis. Statistically significant results ($p < 0.05$ *, $p < 0.01$ **) were calculated using a two-tailed paired Student's t-test. Reproduced from Ref [22] with permission from The Royal Society of Chemistry.

More recently, similar preliminary experiments have been carried out on complexes based on 9-N_3 with pyridylarylalkynyl chromophores. Early indications are that these complexes are also internalised by macropinocytosis but no other mechanisms were studied in this work. Notably, a complex derivatised with a biotin tag was internalised independently of any promoters or inhibitors, which is indicative of a biotin-specific pathway.[100]

1.6 Lanthanides in security labelling

Lanthanides have been used in anti-counterfeiting for a number of years, with the most well-known application being the incorporation of various species containing Eu(III) and Eu(II) as luminescent security features in Euro bank notes (see Fig. 1.48). Due to the nature of the application, much of the information about these features is not in the public domain and several examples are protected by patents. Polymer banknotes have been used in Australia since 1988,[118] and are now in circulation in more than 30 countries across the world.[119] Polymer £5 notes were introduced to circulation in the UK in 2016, with polymer £10 notes released in September 2017. Polymer £20 notes are due to be released in 2020. This rapidly advancing field presents an interesting possibility as a target for new-anti-counterfeiting features.

In 2002, C_2W (the magazine of the Royal Dutch Chemical Society) published an article by Suyver and Meijerink in which they had attempted to identify the red, green and blue phosphors in a €5 note.[120] Based on studies of the emission, excitation and lifetimes of the phosphors they suggested that the red emission is from a Eu(III) β-diketonate complex, the broad emission band of the green dye is due to a *d-f* transition in $SrGa_2S_4$ doped with Eu(II), and the blue emission is from $(BaO)_x \cdot 6Al_2O_3$ doped with Eu(II). They contacted De Nederlandse Bank (the central bank of the Netherlands) who, unsurprisingly, refused to confirm their findings.

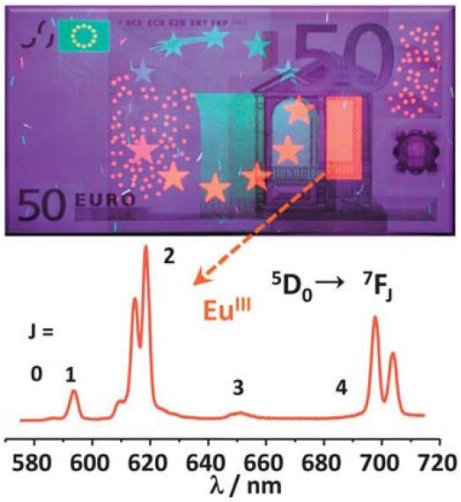

Figure 1.48 A €50 note irradiated at 366 nm and the resulting emission spectrum from area indicated by the arrow. The red-emitting europium species is probably a tris (β-diketonate) complex. Reproduced from Ref. [121] with permission of The Royal Society of Chemistry.

The use of Eu(III) and Eu(II) in banknotes is an example of UV-excited species emitting in the visible region (downconversion). A recent example of downconverting sensitised europium complexes for anti-counterfeiting has used $[Eu(dpa)_3]^{3-}$ and $[Tb(dpa)_3]^{3-}$ (see Fig. 1.49) as water-soluble inks for full colour inkjet printing with a standard household printer. Using europium and terbium for red and green, respectively, combined with a commercially-available blue fluorescent ink (CyanFirefly™), images were printed that are invisible to the naked eye but are full colour luminescent images when irradiated with UV light. A full gamut of colours could be achieved by various combinations of the three inks, calculated using extensive colour-matching algorithms.[122] Comparisons of the colours printed using the luminescent inks with the computer predictions showed an average ΔE_{94} value of 0.9.[§] This represents a colour match that is close enough that the human eye cannot distinguish the difference. In image printing tests, the inks produced vivid full colour luminescent images that reproduced skin tones, natural colours of fruit and 'man-made' colours of plastics in high quality. The applications in the security industry rely on the unique software developed for the colour matching. The inks themselves are easily copied but without the software it would be very difficult to produce an identical image.

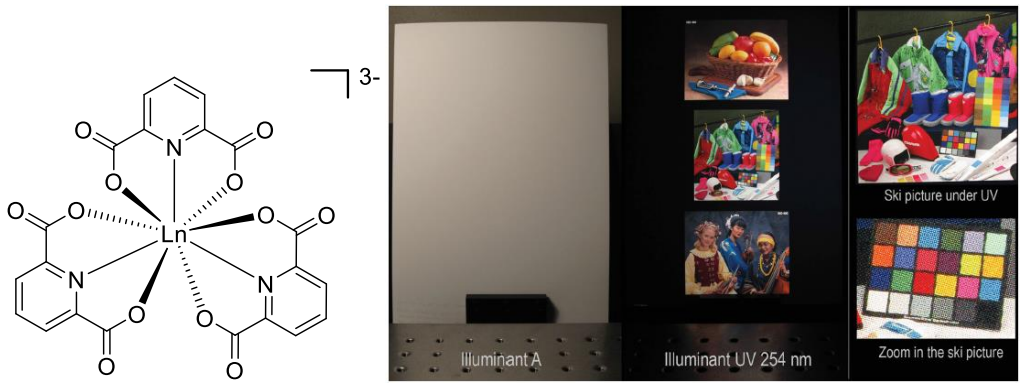

Figure 1.49 The structure of $[Ln(dpa)_3]^{3-}$ complexes and examples of full colour images that are invisible to the naked eye.[122]

There are, however, some challenges that may need to be overcome for this method to become a commercially useful method of anti-counterfeiting. Firstly, the pictures have to be printed on paper that does not contain artificial brighteners, as

[§] ΔE_{94} parameter is a measure of how different the predicted and actual colours appear. Lower values mean a better colour match. A value of 1.0 is the limit of human colour perception.

they are fluorescent and would therefore interfere with the colour reproduction. Also, the quality of the printed images is highly dependent on the paper they are printed on. In the study, several different types of paper were used and each showed different properties with respect to ink spreading, light scattering and colour reproduction. The cost of printing may also be an issue. No indication is given of the quantity of the ink required to print the images but the paper costs approximately 1000 times more than standard printer paper. Finally, the chemical composition of the blue fluorescent ink is unknown. It could be envisaged that an extra unique feature could be incorporated that takes advantage of the long luminescent lifetimes of the lanthanides. With the present system, only the red and green components of the image possess long-lived emission. Replacing the blue fluorescent ink with a lanthanide-based blue emitter could allow all three colour components to be phosphorescent. However, lanthanide blue emission is extremely difficult to produce. Thulium has been used to provide a blue component in white light emission,[123] but efficient sensitised emission from thulium is challenging, due to competitive vibrational deactivation of the thulium excited state.[124] Alternative options include the use of ligand-centred blue emission, though this would not overcome the problem of short lived emission.

Very recently, work by Gupta *et al*. has used lanthanide(III) doped Y_2O_3 nanorods to produce multicoloured luminescent security codes which are 'unclonable'.[125] In this example, Eu(III), Tb(III) and Ce(III) were used for red, green and blue emission, respectively. An optimised concentration of 15 mol% Ln^{3+} was used giving nanorods of the formula $Y_{1.7}O_3{:}Ln_{0.3}{}^{3+}$, and synthesis was carried out by a hydrothermal method where aqueous solutions of the reagents are heated to 185 °C under pressure. The nanorods precipitated from solution and were separated and dried. Scanning electron microscopy showed that the rods were uniform in size with a diameter of 80-120 nm and a length of 2-5 μm. The photophysical properties of the nanorods are shown in Figure 1.50. The Eu^{3+}-doped nanorods displayed a broad excitation band around 254 nm attributed to O^{2-} - Eu^{3+} charge transfer, along with small bands between 300 and 500 nm assigned to f-f transitions. Specifically, the peaks at 395 nm and 465 nm are due to $^7F_0 \rightarrow {}^5L_6$ and $^7F_0 \rightarrow {}^5D_2$ transitions,

respectively. The Tb^{3+}-doped nanorods have a similar broad charge transfer excitation band around 300 nm, and for the Ce^{3+}-doped nanorods, maximal excitation was around 380 nm. The Eu^{3+}- and Tb^{3+}-doped nanorods displayed characteristic emission spectra ascribed to $^5D_{0,1} \rightarrow {}^7F_J$ (J = 0-5) and $^5D_4 \rightarrow {}^7F_J$ (J = 3-6) respectively. Meanwhile, the Ce^{3+}-doped nanorods display a broad emission band centred around 440 nm. The only *f-f* transition which exists for Ce(III) is in the infra-red (approx. 2000 cm^{-1}) whereas this blue emission arises from a $4f^0\ 5d^1 \rightarrow 4f^1\ 5d^0$ transition.[126]

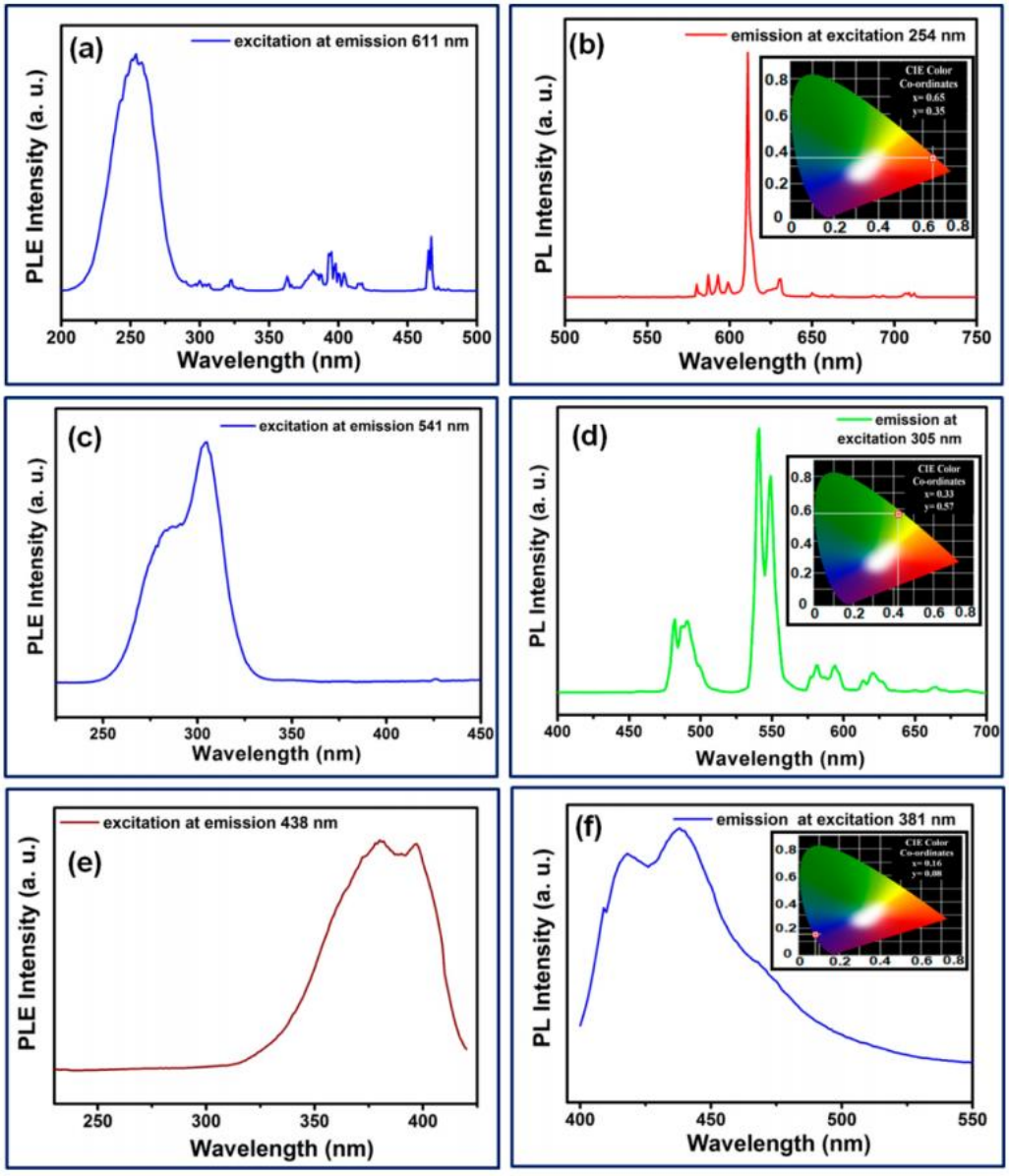

Figure 1.50 Excitation (*left*) and emission spectra (*right*) of Eu^{3+}- (*top*), Tb^{3+}- (*middle*) and Ce^{3+}-doped (*bottom*) Y_2O_3 nanorods. CIE colour coordinates are shown in the insets. Wavelengths of excitation and emission are displayed on the spectra. Reprinted with permission from Ref. [125]. Copyright (2017) American Chemical Society.

The nanorods were then dispersed in a PVC medium which is used for commercial screen printing and the logo of the Council of Scientific and Industrial Research - National Physical Laboratory of India (CSIR-NPL) was printed onto black paper. The printed logos are not visible under normal light but appear brightly under UV light. Confocal microscopy showed that the printed nanorods had a uniform distribution on the paper. The authors claim that the common host material makes synthesis simpler, and that this collection of three species of nanorod opens the door to simple multicolour anti-counterfeiting features. However, each coloured nanorod requires different excitation wavelengths so designs featuring different doped nanorods would not necessarily emit in the red, green and blue regions simultaneously. It could be envisaged, however, that each coloured ink could be used to print a different image and that the anti-counterfeiting feature was based on different images becoming visible under different excitation sources.

Figure 1.51 The CSIR-NPL logo printed with Eu^{3+}-, Tb^{3+}- and Ce^{3+}-doped Y_2O_3 nanorods, visualised under UV excitation. Adapted with permission from Ref. [125]. Copyright (2017) American Chemical Society.

Other examples of downconverting systems patented for use in security coatings include a DuPont patent for lanthanide complexes containing chelating amide ligands where comparison of an emission spectrum to that of a known standard can be used to distinguish forgeries from genuine items.[127] The complexes are dissolved in toluene and printed as inks onto the surface of interest. Amide ligands can contain alkyl, aryl or heteroaryl groups and can be combined with other non-amide ligands to form the complexes. The structures proposed in the patent are shown in Fig. 1.52. However, both structures include amide groups binding through both the nitrogen and oxygen atoms, forming a 4-membered chelate. This arrangement is

unlikely due to the very tight chelating angle, and it is certain that the amides bind only through the carbonyl oxygen. This would leave further vacant coordination sites that might be occupied by further equivalents of amide or non-amide ligands.

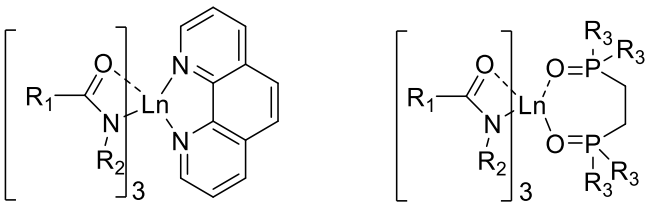

Figure 1.52 Putative structures of complexes based on amide ligands that have been printed in toluene-based inks; R_1 and R_2 are alkyl, aryl or heteroaryl, R_3 is an alkyl chain C1-C8.

Another example in a patent owned by Samsung Electronics Co., used phenanthroline-based complexes containing an acetylacetonate ligand which can be excited both in the UV range and using X-rays (see Fig. 1.53). In this proposed structure, the lanthanide ion is 10-coordinate. As lanthanide complexes are usually 8- or 9-coordinate, this is unlikely to be a true representation of the structure. It is more likely that the nitrate anions are unidentate. The complexes contain mixed lanthanides where Ln is Tb_xEr_{1-x}. Excitation with UV or X-rays leads to green emission that can be compared to a known standard.[128]

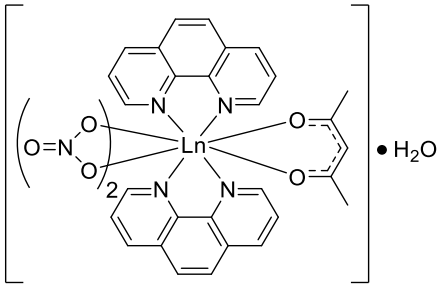

Figure 1.53 The proposed structure of a lanthanide complex capable of luminescence when excited by UV or X-ray radiation; Ln = Tb_xEr_{1-x}).

A second use of lanthanides in security applications is based on inks containing upconverting lanthanide-doped nanoparticles. Upconversion refers to emission that is at shorter wavelengths than the excitation light. In the case of lanthanide-doped nanoparticles, visible emission is produced as a result of near-infrared excitation.[129] There are several benefits to this class of compounds in the security printing field. Firstly, patterns can be printed and detected on fluorescent surfaces (such as

papers containing brighteners) as the near-IR excitation will not excite the interfering fluorescent species. Secondly, the nanoparticles themselves are very difficult to copy and excitation sources in the near-IR range are also hard to duplicate. Recent work by Meruga *et al.* has used inks composed of $NaYF_4$ nanoparticles doped with Yb^{3+}, Er^{3+} and Tm^{3+} to produce green and blue upconverting inks that are invisible to the naked eye.[130] Within the nanoparticles, Yb^{3+} acts as a sensitiser for the visible-emitting Er^{3+} and Tm^{3+}. The Yb^{3+} is excited from its $^2F_{7/2}$ ground state to the $^2F_{5/2}$ state upon absorption of light at 980 nm. Consecutive non-radiative energy transfer from the $^2F_{5/2}$ state of Yb^{3+} to the emitting states of Er^{3+} and Tm^{3+} results in various emissive transitions in the visible region of the spectrum (see Fig. 1.54). Emission from Er(III) is perceived by the eye as green, while emission from Tm(III) is perceived as blue.

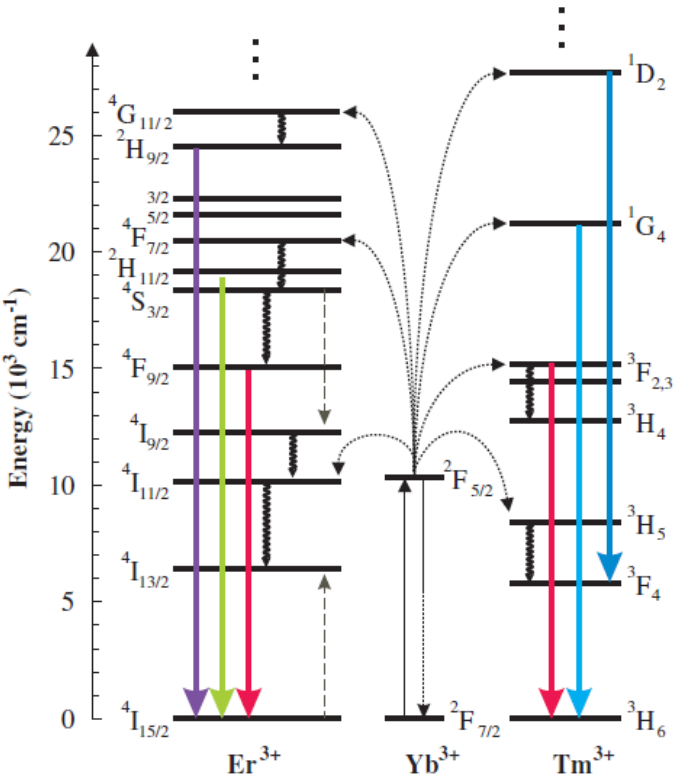

Figure 1.54 An energy level diagram showing the IR to visible upconversion processes in $NaYF_4$ doped with Yb^{3+}/Er^{3+} and Yb^{3+}/Tm^{3+}. Only emissive transitions in the visible region are shown here. Reprinted from Ref. [129], Copyright (2005), with permission from Elsevier B. V.

The nanoparticles themselves are capped with oleic acid and are then dissolved in a 90:10 mixture of toluene and methyl benzoate with poly(methyl methacrylate) (PMMA) beads. The PMMA acts as a binding agent after printing and solvent

evaporation. The inks contain 2 wt% of nanoparticles and were used to print quick response (QR) codes, two-dimensional barcodes that are capable of holding more than 100 times more information than a traditional barcode, and can be quickly read by scanning applications on smart phones (see Fig. 1.55).[131] The process of printing the QR codes begins with the code generation online. The code is then converted to an AutoCAD file which is used to print the invisible code. The printed code was then excited at 980 nm using an infrared diode laser, and a photograph taken using a Nikon DSLR camera (15 s exposure). This photo was then successfully scanned using a QR reader on a smart phone.[130]

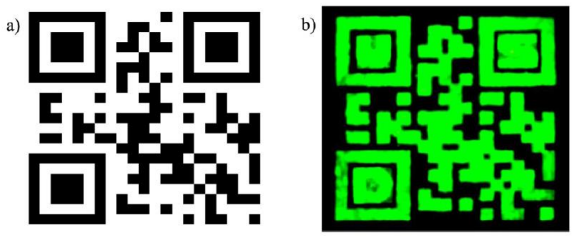

Figure 1.55 (*a*) A standard black and white QR code and (*b*) the same QR code printed using the invisible Er(III) doped upconverting nanoparticle ink, irradiated at 980 nm. Reproduced with permission from Ref. [130]. Copyright 2012 IOP.

These codes have been printed on paper and glass and can be read in both cases. Despite some spreading of the ink giving a less well-defined pattern, the scanner is still able to recognise the code. Approximately 0.3-0.4 mL of ink is required to print each code. The codes were also shown to be mechanically stable and could still be read electronically after the paper was folded 50 times. Additionally, codes could be overprinted with a second ink to add an extra level of security. Printing with the Tm(III)-doped blue-emitting ink over the green-emitting Er(III) ink gave three discernible coloured regions – one each for the two inks on their own and a third colour where both inks were present on top of each other. The perceived colour could also be altered by the power density used in the excitation. The upconversion transitions to excite Tm(III) are three- and four-photon processes, whereas for Er(III) it is only a two-photon process. As a result, the Tm(III)-doped ink is more sensitive to changes in excitation power. This effect can be seen by comparing the emission spectra from mixtures of the two inks at various levels of excitation power density (see Fig. 1.56). As excitation power is increased, the emission intensity from Tm(III)

transitions ($^1D_2 \rightarrow {}^3F_4$ and $^1G_4 \rightarrow {}^3H_6$) in the blue region of the spectrum increased proportionally more than the Er(III) transitions in the green region of the spectrum, meaning the eye perceives a bluer colour from the ink.

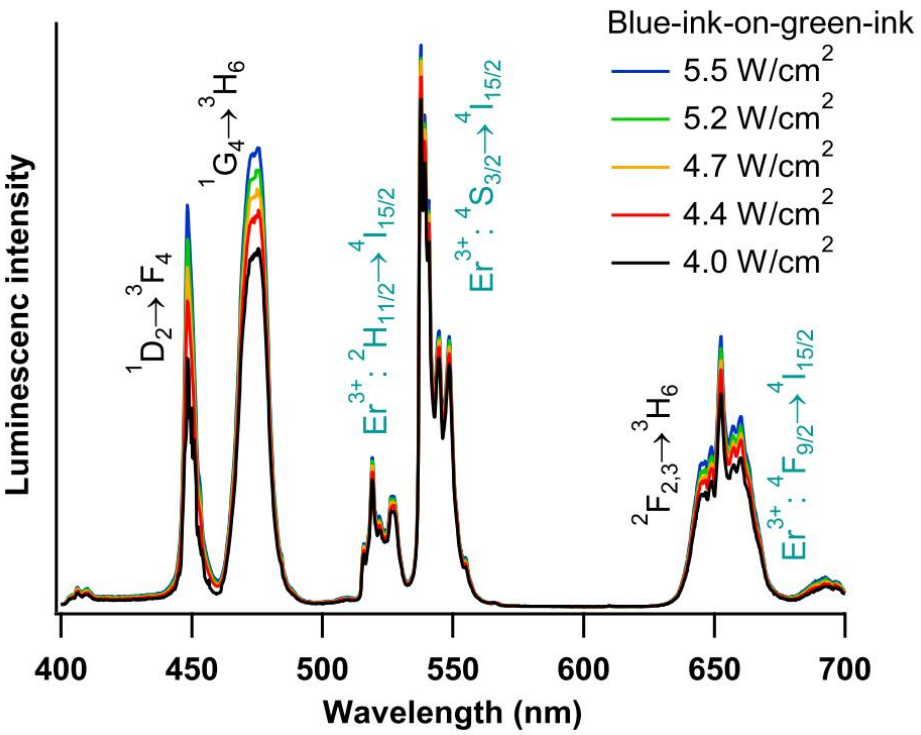

Figure 1.56 Visible upconversion luminescence spectra as a function of excitation power density of a region of the QR code with blue ink and green ink printed together (λ_{exc} = 980 nm). Reproduced with permission from Ref. [130]. Copyright 2012 IOP.

1.7 Project Aims and Outline

The first aim of the project relates to the use of highly emissive chiral europium(III) complexes as security labels. Several examples are known of the use of lanthanide emission in anti-counterfeiting applications, but none has utilised the possibility of chiroptical discrimination. Lanthanide complexes possessing strongly absorbing ligands and efficient sensitised emission provide the ideal target for such a system. To this end, the following specific aims are envisaged:

i) The synthesis of novel emissive, water insoluble europium(III) complexes with high quantum yields that can be processed in organic solvents and are amenable to excitation by commonly available light sources at 355 and 365 nm.

ii) The chiral resolution of the europium(III) complexes and a study of their thermal stability to racemisation.

iii) Study of the chiroptical properties of the resulting enantiopure complexes, with particular attention to identifying a suitable complex for use in a CPL-based anti-counterfeiting feature.

iv) Development of a simple system capable of distinguishing emission from a chiral europium(III) complex from a 'fake' emitter. Ideally, the system should be relatively cheap and simple to operate.

v) Use of this system to demonstrate chiroptical, wavelength and lifetime discrimination in europium(III) complexes, both in solution and the solid state.

The synthesis of several novel europium(III) complexes is described, together with analysis of their photophysical properties and rates of racemisation. The development of a new detection method for these complexes as security labels is also reported.

The solvent dependent emission behaviour of the rare earth complexes is described. In particular, studies into the effects of varying solvent on the total emission and CPL of europium(III) complexes are defined and a combined emission and NMR study is given, examining the unusual properties of a series of simple C_3-symmetric lanthanide(III) complexes.

In addition to their use in security labelling, the behaviour of chiral complexes in a biological environment is explored. Whilst racemic lanthanide(III) complexes have been used extensively as probes and stains *in cellulo*, the effect of chirality on cell uptake and sub-cellular localisation has not been studied before. Preliminary experiments into the mechanism of cell uptake of 9-N_3 complexes with pyridylarylalkynyl chromophores are given, identifying the mechanism of internalisation of this class of complexes. Moreover, the effect of complex chirality on the extent and nature of cellular localisation has been studied.

CHAPTER TWO : CHIRAL Eu(III) COMPLEXES FOR SECURITY LABELLING

2.1 Requirements for a security label

In order for an emissive species to be suitable for use as a security label, it must possess several key properties. Primarily, it must contain at least one unique feature that can be used to distinguish it from 'counterfeit' labels. This feature may take the form of wavelength selection in either absorption or emission, emission lifetime, or various chiroptical properties. Ideally, multiple unique features should be incorporated, in order to make imitation of the label unfeasible. Secondly, the method of detection should be simple and relatively inexpensive. In the various applications of emissive security labels, detection without the use of specialist spectroscopic equipment is required. Therefore, systems using readily-available components that do not require specialist training in operation are desirable. Finally, the compounds must be simple to process and apply to the target substrate and must then be durable. The necessity for durability is both with respect to physical processes as may be expected to occur during the lifetime of a labelled item, and in chemical degradation that could occur over time. In the context of documents and banknotes, stability with respect to long term exposure to daylight, repeated exposure to UV light, folding, heating, handling by humans and processing by machines needs to be considered. For anti-counterfeiting labels in clothing or similar items, resistance to repeated washing would also be required. For example, the lifetime of a passport or driving licence in the UK is 10 years, while a cotton £20 note is estimated to circulate for 113 months and change hands over 2000 times before being withdrawn.[132] Any emissive label would need to be stable over such an extended time period.

Emissive lanthanide(III) complexes possess several properties that make them near ideal candidates for security labels. These include their relatively long luminescent lifetimes (compared to organic emitters) which allow time-resolved measurements, the ability to tune their excitation wavelength by alterations to the organic antenna

groups, and their favourable chiroptical properties. The line-like appearance of their emission spectra also facilitates wavelength selection of specific transitions using optical filters.

2.2 Synthesis of target systems

The synthetic targets for the investigation are the complexes **[EuL^1]** and **[EuL^2]** (see Fig. 2.1). Based on previous work, their absorption maxima were expected to be around 360 and 340 nm respectively, making them ideal for excitation with commonly available light sources as discussed in Section 1.5.1. They contain pyridylarylalkynyl chromophores which have been shown to have very high molar extinction coefficients (55 000-60 000 M^{-1} cm^{-1}).[29] Phenyl substituted phosphinate donors have been chosen to reduce the water solubility, in anticipation that this may increase the durability of the complexes. The phenyl groups were also expected to increase the rigidity (and therefore stability to racemisation) and the emission lifetimes of the complexes. Once resolved by chiral HPLC, the complexes were expected to have strong CPL signals, following UV excitation.

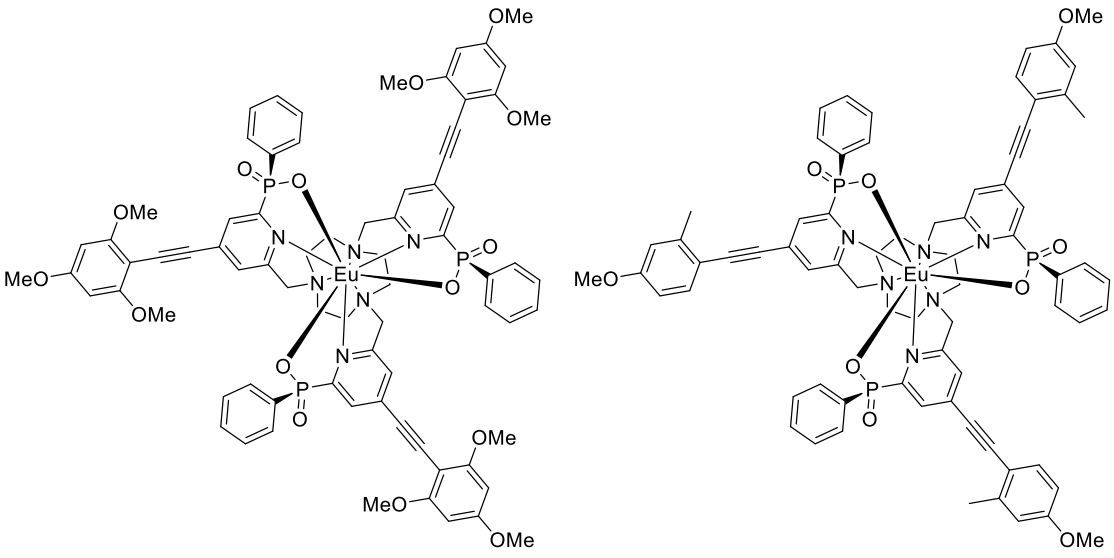

Figure 2.1 The structures of target complexes **[EuL^1]** and **[EuL^2]**.

The choice of **[EuL^1]** and **[EuL^2]** also allows their properties to be compared to the more hydrophilic methyl phosphinate analogues, **[EuL^3]** and **[EuL^4]** (see Fig. 2.2), which have been prepared previously.[29]

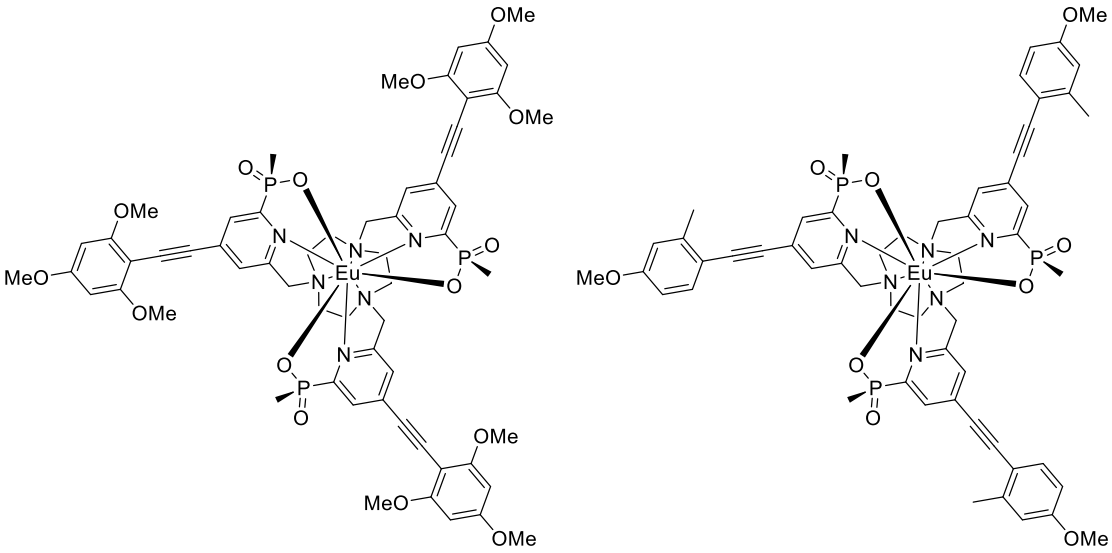

Figure 2.2 The structures of the methyl phosphinate analogues **[EuL^3]** and **[EuL^4]**.

2.2.1 Synthesis of [EuL^1]

The synthesis of **[EuL^1]** was carried out using modified literature procedures for structurally similar complexes. Various synthetic routes have been explored for such complexes. The two primary routes are to synthesise each ligand separately, before complexation with a europium(III) salt as the final step, or to prepare them by a divergent route involving the synthesis of a common intermediate, which could then be functionalised further under mild reaction conditions (see Scheme 2.1). In the case of the pyridylarylalkynyl complexes, a tris-(4-bromopyridyl) europium complex can be identified as the common intermediate.[133] The complex contains a C-Br bond which allows functionalisation by palladium-catalysed C-C bond forming reactions, such as a Sonogashira coupling reaction. In another example, the bromine atom was displaced by an azide group, before Cu(I)-catalysed 'click' chemistry was used to form a triazole ring.[133]

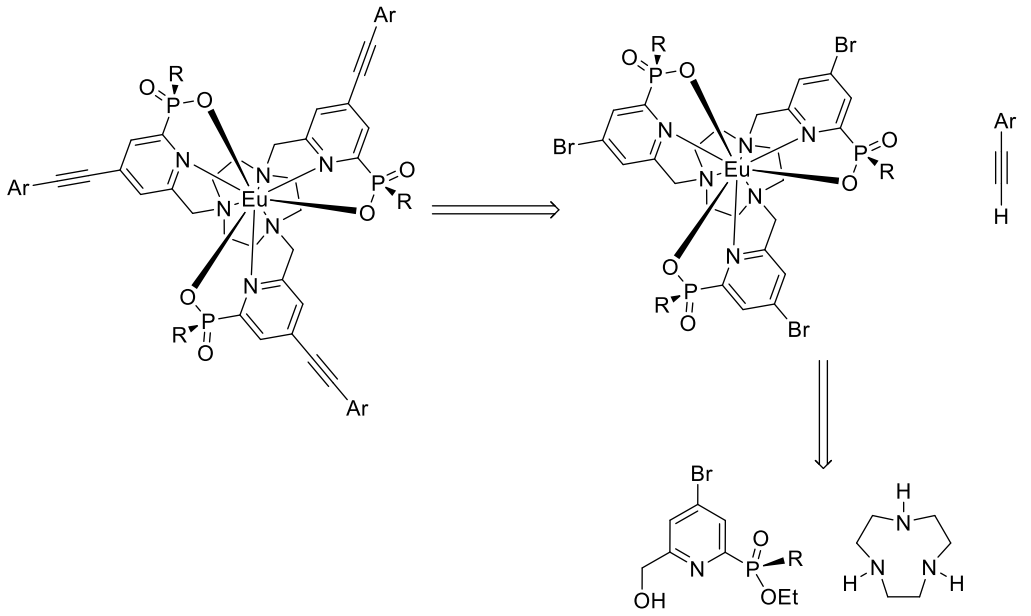

Scheme 2.1 A retrosynthetic analysis showing the common tris (4-bromopyridyl) europium complex which can be used in a divergent synthetic pathway.

Although the divergent route appears to be more economical, purification of the final complexes proved challenging, as multiple chromatographic separations under both normal and reverse phase conditions were required to separate the complexes from palladium catalyst residues, which led to rather low isolated yields of complex. Therefore, for the synthesis of **[EuL^1]** and **[EuL^2]**, it was decided to synthesise the complete ligand before complexation of the metal as the final step.[134] Retrosynthetic analysis of **[EuL^1]** identifies the required fragments, as shown in Scheme 2.2.

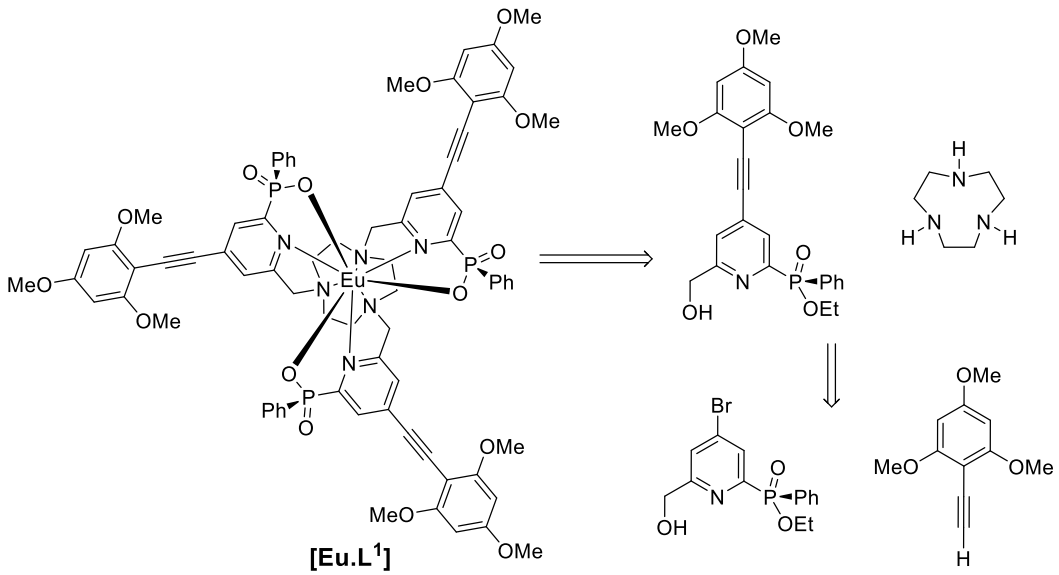

Scheme 2.2 An alternative retrosynthetic analysis for **[EuL^1]**.

The chromophore head group was synthesised via a two-step Corey-Fuchs reaction from 2,4,6-trimethoxybenzaldehyde **1**. In the first step, the aldehyde **1** was converted to the dibromoalkene **2**, which was then transformed to the terminal alkyne **3** (see Scheme 2.3).

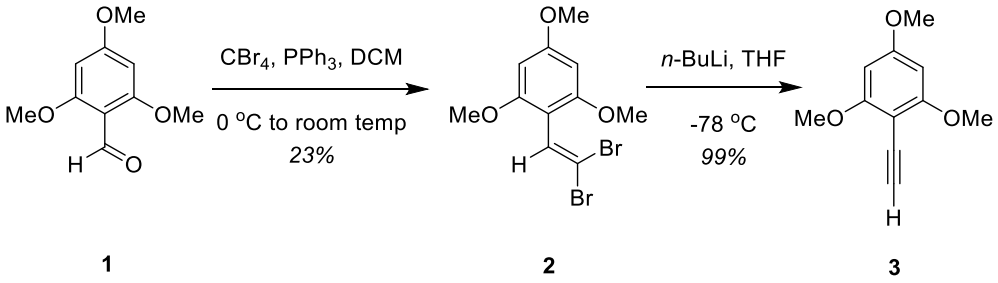

Scheme 2.3 The Corey-Fuchs method of terminal alkyne formation.

The conversion of the aldehyde **1** to the dibromoalkene **2** was very slow (28 hours), compared to Corey and Fuchs' original example where benzaldehyde was converted to the corresponding dibromoalkene in 5 mins at 0 °C.[135] There are two possible explanations for this. The reaction involves attack at the aldehyde by a phosphorus ylid. An electron rich aromatic ring such as in aldehyde **1** reduces the electrophilicity of the aldehyde group. Also, the aldehyde is sterically hindered by two *ortho*-methoxy groups, making the approach of the bulky ylid ($Br_2C{=}PPh_3$) more challenging. Subsequent conversion of the dibromoalkene **2** to the alkyne **3** was successful using *n*-butyllithium, and resulted in a high yield of product. In this step, the dibromoalkene undergoes an elimination reaction to give a bromoalkyne, followed by a lithium-halogen exchange which yields the terminal alkyne upon aqueous work up.

The synthesis of the phenyl-phosphinate pyridine platform **4** has been reported previously,[30] and began from 2-bromo-6-methylpyridine **5**, which was oxidised with *meta*-chloroperbenzoic acid to form the *N*-oxide **6**, allowing addition of a nitro group in the pyridine 4-position to form **7**. The *N*-oxide was reduced using PBr_3 to give 2-bromo-6-methyl-4-nitropyridine, **8** (see Scheme 2.4).

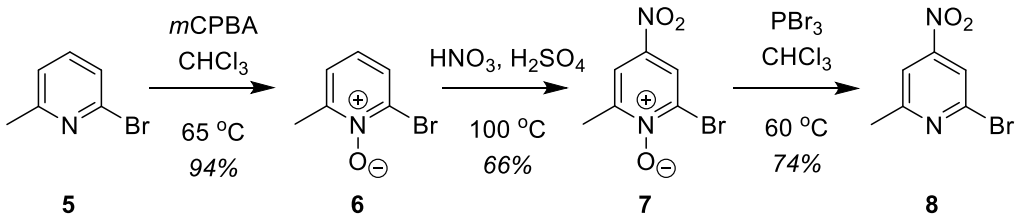

Scheme 2.4 Activation of the pyridine to allow nitration by S_NAr.

The next step was to introduce the phenyl phosphinate group, which was achieved by a palladium-catalysed C-P bond forming reaction with ethyl phenylphosphinate. Subsequent conversion of the nitro group of **9** to a bromine atom was carried out using acetyl bromide. Unfortunately, this step simultaneously hydrolyses the ethyl phosphinate ester which had to be restored by refluxing the phosphinic acid in triethylorthoformate to yield the phosphinate ester **10**. In order to introduce the alcohol functionality, it was necessary to re-oxidise the pyridine nitrogen to form the *N*-oxide **11**, before a Boekelheide rearrangement using trifluoroacetic anhydride furnished the ester **12**. Room temperature solvolysis of this ester yielded the final pyridine platform **4**.

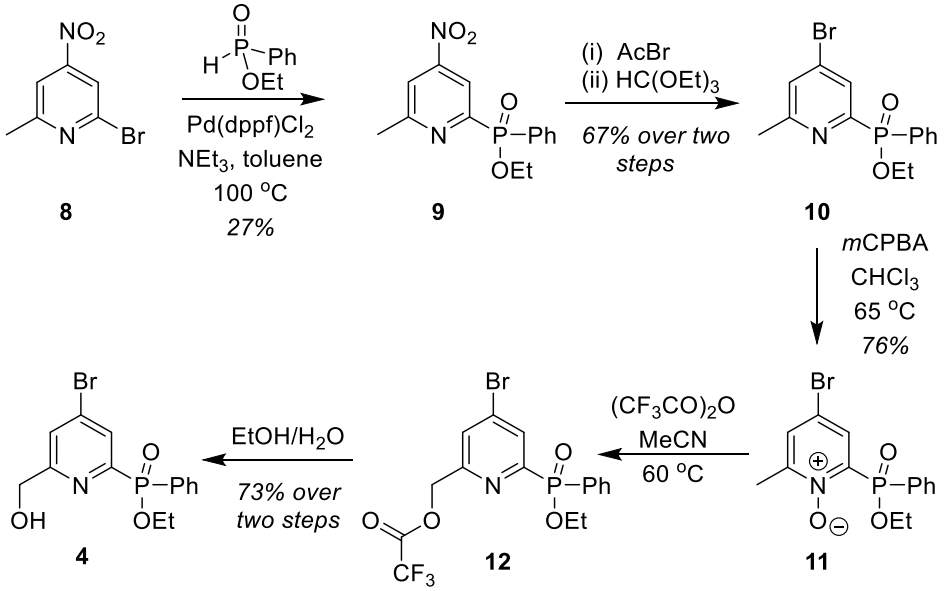

Scheme 2.5 Palladium-catalysed coupling of the phenyl phosphinate group followed by a Boekelheide rearrangement to introduce the alcohol functional group.

The mechanism of the Boekelheide rearrangement (see Scheme 2.6) has been proposed to proceed via either a concerted [3.3]-sigmatropic rearrangement or an ion pair mechanism. Experiments using ^{18}O- labelled acetic anhydride suggest that the ion pair mechanism is the more likely.[136]

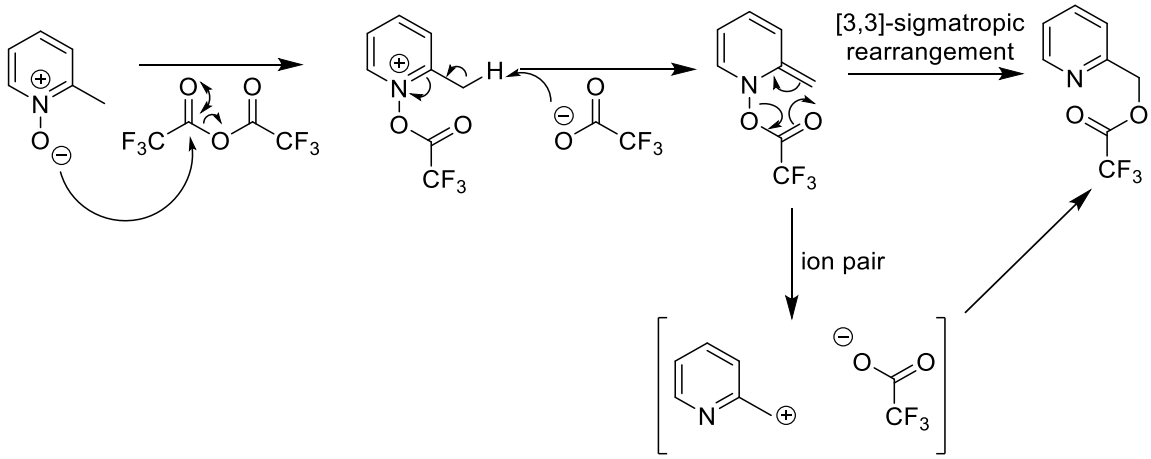

Scheme 2.6 Two possible mechanisms of the Boekelheide rearrangement.

The Boekelheide rearrangement reaction was difficult to monitor by mass spectrometry as the trifluoroacetate ester is susceptible to hydrolysis at room temperature which presents a problem for reverse phase liquid chromatography. Additionally, the *N*-oxide **11** and alcohol **4** have identical molecular masses. Instead, it was possible to monitor the reaction by ^{1}H NMR. The 6-methyl pyridine substituent of **11** has a ^{1}H resonance at 2.47 ppm (3 H, s, $CDCl_3$). As the Boekelheide rearrangement occurred, this peak disappeared whilst a new peak appeared at 5.44 ppm (2 H, s, $CDCl_3$), corresponding to the $–CH_2OCOCF_3$ protons in **12**. The trifluoroacetate ester hydrolysis can also be monitored by ^{1}H NMR as the chemical shift of the aforementioned CH_2 group moves from 5.44 ppm to 4.75 ppm.

With both fragments of the chromophore now synthesised, a Sonogashira reaction was used to couple them together (see Scheme 2.7). This reaction forms a carbon-carbon bond between a terminal alkyne and an aryl halide and is catalysed by palladium(0) and a copper(I) co-catalyst. The reaction is useful due to its relatively mild conditions. The reaction is sensitive to oxygen and so must be carried out in degassed solvents. Typically a palladium(II) pre-catalyst is used which is more stable for long term storage. This is reduced *in situ* to provide the palladium(0) species required to catalyse the coupling. Prior work in the group had established that $Pd(dppf)Cl_2$ ([1,1'-bis(diphenylphosphino)ferrocene]dichloropalladium(II)) was a suitable catalyst for this coupling reaction.

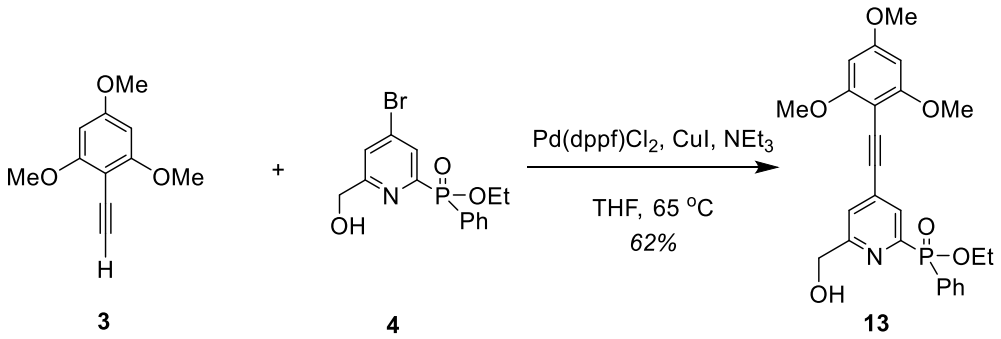

Scheme 2.7 The Sonogashira coupling reaction of alkyne **3** to ethyl [4-bromo-6-(hydroxymethyl)pyridine-2-yl](phenyl) phosphinate **4**.

The reaction was complete after 4 hours. Initial purification of **13** by column chromatography using dichloromethane and methanol as eluent (very gradual increase from neat dichloromethane to 3% methanol) did result in separation of some of the catalyst by-products. However, the product co-eluted with other by-products. Various solvent systems were tested to see whether the product could be separated from the by-products. Reasonable separation was achieved in neat ethyl acetate. Therefore, a second purification by column chromatography was carried out using an ethyl acetate/hexane eluent system. This time, the product could be isolated from the remaining catalyst in a reasonable yield.

Mesylation of **13** with methanesulfonyl chloride and triethylamine led to the mesylate **14** in quantitative yield. The mesylates are reactive and must be used in the alkylation step without further purification (see Scheme 2.8). Alkylation of 1,4,7-triazacyclononane was carried out in acetonitrile using potassium carbonate as the base. After stirring at 60 °C overnight, the suspension was centrifuged to remove inorganic salts and the solution was decanted. The solid was then washed repeatedly with acetonitrile and centrifuged again. The crude ligand was purified by column chromatography and gave the product in a rather low isolated yield.

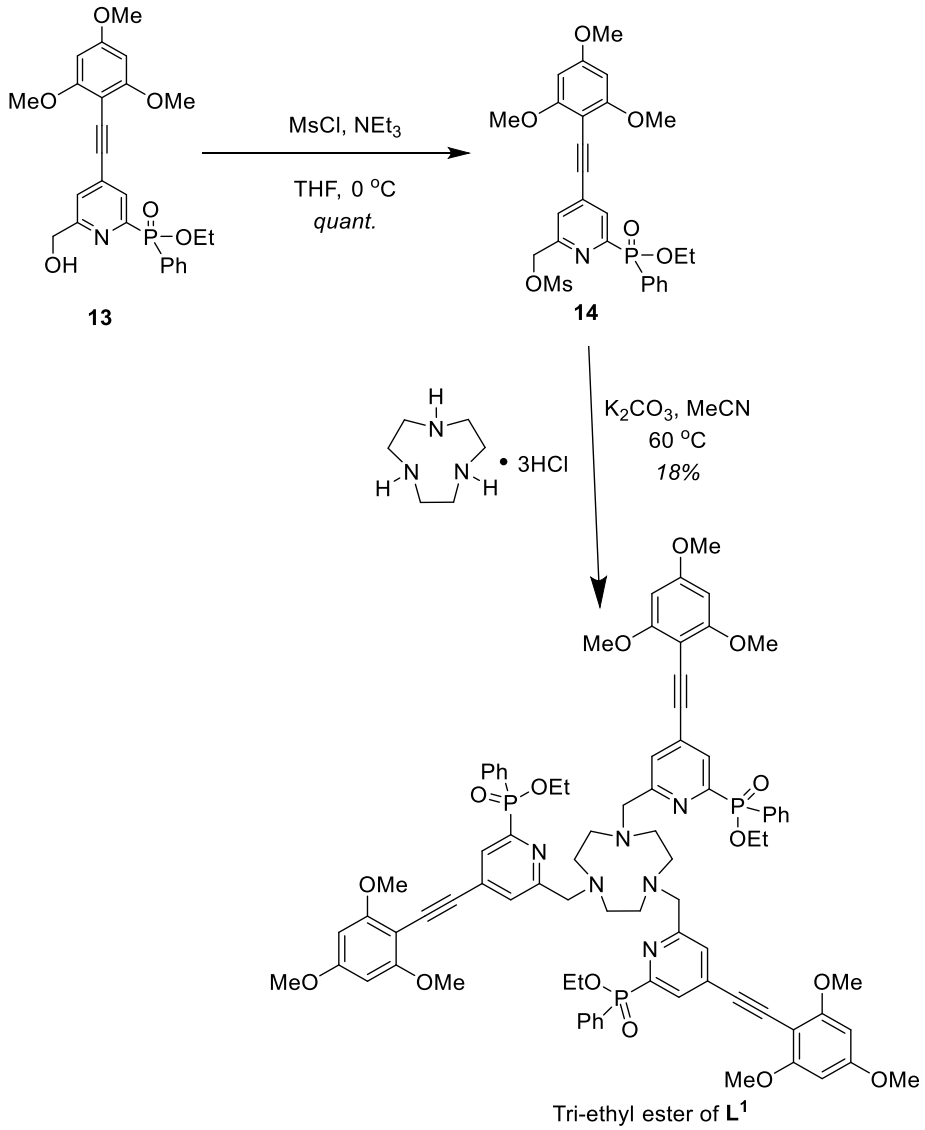

Scheme 2.8 The mesylation of alcohol **13** and the subsequent alkylation of triazacyclononane with mesylate **14** to give the tri-ethyl ester of $\mathbf{L^1}$.

Finally, phosphinate ester hydrolysis and complexation were required to reach the final complex. Phosphinate ester hydrolysis was carried out in a CD_3OD/D_2O mixture with potassium hydroxide at 60 °C (see Scheme 2.9). The use of deuterated solvents allows the reaction to be monitored by NMR. Disappearance of the proton resonances for the ethyl esters can be observed but more useful is the change in the shift of the phosphorus resonance in the ^{31}P NMR spectrum, from approximately +25 ppm for the ethyl ester to +16 ppm for the free phosphinate. This method of reaction monitoring is favoured as the hydrolysed ligands are difficult to observe by mass spectrometry. After 8 days, ^{31}P NMR showed the hydrolysis to be complete. This reaction was significantly slower than has been

reported for the methyl phosphinate analogues,[29] which could be attributed to a more hindered approach of the solvated OH^- nucleophile to the phosphorus atom due to the large phenyl substituent. In earlier work on these systems, phenyl phosphinate ester hydrolysis was achieved using 6 M HCl. However, this method is not compatible with the extended chromophores as the alkyne bond is hydrated in similar complexes under acidic conditions.[137] Evidence for this process was obtained by mass spectrometry (increase of 54 Da, consistent with addition of three water molecules), by significant changes in the absorption spectra, and by loss of observable emission after exposure to acidic solution. A possible mechanism for this process is shown in Scheme 2.10.

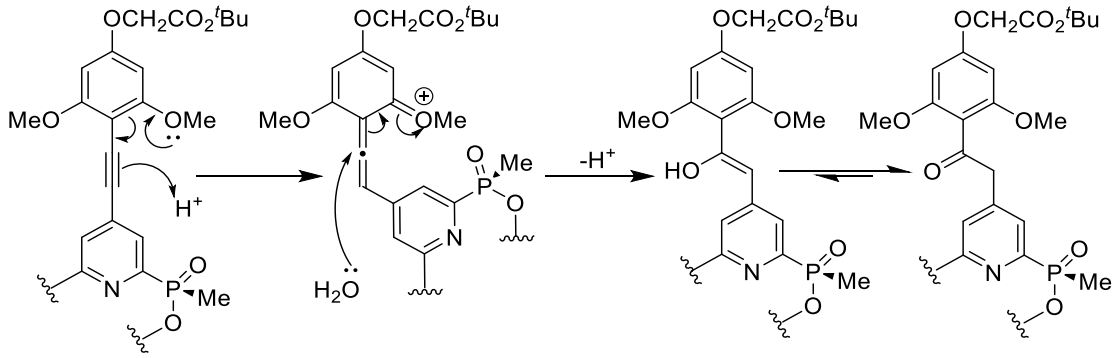

Scheme 2.10 Proposed mechanism of acid-catalysed addition of water to a pyridylarylalkynyl chromophore.[137]

Once the ester hydrolysis was complete, europium(III) chloride hexahydrate was added. The reaction was stirred overnight at 60 °C, after which time the mass spectrum of the reaction mixture showed formation of the complex. The reaction was neutralised with dilute aqueous acid and concentrated, before the crude complex was purified by reverse phase HPLC. Due to the reduced solubility of these complexes in water, the crude complexes were purified in multiple small injections to limit precipitation of the complex in the HPLC instrument.

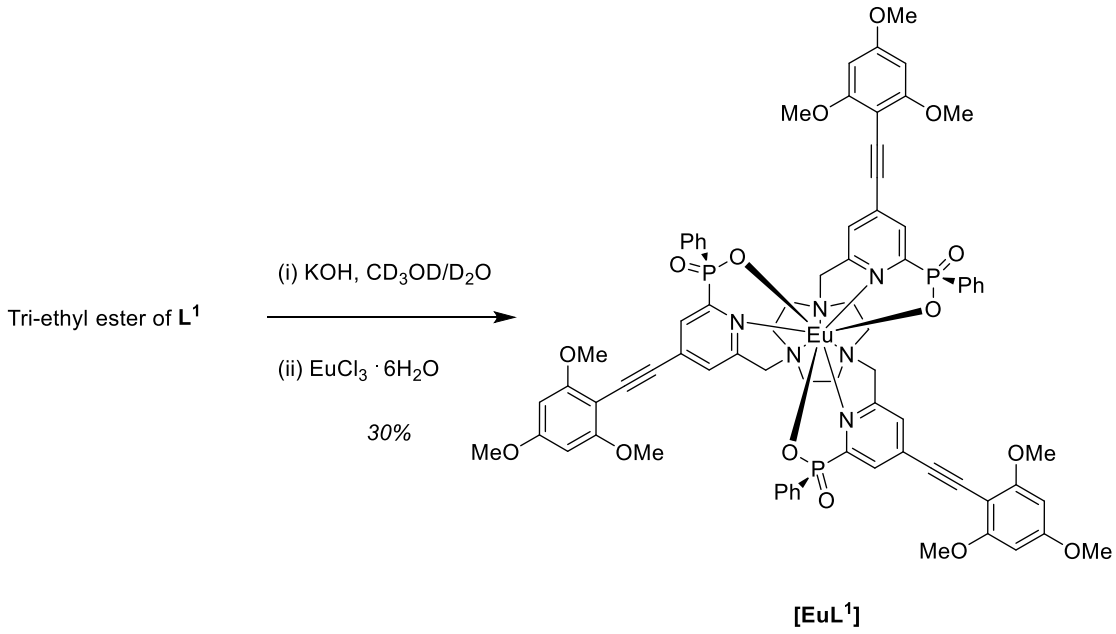

Scheme 2.10 Phosphinate ester hydrolysis and complexation to form **[EuL^1]**.

2.2.2 Synthesis of [EuL^2]

Due to the commercial availability of the starting material 4-bromo-3-methylanisole **15**, the synthesis of the chromophore head group of **[EuL^2]** follows a different route. An alkyne group was introduced by a Sonogashira coupling of **15** to ethynyltrimethylsilane to form the silane **16**. The trimethylsilyl protecting group was removed with triethylamine trihydrofluoride to give the terminal alkyne **17** in good yield (see Scheme 2.11). The deprotection reaction was slow, taking 6 days for complete deprotection. An alternative method for the deprotection has been tested in the group using tetrabutylammonium fluoride (TBAF) instead. This reaction was much quicker but the product could not be easily isolated from the reaction mixture.

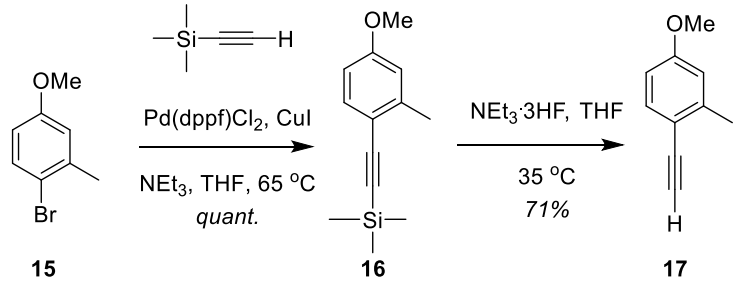

Scheme 2.11 The synthetic route to 1-ethynyl-4-methoxy-2-methylbenzene **17**.

This terminal alkyne **17** could then be coupled to the *p*-bromopyridyl moiety **4** using a Sonogashira coupling reaction to give the extended pendant chromophore arm **18** (see Scheme 2.12). As with the purification of **13**, the crude product was subjected to two column chromatography purifications in order to remove all the catalyst residues.

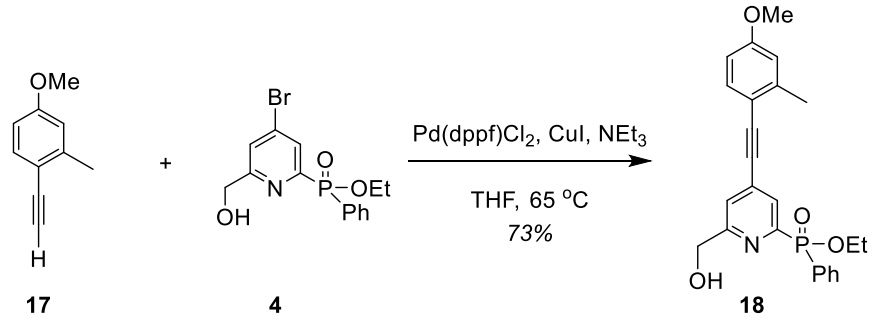

17 **4** **18**

Scheme 2.12 The Sonogashira coupling of alkyne **17** to ethyl [4-bromo-6-(hydroxymethyl)pyridine-2-yl](phenyl) phosphinate 4.

Following the same route as for complex **[EuL^1]**, fragment **18** was converted to the mesylate **19** in quantitative yield and was then used to alkylate triazacyclononane (see Scheme 2.13). When TLC conditions were tested for purification of the crude alkylation product, no separation could be achieved. It was therefore decided to complex the unpurified ligand, rather than risk losing a large quantity of the material on a silica column. Identification of the desired product in the crude mixture was achieved by NMR spectroscopy and mass spectrometry (see Chapter 5).

Consequently, phosphinate ester hydrolysis was carried out with potassium hydroxide in a CH_3OH/H_2O mixture and addition of europium(III) chloride hexahydrate led to the desired complex **[EuL^2]** which was purified by RP-HPLC. Solubility of the crude product in the HPLC solvent was again a problem. The solutions to be injected were filtered to avoid any solid particles being injected onto the columns.

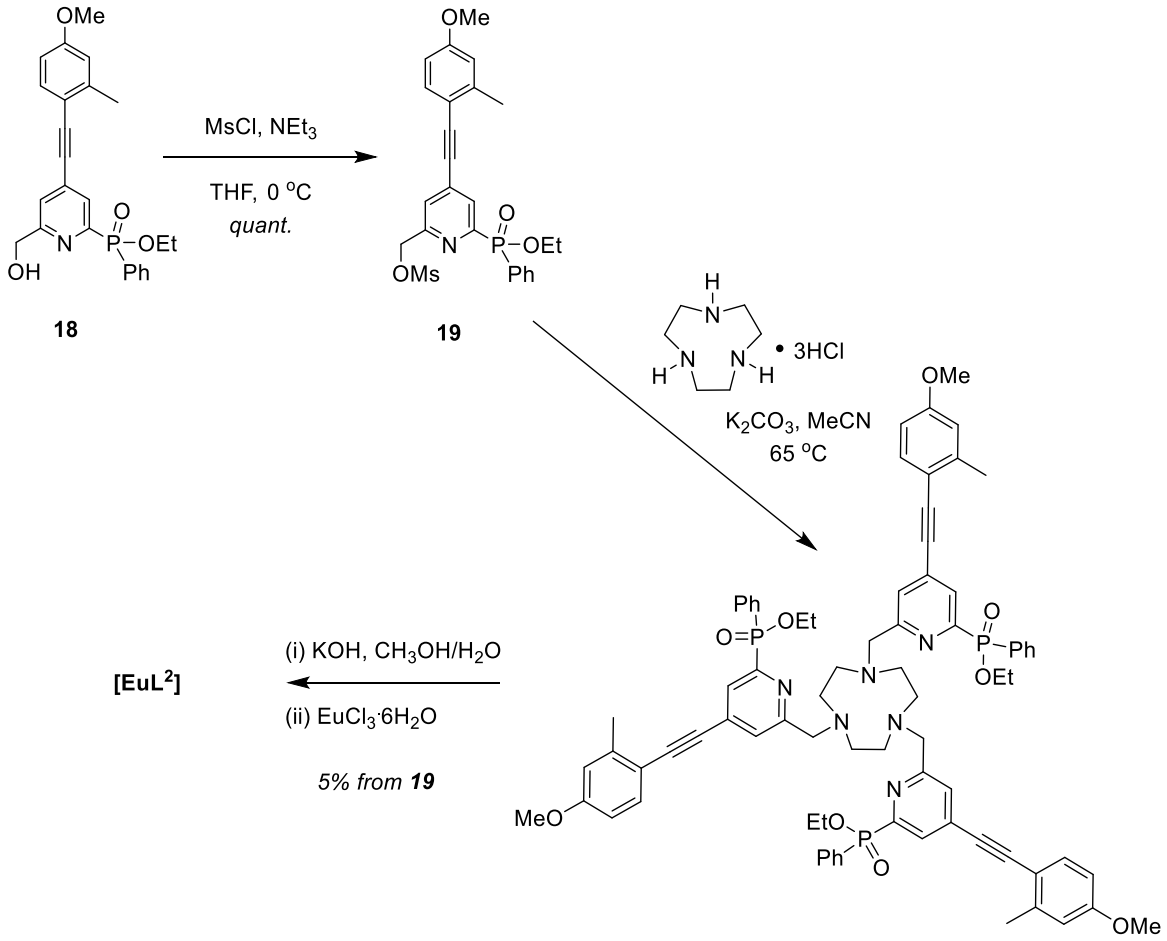

Scheme 2.13 The synthesis of the tri-ethyl ester of $\mathbf{L^2}$ and the complexation reaction to form $\mathbf{[EuL^2]}$.

2.3 Photophysical properties of [EuL^1] and [EuL^2]

The photophysical properties of the novel europium(III) complexes, **[EuL^1]** and **[EuL^2]**, were measured in methanol. As predicted, the absorption spectra of **[EuL^1]** and **[EuL^2]** show broad absorption bands that closely resembled those of the methyl-phosphinate analogues, **[EuL^3]** and **[EuL^4]** (see Fig. 2.3).

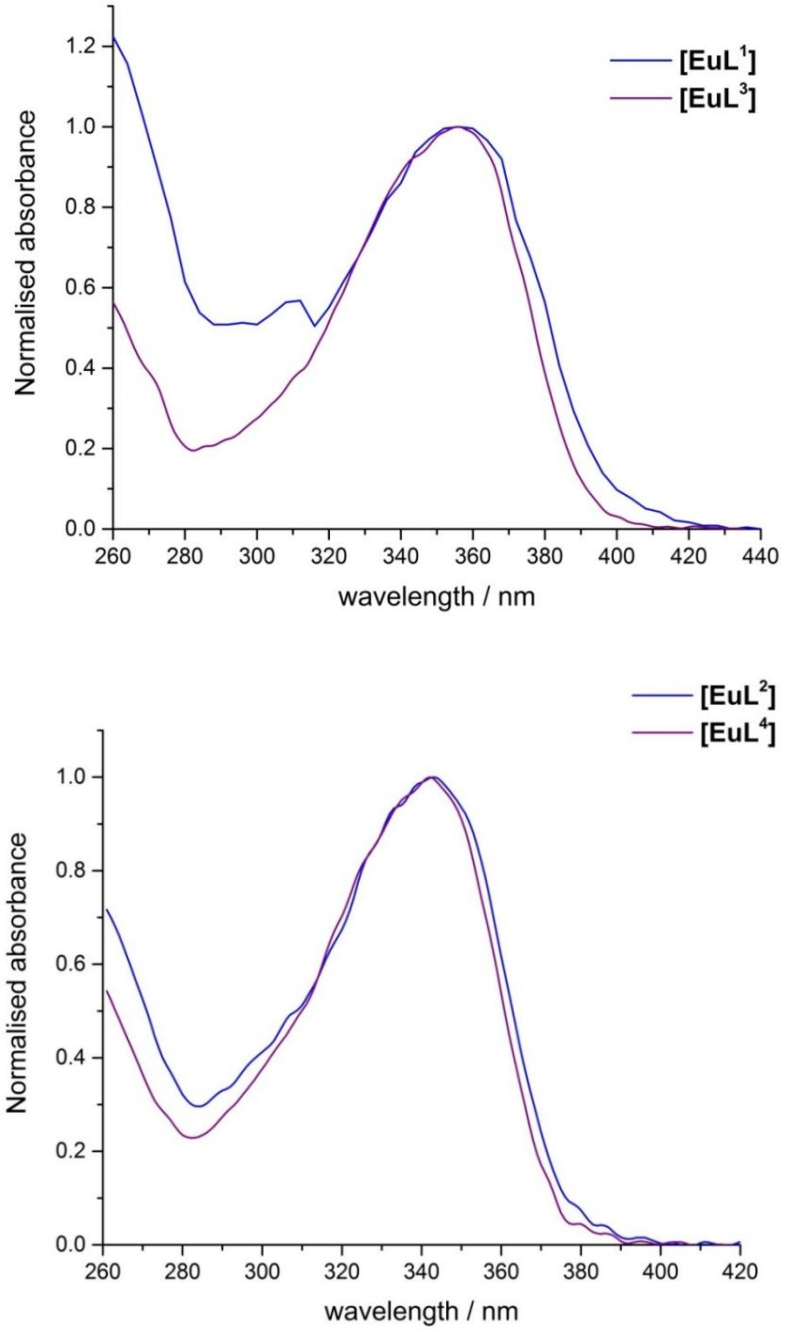

Figure 2.3 Absorption spectra of **[EuL$^{1-4}$]** (MeOH, 295 K), showing broad, featureless absorption bands assigned to an internal charge transfer transition.

Excitation spectra (example shown in Fig. 2.4) also confirmed that sensitisation of the europium(III) ion did indeed occur via this broad absorptive transition, attributed to an internal charge transfer state. These broad bands mean that the complexes bearing trimethoxy-substituted chromophores (**[EuL^1]** and **[EuL^3]**), absorb almost the same amount of light at 365 nm (the wavelength of a UV-LED) as they do at their absorption maxima (356 and 355 nm, respectively). For **[EuL^2]** and **[EuL^4]**, bearing the *p*-methoxy-*o*-methyl substituted chromophores, there is still 40% efficiency in absorption at 365 nm, despite their absorption maxima being over 20 nm away. At 355 nm (3rd harmonic of Nd:YAG lasers), there is approximately 70% absorption efficiency, demonstrating the potential utility of these complexes in security applications using 355 or 365 nm excitation.

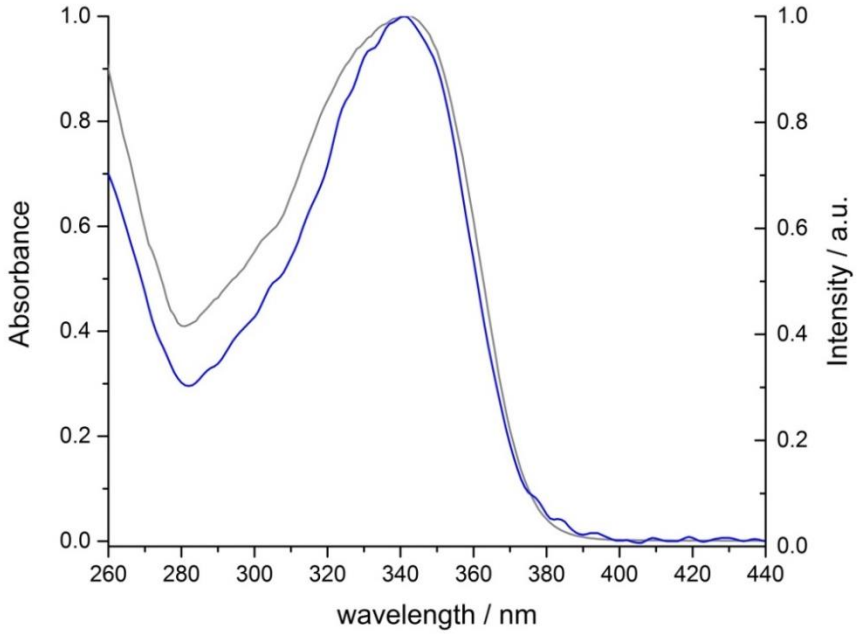

Figure 2.4 Overlaid absorption (*blue*) and excitation (*grey*) spectra for **[EuL^2]** confirming europium(III) excitation via the internal charge transfer absorption band (MeOH, 295 K, λ_{em} 614 nm).

The emission spectra of **[EuL^1]** and **[EuL^2]** also closely resemble their methyl phosphinate analogues (see Fig. 2.5). Given that the N_6O_3 coordination cage is the same in both instances, this is perhaps unsurprising. However, small differences can be observed in the relative intensities of the transitions in the ΔJ = 4 manifold (680-710 nm), and also between the major band and the smaller doublet in the ΔJ = 2 manifold (610-630 nm). These differences are conserved on changing the chromophore group. Since the ΔJ = 2 and 4 transitions are sensitive to ligand to

ligand environment (indeed $\Delta J = 2$ is hypersensitive), it is possible that these minor differences are due to a small change in geometry or Eu-O bond distance upon changing from a methyl phosphinate to a phenyl phosphinate donor group.

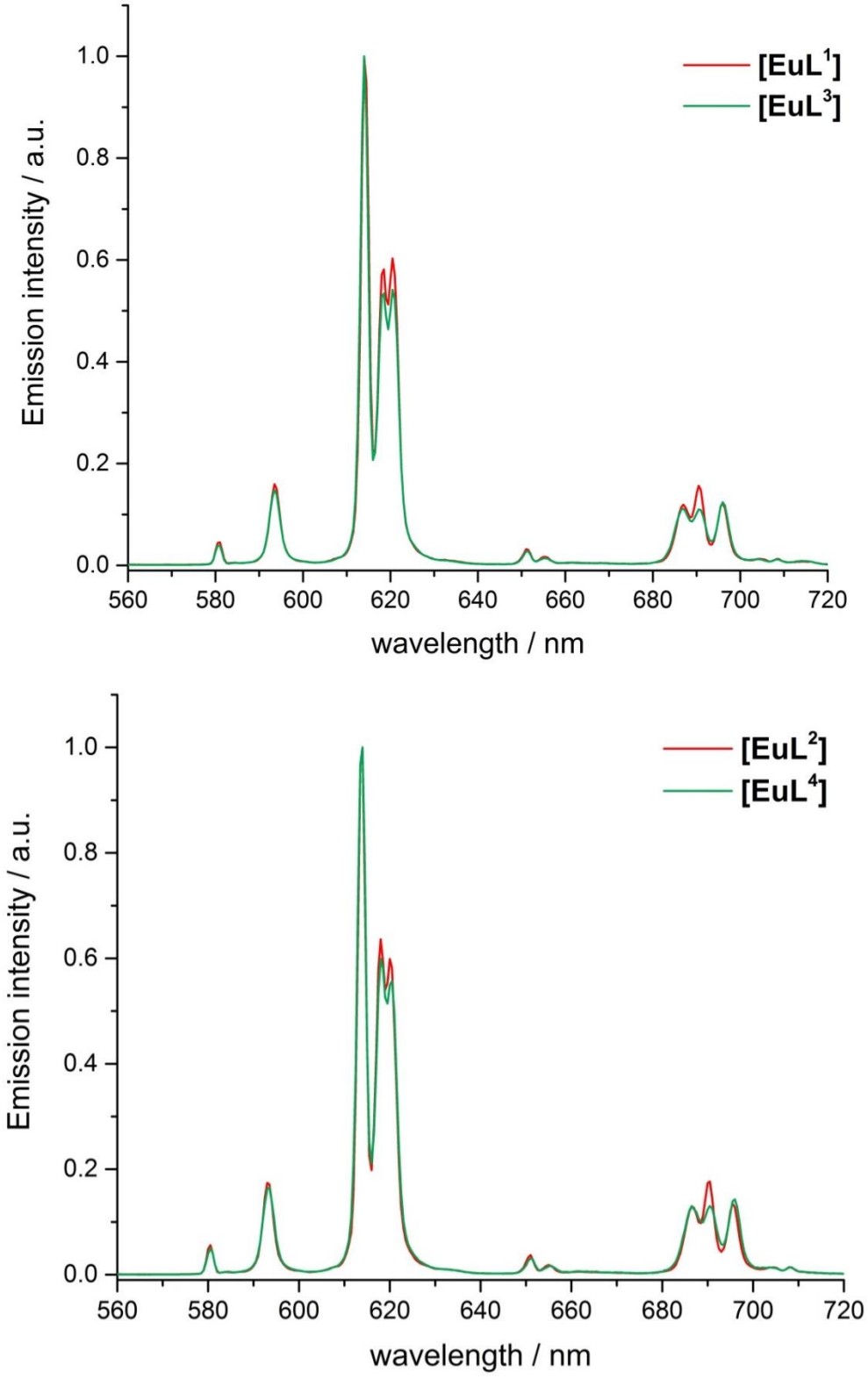

Figure 2.5 The normalised emission spectra of **[EuL$^{1\text{-}4}$]** (MeOH, 295 K, 5 µM complex, excited at the absorption maximum for each complex).

Emission lifetimes were also recorded for **[EuL^1]** and **[EuL^2]** and were found to be longer than for the methyl phosphinate analogues, and consistent with related similar phenyl phosphinate complexes. The molar extinction coefficients for **[EuL$^{1-4}$]** are all in the range 57 000 – 65 000 M^{-1} cm^{-1}, consistent with other complexes of this type.[29] The key photophysical properties of **[EuL$^{1-4}$]** are summarised in Table 2.1. Absorbance values at 365 nm are also quoted as a percentage of the absorbance at λ_{max} as this is a common LED excitation wavelength, as used in these experiments. The complexes possess brightness values in the range 16.8 – 30.2 mM^{-1} cm^{-1}, compared to the red fluorescent protein mCherry, with a brightness of 19 mM^{-1} cm^{-1} (mCherry has an emission maximum at 612 nm, corresponding to the emission maximum in the ΔJ = 2 manifold of **[EuL$^{1-4}$]**).[138]

Due to their broad absorption bands, the complexes possess brightness parameters up to 23 mM^{-1} cm^{-1} at the common excitation wavelengths of 355 and 365 nm. Quantum yields were measured by an absolute method using an integrating sphere rather than by comparison to a standard.[139] The phenyl phosphinate complexes have higher quantum yields than the analogous methyl phosphinate complexes, consistent with more effective shielding of the metal centre by the bulkier phenyl groups. However, it is clear to see that the complexes bearing the more electron rich trimethoxy-substituted chromophore (**[EuL^1]** and **[EuL^3]**) have lower quantum yields than the *p*-methoxy-*o*-methyl-substituted complexes, **[EuL^2]** and **[EuL^4]**. The more electron rich trimethoxy-substituted chromophore is more easily oxidisable which, in combination with the reducibility of Eu(III) to Eu(II), could lead to the ligand excited state being quenched by electron transfer to the metal centre.[5] Such a process would lower the quantum yield of the complexes bearing these chromophores.

Table 2.1 Key photophysical properties of the europium(III) complexes **[EuL$^{1\text{-}4}$]** (295 K, MeOH).

Complex	λ_{max}[a]/ nm	Normalised absorbance at 365 nm / %	Φ_{em} / %	τ_{Eu}/ ms	Brightness, *B*, at 365 nm[b] / mM^{-1} cm^{-1}
[EuL^1]	356	98	39	1.18	22.9
[EuL^2]	343	40	50	1.22	12.0
[EuL^3]	355	100	28	1.10	16.8
[EuL^4]	342	37	42	1.14	9.3

[a] Extinction coefficients for these complexes are 60 000 (±5 000) M^{-1} cm^{-1}.

[b] These brightness calculations assume that the quantum yields are constant across the excitation band.

2.4 Complex chirality and resolution by chiral HPLC

In complexes of this type based on 9-N_3, three different forms of chirality arise (see Fig. 2.6). The first is the configuration around the tetrahedral phosphorus atoms in the phosphinate groups, which can be described as *R* or *S* in the same way as for point chirality at a carbon atom, following Cahn-Ingold-Prelog rules (green in Fig. 2.6). In this instance, the oxygen coordinated to the metal takes the highest priority, followed by the second oxygen atom, then the pyridine carbon, with the *P*-methyl or *P*-phenyl substituent in lowest priority. Secondly, the $NCCN_{pyr}$ torsion angle (viewed along the C-C bond indicated by the blue arrow) can be described as either positive or negative, which confers *Δ* or *Λ* helicity, respectively, on the complex. Thirdly, the torsion angle of the NCCN link in the macrocycle (viewed along the C-C bond indicated by the red arrow) can either have a positive or negative sign, which define a *δ* or *λ* conformation, respectively.

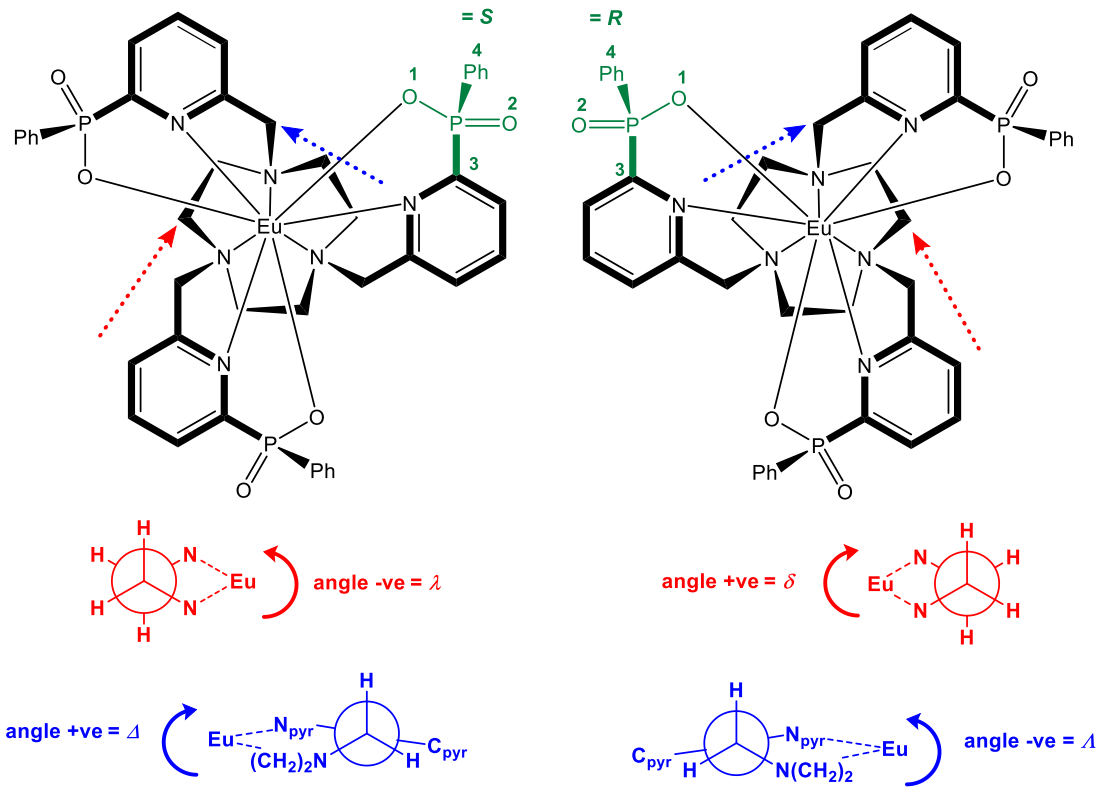

Figure 2.6 Schematic diagrams showing the definitions of the chirality at phosphorus (*green*), complex helicity (*blue*) and macrocycle conformation (*red*) in 9-N_3 based pyridylphosphinate complexes.

Such complexes could theoretically exist in any combination of *R*/*S* configuration, *Δ*/*Λ* helicity and *δ*/*λ* conformation. However, the steric bulk of the pyridine groups and the phosphinate substituents impose conditions on the structure. It is necessary that all three pyridine arms possess the same helicity to avoid a steric clash of the phosphinate groups. The methyl and phenyl substituents of the phosphinate groups are also required to point away from the macrocyclic ring. Taking into account these restrictions, four possible stereoisomers exist as shown in Figure 2.7.

In systems where X-ray crystal structure determination has been possible, only the *SSS*–*Δ*(*λλλ*) and *RRR*-*Λ*(*δδδ*) isomers have been observed.[140] Interconversion between stereoisomers requires cooperative ring inversion, arm rotation and inversion of the configuration at the phosphorus atom. The same arguments can be used to assign the chirality of complexes with carboxylate donors rather than phosphinates, and similar analyses are possible for complexes based on 12-N_4 macrocycles.

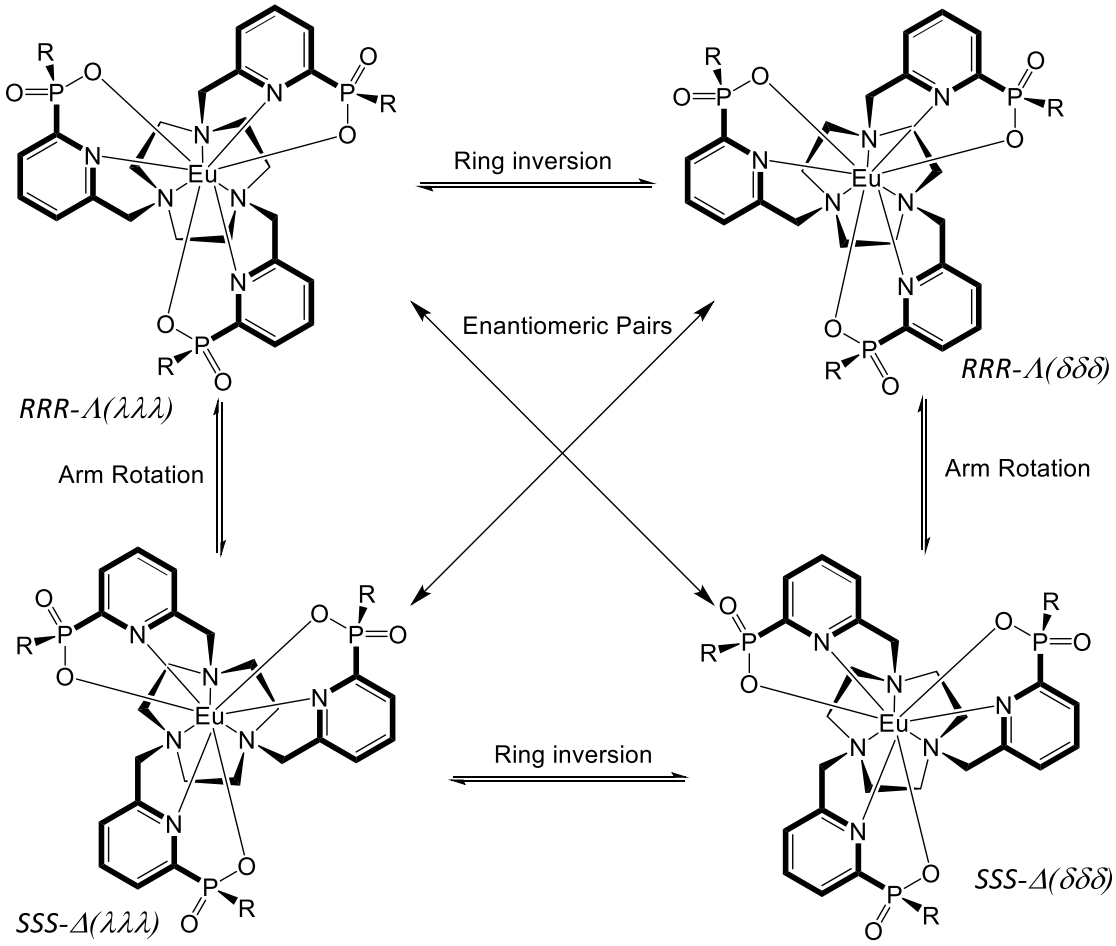

Figure 2.7 The four possible stereoisomers of a pyridylphosphinate 9-N_3 complex.

In order for europium complexes of this type to be used as CPL-emitting security labels, it was necessary to separate the racemic mixtures to obtain enantiopure complexes. The separation was achieved by chiral HPLC. Briefly, chiral HPLC differs from conventional HPLC in the use of a chiral stationary phase (CSP), leading to diastereomeric interactions between the CSP and the compound to be separated. The strength of these transient diastereomeric complexes can be different for different enantiomers of the same molecule, allowing the separation of the enantiomers. There is a very wide range of CSPs available, varying from synthetic and natural polymers (methacrylates, cellulose, amylose, proteins) to small molecules (crown ethers, cyclodextrins and macrocyclic glycopeptides). For the purposes of this work, chiral columns based on cellulose and amylose have been used (see Fig. 2.8). The structures of the chiral stationary phases imply that they are fully derivatised with the phenylcarbamate groups, but in reality it is rather difficult to measure the precise degree of derivatisation.

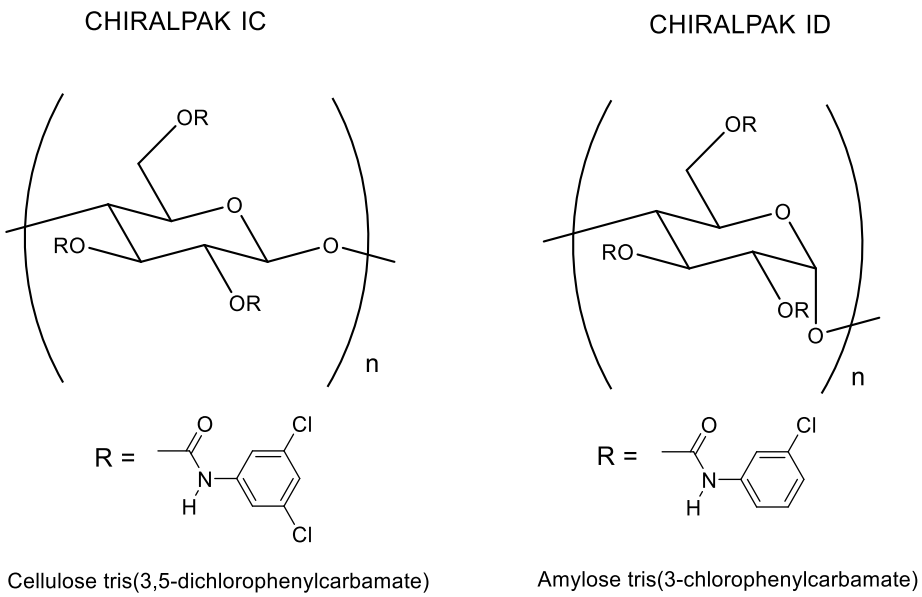

Figure 2.8 The chiral stationary phases used in Daicel CHIRALPAK-IC and ID columns.

Chiral HPLC separation has been investigated for both of the complexes **[EuL^1]** and **[EuL^2]**, as well as their methyl phosphinate analogues **[EuL^3]** and **[EuL^4]**. In each case, resolution of the enantiomers was achieved at room temperature using isocratic methanol as the eluent.[134] For complexes **[EuL^2]**, **[EuL^3]** and **[EuL^4]**, the best separation was achieved on the CHIRALPAK-ID columns. However, for complex **[EuL^1],** poor separation was observed using the CHIRALPAK-ID column but good separation was achieved with the CHIRALPAK-IC column (see Fig. 2.9). Interestingly, the order of the enantiomer elution was the same for **[EuL$^{2\text{-}4}$]** (using CHIRALPAK-ID) whereas the enantiomers of **[EuL^1]** eluted in the reverse order. Such behaviour suggests that the difference in chirality at the anomeric carbon in the cellulose and amylose stationary phases contributes to the separation of the enantiomers.

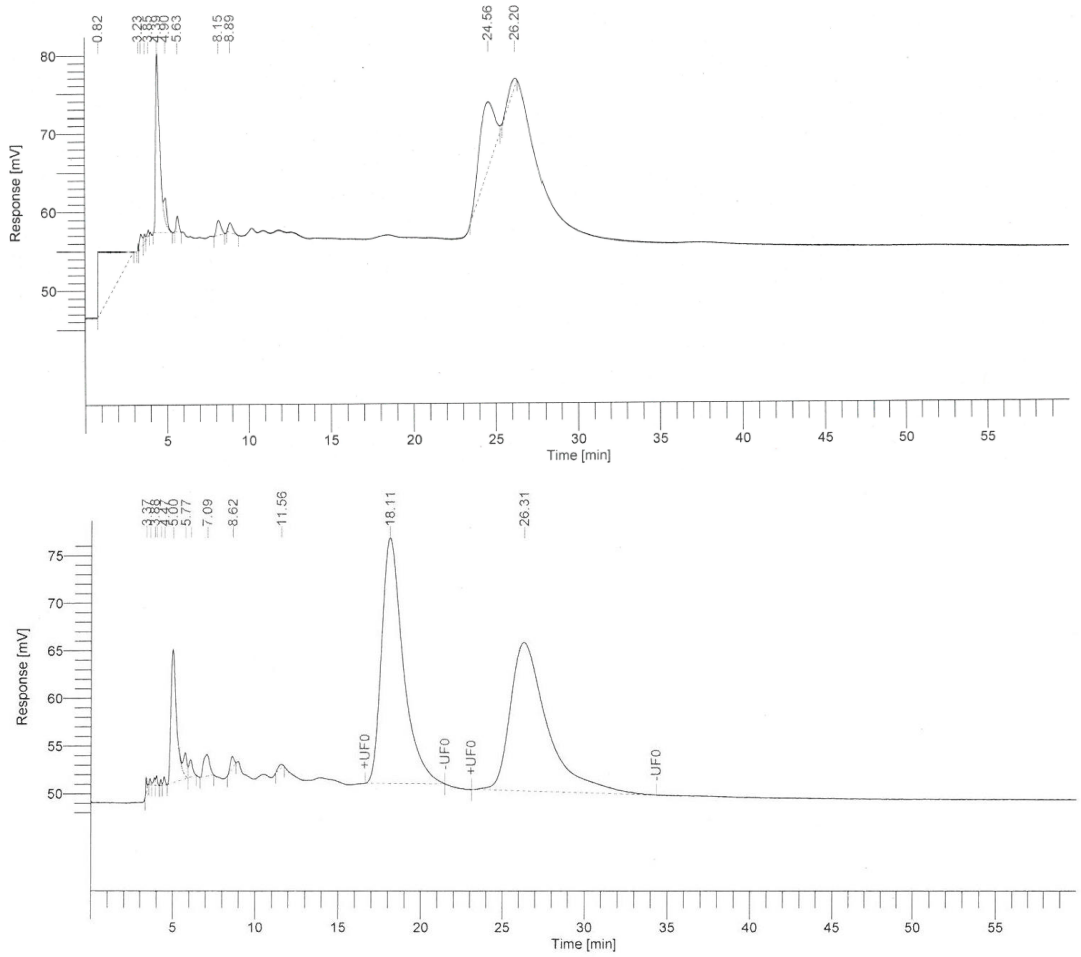

Figure 2.9 Analytical chiral HPLC traces for crude **[EuL^1]** on CHIRALPAK-ID (*top*) and CHIRALPAK-IC (*bottom*) (295 K, MeOH, 1 mL/min, UV detector λ = 356 nm).

The longer the retention time of the compound, the broader the peak and the longer the tail. Such features can be seen very clearly for the analytical trace of **[EuL^4]** (see Fig. 2.10). Therefore, the ideal conditions must strike a balance between a relatively short retention time and good separation. One variable that can be controlled is the flow rate. However, the range over which this can be changed is limited by the maximum pressure at which the columns can be used. Operating the columns at high pressure for extended periods of time can result in the stationary phase being damaged.

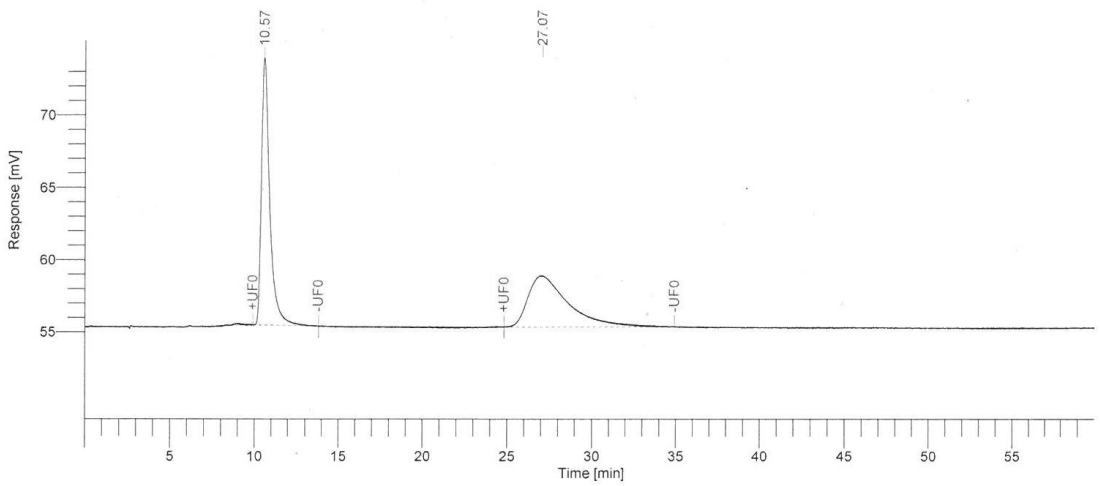

Figure 2.10 The analytical HPLC trace for the racemate of **[EuL^4]** showing how longer retention times result in broad peaks with long tails (CHIRALPAK-ID, 295 K, MeOH, 1 mL/min, UV detection λ = 342 nm).

Once it had been determined that all four complexes could be resolved by chiral HPLC on an analytical scale, preparative separations were carried out. In order to replicate the conditions as closely as possible on moving from the analytical to semi-preparative columns, a flow rate of 4.4 mL/min was used. Such conditions represent a compromise between retention time and back pressure to prolong the lifetime of the columns. Thus, in preparative LC traces were observed with similar profiles to the analytical traces but slightly longer retention times. An example of this behaviour for **[EuL^3]** can be seen in Fig. 2.11. In each case, removal of solvent from the collected fractions was carried out at room temperature to minimise the possibility of racemisation.

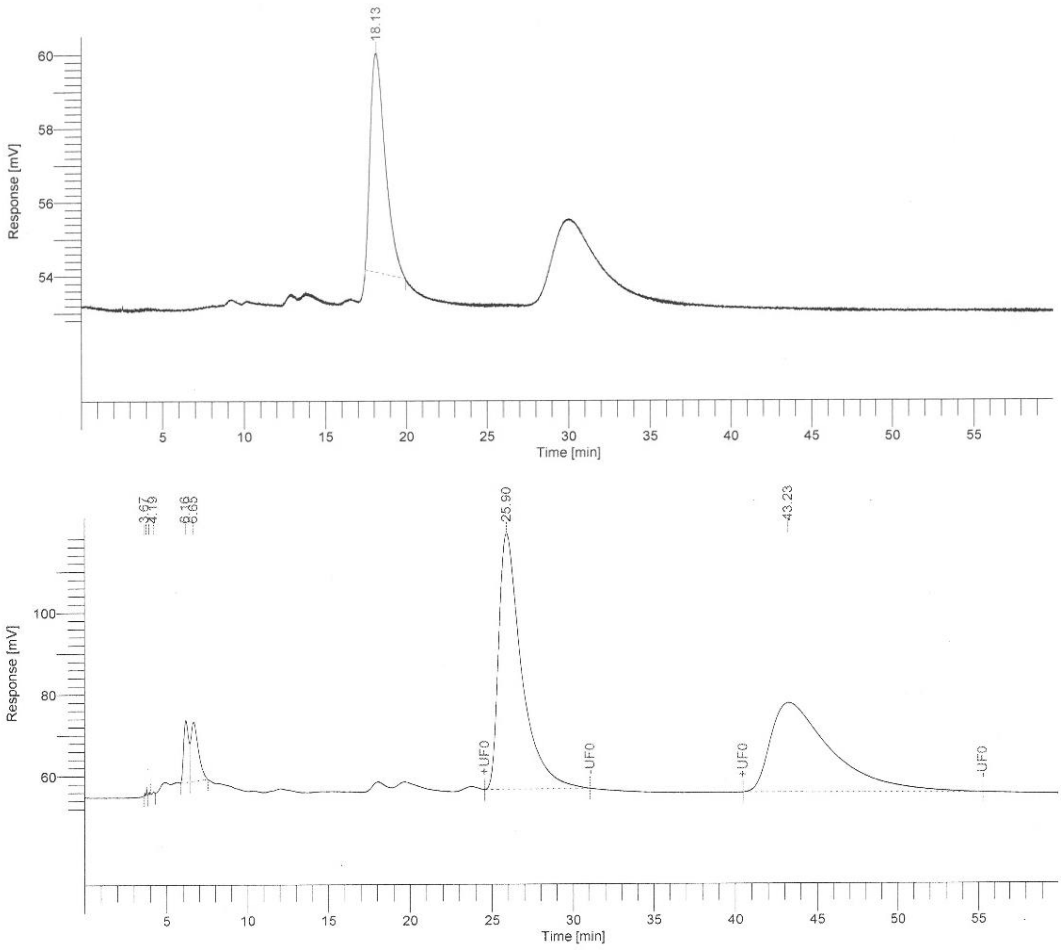

Figure 2.11 Analytical (*top*) and preparative (*bottom*) traces for **[EuL^3]** (CHIRALPAK-ID, 295 K, MeOH, 1.0 mL/min for analytical, 4.4 mL/min for preparative, UV detector λ = 356 nm)

2.5 CPL characterisation

CPL spectra have been recorded for each enantiomer of the complexes **[EuL$^{1\text{-}4}$]** (see Figs. 2.12-2.15).[134] In every case, mirror imaged CPL spectra were observed for enantiomers of the same complex. Comparison of the profiles of **[EuL$^{1\text{-}4}$]** to the parent complexes **[EuL^5]** and **[EuL^6]** (see Figs. 2.16 and 2.17) allowed the absolute configuration of the enantiomers to be identified, due to the fingerprint-like profile in the Δ*J* = 4 manifold (680-710 nm). The absolute configuration of the enantiopure parent complexes **[EuL^5]** and **[EuL^6]** has been established previously from X-ray crystal structure analysis.[39,140]

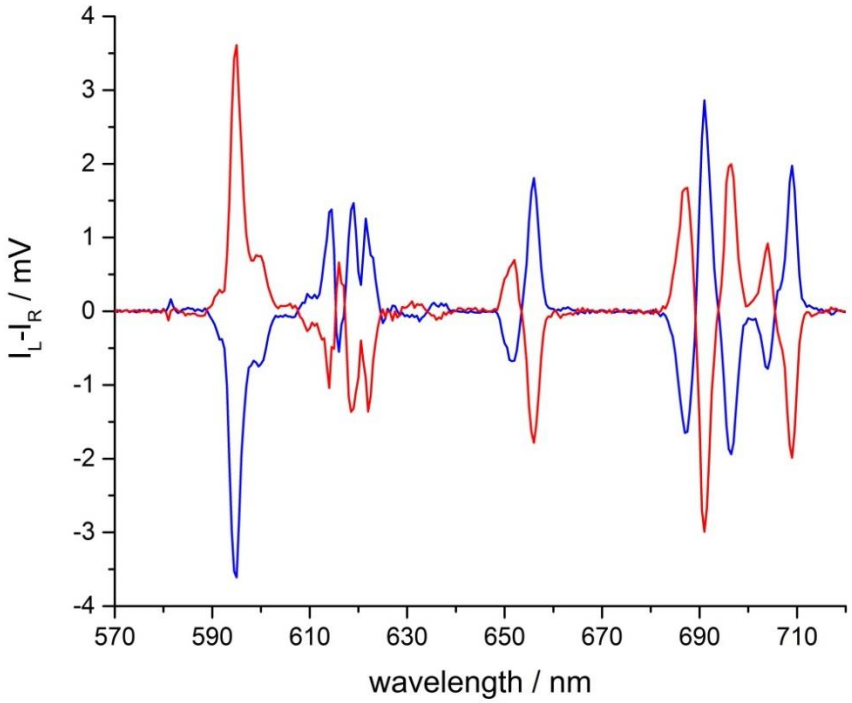

Figure 2.12 CPL spectra of the *Δ*- (*red*) and *Λ*- (*blue*) enantiomers of **[EuL^1]** (MeOH, 295 K, 5 µM complex, λ_{exc} 356 nm, 5 scans averaged).

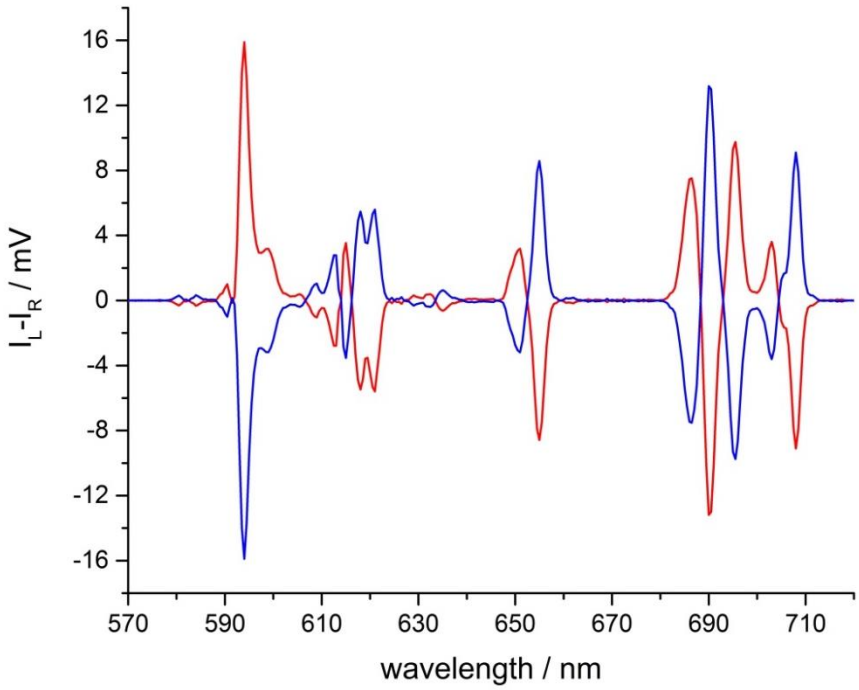

Figure 2.13 CPL spectra of the *Δ*- (*red*) and *Λ*- (*blue*) enantiomers of **[EuL^2]** (MeOH, 295 K, 5 µM complex, λ_{exc} 343 nm, 5 scans averaged).

Comparing the CPL spectra of the two phenyl phosphinate complexes **[EuL^1]** and **[EuL^2]**, very few differences can be observed. Both complexes exhibit similar profiles in all transitions. Of particular importance is the fact that in the ΔJ = 1 transition (590-600 nm) all transitions for a particular enantiomer have the same

handedness. Similarly, for the methyl phosphinate complexes **[EuL^3]** and **[EuL^4]**, almost identical profiles were observed. These results suggest that the nature of the chromophore does not have a significant effect on the form of the CPL spectrum.

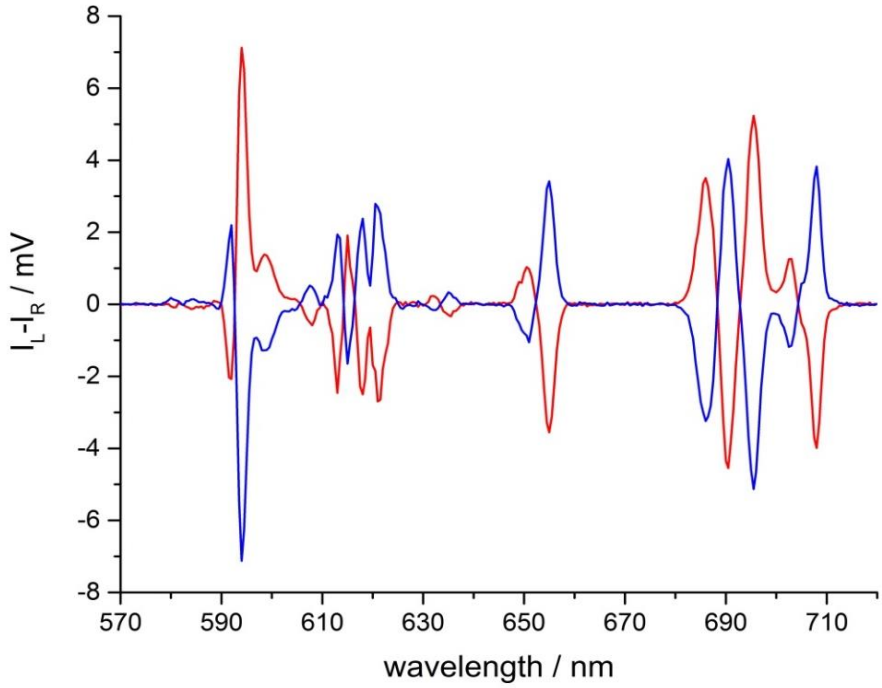

Figure 2.14 CPL spectra of the *Δ*- (*red*) and *Λ*- (*blue*) enantiomers of **[EuL^3]** (MeOH, 295 K, 5 µM complex, λ_{exc} 355 nm, 5 scans averaged).

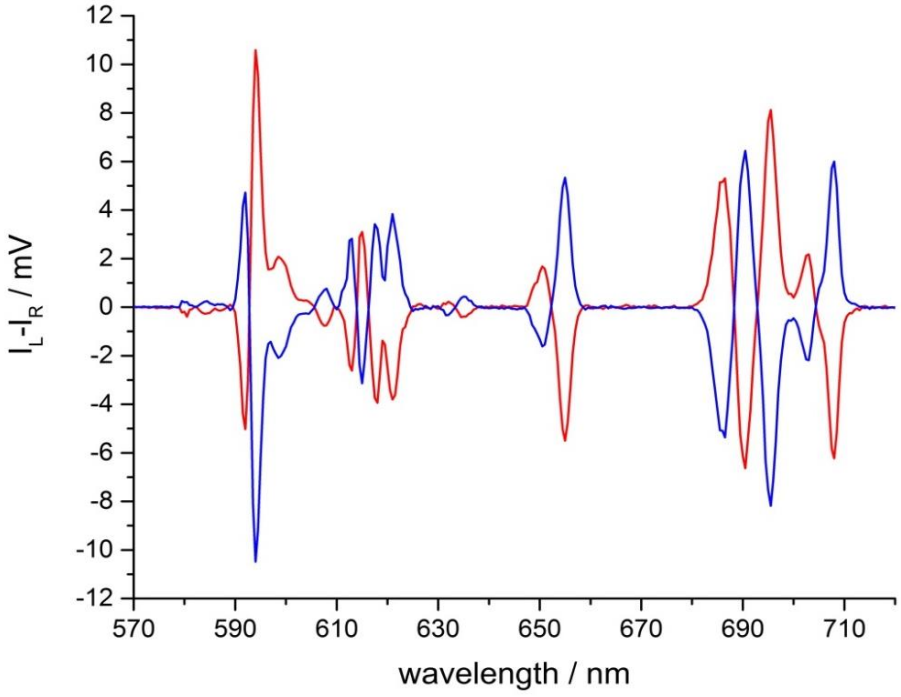

Figure 2.15 CPL spectra of the *Δ*- (*red*) and *Λ*- (*blue*) enantiomers of **[EuL^4]** (MeOH, 295 K, 5 µM complex, λ_{exc} 342nm, 5 scans averaged).

When compared to the parent complexes **[EuL^{5}]** and **[EuL^{6}]**, the CPL spectra for **[EuL$^{1\text{-}4}$]** show that, in general, the spectral form is conserved on addition of the extended chromophores. There are differences in the relative intensities of some of the transitions but the ordering and handedness of each transition is the same.

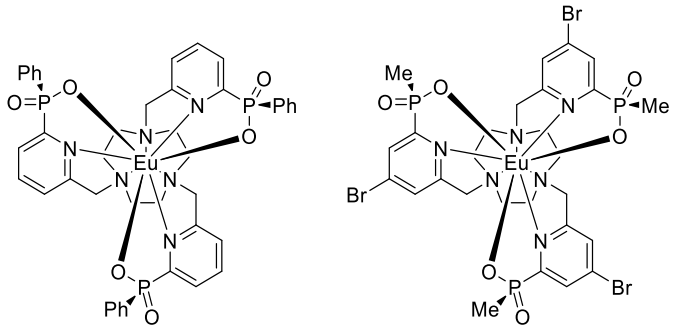

[EuL^{5}] **[EuL^{6}]**

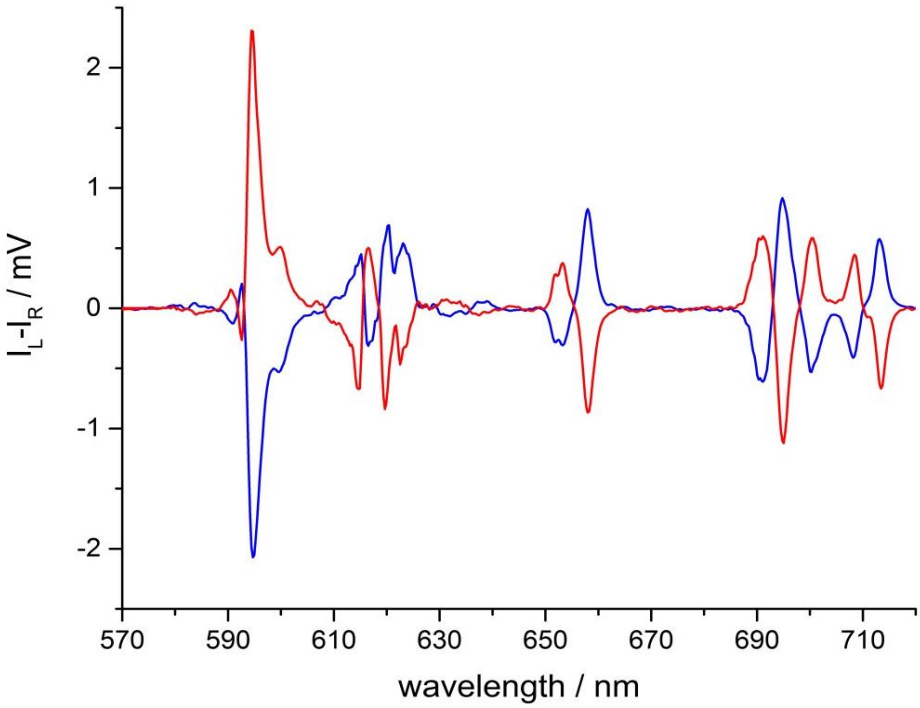

Figure 2.16 The CPL spectra of the *Δ*- (*red*) and *Λ*- (*blue*) enantiomers of the phenyl phosphinate parent complex **[EuL^{5}]** (1:1 MeOH:H_2O, 295 K). Data replotted from Ref. [141].

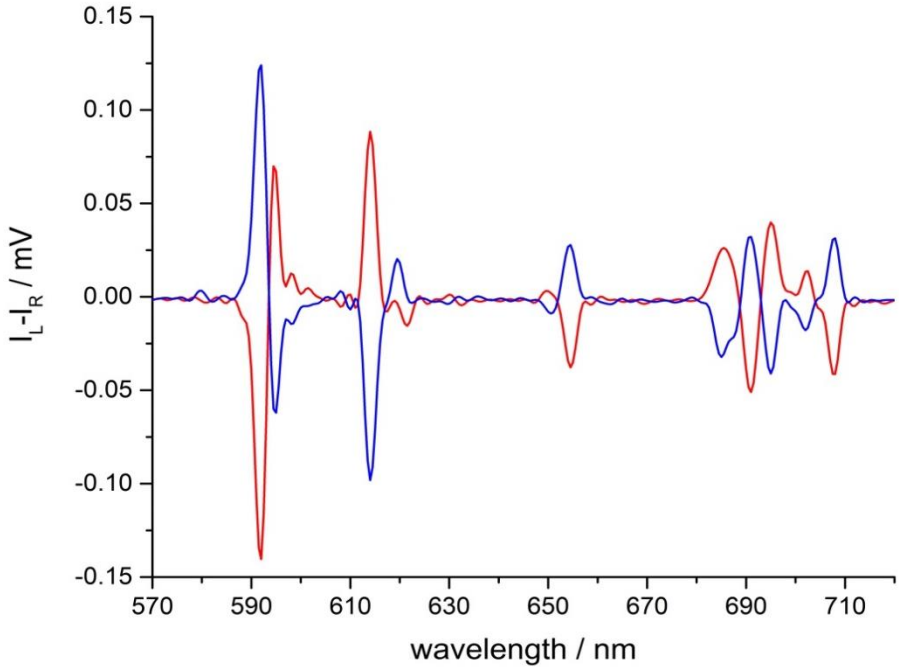

Figure 2.17 CPL spectra of the *Δ*- (*red*) and *Λ*- (*blue*) enantiomers of the methyl phosphinate parent complex **[EuL^6]** (H_2O, 295 K). Data replotted from Ref. [39].

Interestingly, differences are observed when CPL spectra of phenyl and methyl phosphinates are compared. For example, in the Δ*J* = 1 region (590-600 nm), the phenyl phosphinates (**[EuL^1]** and **[EuL^2]**) appear to show three transitions, centred at 590, 594, and 597 nm, all with the same sign. In contrast, the methyl phosphinates (**[EuL^3]** and **[EuL^4]**), exhibit three distinct transitions at 592, 594 and 599 nm, with the first of opposite sign to the remaining two. Additionally, in the Δ*J* = 4 manifold (680-710 nm), the transition at 690 nm is proportionally larger in the phenyl phosphinates than in the methyl phosphinates, a difference that is mirrored in the total emission spectra (see Fig. 2.18).

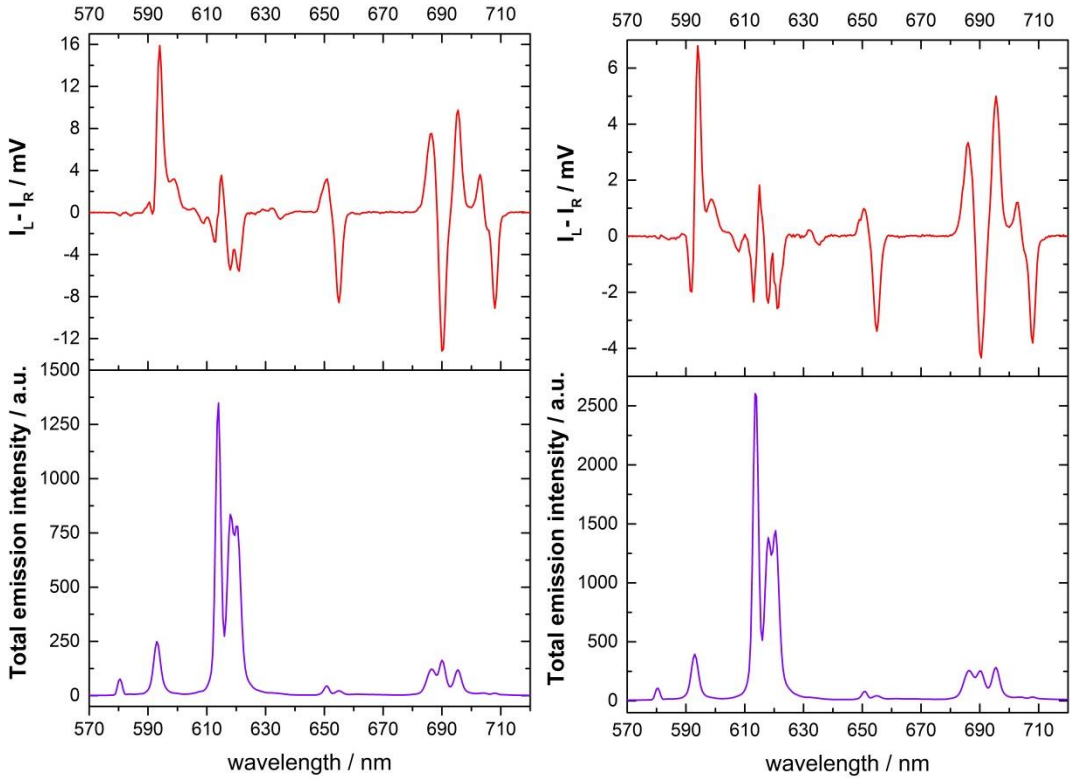

Figure 2.18 The total emission and CPL spectra for *Δ*-**[EuL^2]** (*left*) and *Δ*-**[EuL^3]** (*right*) showing the difference in relative intensity of the transition at 690 nm.

It is worth noting that the Δ*J* = 1 manifolds in the CPL spectra of all four complexes appear to contain at least 3 distinct transitions. In C_3 symmetry, only two bands are expected, as the 2*J* + 1 states are split into a singlet A level and a doubly degenerate E level.[142] The appearance of 3 bands suggests that perhaps the complexes are not perfectly C_3 symmetric in solution. There is evidence for this in DFT calculations carried out on analogous complexes, where the coordination polyhedron is slightly distorted from the C_3-symmetrical tricapped trigonal prism structure.[29] Additionally, X-ray crystal structure analysis of an analogous complex showed slightly distorted C_3-symmetry in the solid state.[30] It is clear to see from these spectra that the CPL spectra provide increased resolution when compared to the total emission spectra in all observed transitions, as a result of some transitions being of opposite handedness to neighbouring bands.

Initially, only scans between 570 and 720 nm were taken in order to record the emission from the $^5D_0 \rightarrow {}^7F_{0\text{-}4}$ transitions (although circularly polarised emission is forbidden in the $^5D_0 \rightarrow {}^7F_0$ transition). In the spectra presented thus far, it is evident that additional transitions are visible in regions outside the $^5D_0 \rightarrow {}^7F_{0\text{-}4}$ manifolds.

For example, weak transitions are visible around 580 nm and between 625 and 640 nm. It was hypothesised that these belonged to transitions from the Eu(III) $^5D_1$ excited state, as the wavelength ranges concerned correspond closely to those in systems where $^5D_1 \rightarrow {}^7F_J$ transitions have been observed previously.[2]

CPL and total emission spectra of **[EuL$^{1\text{-}4}$]** were recorded across a wider wavelength range in an attempt to observe further transitions. In every case, bands attributed to transitions from $^5D_1$ to $^7F_2$ (550-560 nm), $^7F_3$ (575-585 nm), and $^7F_4$ (625-640 nm) were observed in the CPL spectra, along with the weak $^5D_0 \rightarrow {}^7F_5$ manifold around 750 nm (see Fig. 2.19).[134] Most reports of Eu(III) emission do not include the $^5D_0 \rightarrow {}^7F_5$ transition because it is much weaker than the $^5D_0 \rightarrow {}^7F_{0\text{-}4}$ transitions, making it difficult to measure with standard photomultiplier tubes, which are inherently less sensitive at longer wavelengths. Even with specialist red-sensitive photomultiplier tubes, the $^5D_0 \rightarrow {}^7F_5$ transition is only usually observed in crystalline matrices and frozen solution. Transitions from $^5D_1$ are rarely observed in molecular systems at room temperature due to the stronger radiationless deactivation of this excited state, although emission from this level and higher excited states are often observed from Eu(III) in inorganic host lattices.

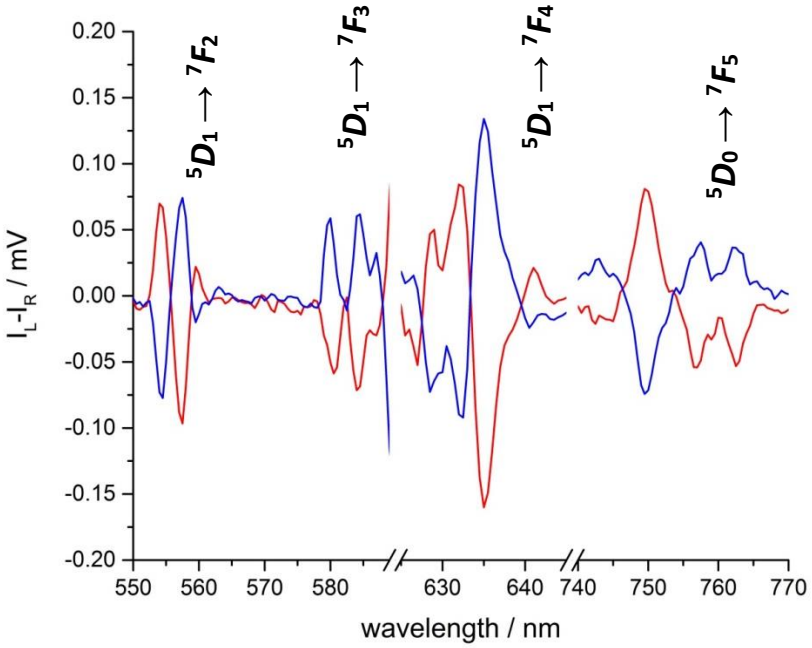

Figure 2.19 Expanded CPL spectra of the *Δ*-(*red*) and *Λ*-(*blue*) enantiomers of **[EuL^2]** showing less commonly observed transitions (MeOH, 295 K, 5 µM complex, λ_{exc} 343 nm, 5 scans averaged). Note cut x-axis.

In the total emission spectrum of **[EuL^2]** (see Fig. 2.20), the $^5D_1 \rightarrow {}^7F_2$ and $^5D_0 \rightarrow {}^7F_5$ transitions are visible along with the $^5D_1 \rightarrow {}^7F_1$ transition at 537 nm, although perhaps surprisingly no corresponding CPL is observed in this region. According to the selection rules developed by Richardson,[143] the $^5D_1 \rightarrow {}^7F_1$ transition is a magnetic dipole allowed transition. As such, one might expect to observe strong CPL from this transition. However, recent work has suggested that the $^5D_1 \rightarrow {}^7F_1$ possesses significant electric dipole character.[144] Such transitions are expected to be weak in CPL, which could explain the absence of a CPL signal corresponding to this transition. The $^5D_1 \rightarrow {}^7F_3$ and $^5D_1 \rightarrow {}^7F_4$ transitions in the total emission spectrum are obscured by the much stronger transitions from $^5D_0$ in the similar wavelength regions. Addition of a 60 µs time-gate to the total emission spectrum acquisition renders the peaks corresponding to the $^5D_1 \rightarrow {}^7F_1$ and $^5D_1 \rightarrow {}^7F_2$ transitions indistinguishable from the baseline noise. Lifetimes of the order of a few microseconds for the $^5D_1$ excited state have been reported previously.[145–147]

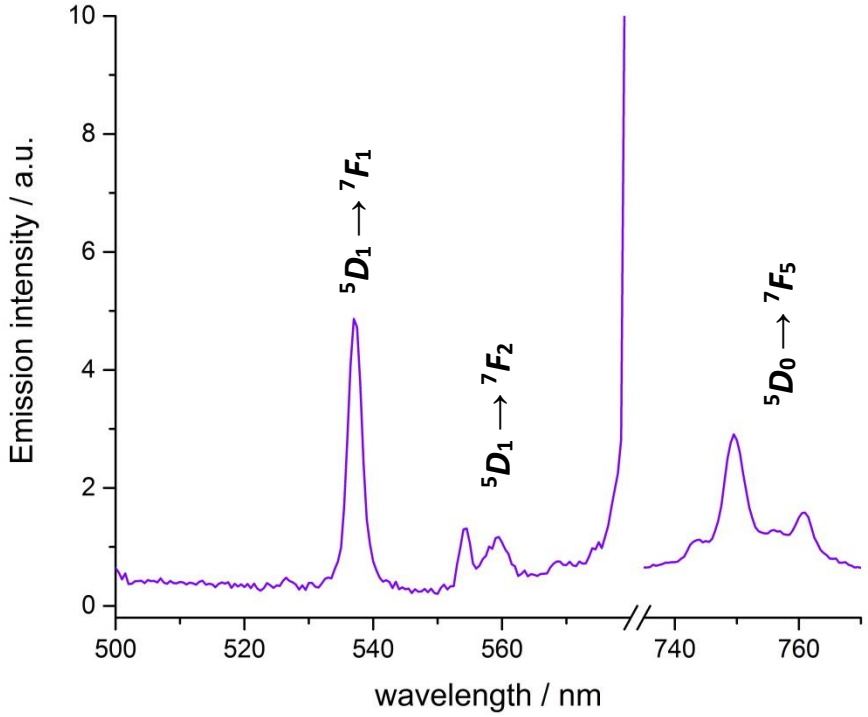

Figure 2.20 Expanded total emission spectrum for **[EuL^2]** showing some transitions rarely observed in solution for molecular systems (MeOH, 295 K, 5 µM complex, λ_{exc} 343 nm, 5 scans averaged).

Selected g_{em} values for **[EuL$^{1\text{-}4}$]** of various emissive transitions are shown in Table 2.2. The g_{em} values are broadly similar for all complexes at each wavelength, with the exception of the $^5D_1 \rightarrow {}^7F_2$ transition which displays larger CPL signals for the methyl phosphinates than for the phenyl phosphinates. All the emission dissymmetry values are within the expected range for lanthanide complexes of this type.

Table 2.2 Selected g_{em} values for **[EuL$^{1\text{-}4}$]** (MeOH, 295 K)

		g_{em} / arb					
λ / nm		**554**	**557**	**599**	**655**	**708**	**757**
[EuL^1]	**Δ**	+0.14	-0.18	+0.11	-0.13	-0.23	-0.06
	Λ	-0.15	+0.20	-0.13	+0.15	+0.26	+0.09
[EuL^2]	**Δ**	+0.11	-0.22	+0.14	-0.18	-0.30	-0.14
	Λ	-0.13	+0.19	-0.14	+0.18	+0.29	+0.12
[EuL^3]	**Δ**	+0.17	-0.33	+0.12	-0.19	-0.31	-0.12
	Λ	-0.17	+0.32	-0.13	+0.19	+0.31	+0.11
[EuL^4]	**Δ**	+0.18	-0.33	+0.12	-0.18	-0.30	-0.13
	Λ	-0.18	+0.33	-0.11	+0.17	+0.29	+0.12

In order to examine whether any spectra-structure correlation could be observed for these C_3-symmetric 9-N_3 complexes, the CPL spectra of **[EuL$^{1\text{-}4}$]** were compared to similar complexes, where the phosphinate donors are replaced with amide and carboxylate groups. Initial comparisons to the carboxylate parent system **[EuL^7]** (see Fig. 2.21) and a complex with extended chromophore arms and amide donor groups **[EuL^8]** (see Fig. 2.22) were made. The CPL spectra of the enantiomers of **[EuL^7]** show similar profiles in the ΔJ = 1 manifold to the phenyl phosphinate complexes **[EuL^1]** and **[EuL^2]** with every transition of the same sign. Additionally, the

fingerprint-like pattern observed in **[EuL$^{1-4}$]** in the Δ*J* = 4 manifold is common to **[EuL^{7}]**. However, the Δ*J* = 2 manifold is significantly different in **[EuL^{7}]**, comprising one strong transition at 615 nm accompanied by several weaker transitions of varying sign at higher and lower energy. In the phosphinate systems, the Δ*J* = 2 manifold is made up of several transitions of approximately equal intensity. In the amide system, two strong transitions of opposite sign are observed in the Δ*J* = 1 manifold (similar to the methyl phosphinates), but the patterns of the Δ*J* = 3 and Δ*J* = 4 manifolds are distinctly different from both the phosphinate and carboxylate complexes.

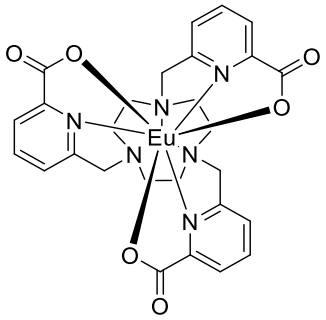

[EuL^{7}]

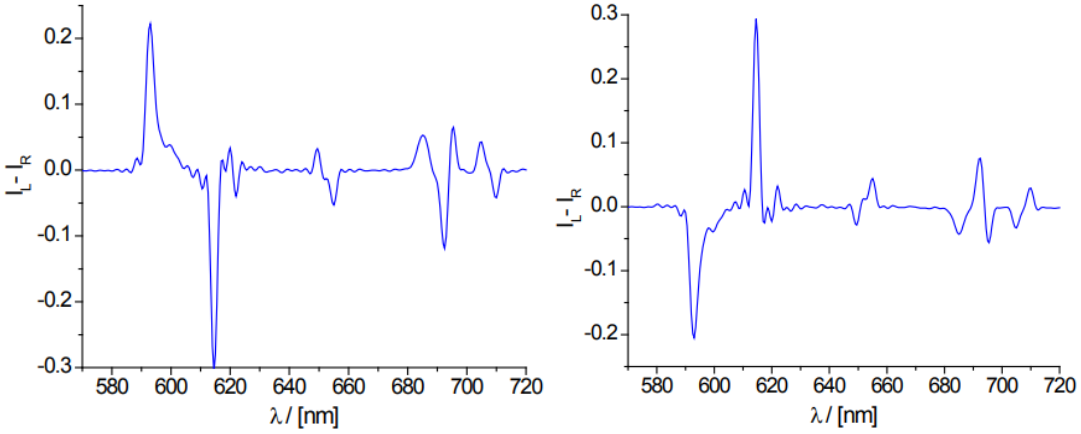

Figure 2.21 The CPL spectra of the *Δ*- (*left*) and *Λ*- (*right*) enantiomers of **[EuL^{7}]** (H_2O, 295 K, λ_{exc} 272 nm). Adapted from Ref. [39] with permission from The Royal Society of Chemistry.

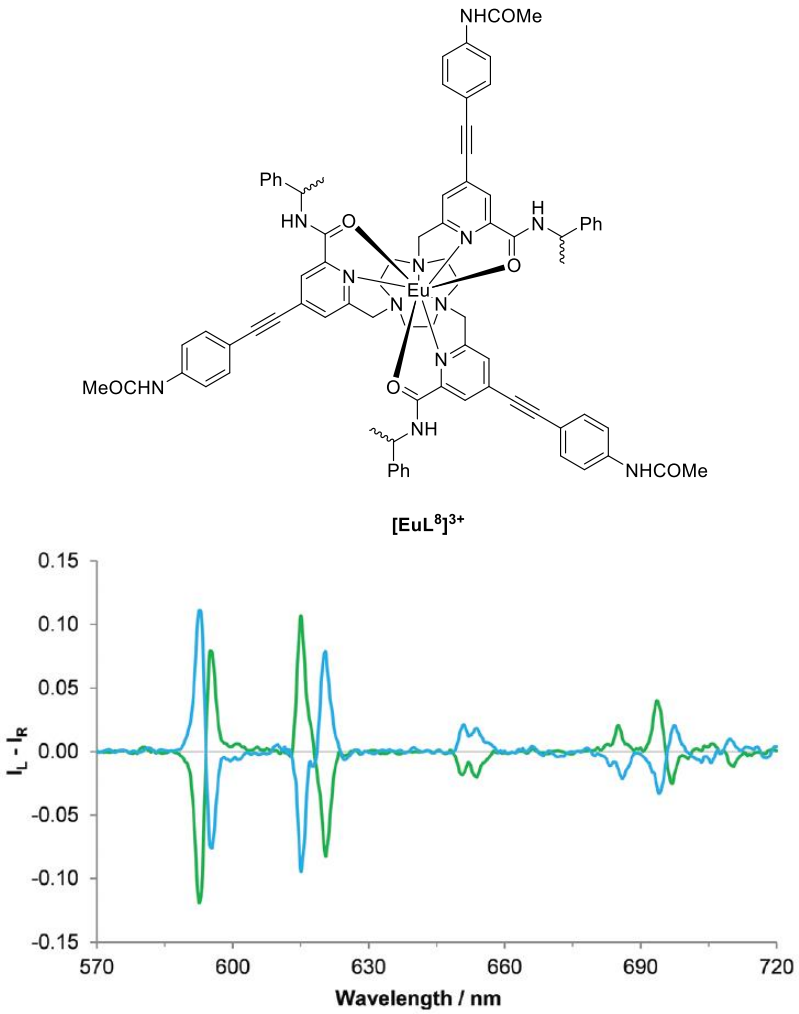

Figure 2.22 The CPL spectra of the S-*Δ* (*green*) and R-*Λ* (*blue*) enantiomers of **[EuL^{8}]$^{3+}$** (H_2O, 295 K, λ_{exc} 348 nm). Reproduced from Ref. [75] with permission from The Royal Society of Chemistry.

These initial observations suggest that within a series of complexes containing the same donor groups, similar CPL profiles are observed. However, these similarities do not extend to complexes of different donor groups, even those containing the same donor atom set. Importantly, subsequent work has shown that the CPL and total emission profiles are strongly dependent on the solvent, so comparisons of spectra in different solvents may inhibit conclusive comparisons being drawn. Further discussion on solvent effects in the photophysical properties of these complexes can be found in Chapter 3.

The complex **[EuL^{9}]** (synthesised by Dr. Matthieu Starck) is structurally similar to **[EuL^{4}]**, possessing two methyl phosphinate donor groups and one carboxylate group. The complex exhibits similar photophysical properties to **[EuL^{4}]** (λ_{max} = 340 nm, τ_{Eu} (MeOH) = 1.12 ms) and can be resolved by chiral HPLC using the same

method as for **[EuL^4]**.[148] Comparison of the CPL form of **[EuL^4]** to **[EuL^9]** shows that the Δ*J* = 3 and 4 manifolds are very similar to those in **[EuL$^{1\text{-}4}$]** and **[EuL^7]**, which is not surprising given the donor groups are the same. However, the Δ*J* = 1 and 2 manifolds differ considerably from both the symmetric phosphinate and carboxylate complexes. This is perhaps as result of the C_3 symmetry being broken in **[EuL^9]**, resulting in these transitions resembling neither the symmetric carboxylate nor methyl phosphinate complexes. Indeed, in the Δ*J* = 1 manifold, the transitions differ in both energy and sign between **[EuL^9]** and **[EuL^4]**.

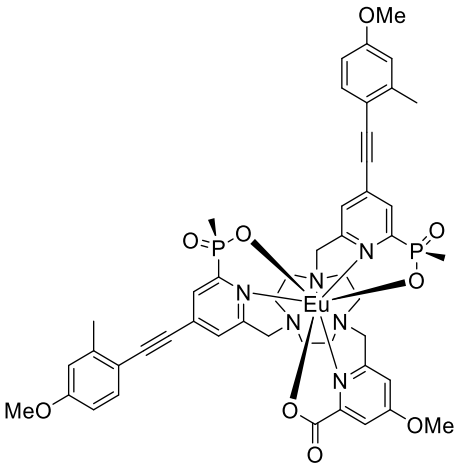

[Eu.L^9]

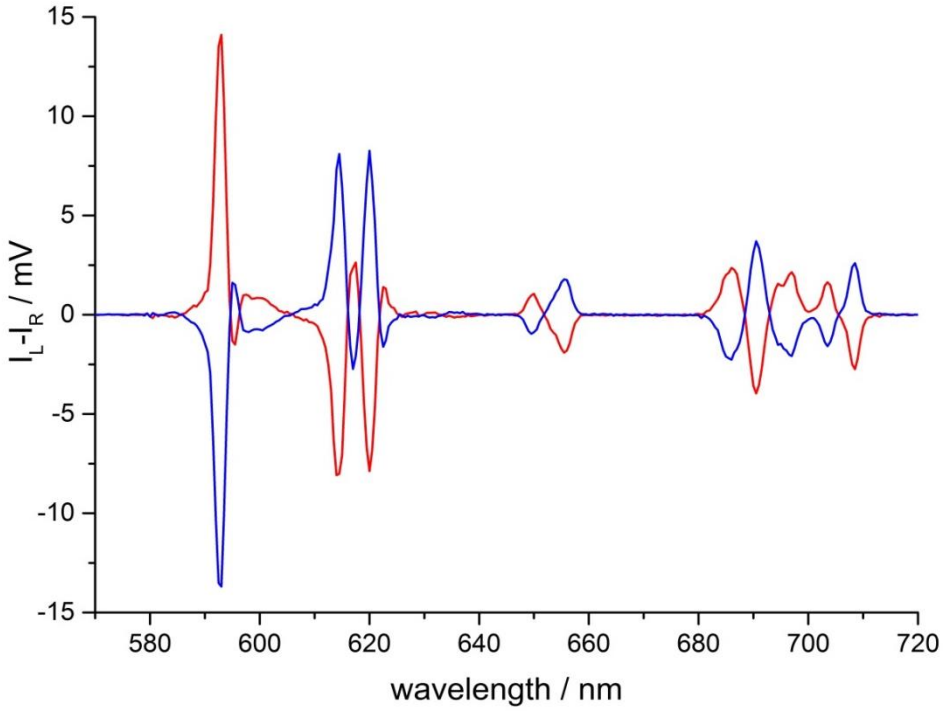

Figure 2.23 The CPL spectra of the *Δ*-(*red*) and *Λ*-(*blue*) enantiomers of **[EuL^9]** (MeOH, 295 K, λ_{exc} 340 nm).

In order to further investigate the possible differences in the CPL spectra of complexes containing phosphinate and carboxylate donors, it was also decided to attempt separation of complex **[EuL^{10}]**, which also has extended arylalkynyl chromophores. The chromophore on this complex contains a second *ortho*-methyl group, which shifts the absorption maximum to slightly longer wavelengths than for **[EuL^{2}]** and **[EuL^{4}]**.

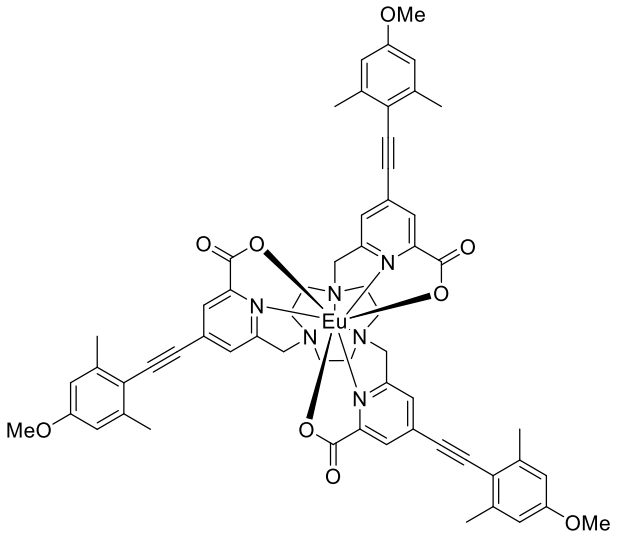

[EuL^{9}]

Extensive attempts were made to resolve **[EuL^{10}]** by chiral HPLC using both CHIRALPAK-IC and ID columns including using alternative solvent systems. No analytical scale injections showed any indication of chiral resolution. Therefore, it was decided to synthesise an analogous carboxylate complex via an alternative route.

2.6 An alternative strategy for the synthesis of enantiopure carboxylate complexes

Since direct chiral resolution of **[EuL^{10}]** could not be achieved, an alternative strategy for the synthesis of enantiopure carboxylate complexes with extended arylalkynyl chromophores was required. It has already been demonstrated that the pyridine carboxylate parent complex **[EuL^{7}],** and the 4-bromo substituted methylphosphinate parent complex **[EuL^{6}]** could be resolved using CHIRALPAK-IC and ID columns, respectively, using isocratic methanol as the mobile phase.

Therefore, it was envisaged that 4-substituted carboxylate parent complexes could be resolved under similar conditions. As such, a divergent synthetic route was proposed (see Scheme 2.14), featuring initial synthesis of the racemic 4-iodo substituted carboxylate complex **[EuL^{11}]**, followed by resolution using chiral HPLC. Then, coupling of the enantiomers of this intermediate complex with an alkyne-bearing head group under mild Sonogashira conditions would lead to the enantiopure complex. The utility of this divergent route has been demonstrated previously.[133]

Rather than the 4-bromo substituted intermediate complex used in that study, the 4-iodo analogue was chosen in this case, as more facile Sonogashira coupling is observed for aryl iodides than aryl bromides.[149] The use of milder reaction conditions was expected to reduce the possibility of racemisation of the complex during the reaction. It also worth noting that the electron-poor nature of the pyridine (due to metal coordination) is expected to increase the reaction rate, compared to an uncoordinated pyridine ligand.

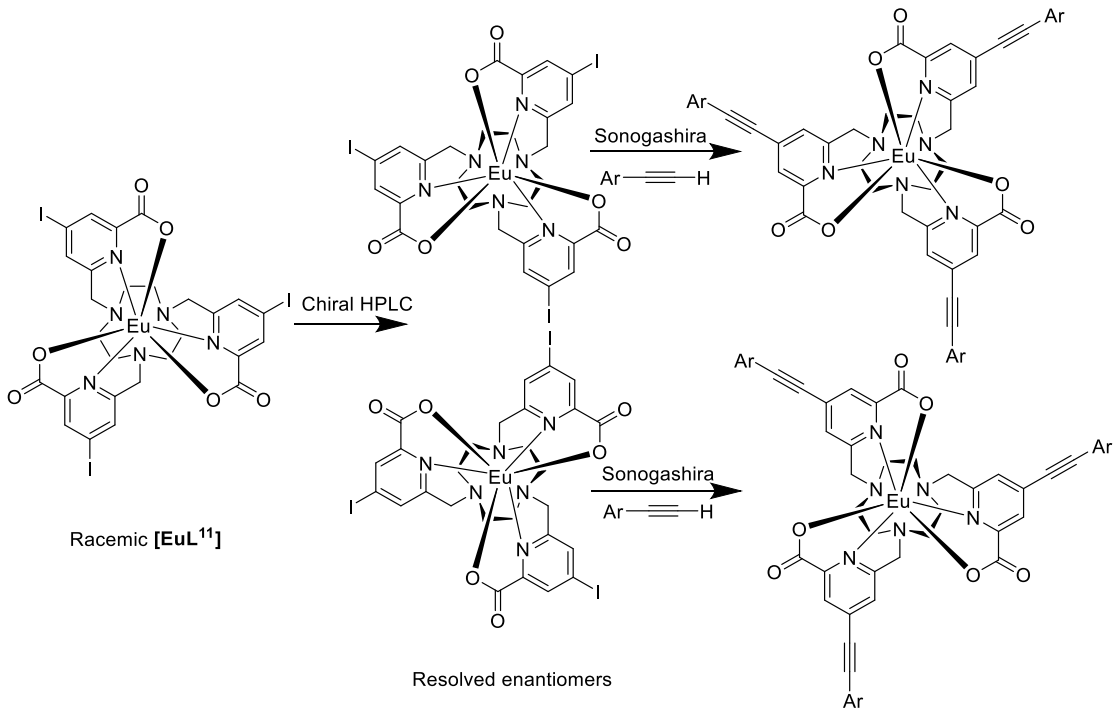

Scheme 2.14 Proposed strategy for the synthesis of enantiopure carboxylate complexes.

The synthesis of the ligand was carried out using established methods,[150] starting from chelidamic acid **20** (see Scheme 2.15). Treatment with thionyl chloride

replaced the 4-hydroxy substituent with a chlorine atom and converted the carboxylic acid groups to acid chlorides. The reaction was quenched by dropwise addition of methanol, converting the acid chloride groups to methyl esters. Subsequent displacement of the 4-chloro substituent of diester **21** using sodium iodide and acetyl chloride with sonication yielded 4-iodo diester **22.** Careful mono-reduction of **22** using sodium borohydride in CH_2Cl_2/CH_3OH gave the alcohol **23.** A compromise must be achieved between consumption of the starting material and over reduction to the diol. Consequently, reduction of **22** was carried out in ice and monitored regularly by TLC until the reaction was quenched with aqueous HCl. The crude mixture of starting material, desired product and a small amount of diol side product was separated by column chromatography to give the mono-reduced product **23** in good yield. Unreacted starting material was recovered from the purification and reused. Mesylation of the hydroxyl group to give **24** provided the required pyridine moiety for alkylation of triazacyclononane.

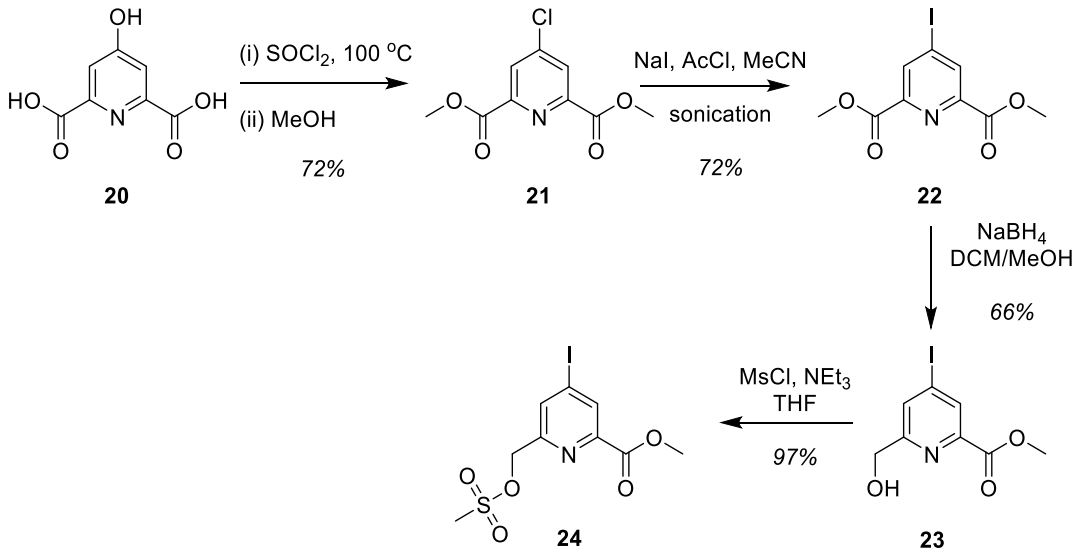

Scheme 2.15 Synthesis of the 4-iodopyridine derivative, **24**, from chelidamic acid.

Alkylation of triazacyclononane was carried out in acetonitrile with potassium carbonate as the base, and the reaction was monitored by LCMS. Previous work in the group had identified the occurrence of ester hydrolysis during column chromatography of similar compounds. As a result, the crude ligand was directly hydrolysed under basic conditions before complexation using europium(III) chloride (see Scheme 2.16). The complexation reaction was carried out in aqueous solution

and after stirring at 70 °C, a white precipitate had formed. This solid exhibited bright red emission by visual inspection using a TLC reader lamp, but was insoluble in all common laboratory solvents, with the exception of DMSO.

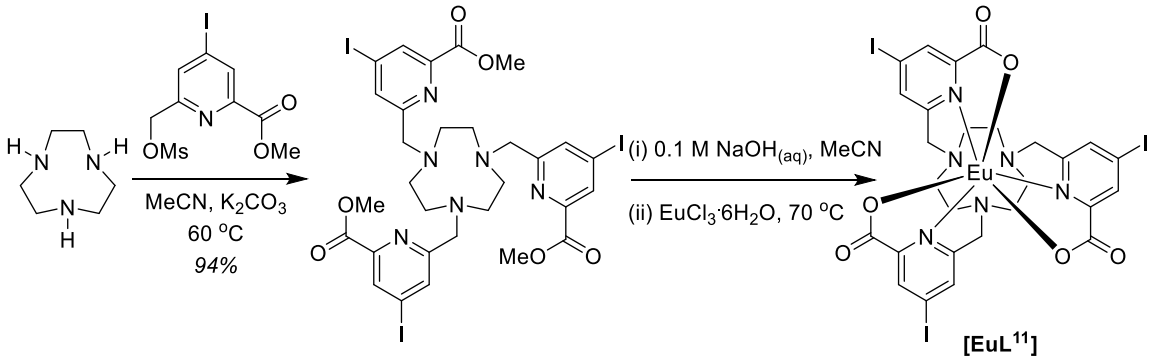

Scheme 2.16 Formation of the trimethyl ester of ligand **L[11]**, and complexation to form **[EuL[11]]**.

Stirring the white solid in warm DMSO for 48 hours yielded a solution from which some photophysical properties of **[EuL[11]]** could be obtained (see Fig. 2.23). The absorption spectrum was consistent with the expected product, with an absorption maximum of 277 nm. The complex also exhibited weak sensitised europium(III) emission with an emission lifetime of 1.18 ms in DMSO. Unfortunately, due to the limited solubility of the complex, reliable NMR spectra could not be recorded. Due to the incompatibility of DMSO with LCMS, no mass spectral data could be obtained either.

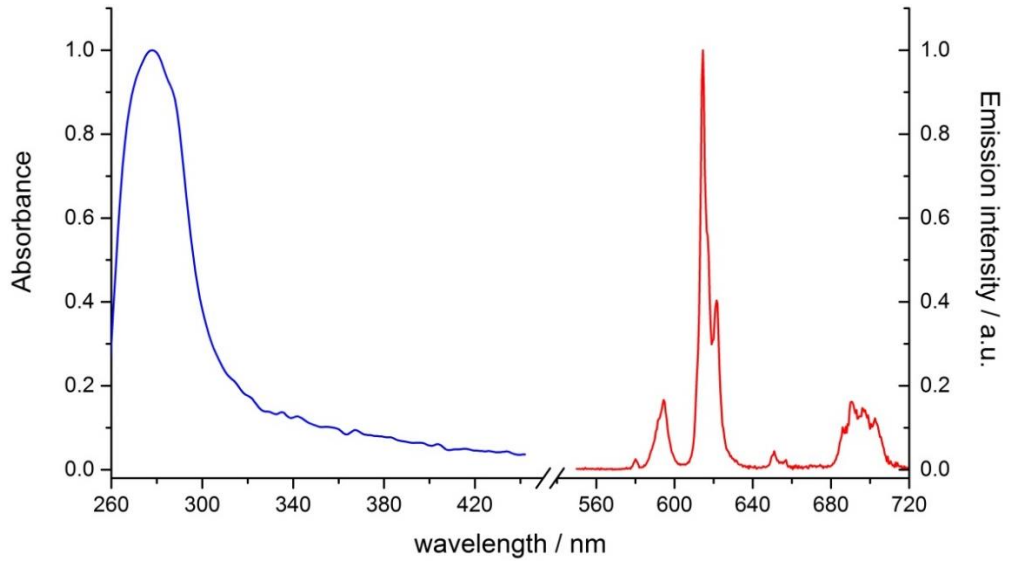

Figure 2.23 Absorption and emission spectra for crude **[EuL[11]]** after heating precipitate in DMSO for 48 hours (DMSO, 295 K, λ_{exc} 277 nm).

Since the complex was insoluble in everything except DMSO, chiral HPLC could not be carried out. A Sonogashira coupling of the racemic complex with 2-ethynyl-1,3,5-trimethoxybenzene was attempted in DMSO, to compare the photophysical properties of the resulting complex with **[EuL^{1}]** and **[EuL^{3}]** which bear the same chromophore. Previous Sonogashira couplings on complexes were carried out in DMF/THF mixtures to ensure solubility of all reagents and catalysts.[133] In this instance, the starting material is poorly soluble in DMSO, but the product was expected to be soluble. Due to the presence of DMSO, the reaction could not be monitored by LCMS, so TLC and absorbance spectra were used to monitor the progress of the coupling, by observing the appearance of the internal charge transfer absorption band of the extended chromophore around 360 nm. After completion, the reaction mixture was added dropwise with stirring to 400 mL of cold diethyl ether, causing the product to precipitate. The solution was decanted and the precipitate recovered. LCMS analysis of the crude product showed that the expected C_3 symmetric complex **[EuL^{12}]** with extended arylalkynyl chromophores was indeed the major product. The complex **[EuL^{13}]** with two extended chromophores and one 4-chloropyridine arm was identified as the minor product (see Fig. 2.24).

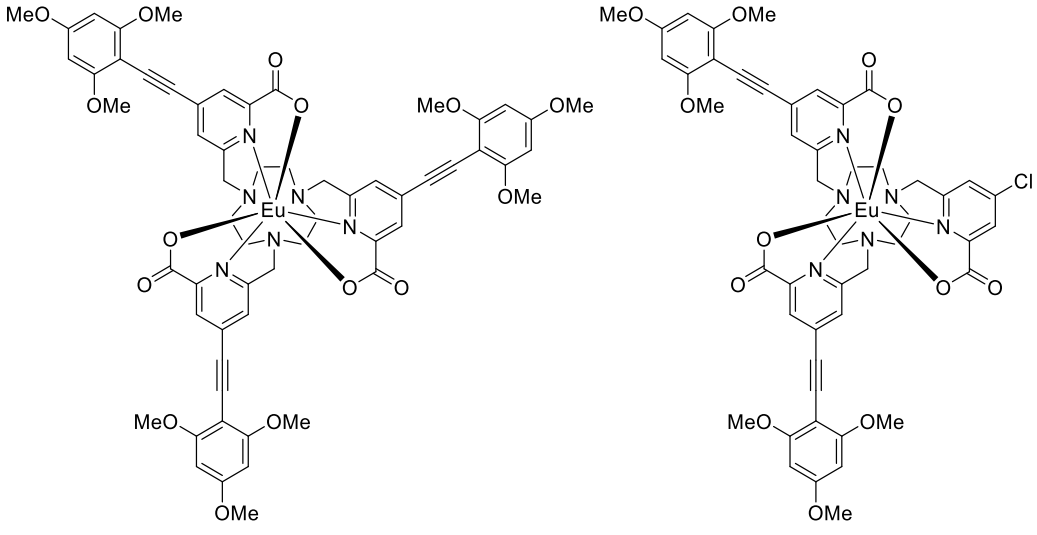

[EuL^{12}] **[EuL^{13}]**

Figure 2.24 The structures of **[EuL^{12}]** and **[EuL^{13}]** formed from the Sonogashira coupling of an arylalkynyl chromophore onto **[EuL^{11}]** in DMSO.

Purification of the crude mixture of the two complexes was initially attempted using flash chromatography on alumina, which was successful in removing catalyst residues from the crude mixture but did not result in separation of **[EuL^{12}]** and **[EuL^{13}]**. Therefore, reverse phase HPLC was used to separate the two complexes (see Fig. 2.25).

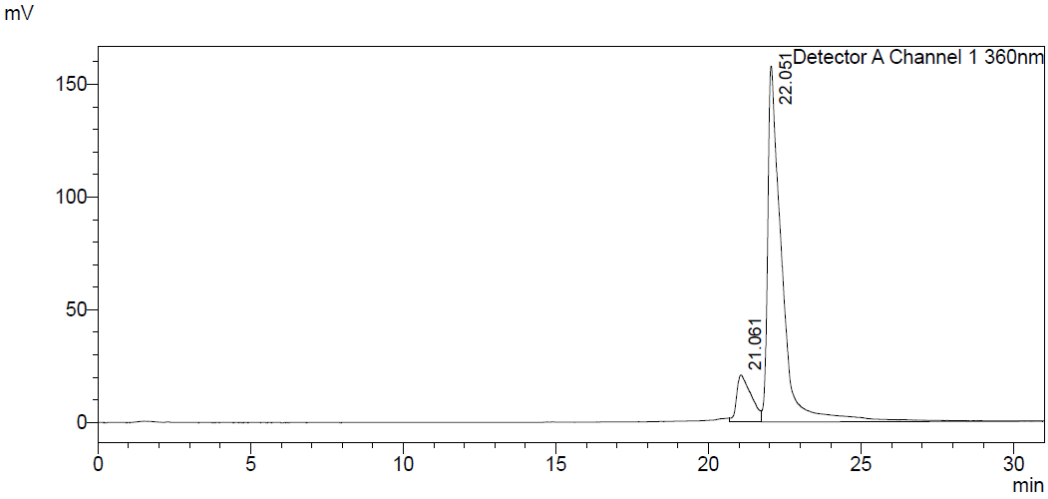

Figure 2.25 The RP-HPLC trace for the mixture of complexes **[EuL^{12}]** and **[EuL^{13}]**. (H_2O/MeOH mobile phase, XBridge C18 OBD column (19 x 100 mm, 5 µm), flow rate 17 mL/min, 295 K).

Photophysical properties of **[EuL^{12}]** and **[EuL^{13}]** were recorded in methanol solution (see Fig. 2.26). Both complexes exhibit broad absorption bands around 360 nm, as expected, due to the electron-rich chromophore. The complexes also demonstrate emission spectra consistent with previously synthesised carboxylate complexes.[29] The similarity in photophysical properties between **[EuL^{12}]** and **[EuL^{13}]** is hardly surprising, as they possess the same donor atom set and the absorption spectral behaviour will be dominated by the presence of the extended chromophores.

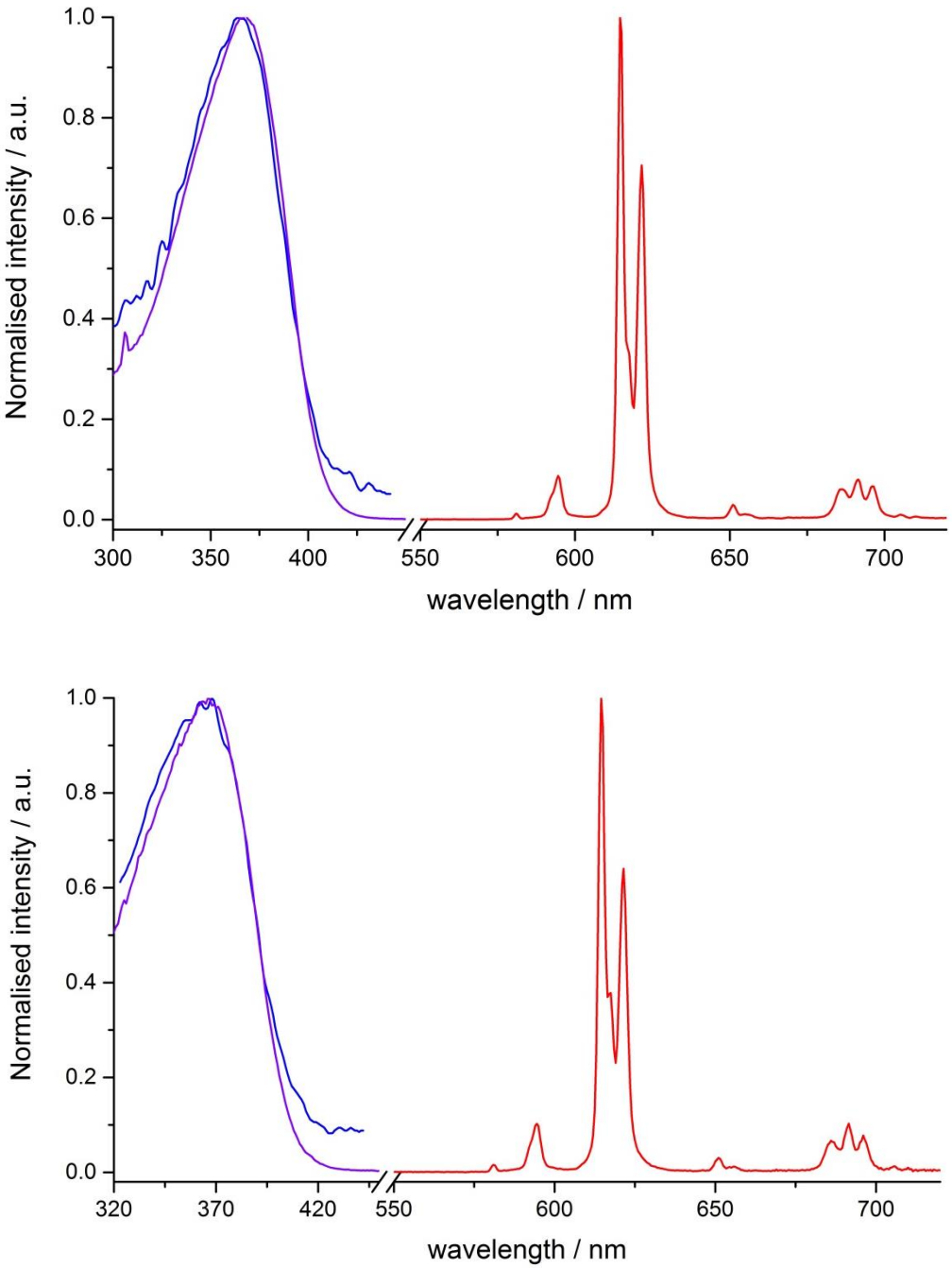

Figure 2.26 Absorption (*blue*), excitation (*purple*) and emission (*red*) for **[EuL^{12}]** (top, MeOH, 295 K, λ_{exc} 363 nm, λ_{em} 614 nm) and **[EuL^{13}]** (bottom, MeOH, 295 K, λ_{exc} 362 nm, λ_{em} 614 nm).

Although the use of 4-iodopyridine groups had been intended to make subsequent Sonogashira couplings easier, it clearly had a major effect on the solubility of the complex. Therefore, it was decided that the 4-bromopyridine analogue **[EuL^{14}]** would be used instead, despite this potentially sacrificing some of the enantiopurity of the final products as the Sonogashira couplings may have to be carried out at higher temperatures with longer reaction times. The synthesis followed a very similar pathway to **[EuL^{11}]**, except that the initial step was to convert chelidamic

acid **20** to the 4-bromo substituted acid bromide with molten PBr_5, followed by methanolic work up to introduce the two methyl esters (see Scheme 2.17). Carefully controlled mono-reduction of **25** with sodium borohydride yielded alcohol **26**, before transformation to the mesylate **27**. Alkylation of triazacyclononane with mesylate **27** followed by base-catalysed ester hydrolysis and complexation with europium(III) chloride afforded the desired complex **[EuL^{14}]**.

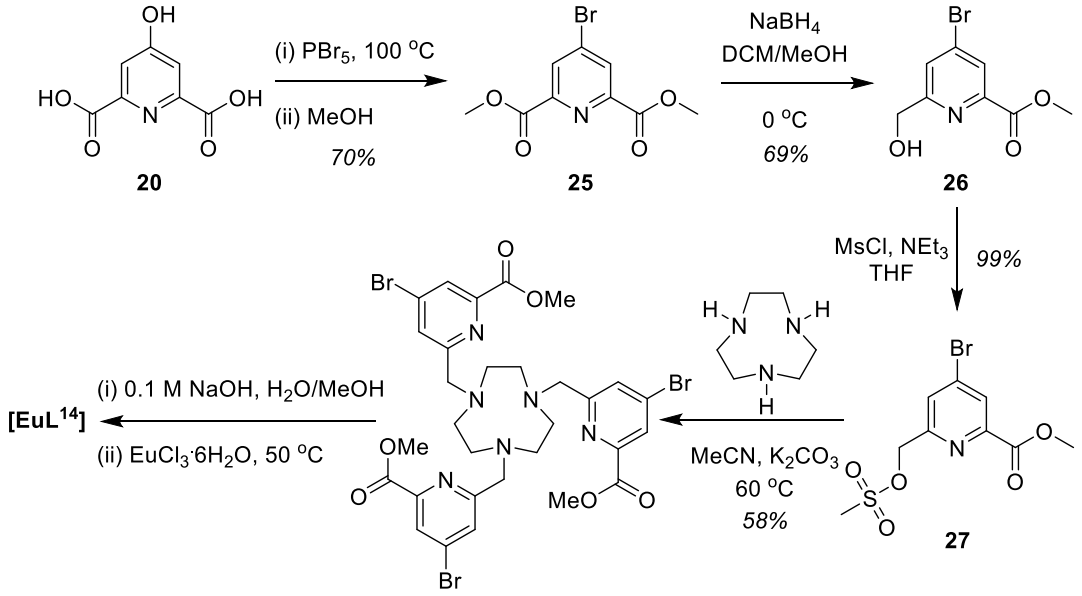

Scheme 2.17 Synthetic route to **[EuL^{14}]**.

Again, the complex **[EuL^{14}]** was isolated as the precipitate from the aqueous solution of the complexation reaction. The solid was isolated by centrifugation and, like **[EuL^{11}]**, was found to be insoluble in all common solvents, except warm DMSO. After heating overnight in DMSO, photophysical properties of **[EuL^{14}]** were recorded (see Fig. 2.27). The broad absorption band around 275 nm contains multiple local maxima, which may indicate that there are several absorbing species present in the solution. The emission lifetime of 1.19 ms in DMSO was similar to that measured for the 4-iodo complex **[EuL^{11}]**.

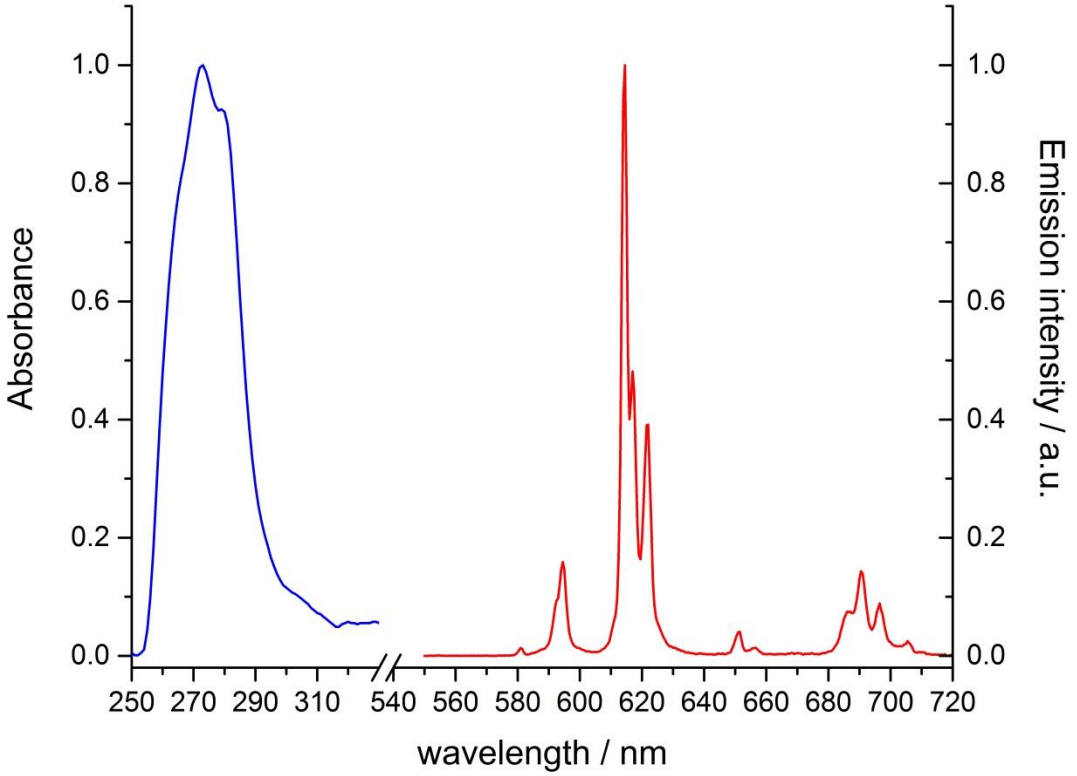

Figure 2.27 Absorption and emission spectra of **[EuL^{14}]** (DMSO, 295 K, λ_{exc} 272 nm).

From these investigations, it is evident that the solubility of these complexes is strongly influenced by structure. The unsubstituted tris-pyridine parent complex **[EuL^{7}]** is soluble in a variety of solvents, including water and methanol. However, addition of a 4-halo substituent makes them virtually insoluble. The analogous methyl phosphinate complex **[EuL^{6}]** is also soluble in a variety of solvents, highlighting the importance of the phosphinate group in controlling complex solubility.

2.7 Racemisation kinetics

In order for this class of complex to have utility in security labelling, they must be kinetically stable with respect to racemisation. For an enantiopure complex to emit CPL as an anti-counterfeiting feature, it must be stable to racemisation for the lifetime of the item in which it is embedded.

The experiment to assess racemisation kinetics involved heating a solution of the enantiopure complex and taking small aliquots at regular intervals for analytical chiral HPLC analysis. As racemisation occurs, the ratio of the area of the peaks for

the two enantiomers approaches 1:1. A kinetic relationship can be derived to describe the racemisation process as follows, and here it assumes the racemisation begins with enantiopure *Δ*-complex.

From the equilibrium,

$$\Delta \underset{k_{-1}}{\overset{k_1}{\rightleftharpoons}} \Lambda \tag{2.1}$$

and assuming $k_1 = k_{-1} = k$, the rate constant for enantiomeric interconversion, the following expressions for the rate of interconversion of enantiomers can be written.

$$\frac{-\mathrm{d}[\Delta]}{\mathrm{d}t} = k[\Delta] - k[\Lambda] \tag{2.2}$$

$$\frac{1}{[\Delta] - [\Lambda]}\,\mathrm{d}[\Delta] = -k\,\mathrm{d}t \tag{2.3}$$

Since $[\Lambda] = [\Delta]_0 - [\Delta]$, an integrated rate law can be derived as follows:

$$\int_{[\Delta]_0}^{[\Delta]} \frac{1}{2[\Delta] - [\Delta]_0}\,\mathrm{d}[\Delta] = \int_{t_0}^{t} -k\,\mathrm{d}t \tag{2.4}$$

$$\frac{1}{2}\ln(2[\Delta] - [\Delta]_0) - \frac{1}{2}\ln(2[\Delta]_0 - [\Delta]_0) = -kt \tag{2.5}$$

$$\ln\frac{2[\Delta] - [\Delta]_0}{[\Delta]_0} = -2kt \tag{2.6}$$

$$\ln\frac{[\Delta]_0}{2[\Delta] - [\Delta]_0} = 2kt \tag{2.7}$$

Therefore, a plot of $\ln\frac{[\Delta]_0}{2[\Delta]-[\Delta]_0}$ against t will have a gradient of $2k$. A half-life for racemisation can also be defined as the time required to reach an enantiomeric excess (ee) of 50%.

$$t_{1/2} = \frac{\ln 2}{2k} \qquad \textbf{(2.8)}$$

Previous work had measured the racemisation kinetics for the parent complexes **[EuL^6]** and **[EuL^7]** (see Fig. 2.28).[39] Using the mathematical treatment described above, the half lives for racemisation are found to be 74 ± 8 h for **[EuL^6]** and 99 ± 1 h for **[EuL^7]** in aqueous solution at 60 °C.

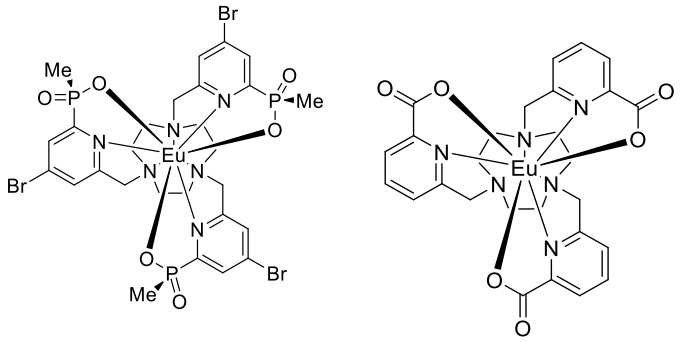

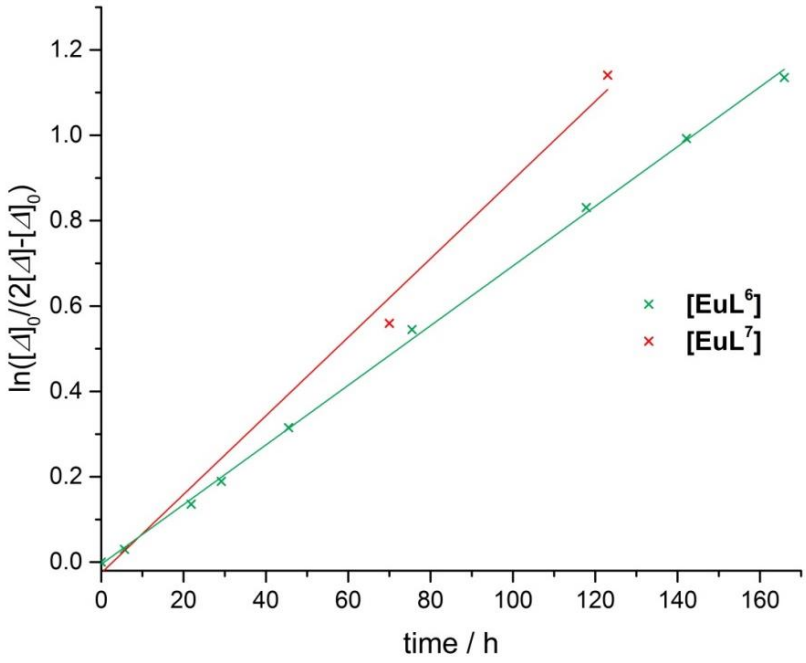

Figure 2.28 Kinetic plot of the rate of interconversion of enantiomers for **[EuL^6]** and **[EuL^7]** (60 °C, H_2O).

Similar experiments were carried out for the phenyl phosphinate complex **[EuL^2]** and methyl phosphinate complex **[EuL^4].** Due to the limited aqueous solubility of these complexes, these experiments were performed in methanol. For **[EuL^4]**, racemisation from the enantiopure *Λ*-complex (t_R ~ 25 min) could be observed over the course of a week (see Fig. 2.29), with the appearance of the peak corresponding

to the *Δ*-enantiomer (t_R ~ 11 min). Over the same time period, no racemisation was observed for *Λ*-**[EuL^2]** (see Fig. 2.30). Even after 3 weeks, no peak for the *Δ*-enantiomer (t_R ~ 13 min) could be distinguished from the baseline.

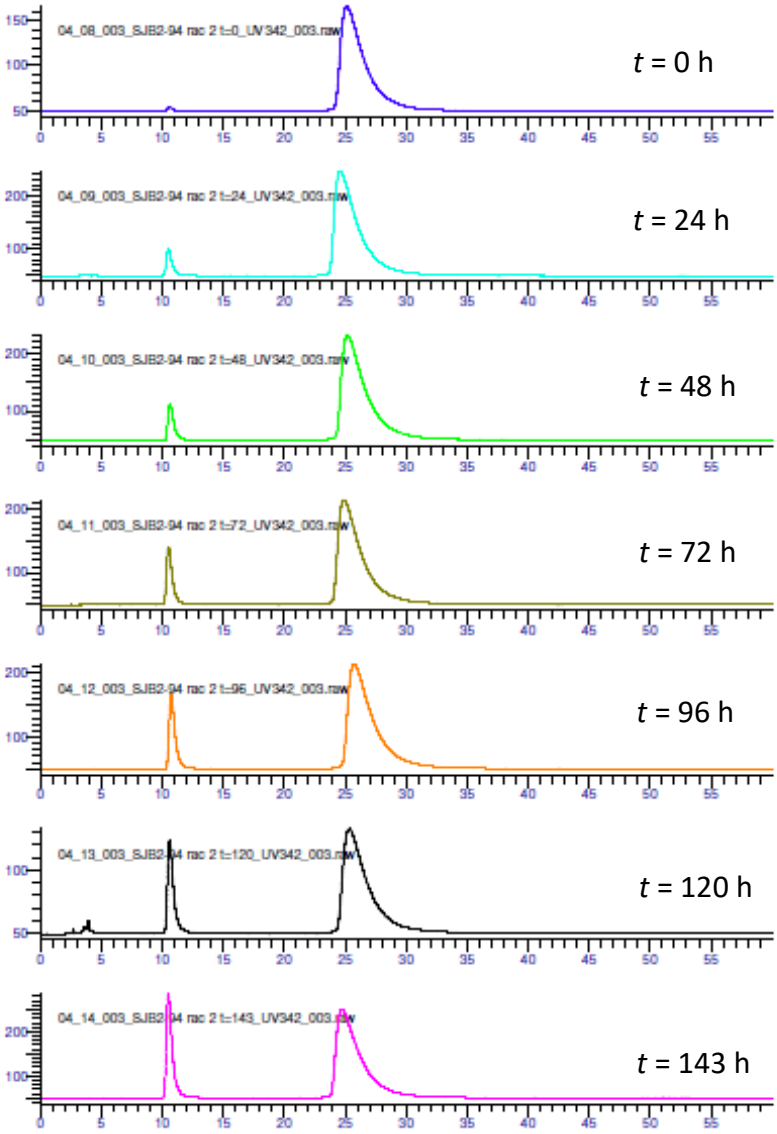

Figure 2.29 Stacked chiral HPLC traces monitoring the racemisation of **[EuL^4]** showing the appearance of the peak corresponding to the *Δ*-enantiomer (t_R = 10.6 min) as a function of time (racemisation in MeOH at 60 °C; CHIRALPAK ID, isocratic MeOH, 1.0 mL/min, 295 K).

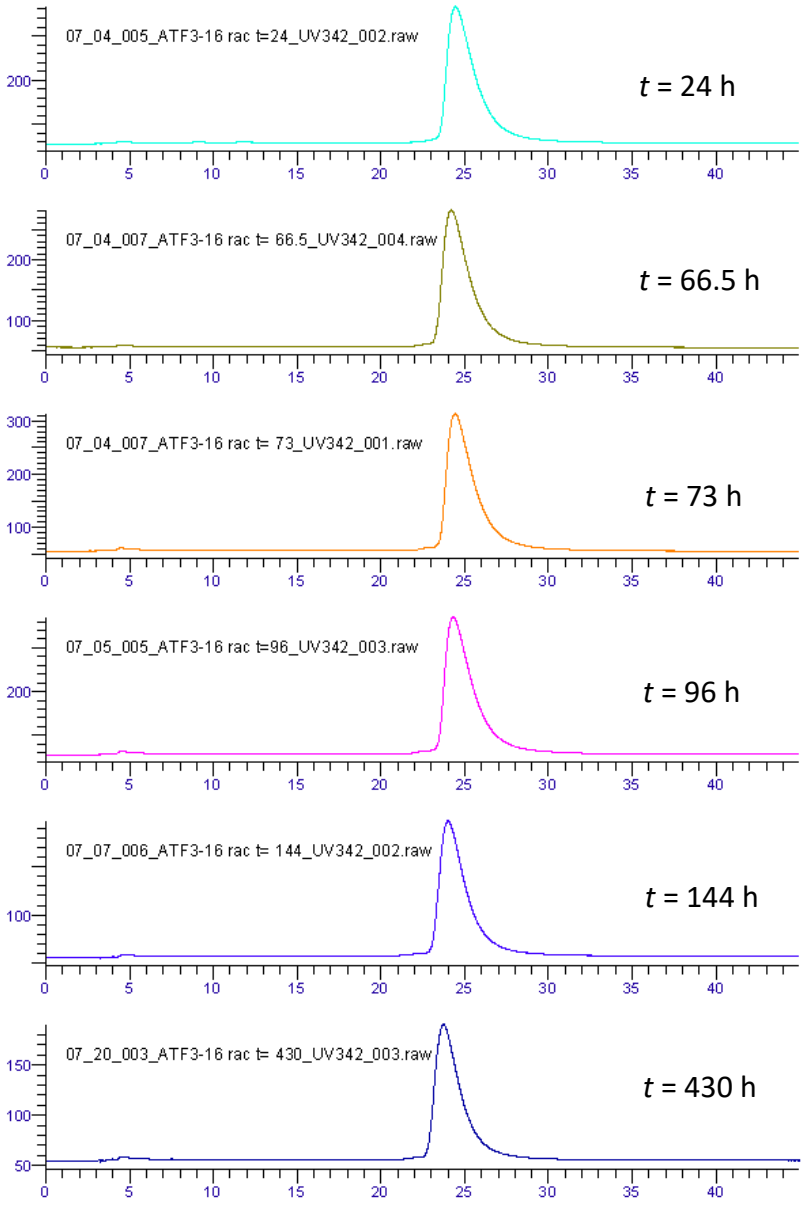

Figure 2.30 Stacked chiral HPLC traces monitoring the racemisation of **[EuL^2]** as a function of time, showing only the peak corresponding to the *Λ*-enantiomer (t_R ~ 24 min) (racemisation in MeOH at 60 °C; CHIRALPAK ID, isocratic MeOH, 1.0 mL/min, 295 K).

Plotting the proportions of each enantiomer according to Eqn. 2.7 (see Fig. 2.31) allows the half life for racemisation for **[EuL^4]** to be found. The result of 180 ± 10 h is a factor of two longer than was observed for the parent complexes **[EuL^6]** and **[EuL^7]**. Due to the absence of any observable racemisation, no half life could be calculated for **[EuL^2]**.

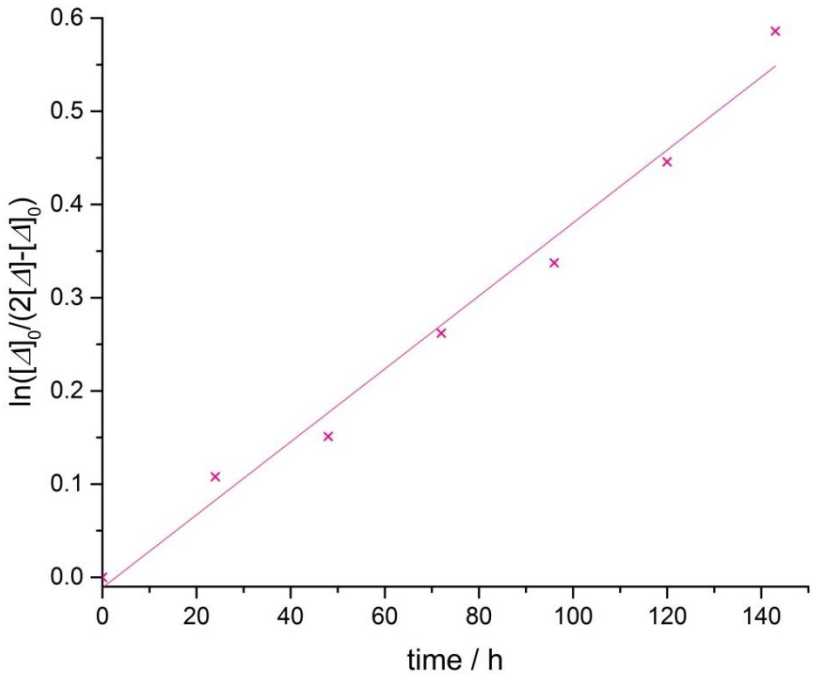

Figure 2.31 Kinetic plot of the rate of interconversion of enantiomers for **[EuL^4]** (60 °C, MeOH).

As shown in Section 2.4, interconversion between enantiomers requires cooperative arm rotation, inversion of the macrocycle ring, and in the case of complexes with phosphinate donor groups, inversion of the configuration at phosphorus. The difference in rates of racemisation between **[EuL^4]** and **[EuL^6]** could be attributed to the presence of the extended chromophore arms. When these extended chromophores are present, the push-pull system creates a larger dipole along the chromophore. As a result, the pyridine nitrogen is more polarisable, creating a stronger Eu-N_{py} bond, which would limit the rate of arm rotation and inhibit Eu-N_{py} dissociation. In the case of the phenyl phosphinate **[EuL^2]**, which exhibits no discernable racemisation over 3 weeks, the stability could be attributed to the increased overall rigidity of the complex and the more demanding steric nature of the phosphinate group making epimerisation at the phosphorus centres less favourable.

In order to attempt to quantify the activation energy of the racemisation of **[EuL^4]**, the experiment was repeated at different temperatures. In order to access higher temperatures, ethylene glycol was chosen as the solvent. Initial experiments on *Δ*-**[EuL^4]** in ethylene glycol at 80 °C showed no appearance of a peak for the *Λ*-enantiomer after 120 hours. To rule out that possibility that injecting the complex

onto the chiral HPLC column in ethylene glycol was affecting the resolution, a sample of racemic complex in ethylene glycol was analysed. Both enantiomers were observed, eluting at the same time as when injected in methanol, confirming that the appearance of only one peak was due to no racemisation having occurred. Therefore, the temperature was increased to 130 °C. Monitoring the racemisation for 240 hours showed gradual interconversion of the enantiomers. However, plotting the data according to Eqn. 2.7 did not appear to yield a linear relationship (see Fig. 2.32). Unfortunately, at later time points, the appearance of other overlapping peaks in the chiral HPLC trace suggested that decomposition of the complex was occurring.

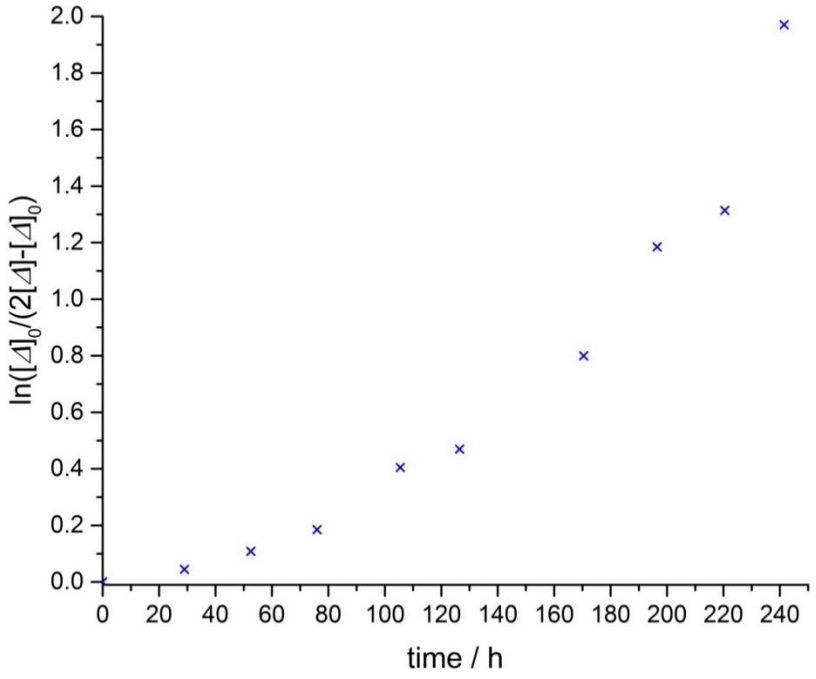

Figure 2.32 Kinetic plot of the rate of interconversion of enantiomers for **[EuL^4]** (130 °C, ethylene glycol).

These data clearly show that the racemisation of **[EuL^4]** is solvent dependent. These well-shielded 9-coordinate complexes are presumed to racemise via a dissociative mechanism, rather than a solvent molecule displacing a donor group initiating racemisation. Therefore, the slightly increased size of ethylene glycol compared to methanol is unlikely to be the reason for the difference in rate. One tentative explanation for the slower racemisation is that ethylene glycol is more viscous than

methanol. At a molecular level, the energy required to move the chromophore arms through the solvent would be higher, making the process slower.

The stability to racemisation observed for **[EuL^2]** and **[EuL^4]** makes these complexes promising candidates for use in a security labelling system. It is unlikely that in a 'real world' setting the complex would ever reach 60 °C. Based on the rule of thumb that a reaction rate halves for every 10 °C decrease in temperature, the half-life for racemisation of **[EuL^4]** at 20 °C would be of the order of 6600 hours (= 9 months) in methanol solution. As a security label, the complex would be printed onto or embedded into a material rather than existing in solution. Moreover, in the solid state the rate of racemisation is expected to be much slower than in solution.

2.8 Development of time-gated photography in security labelling

The aim of the project is to develop a system where a solution-processible chiral europium(III) complex can be used to mark a region of interest for use as an emissive label. The emissive label should be detectable using a simple assembly comprising off-the-shelf components, which could distinguish an enantiopure Eu(III) complex from a 'fake' emissive label perhaps incorporating organic or transition metal red emitting species. It was envisaged that the unique combination of excitation wavelength, emission wavelength, lifetime and circular polarisation of emission of the Eu(III) complex would be sufficient to distinguish it from a counterfeit label.

As such, the following detection setup was proposed. A digital single-lens reflex camera (DSLR) equipped with a xenon flash lamp would form the basis of the equipment. Band pass filters could be mounted onto both the flash lamp and camera to select the excitation and emission spectral regions of interest. Addition of a quarter-wave plate and linear polariser would allow selection of a particular circular polarisation of the emission, and a distance-controlled time gate could introduce a time-dependence to the measurement. Therefore, a 'genuine' europium(III) complex possessing a long lifetime, excitation in the correct spectral

region and CPL of the correct sign at the selected detection wavelength would be observed, while a 'fake' which does not possess the same combination of properties would not be observed.

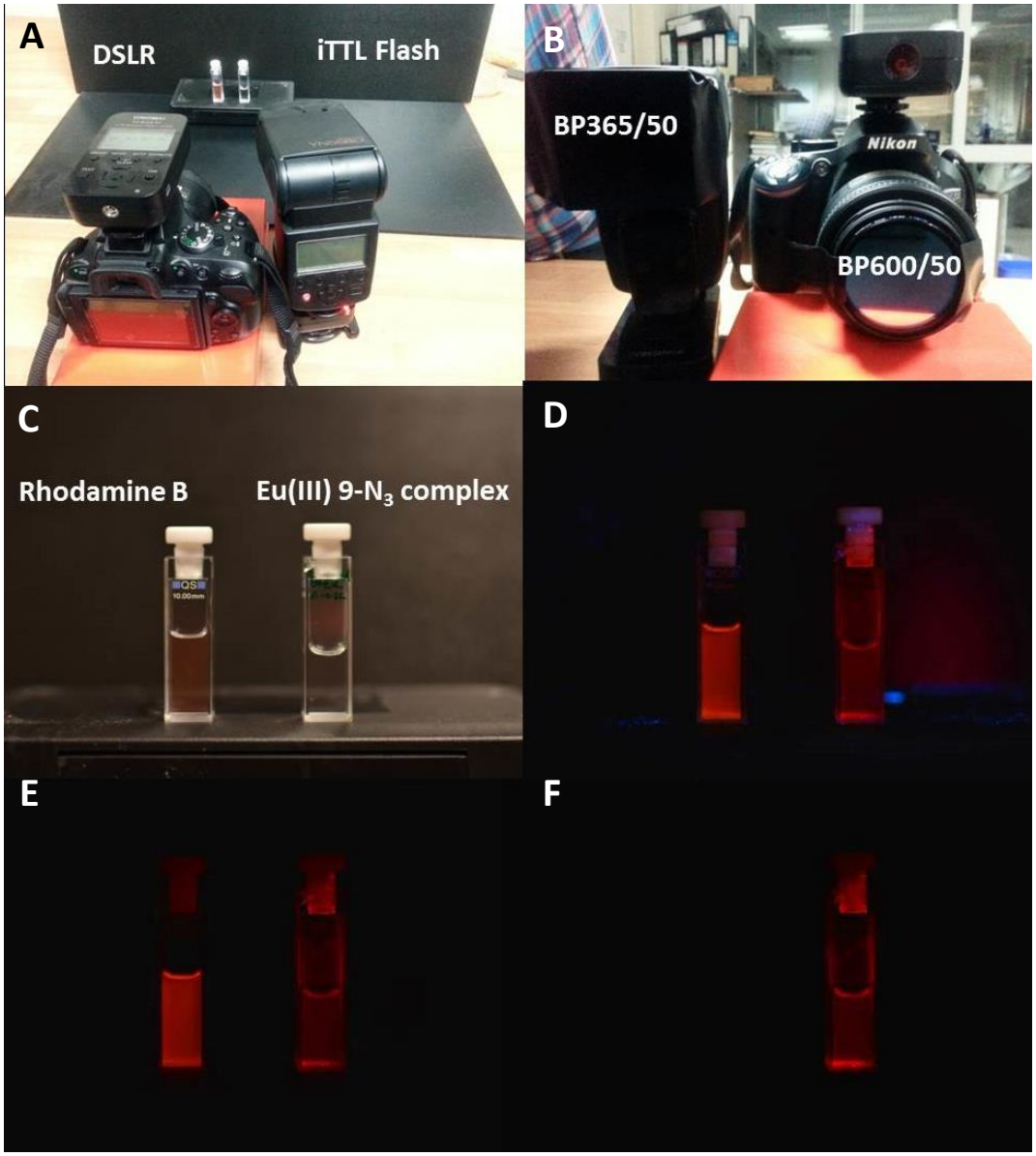

Figure 2.33 Off-the-shelf DSLR camera setup allowing wavelength selection and time gated photography (*A* and *B*), demonstrated with rhodamine B and a 9-N_3 based europium complex: (*C*) Standard photograph showing cuvette arrangement; (*D*) Standard photograph with UV excitation; (*E*) Photograph with the addition of a 600 ± 25 nm band pass filter to the camera and (*F*) with the addition of a time delay before detection.

Initial testing of the setup described above was carried out using a solution of a 9-N_3 based Eu(III) complex and a solution of the red-emitting organic dye rhodamine B (see Fig. 2.33). A 365 ± 25 nm band pass filter was fitted to the flash lamp to select for long wavelength UV excitation. With no emission wavelength

selection and no time-gating, red emission from both cuvettes was observed, with some blue light scattering from the excitation (Fig. 2.33D). Addition of a 600 ± 25 nm band pass filter to the camera removed this scattered blue light (Fig. 2.33E). Finally, addition of the time-gating resulted in selective imaging of the long-lived europium(III) emission (Fig. 2.33F).[134]

The combination of multiple emissive species with various emission wavelengths and lifetimes was expected to allow more complicated security labels to be developed. Such an approach could include marking of mixed compounds appearing as different colours depending on the use of time gating, or multiple spots which appear the same colour but disappear with the introduction of a time-gate. Obviously, any compound to be used in conjunction with **[EuL$^{1-4}$]** would need to be excited in the same wavelength range. A variety of complexes was explored (see Fig. 2.34) including fluorescent organic molecules, an aluminium phthalocyanine dye (kindly donated by Prof. A. Beeby) and three transition metal complexes (kindly donated by Prof. J. A. G. Williams), to find a suitable candidate for combination with a europium(III) complex in a multi-component security marking.

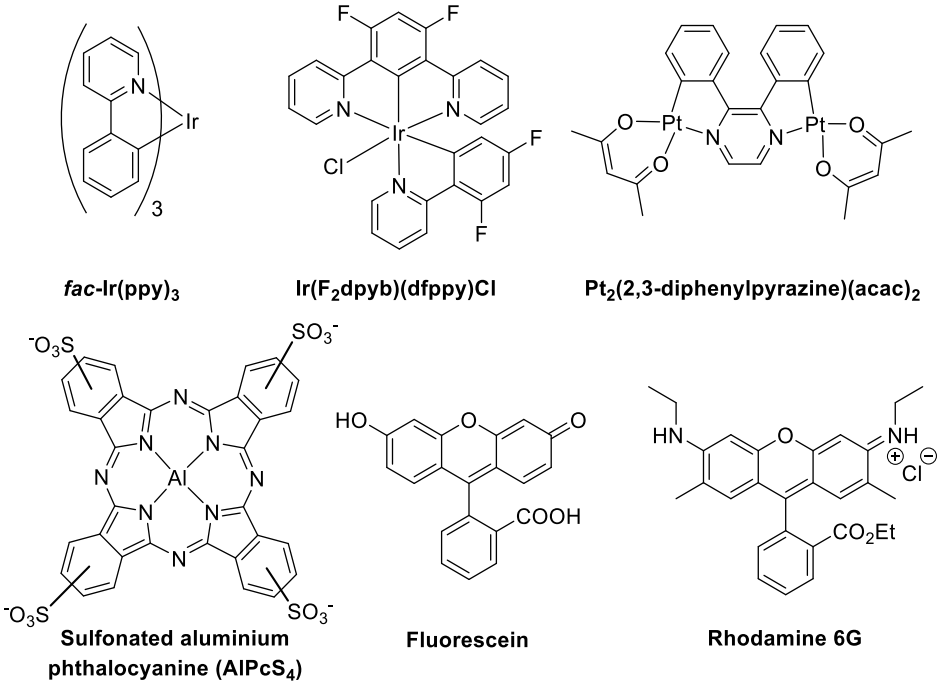

Figure 2.34 A range of compounds studied as possible ingredients of a two-component anti-counterfeiting label. The photophysical properties of *fac*-Ir(ppy)$_3$, Ir(F$_2$dpyb)(dfppy)Cl and Pt$_2$(2,3-diphenylpyrazine)(acac)$_2$ are described in detail elsewhere.[151–153]

Each transition metal complex is reported to have an emission lifetime of the order of a few microseconds and can be excited in the long wavelength UV region. Ir(ppy)$_3$ and Ir(F$_2$dpyb)(dfppy)Cl display broad emission bands in the green and yellow regions of the spectrum, respectively (see Fig. 2.35). This region corresponds to emission observed by the naked eye. Such emission profiles would allow the iridium complexes to be used in a two-component security marking based on a colour. The complex Pt$_2$(2,3-diphenylpyrazine)(acac)$_2$ emits red light with an emission maximum exactly corresponding to the maximum of the $\Delta J = 2$ transition of **[EuL^1]**. Such an overlap would preclude the use of this platinum complex in a multi-coloured marking, but the similar overall appearance of the emission to the naked eye would still allow its use in markings where differentiation of the components was based on lifetime or polarisation of emission.

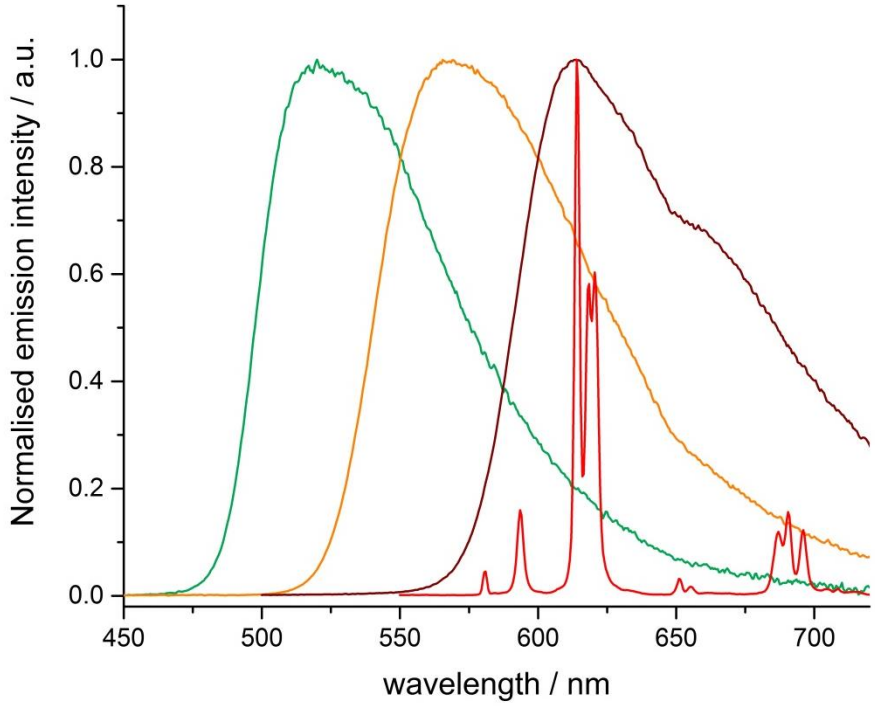

Figure 2.35 Normalised emission spectra of *fac*-Ir(ppy)$_3$ (*green*), Ir(F$_2$dpyb)(dfppy)Cl (*orange*), Pt$_2$(2,3-diphenylpyrazine)(acac)$_2$ (*brown*) and **[EuL^1]** (*red*), excited at a common wavelength of 356 nm (295 K, CH$_2$Cl$_2$ except **[EuL^1]** in MeOH).

A mixture (in appropriate ratios) of a green emitter and a red-emitting europium complex would appear yellow to the naked eye, assuming no time-gating. However,

on introduction of a time gate, green emission would be lost, leaving just the red emission from europium. It might be envisaged that a camera system such as that described above could take two images, one without time gating and the other with time gating. Comparison of the two images should show two different coloured spots for the same region of interest.

The time-gating method employed in the images in Fig. 2.33 uses the distance between the sample and the camera to distinguish between nanosecond rhodamine fluorescence and millisecond europium luminescence. Since light travels at 0.3 m ns^{-1}, a 5 ns time gate can be introduced with a 1.5 m separation between sample and camera. This distance is more than sufficient to gate out rhodamine emission. However, transition metal complexes such as those shown in Fig. 2.34 have lifetimes of the order of a microsecond in degassed dichloromethane. Time-gating of this magnitude would not be possible using a distance-based method. These transition metal complexes could still be used in colour-based security markings that do not rely on differentiation of their emission lifetimes from those of europium(III) complexes. However, using this system, it would be possible to distinguish microsecond iridium emission from nanosecond fluorescence.

The sulfonated aluminium phthalocyanine was also investigated as a possible co-spotting compound. Generally, unsubstituted phthalocyanines are very insoluble, but addition of sulfonate groups in this example makes the complex water soluble. Phthalocyanines have many modern uses such as in the textiles and paper industries as well as their use as dyes in the manufacture of compact discs (CDs). This particular phthalocyanine exhibits a broad absorption band centred at 350 nm which would allow co-excitation with a pyridylarylalkynyl-based europium complex and deep red emission from 660 to 760 nm (see Fig. 2.36). However, it also displays absorption bands between 600 and 700 nm, which corresponds to the region in which europium emission occurs leading to reabsorption of europium emission by the phthalocyanine, thereby reducing emission. Additionally, the region in which the phthalocyanine emits is close to the europium emission, meaning differentiation of its emission colour by eye might be difficult. Finally, due to its strong absorption profile in the red region, the aluminium phthalocyanine appears

deep blue to the naked eye. This means that any security label containing it would not be invisible in daylight. As a result of these properties, it was ruled out as a possible component of the proposed security markings.

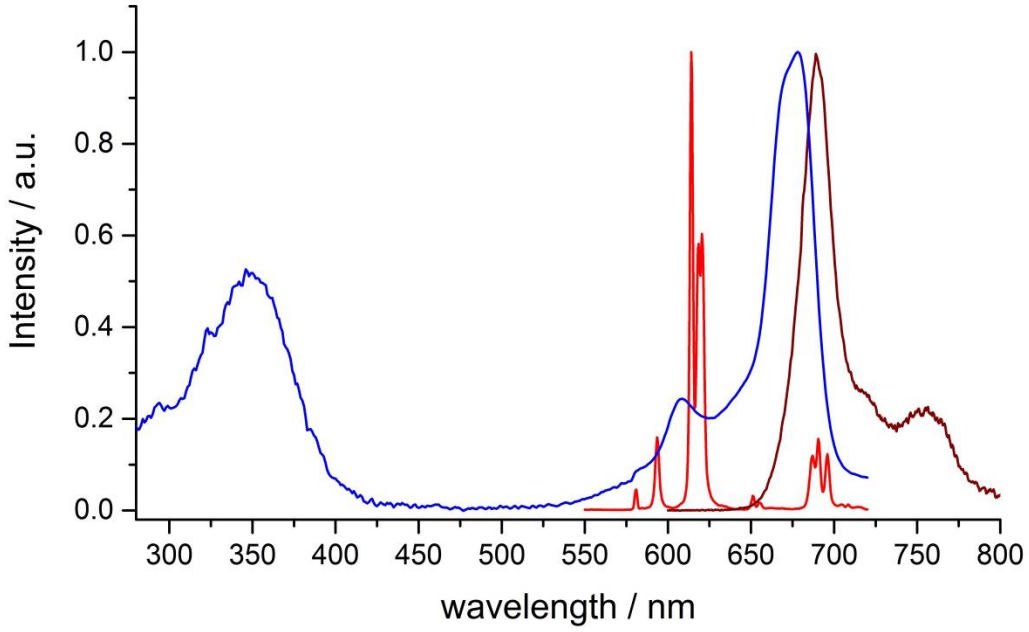

Figure 2.36 Absorption (*blue*) and emission (*brown*) of the sulfonated aluminium phthalocyanine dye (H_2O, λ_{exc} 350 nm, 295 K) and the emission of **[EuL^1]** (*red*, MeOH, λ_{exc} 356 nm, 295 K).

With a time-gated multi-coloured security marking still in mind, fluorescent organic molecules with emission in the green/yellow region of the spectrum were studied. While the major absorption bands for both fluorescein and rhodamine 6G fall in the visible region, both can be excited around 350 nm. The broad emission band of fluorescein has a maximum at 520 nm (green) with a long tail into the red region of the spectrum whilst rhodamine 6G emits around 560 nm (yellow-orange) (see Fig. 2.37). The absorption bands of both fluorophores are well separated from the emission of europium(III), meaning re-absorption of europium(III) emission would not occur. Emission from a mixture of rhodamine 6G and europium complex appears orange to the naked eye, which may be difficult to distinguish from the red-orange emission from europium alone. Therefore, further studies were carried out using fluorescein.

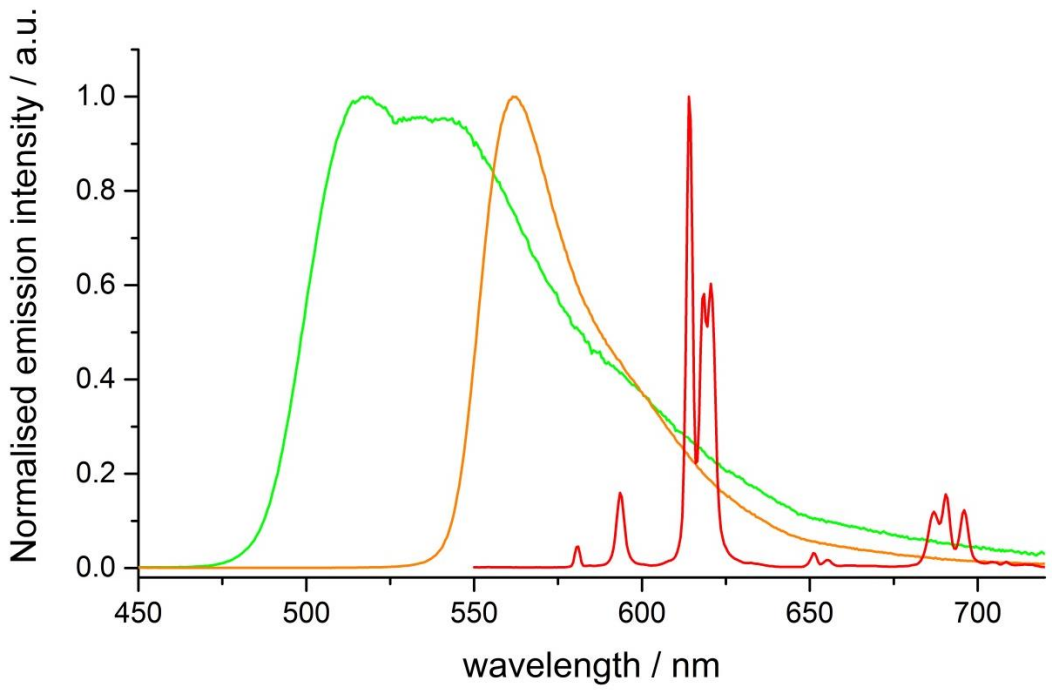

Figure 2.37 Normalised emission spectra of fluorescein (*green*, MeOH, λ_{exc} 354 nm, 295 K), rhodamine 6G (*orange*, MeOH, λ_{exc} 348 nm, 295 K) and **[EuL^1]** (*red*, MeOH, λ_{exc} 356 nm, 295 K).

Another important factor in the use of a two-component mixture is whether europium emission is affected by the addition of a second species. In order to study this issue, a titration of fluorescein and **[EuL^1]** was carried out. The internal charge transfer absorption band, emission spectrum and emission lifetime of **[EuL^1]** were recorded as a function of up to 10 equivalents of added fluorescein. No change was observed in the absorption spectrum of the complex. After addition of 10 equivalents of fluorescein, the emission lifetime of **[EuL^1]** was reduced by approximately 15%. However, this effect would not stop this mixture functioning as a two-component label as the europium emission lifetime of **[EuL^1]** (1.18 ms in MeOH) is still over 200 000 times longer than that of fluorescein (5.49 ns in MeOH).[154] The emission intensity of **[EuL^1]** at 614 nm was also monitored as a function of added fluorescein. A small drop in emission intensity (30%) was observed until approximately two equivalents of fluorescein had been added. As more fluorescein was added, the emission intensity of **[EuL^1]** began to recover. These changes in emission intensity were not accompanied by a change in spectral form, which suggests that the inner coordination environment is not affected. Since no changes were observed in the absorption spectra of **[EuL^1]** on addition of

fluorescein, it is unlikely that fluorescein is interacting significantly with the extended chromophores of the complex by a π-stacking interaction, for example. It is possible that some other long range interaction is responsible for this quenching behaviour. In any case, the quenching behaviour in solution cannot be used to accurately predict the effect of a mixture of fluorescein and europium complex on a surface in the solid state. Based on these results, it does not appear that emission is quenched to such an extent that the mixture could not be used as a two component system.

In order to test the applicability of fluorescein and a europium(III) complex in a two component multi-coloured time dependent security marking, a proof of concept test paper was designed (see Fig. 2.38). Non-brightened paper (Canson Infinity Rag Photographique 2010 g/m^2) was used to ensure that fluorescence interference from brightening agents used in standard printer paper would not affect the measurements. The test paper possessed three spots. The left-hand spot contained **[EuL^1]**, the right-hand spot contained fluorescein, while the central spot was a co-spot of **[EuL^1]** and fluorescein. Each spot was deposited onto the paper as a solution in methanol using a TLC capillary spotter, before being allowed to dry in air. It was envisaged that images recorded without a time delay would show three spots (red, yellow and green), while images recorded with the time gating would show only two red spots.

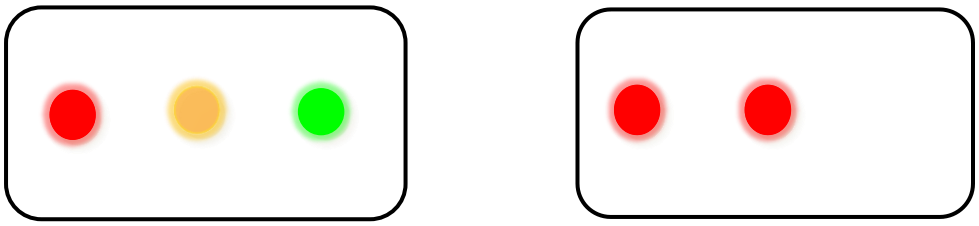

Figure 2.38 *Left*: proposed layout of test paper for a two-component security marking using time-gated photography, comprising **[EuL^1]**, fluorescein and a co-spot. *Right*: the expected appearance of the test paper using time-gated photography.

Initial tests confirmed that the addition of a 600 ± 25 nm band pass filter to the camera was not sufficient to remove the fluorescein emission from the image. This result was expected, based on the emission spectral profile of fluorescein (see Fig. 2.37) as it exhibits a long tail into the red region of the spectrum, despite the overall

fluorescence appearing green. As expected, on introduction of the distance-based time gate, the fluorescein spot disappeared fully (see Fig. 2.39).[134]

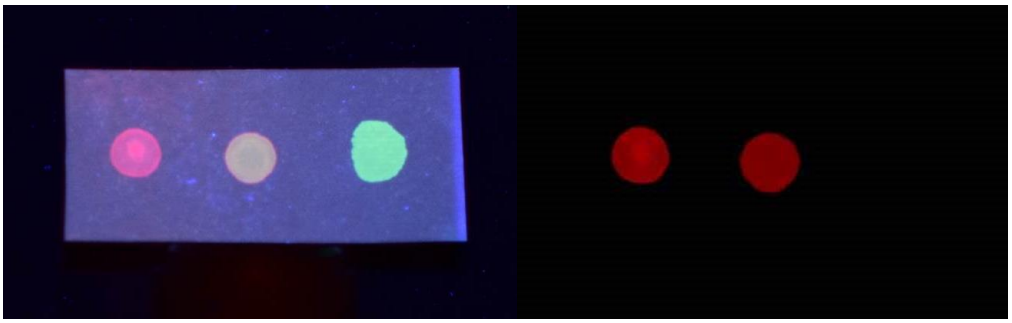

Figure 2.39 *Left*: photograph of the two-component test paper under UV excitation with no wavelength selection or time gating. *Right*: the same test paper after introduction of a time gate and a 600 ± 25 nm band pass filter.

Spectral imaging of the central spot of the paper with and without a time gate confirmed that the fluorescein emission could be removed from the spectral profile (see Fig. 2.40). The lifetime of the **[EuL^1]** emission was also measured and found to be 1.02 ms, similar to that observed in methanol solution.

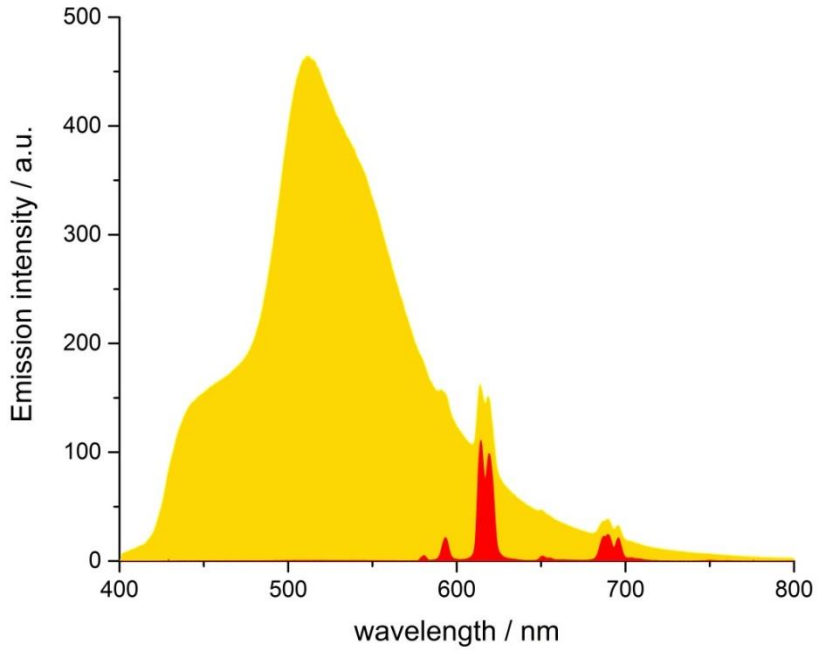

Figure 2.40 Spectral imaging of the central test paper spot before (*yellow*) and after (*red*) addition of a time gate. Introduction of the time gate removes the broad fluorescein emission band.

To confirm the applicability of these complexes as chiroptical labels in the solid state, total emission and CPL spectra were recorded of spots of enantiopure **[EuL^2]** deposited onto paper (see Fig. 2.41). The total emission and CPL spectra of **[EuL^2]**

on the paper show very similar profiles to the spectra acquired in methanol solution. The only difference is the relative intensity of the CPL transition at 614 nm which is stronger in the solid state than in solution.

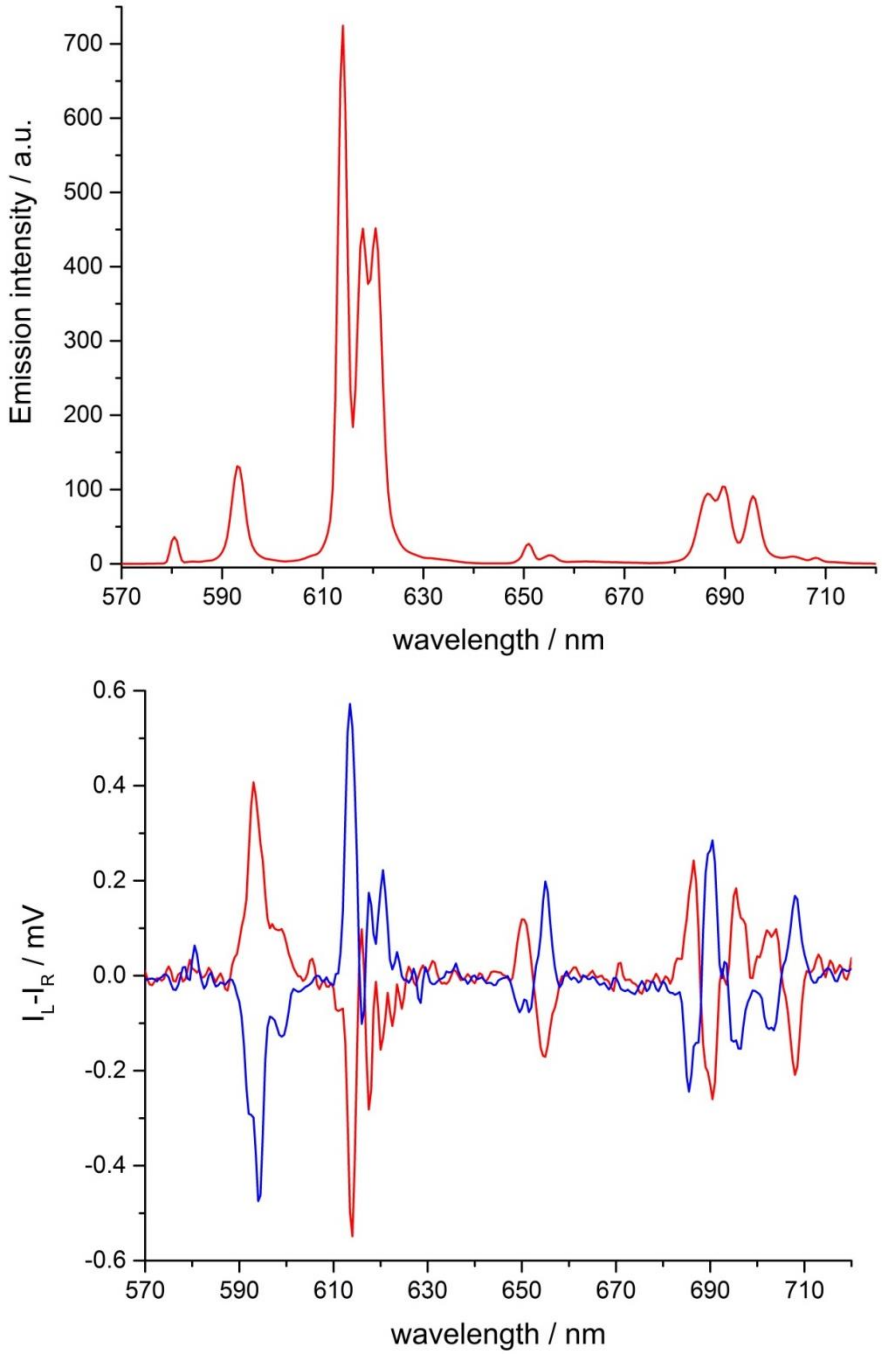

Figure 2.41 Total emission (*top*) and CPL spectra (*bottom*) of the *Δ*- (*red*) and *Λ*- (*blue*) enantiomers of **[EuL^2]** deposited on non-optically brightened paper (295 K, λ_{exc} 342 nm, 3 scans averaged).

In addition to the test paper, the enantiomers of the complex **[EuL^2]** were doped into poly(methyl methacrylate) (PMMA) and deposited as thin films on quartz discs (for details of the preparation of these films, see Chapter 5). In these preliminary

experiments, controlling the homogeneity of the film was challenging, although films suitable for CPL spectral acquisition were produced. The appearance of the excitation, total emission (Fig. 2.42) and CPL spectra (Fig. 2.43) in these films was very similar to that observed in solution, and the emission dissymmetry values were consistent with those observed in methanol solution. As in methanol solution, the $^5D_0 \rightarrow {}^7F_5$ manifold and various manifolds corresponding to emission from the $^5D_1$ state were visible (Fig. 2.42). An emission lifetime of 1.15 ms was observed from the immobilised complex, consistent with that observed in solution.

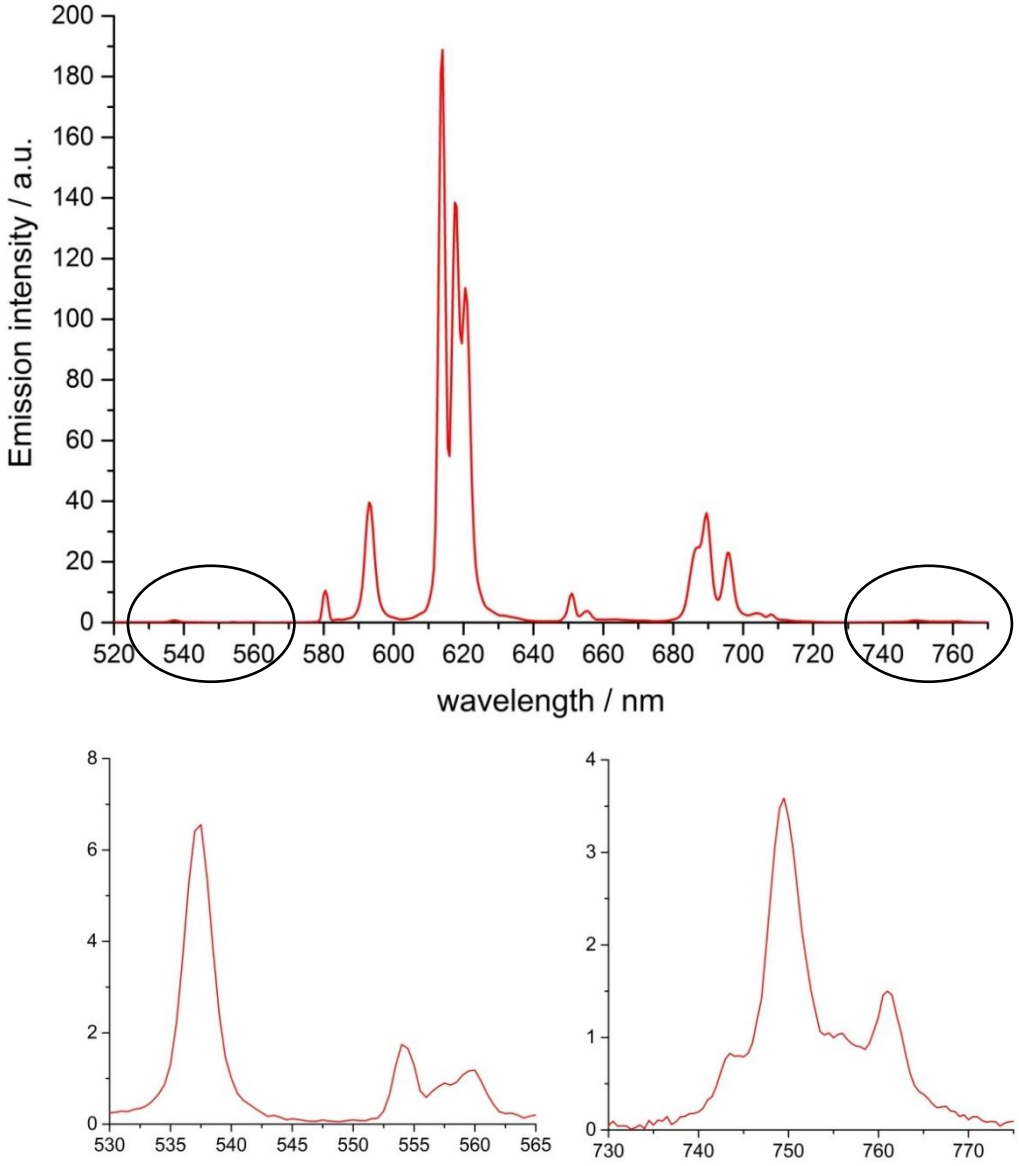

Figure 2.42 Total emission spectrum (*top*) of 1% **[EuL^2]**-doped PMMA film, deposited on a quartz disc, with circled regions expanded (*bottom*) (295 K, λ_{exc} 342 nm).

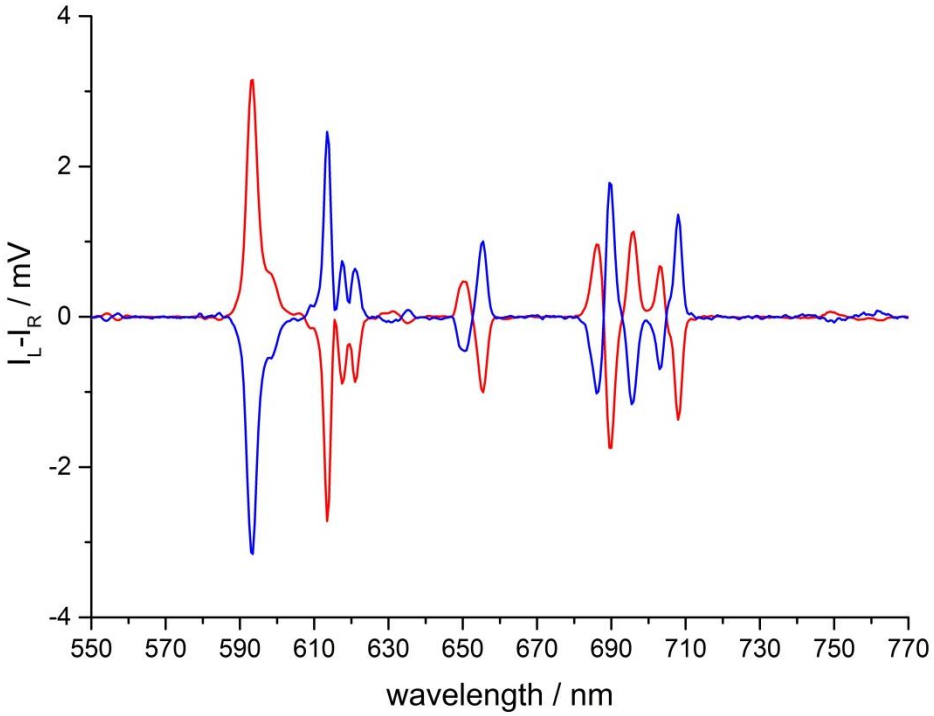

Figure 2.43 The CPL spectra of the *Δ*- (*red*) and *Λ*- (*blue*) enantiomers of **[EuL^2]** in a PMMA film deposited on a quartz disc (295 K, λ_{exc} 342 nm). Selected g_{em} values for *Δ*-**[EuL^2]**: -0.45 (557 nm); +0.18 (599 nm); -0.18 (655 nm); -0.38 (708 nm).

A second test paper was designed for the purpose of incorporating chiroptical selection into the photographic detection method (see Fig. 2.44). The phenylphosphinate complexes **[EuL^1]** and **[EuL^2]** show strong CPL signals in the Δ*J* = 1 manifold. Importantly, in this region all the transitions show CPL signals of the same sign, i.e. all positive or all negative. Such a feature presents a useful target for CPL detection using the camera. Using a band pass filter to select the Δ*J* = 1 region, in combination with a quarter-wave plate and linear polariser to select for CPL sign, it was predicted that spots of enantiopure Eu(III) complex could be distinguished from each other by their emission polarisation. As such, a series of three spots, comprising enantiopure *Λ*- and *Δ*-enantiomers along with racemic complex, would appear differently under different chiroptical selection properties. For example, in both **[EuL^1]** and **[EuL^2]**, positive CPL is emitted in the Δ*J* = 1 transition of the *Δ*-enantiomer, while negative CPL is emitted by the *Λ*-enantiomer. Therefore, orientating the linear polariser such that left-handed CPL is collected by the camera, should allow the spot containing the *Δ*-enantiomer to be selectively imaged, and vice versa. The racemic complex would be observed in both images.

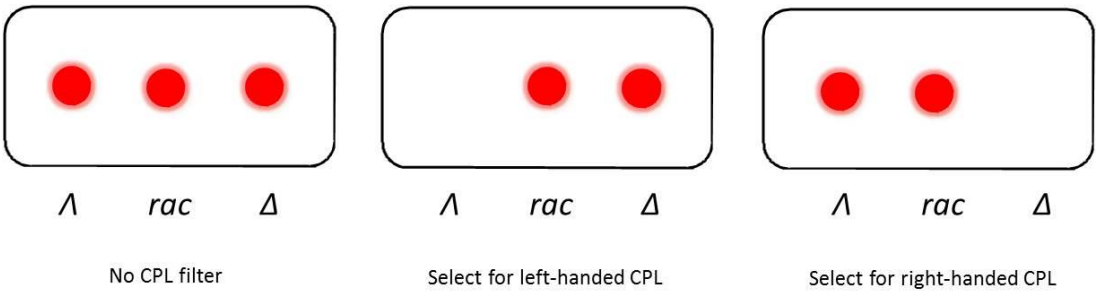

Figure 2.44 *Left*: a test paper for chiroptical contrast photography comprising two spots of enantiopure complex and a central spot of racemic complex. *Centre* and *right*: the expected appearance of the test paper while selecting for positive or negative CPL, respectively.

Unfortunately, addition of the quarter-wave plate and linear polariser reduced the light reaching the camera CCD to such an extent that the spots were too dim for chiroptical discrimination to occur. It is possible that more concentrated spots of complex could allow successful chiroptical discrimination using this setup, but lack of light due to additional filters being used will always be a limiting factor in these measurements.

2.9 Time-gated chiral contrast microscopy

After the difficulties encountered in chiroptical discrimination using an off-the-shelf camera setup, it was decided to attempt to observe chiral contrast imaging by microscopy. Modification of a time-resolved Zeiss Axiovert 200M epifluorescence microscope to allow chiroptical contrast detection was achieved by careful consideration of the components in the pathway of the emitted light. The microscope is equipped with a variable pulse sequence generator, permitting control of the excitation pulse and emission collection, which allows both continuous and time-gated imaging. Emitted light is guided to the detectors, which consist of separate CCDs for imaging and spectral measurement, as well as a photomultiplier tube for measuring emission lifetime. Since the microscope was originally set up for measurements of biological samples, it contains a de Sénarmont compensator. Normally, this component is used to account for elliptically polarised light generated when linearly polarised incident light is transmitted through a biological sample. It contains a rotatable quarter-wave plate and linear polariser combination to convert elliptically polarised light back to

linearly polarised light for imaging. Obviously, such a component would significantly affect the ability for chiroptical selection, making its removal a vital requirement in this setup.[134]

Addition of a band pass filter in the path of the emitted light allows wavelength selection, before the emitted light is guided through a broad wavelength (400-800 nm) quarter-wave plate, allowing translation of circularly polarised light into linearly polarised light. Left-handed CPL is translated to vertical linearly polarised light, while right-handed CPL is translated to horizontal linearly polarised light. Unfortunately, the small size (10 mm) of the commercially available quarter-wave plate restricts the size of the aperture. To overcome the potential loss of signal, a beam expander lens and a pair of variable irises were inserted to compensate for the small size of the aperture. The final element in the optical setup is a pair of linear polarisers, orientated at 90° to each other, and mounted in a sliding holder, allowing simple swapping between detection of either the horizontal or vertical linear polarised light generated by the quarter-wave plate. The selected linearly polarised light is then focused onto the CCD for image acquisition.[134]

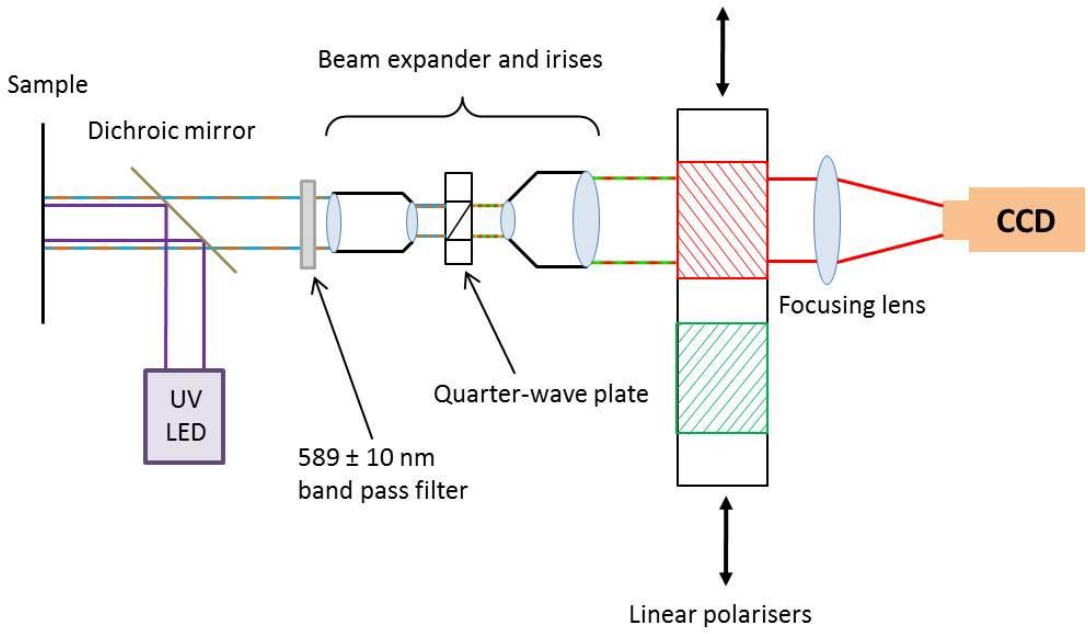

Figure 2.45 Schematic diagram of chiroptical microscopy setup, showing various optical components required for the discrimination of circularly polarised light. In this diagram, circularly polarised emitted light (represented by the orange and blue lines) is converted to perpendicular linearly polarised light (represented by red and green lines). The sliding linear polarisers allow only one perpendicular component to reach the CCD detector.

Image acquisition using this optical setup was achieved using pulsed excitation from a 365 nm UV-LED, followed by time gating (typically 6-10 µs) with images collected for 7.2 ms per frame. Images were collected using an accumulation sequence, allowing frames to be averaged using a saturation limiting algorithm. Using this algorithm, images were accumulated until a predefined maximum contrast value of 255 was reached for a cluster of 20 pixels. Any difference in polarised emission (as defined by the g_{em} value at a particular wavelength) is amplified, as the total contrast in the accumulated image is proportional to the number of images acquired. The total number of images acquired was governed by the maximum single image brightness; this was set automatically to be a minimum of five times the signal to noise ratio.

Various microscopy images were recorded using this system, demonstrating both time-gating and chiroptical selection (see Fig. 2.46). In each case, the samples were deposited onto non-optically brightened paper as solutions in methanol and allowed to dry in air. Areas of similar brightness were selected and well-defined rectangular pieces were cut using a dye punch. These pieces were mounted onto a microscope slide and covered with a coverslip. Microscopy images (Figure 2.46A and B) show racemic **[EuL^1]** and fluorescein and demonstrate that the time gating shown in Fig. 2.39 is also possible using optical microscopy. Figure 2.46C-F shows the development of the chiroptical contrast system using the two enantiomers of **[EuL^2]**. In Fig. 2.46C, the time-resolved image of the *Λ*- (top) and *Δ*- (bottom) enantiomers of **[EuL^2]** is revealed, demonstrating that with no chiroptical selection, both pieces of paper exhibit equal image contrast. Introduction of a band pass filter selective to the $\Delta J = 1$ region of the europium(III) emission (Fig. 2.46D), does not affect the relative contrast of the two pieces of paper. In Fig. 2.46E and F, selection of horizontal and vertical linearly polarised light, respectively, shows differential image contrast between the two pieces of paper. In image E, where horizontal linearly polarised light is selected, the top piece of paper (*Λ*-**[EuL^2]**) appears brighter. Since horizontal linearly polarised light originates from the right-handed CPL, this corresponds to a negative CPL signal. *Λ*-**[EuL^2]** has a strong negative CPL signal in the region of interest, consistent with the microscopy images. The reverse

behaviour is observed in image F, when selecting for vertical linearly polarised light (= left-handed CPL) as the lower piece of paper with *Δ*-**[EuL^2]** appears brighter. In the control experiment, racemic **[EuL^1]** gave rise to constant image brightness, irrespective of which chiroptical channel was selected.[134]

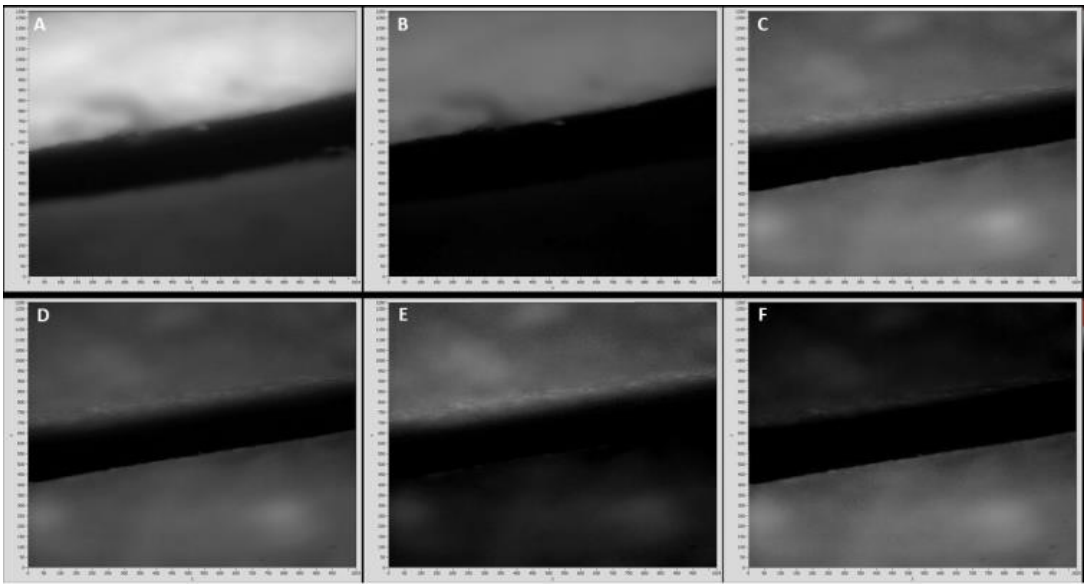

Figure 2.46 Microscopy images following sample excitation using a 365 nm UV-LED ($t_{acq.}$ = 7.2 ms/frame, 395 nm dichroic mirror, λ_{em} LP-420 nm) of fluorescein, *Λ*- and *Δ*- europium(III) complex recorded on a custom-built microscope incorporating a chiroptical selector unit. (*A*) Ungated image of (*top*) racemic **[EuL^1]** (1:1) and (*bottom*) fluorescein, using 10 frame accumulation imaging sequence. (*B*) Time-resolved image of (*top*) *Λ*– and *Δ*-**[EuL^1]** (1:1) and (*bottom*) fluorescein (t_d = 6 µs, λ_{em} LP-420 nm, 50 frame acc.). (*C*) Time-resolved image of (*top*) *Λ*-**[EuL^2]** and (*bottom*) *Δ*- **[EuL^2]** (t_d = 6 µs, λ_{em} LP 420 nm, 70 acc.). (*D*) Time-resolved image of (*top*) *Δ*-**[EuL^2]** and *(bottom*) *Λ*-**[EuL^2]** (t_d = 6 µs, λ_{em} BP 595/10 nm, 150 frame acc.). (*E*) Time-resolved image of (*top*) *Λ*-**[EuL^2]** and (*bottom*) *Δ*-**[EuL^2]** using the RIGHT (horizontal polarisation) circularly polarised light chiroptical channel (t_d = 6 µs, λ_{em} BP-589/20 nm, 370 frame acc.; contrast ratio CR $_{Λ:Δ}$ = 3.23 : 1) (*F*) Time-resolved image of (*top*) *Λ*-**[EuL^2]** and (*bottom*) *Δ*-**[EuL^2]**, using the LEFT (vertical polarisation) circularly polarised light channel (t_d = 6 µs, λ_{em} BP-589/20 nm, 370 frame accumulations; contrast ratio, CR $_{Λ:Δ}$ = 1 : 3.64).

Despite the relatively small g_{em} values, the optical setup, in combination with the saturation limiting algorithm, provides contrast ratios in excess of 3:1 when observing enantiopure lanthanide complexes. Although discrimination of chiral molecules has been demonstrated on chiral liquid crystals using scanning tunnelling microscopy,[155,156] and on surfaces patterned with chiral molecules by chemical force microscopy,[157] to the best of our knowledge, this is the first time that chiral image contrast in optical microscopy has been experimentally validated. This experimental set up is unlikely to permit chiroptical discrimination of chiral organic molecules, where the g_{em} values are 100 times smaller.

Attempts to repeat the above microscopy experiments using the doped polymer films were hampered by microscopic surface inhomogeneity. Very small variations in the thickness of the film introduced difficulty in simultaneous imaging of both films in the same focal plane. Due to this inhomogeneity, some regions of the film appeared brighter than others, making comparison of the chiral contrast challenging.

2.10 Conclusions and Future Work

Novel, highly emissive chiral europium complexes, **[EuL^1]** and **[EuL^2]**, based on 9-N_3 macrocycles bearing pendant pyridylarylalkynyl chromophore arms have been synthesised and characterised. Their photophysical properties have been measured and were found to be consistent with related complexes previously synthesised in Durham. Their absorption maxima make them amenable to excitation at 355 or 365 nm using commonly available light sources. Coupled with high quantum yields and molar extinction coefficients, this makes them ideal candidates for use as emissive security labels.

The complexes **[EuL$^{1\text{-}4}$]** have been successfully resolved by chiral HPLC and their CPL spectra were obtained. The enantiomers of each complex exhibit strong mirror imaged CPL spectra which correlate well in form and sequence with the parent complexes that do not possess the extended chromophore arm. Increased resolution in all transitions (ΔJ = 1, 2, 3, 4) has been observed in the CPL spectra when compared to total emission. Large emission dissymmetry values have been observed in the CPL spectra all four complexes. Additionally, the $^5D_0 \rightarrow {}^7F_5$ transition and various $^5D_1 \rightarrow {}^7F_J$ transitions have been observed in both total emission and CPL emission in solution and doped into PMMA films.

An alternative synthetic route to complexes with carboxylate donors was investigated, which would allow chiral resolution of an intermediate complex, prior to further functionalisation. The solubility of the intermediate complex made it difficult to handle, although Sonogashira couplings were achieved in DMSO

solution, allowing the synthesis of a novel carboxylate complex **[EuL^{12}]**, whose photophysical properties were consistent with similar carboxylate complexes.

The racemisation kinetics of the methyl and phenyl phosphinate complexes were investigated, showing that in methanol solution, the half-life for racemisation of **[EuL^{4}]** at 60 °C was 180 ± 10 h, considerably longer than for the parent system. No racemisation was observed for **[EuL^{2}]** after 3 weeks under the same conditions. Repeating the experiments at 80 °C and 130 °C in ethylene glycol showed that the rate of racemisation is clearly solvent dependent, which is an area for future investigation, as it may aid in the elucidation of the racemisation mechanism. Further investigations need to be made into the racemisation kinetics of these complexes at various temperatures and in various solvents.

Various time-gated photography experiments have been carried out, with combinations of europium(III) complexes and fluorescent organic molecules using an off-the-shelf camera system. Short-lived organic fluorescence could be distinguished from longer lived europium(III) emission both in solution and in the solid state. Multi-coloured markings comprising a mixture of emissive components have been used to demonstrate colour and lifetime-based discrimination using the camera system.

Finally, time-gated chiral contrast microscopy has been demonstrated using a custom-built microscope equipped with a quarter-wave plate and linear polariser combination. The system was able to discriminate between regions of paper marked with enantiopure europium(III) complexes emitting equal and opposite CPL. By selecting a spectral region of interest and converting left- and right-handed CPL to vertical and horizontal linearly polarised light, chiral contrast images can be accumulated with contrast ratios in excess of 3:1.

Further development of the deposition of complex-doped polymers is required before such substrates can be used successfully in chiral contrast microscopy. Spin-coating a sol-gel containing emissive complexes onto quartz discs has been achieved previously in the group,[158] and such a method might prove successful

here, allowing homogeneous films to be produced. The preliminary work described here has shown that the desirable photophysical properties and strong polarised luminescence of the complex **[EuL^2]** are retained once immobilised in the polymer, suggesting that deposition of the complex in polymers warrants further investigation.

CHAPTER THREE : SOLVENT EFFECTS IN Ln(III) EMISSION

3.1 Introduction

Solvatochromism in internal charge transfer transitions is a much-investigated phenomenon. The energy of the internal charge transfer excited state is dependent on its environment, including factors such as temperature and solvent polarity. Recent work on the 9-N_3 based pyridylarylalkynyl family of europium(III) complexes has shown that the wavelength of the absorption maximum varies with solvent polarity.[29,137,159] In these studies, bathochromic shifts were observed for the internal charge transfer absorption bands as solvent polarity was increased. Such behaviour can be attributed to the dipole of the polar solvents coupling with the dipole of the extended chromophore, thereby stabilising the chromophore excited state. As a result, the excited state is lower in energy, causing a shift to lower energy (longer wavelength) in the excitation band.

Although the absorption behaviour of these complexes has been studied in some detail, a thorough investigation of the emission profiles of these complexes has not been carried out. Recent work by the group of Faulkner has demonstrated solvatochromism in the emission from bimetallic Eu/Tb complexes in various solvents.[160] On changing from acetonitrile to methanol to water, the emission from Eu(III) was quenched whilst the emission from Tb(III) showed little change. In this instance, the effect was attributed to a combination of differences in O-H oscillator quenching efficiency of the excited state of the two metals by the different solvents, and also to subtle changes in molecular conformation affecting the ability of the chromophore to sensitise europium(III) emission. In this case, the change in conformation was such that the distance between the chromophore and the metal centre was varied significantly. However, it might be expected that more subtle changes in molecular geometry would effect modulation of emission behaviour, especially for the hypersensitive transitions of europium(III).

Sensitisation of europium(III) emission by pyridylarylalkynyl chromophores is known to occur via an internal charge transfer transition that is solvent-dependent. Therefore, it is reasonable to hypothesise that in solvents of different polarity, the electron distribution in the chromophores is affected. Such a change will influence the polarisability of the pyridine nitrogen atom, and hence the strength of the Eu-N_{py} bond. Additionally, interactions such as hydrogen bonding to the phosphinate donor groups may also contribute to small differences in complex geometry. Minor changes in the environment of the metal centre can result in modification of the fine structure of the emissive manifolds. As such, the emission behaviour of several compounds in various solvents has been investigated. In each case, total emission and CPL spectra were recorded in a variety of solvents spanning a wide range of polarities and viscosities.

Solvent polarity can be classified using Reichardt's solvent polarity parameter E_T, based on the transition energy for the longest-wavelength solvatochromic absorption of a pyridinium-*N*-phenoxide betaine dye (see Fig. 3.1). Originally, this solvent polarity parameter was simply defined as the energy of the absorptive transition (in kcal mol^{-1}). Subsequently, these parameters have been normalised to the extreme values of the reference solvents, water and tetramethylsilane, such that water has a value of 1.000 and tetramethylsilane has a value of 0.000 on the E_T^N scale. The Reichardt solvent polarity parameters, E_T^N, for the solvents used in this work are shown in Table 3.1, as well as their respective viscosities at 298 K.

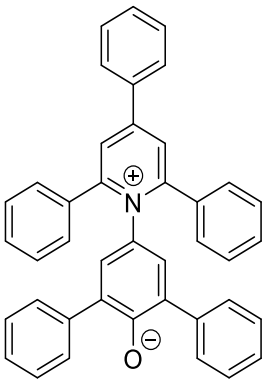

Figure 3.1 The structure of the pyridinium-*N*-phenoxide betaine dye used in the calibration of Reichardt's solvent polarity parameters.

Table 3.1 Solvent polarity parameters and viscosities for the range of solvents used in this work.

Solvent	**Reichardt solvent polarity parameter,**[161] E_T^N	**Viscosity at 25 °C**[162] **/ mPa s**
Water	1.000	0.890
2,2,2-Trifluoroethanol (TFE)	0.898	1.84[a]
Methanol (MeOH)	0.762	0.544
Ethanol (EtOH)	0.654	1.074
Isopropanol (^{i}PrOH)	0.546	2.038
Acetonitrile (MeCN)	0.460	0.369
Dimethylsulfoxide (DMSO)	0.444	1.987
N,N-Dimethylformamide (DMF)	0.404	0.794
Tert-butanol (^{t}BuOH)	0.389	4.312
Acetone	0.355	0.306
Dichloromethane (DCM)	0.309	0.413
Chloroform	0.259	0.537

[a] From Ref. [163]

3.2 Solvent effects in the emission and CPL of [EuL^2]

3.2.1 Solvent effects in the total emission of [EuL^2]

Initially, **[EuL^2]** was selected for study as it was the brightest of the four complexes **[EuL$^{1-4}$]**. Additionally, the presence of the phenyl phosphinate donor group was expected to allow solubility in a greater range of solvents (notwithstanding its lack of solubility in water). As expected, the complex **[EuL^2]** exhibited solvatochromism in absorption, with the absorption maximum varying from 322 nm in acetone to 343 nm in 2,2,2-trifluoroethanol (TFE). No obvious trend in emission lifetime was observed with changing solvent polarity or viscosity.

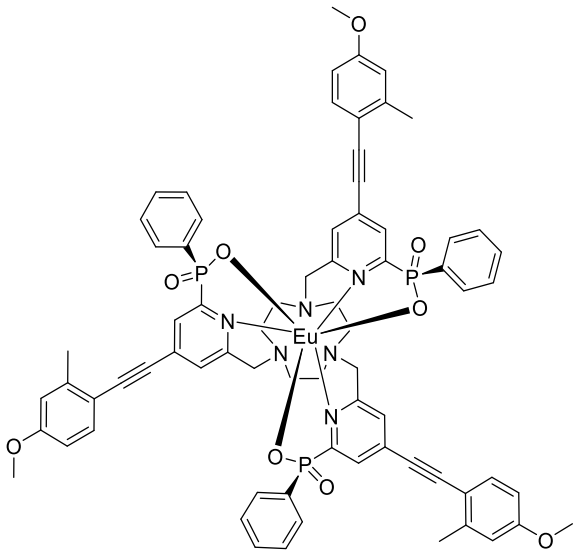

[EuL^2]

In the total emission spectrum, there were significant changes in the spectral form (see Fig. 3.2). In the ΔJ = 2 manifold, the strongest transition around 614 nm (transition A, Fig. 3.3) showed little variation, but the two longer wavelength components (B and C) showed both changing position and intensity ratio. On moving from polar protic solvents (e.g. MeOH) to non-polar solvents (e.g. $CHCl_3$), the two components appeared to move apart with the left-hand transition B moving to shorter wavelength and the right hand transition C moving to longer wavelengths (see Fig. 3.3). Additionally, the relative intensity of these two transitions varied considerably. As solvent polarity decreased, the longer wavelength transition C became less intense compared to transition B.

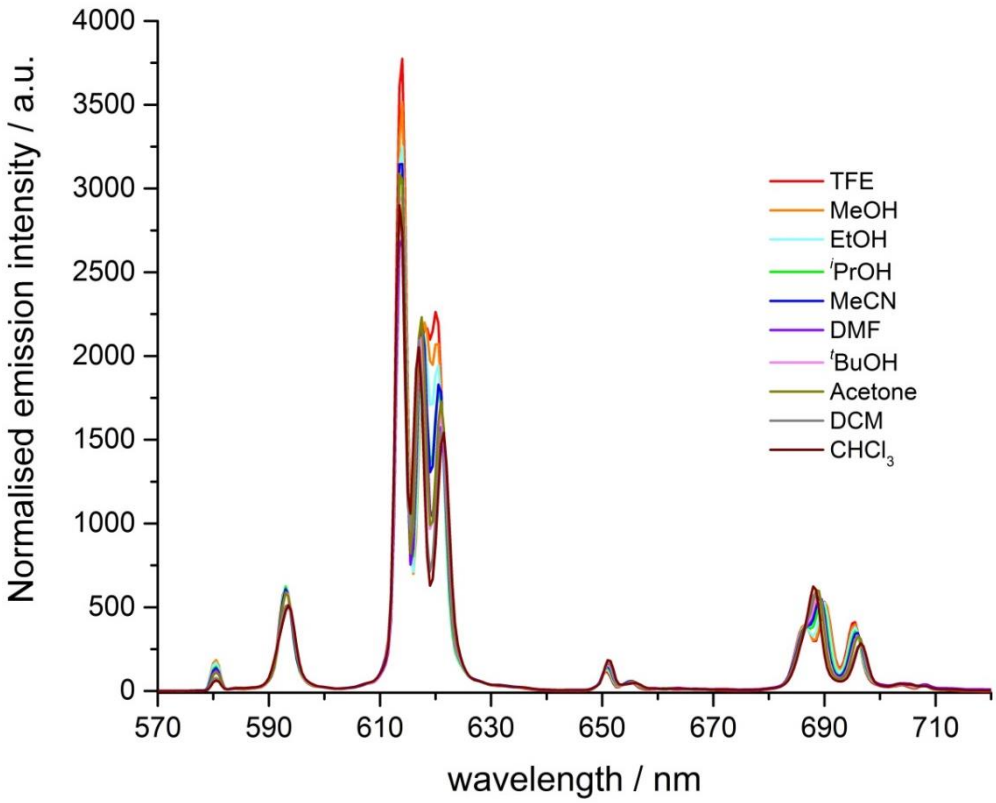

Figure 3.2 The total emission spectra of **[EuL^2]** in various solvents (295 K, excitation at absorption maximum in each solvent). Spectra are normalised to the integrated emission intensity of the Δ*J* = 1 manifold.

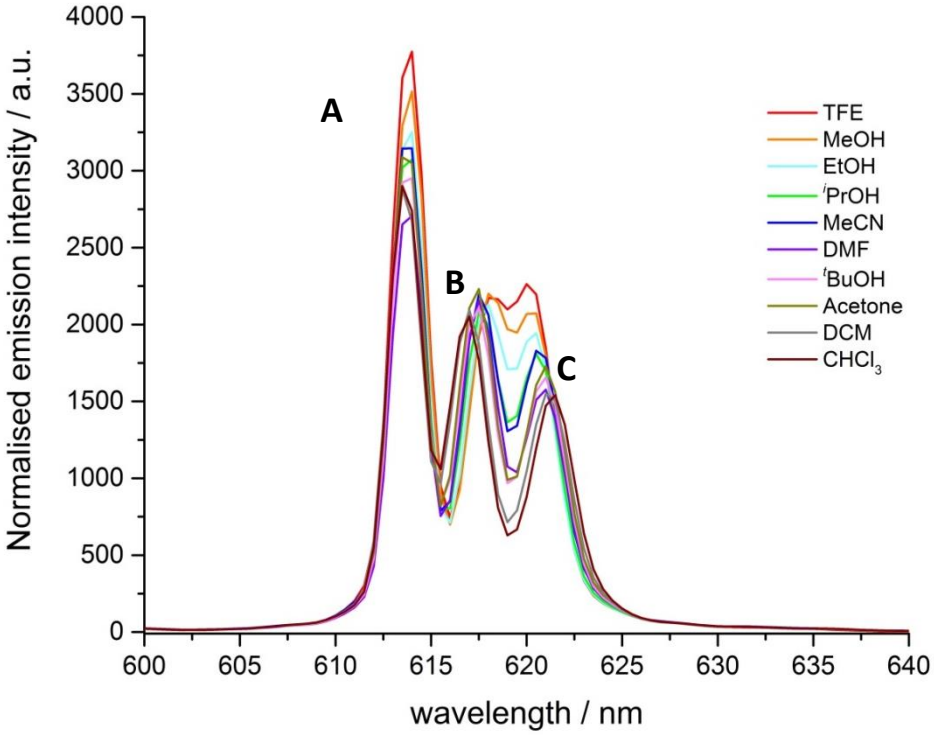

Figure 3.3 Expanded emission spectra of **[EuL^2]** in various solvents in the Δ*J* = 2 manifold. Transitions are labelled as described in the text.

The variation of the intensity ratios between the major transition (A, 614 nm) and transition B (approx. 617 nm), and between transitions B and C (approx. 621 nm), with Reichardt's normalised solvent polarity parameter, showed correlations with solvent polarity in each case (see Fig. 3.4). In each case, the ratios for DMF (E_T^N = 0.404) appeared to be anomalous. Additionally, the ratios in chloroform (E_T^N = 0.259) do not 'fit' the apparent trend. It is possible that these anomalies point towards specific solvation effects in these solvents, rather than their behaviour being governed simply by solvent polarity. However, the overall trends suggest that the energies of transitions B and C are primarily determined by solvent polarity, and that the intensities of transitions A and C are more susceptible to variation in solvent polarity than transition B. The overall integrated emission intensity ratio for the Δ*J* = 2 vs. Δ*J* = 1 manifolds exhibits a modest increase with increasing solvent polarity, consistent with enhanced ligand polarisability in more polar media.

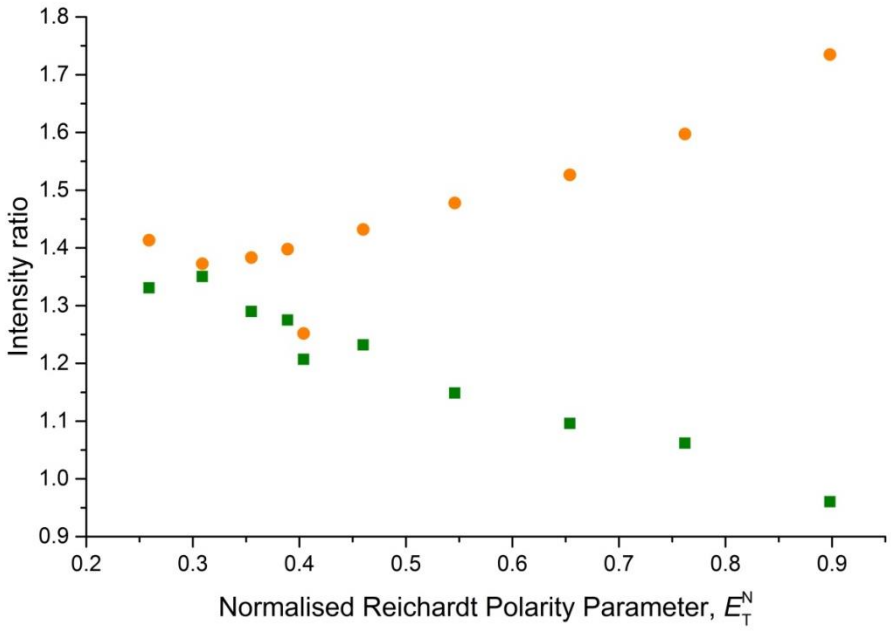

Figure 3.4 Ratios of the intensity of emissive transitions A vs. B (*orange*) and B vs. C (*green*) as a function of solvent polarity.

Similar behaviour was observed in the behaviour of the Δ*J* = 4 manifold (see Fig. 3.5). In this case, the longest wavelength transition, F, exhibits a bathochromic shift as solvent polarity decreases, while transitions D and E appear to coalesce, and increase in intensity. The weak transitions between 702 and 715 nm were not investigated in detail. Whilst the Δ*J* = 4 manifold is not strictly hypersensitive (it

does not meet the selection rule for hypersensitive transitions), the intensities of the transitions are still sensitive to local environment. The significant modulation in spectral form of the ΔJ = 4 manifold is consistent with variations in local polarity causing both intensity changes and changes to the energies of various crystal field states of the $^7F_4$ level. Although it is unlikely that the molecular conformation is modified to any great extent, this behaviour could be tentatively attributed to small changes in metal-ligand bond distances.

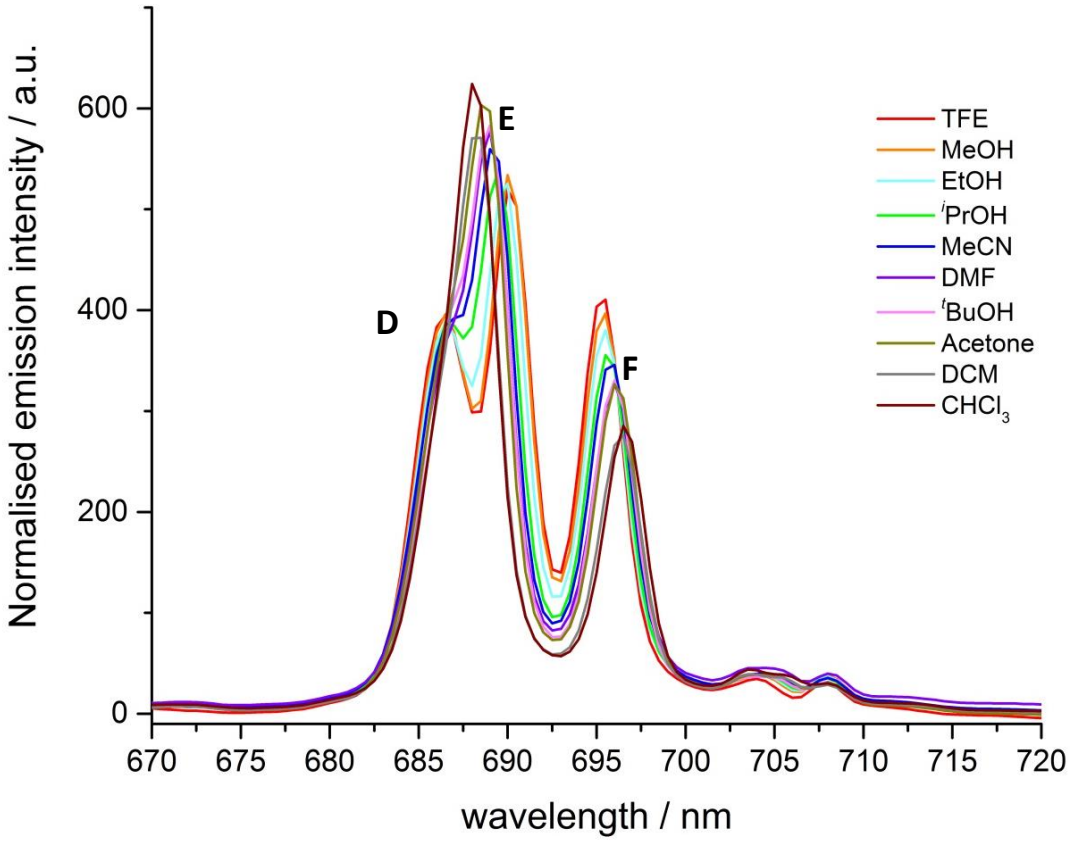

Figure 3.5 Expanded emission spectra of **[EuL^2]** in various solvents in the ΔJ = 4 manifold. Transitions are labelled as described in the text.

The ratio of the intensity of the major transition, E, against the lower energy transition F showed a non-linear decrease as solvent polarity was increased (see Fig. 3.6). Similarly, the intensity of the major transition, E, relative to the intensity of the magnetic dipole allowed transition ΔJ = 1, which is supposedly largely independent of the environment, exhibits the same decrease. Both relationships appear to level off as solvent polarity increases beyond $E_T^N = 0.6$, suggesting that a limit is reached where increasing solvent polarity cannot induce further spectral change. Unfortunately, since the complex is not soluble in water, it was not possible

to obtain further data points in more polar solvents. Common laboratory chemicals with E_T^N values between methanol and water were either solids at room temperature (e.g. phenol) or had boiling points too high to allow recovery of material (e.g. glycerol).

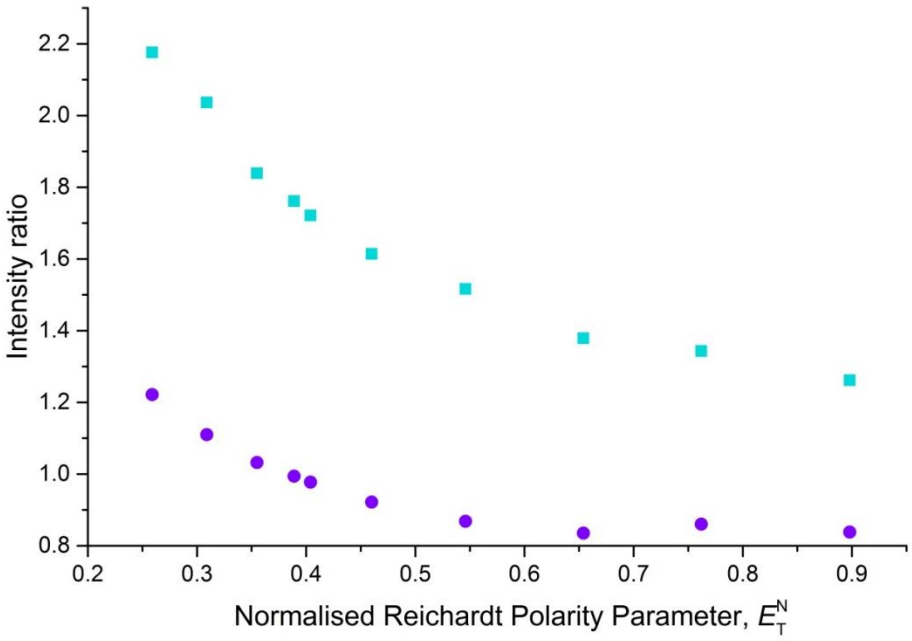

Figure 3.6 Ratios of the intensity of emissive transitions E vs. F (*light blue*) and E vs. Δ*J* = 1 at 593 nm (*purple*) as a function of solvent polarity.

Judd-Ofelt theory is commonly invoked to rationalise the intensity of various transitions in europium(III) emission spectra.[164,165] However, these mathematical models of dipole strength fail to account for the hypersensitive nature of certain Ln(III) transitions.[2] Whilst the observed hypersensitive transitions do obey the selection rules for electric quadrupole transitions, the magnitudes of the hypersensitive transitions far exceed those predicted for quadrupole transitions.[166]

As such, an alternative explanation can be proposed, where the electric quadrupole allowed transition ($^5D_0 \rightarrow {}^7F_2$) gains dipole strength via coupling to a lanthanide quadrupole-induced dipole on the ligand.[167] In systems which are not cylindrically symmetric, it is necessary to include the anisotropy of the ligands in calculated oscillator strengths for hypersensitive transitions.[168] Therefore, the intensity of these hypersensitive transitions is related to the polarisability of the ligand dipole, and is sensitive to the anisotropy of this polarisability. Thus, small variation in

solvation and coupling of solvent dipoles with ligand dipoles may account, in part, for the change in intensity of certain transitions in manifolds that are sensitive to environment.

3.2.2 Solvent effects in the CPL of [EuL^2]

In addition to the modulations of the total emission spectral profile for **[EuL^2]** in different solvents, changes in the spectral form of the CPL emission have also been studied. As discussed previously, the CPL can often provide increased resolution of transitions close in energy, as they may have opposite sign. However, it must be noted that the factors controlling CPL signal intensity are not the same as those regulating the oscillator strength of total emission bands.[143]

The CPL spectrum of *Λ*-**[EuL^2]** was recorded in ten different solvents (Fig. 3.7). Several transitions appear to change sign in different solvents. In particular, the somewhat broad $\Delta J = 1$ manifold appears to resolve into two transitions of opposite sign in TFE (see Fig. 3.8). Had more polar solvents been available, it might be expected that this transition would continue to become more positive with increasing polarity. However, as discussed in Section 3.2.1, spectra in more polar solvents could not easily be obtained. It has already been noted in the methyl phosphinate analogues that transitions of opposite sign were observed in the $\Delta J = 1$ manifold in methanol. It is possible that in more polar solvents, the phenyl phosphinate complexes are either conformationally or electronically more similar to the methyl phosphinate analogues, which could explain the emergence of similar spectral profiles.

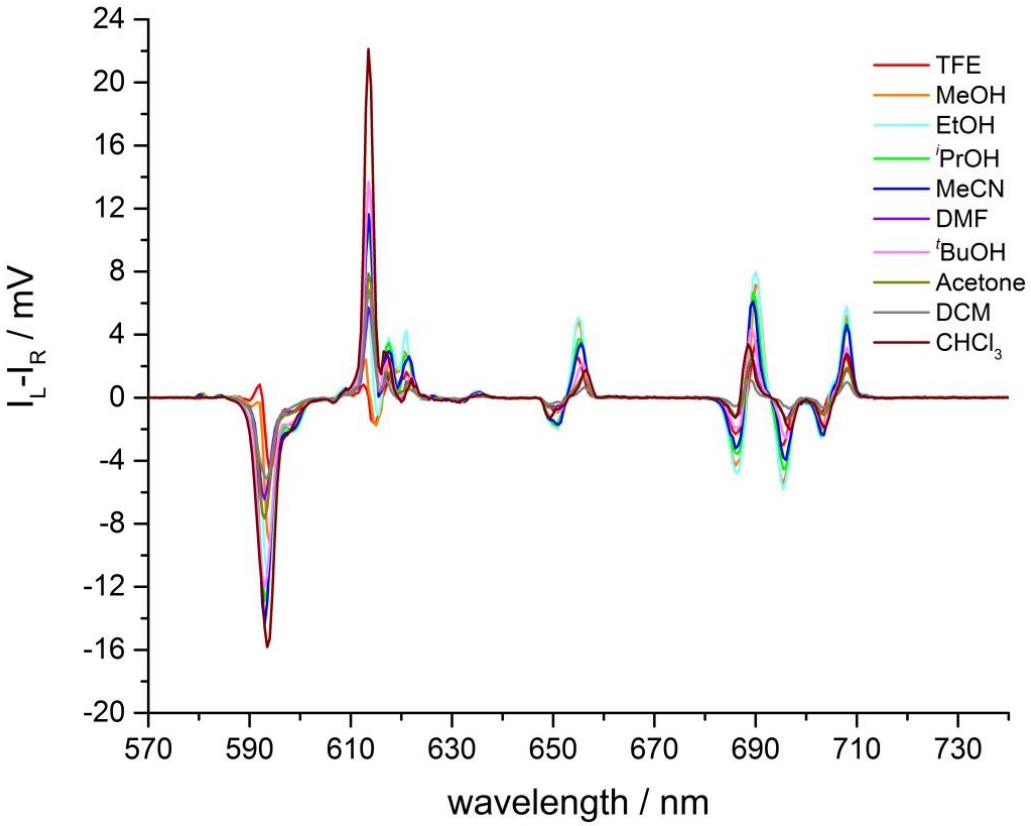

Figure 3.7 Circularly polarised emission spectra of *Λ*-**[EuL^2]** in various solvents (295 K, excitation at absorption maximum in each solvent). Spectra are not normalised.

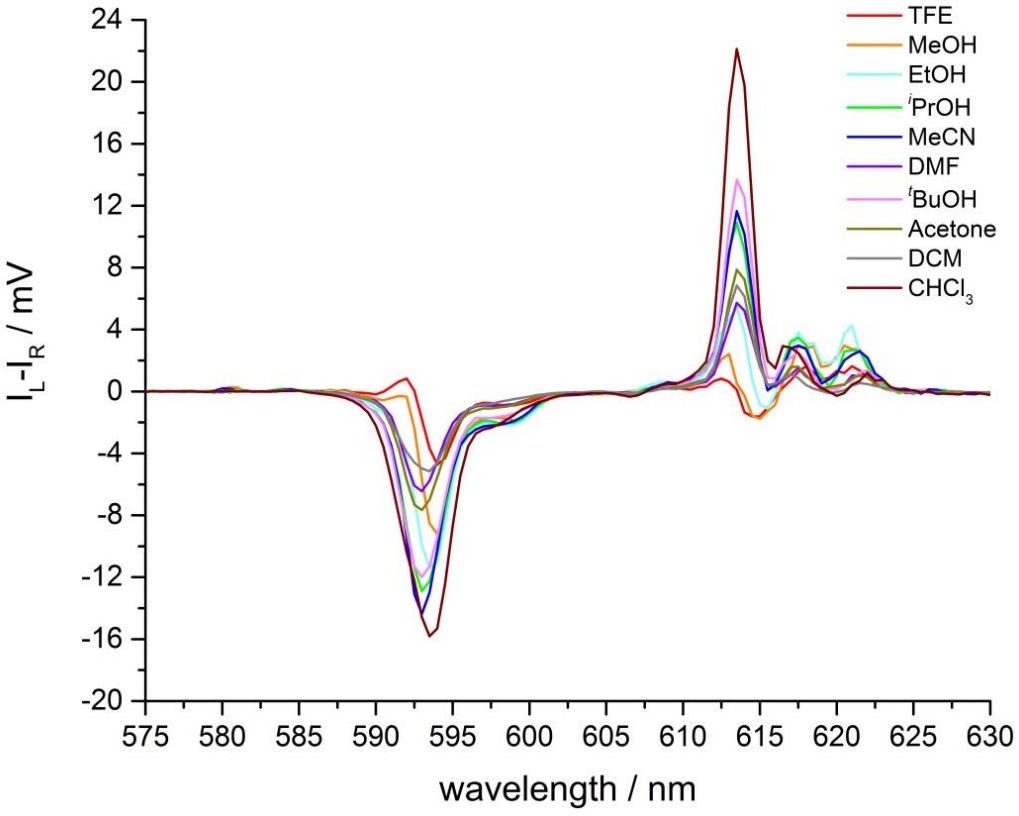

Figure 3.8 Expanded circularly polarised emission spectra of *Λ*-**[EuL^2]** in various solvents in the Δ*J* = 1 and 2 manifolds.

A similar effect can be seen in the Δ*J* = 2 manifold (see Fig. 3.8). As solvent polarity increases, the intensity of the major transition at 613 nm decreases, accompanied by the appearance of a negative CPL transition visible for ethanol, methanol and trifluoroethanol. Such behaviour is in contrast to the changes of the same transition in the total emission spectrum (Fig. 3.3, A), where the total intensity increased as solvent polarity increased. As such, the magnitude of the emission dissymmetry factor, g_{em} of this transition decreases by a factor of 10, on changing from chloroform to TFE, which can be rationalised by considering the factors controlling the magnitude of g_{em} (see Eqn. 3.1).

$$g_{\mathrm{em}} = 4\frac{|\mathbf{m}_{ij}|}{|\boldsymbol{\mu}_{ij}|}\cos\theta_{\boldsymbol{\mu},\mathbf{m}} \qquad \textbf{(3.1)}$$

The oscillator strength of a transition is proportional to the square of the transition dipole moment, meaning an increase in the magnitude of the electric dipole transition moment, $|\boldsymbol{\mu}|$, leads to increased total emission intensity in response to varying solvent polarity. However, the magnitude of g_{em} will reduce. It is unlikely that the magnitude of $|\mathbf{m}|$ is as dependent on solvent polarity and minor changes in θ would not be sufficient to change g_{em} significantly.

Changes can also be observed in the circularly polarised emission of the Δ*J* = 4 manifold (Fig. 3.9). However, in this case, the behaviour in response to changing solvent polarity appears to be reversed, compared to that seen in the Δ*J* = 1 and Δ*J* = 2 manifolds. Here, the CPL intensity decreases as solvent polarity increases. Whilst the two shorter wavelength transitions do not coalesce as they do in the total emission, it is evident that they are closer in energy in non-polar solvents, such as chloroform and dichloromethane, than in polar solvents, such as methanol and ethanol. Interestingly, in the total emission, some transitions within the manifold increased in intensity with changing solvent polarity, while others decreased. The general trend in the CPL spectra is that all components of the manifold decrease in intensity as solvent polarity decreases.

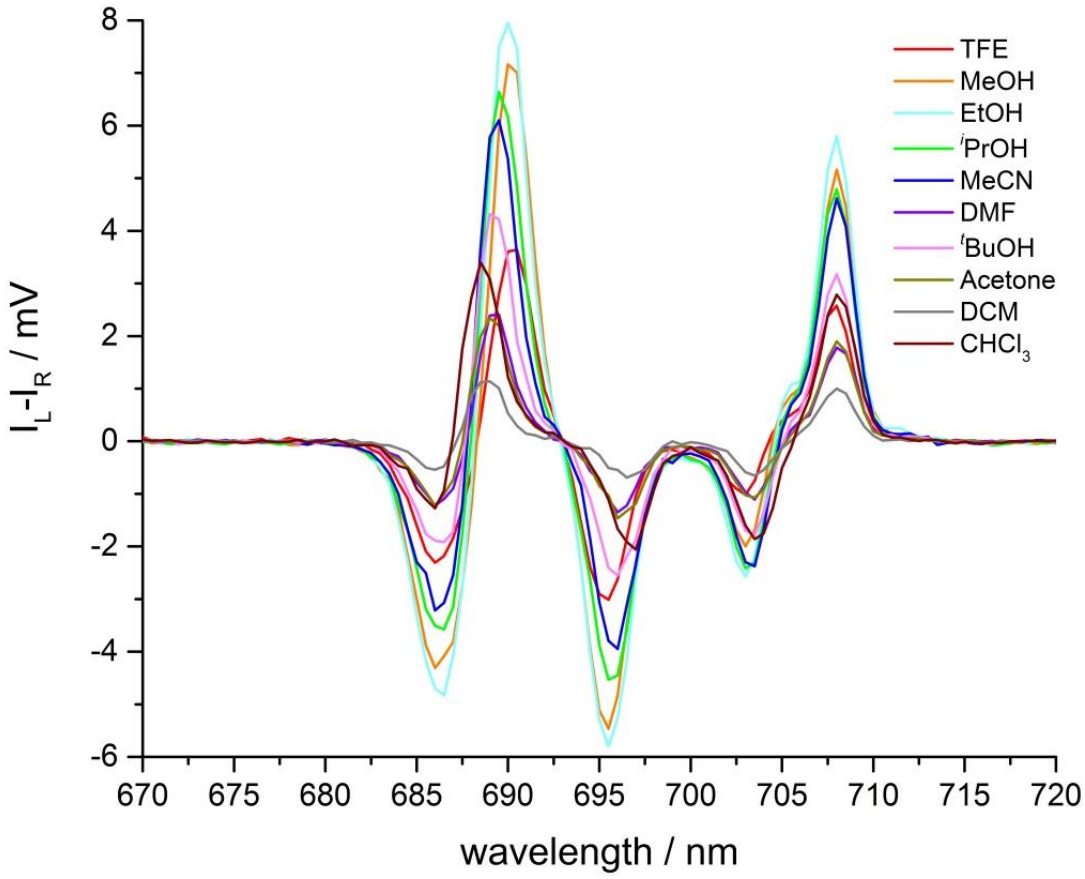

Figure 3.9 Expanded circularly polarised emission spectra of *Λ*-**[EuL^2]** in various solvents in the Δ*J* = 4 manifold.

It is evident from comparing the spectra that the Δ*J* = 4 manifold responds to changes in solvent polarity quite differently from the Δ*J* = 1 and 2 manifolds.

A plot of the intensity ratio of the CPL at 593 nm (Δ*J* = 1) to the CPL at 613 nm (Δ*J* = 2) versus the solvent polarity (Fig. 3.10, green) shows an increase which is initially gradual, but becomes steeper at higher solvent polarity. It is possible that the series of alcohols (isopropanol, ethanol, methanol and trifluoroethanol) which correspond to the solvents with polarities above E_T^N = 0.50, display more specific hydrogen bonding interactions with the complexes than the less polar aprotic solvents. Such a difference may account for the change in gradient of the plot. When comparing the relative intensities of the major transitions of the Δ*J* = 1 or 2 manifolds against the Δ*J* = 4 transitions, it is clear that the ratios both decrease as solvent polarity increases (Fig. 3.10, purple and orange). The biggest change is observed when comparing Δ*J* = 2 and Δ*J* = 4, where in chloroform the Δ*J* = 2 CPL is more than 6 times more intense than Δ*J* = 4. In trifluoroethanol, the ratio is almost reversed with

$\Delta J = 4$ approximately 5 times more intense than $\Delta J = 2$. Plots such as these could be used as calibration curves for use of these complexes as solvent polarity probes.

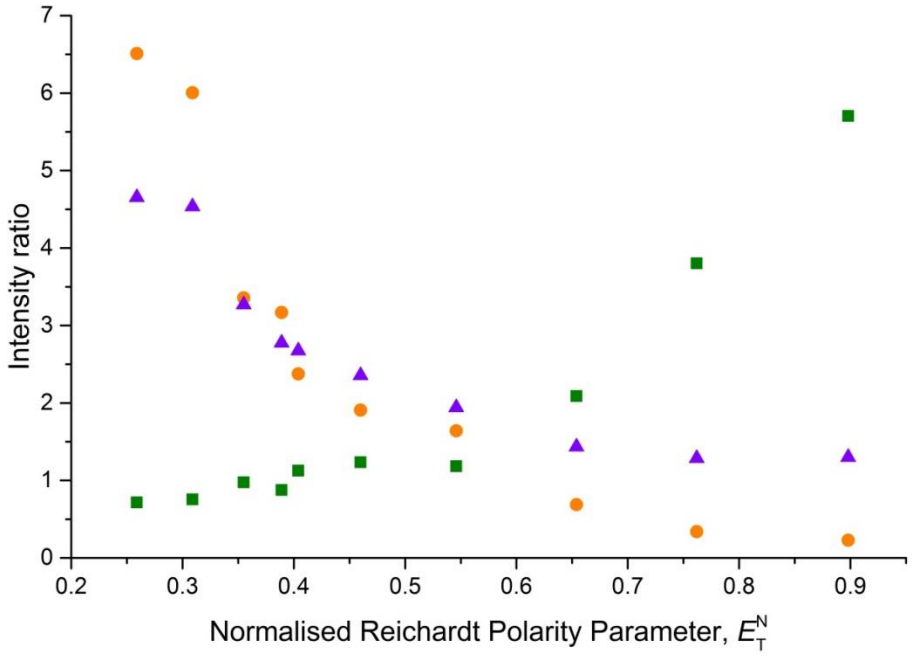

Figure 3.10 Ratios of the intensity of various CPL transitions as a function of solvent polarity: 593 nm / 613 nm (*green*); 593 nm / 690 nm (*purple*); and 613 nm / 690 nm (*orange*).

3.2.3 Chiral additives

Since it was evident that changing solvent polarity affected both the energy of some transitions, and their intensities in both CPL and total emission, it was hypothesised that addition of chiral solvent may induce a modulation in the spectral form of the CPL. Preliminary experiments had shown that addition of very small amounts of achiral polar solvent (e.g. MeOH) to **[EuL^2]** dissolved in less polar solvent (e.g. $CHCl_3$) led to the spectral form resembling those observed in the more polar solvent. Molecular structures of various parent systems obtained by X-ray crystallography have shown that polar protic solvents (MeOH and water) preferentially solvate the complexes via hydrogen bonding to the oxygen atoms in the phosphinate donor groups. Interactions such as these are not possible with aprotic solvents. Therefore, it was envisaged that addition of a chiral protic solvent to a complex dissolved in an aprotic solvent may induce changes in spectral form by differential solvation of the complex.

In order to test such a hypothesis, the complex **[EuL^2]** was dissolved in a non-polar aprotic solvent and a polar protic chiral additive was added in small aliquots. After each addition, CPL and total emission spectra were recorded. Since extinction coefficients had not been obtained in all solvents, samples of complex were prepared in methanol and the absorbance of these solutions was used to calculate the concentration of complex.

Initially, (*R*)-1-phenylethanol was added to solutions of *Δ*- and *Λ*-**[EuL^2]** in THF. 1-Phenylethanol was chosen as it was expected that the significant difference in the size of the substituents around the chiral centre would cause certain diastereoisomeric interactions to be favoured, leading to a change in the CPL form. In the total emission spectrum, no change in form was observed, but a small decrease in intensity was evident across all the bands after addition of 50 equivalents of (*R*)-1-phenylethanol (see Fig. 3.11).

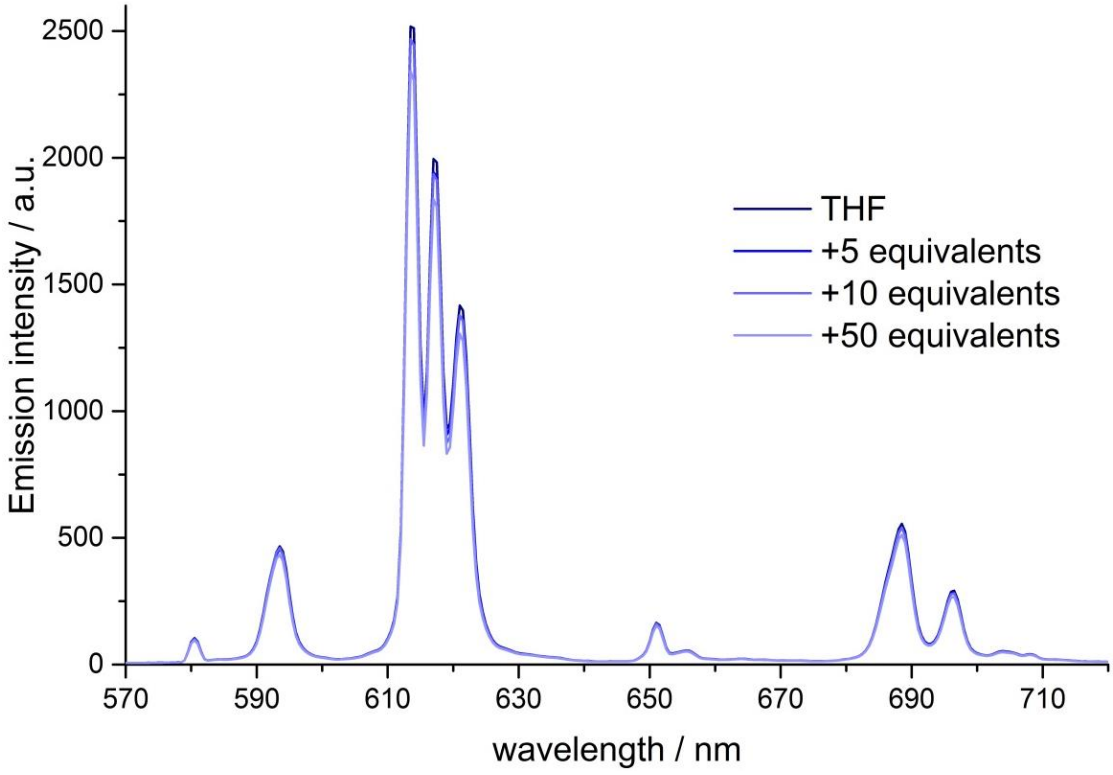

Figure 3.11 Total emission spectra of *Λ*-**[EuL^2]** in THF and with additions of (*R*)-1-phenylethanol (295 K, λ_{exc} 340 nm).

In the CPL spectra of both enantiomers of **[EuL^2]** after addition of (*R*)-1-phenylethanol, no change in spectral form was observed, even after the addition of

50 equivalents (see Fig. 3.12). Again, there was a small reduction in overall intensity, which could be explained by the small increase in volume caused by the addition of the chiral alcohol.

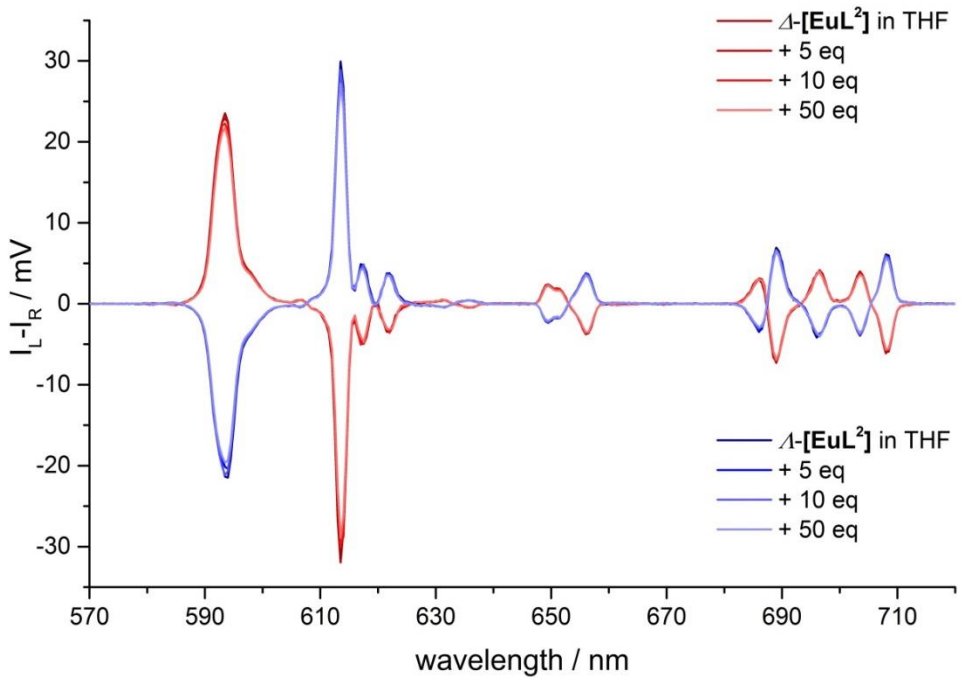

Figure 3.12 CPL spectrum spectra of Δ- and *Λ*-**[EuL²]** in THF and with additions of (*R*)-1-phenylethanol (295 K, λ_{exc} 340 nm).

Since 1-phenylethanol did not stimulate a change in spectral form, it was decided to repeat the experiment with a more polar chiral additive. Again, an additive with large substituents on the chiral carbon was chosen to maximise the potential difference in diastereomeric interactions. As such, aliquots of (*S*)-hexahydromandelic acid were added to solutions of both enantiomers of **[EuL²]**. Again, no change in spectral form in total emission (see Fig. 3.13) or CPL (Fig. 3.14) was observed for either enantiomer on addition of (*S*)-hexahydromandelic acid. A small decrease in intensity was again observed, consistent with the increased sample volume.

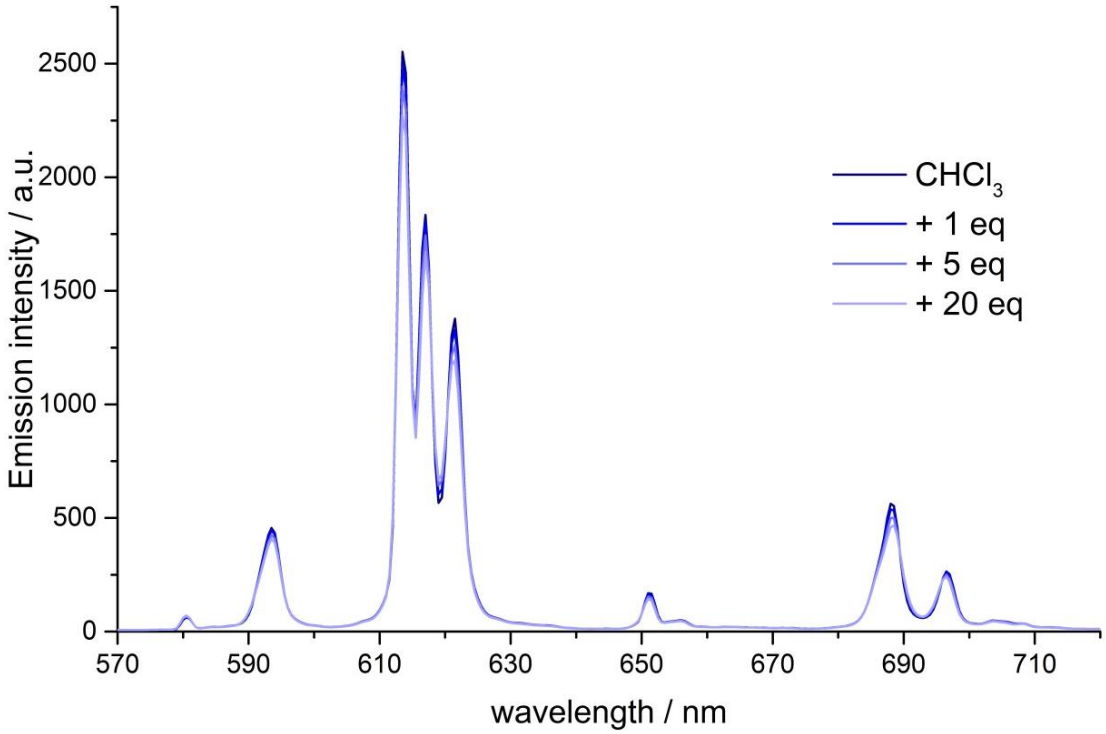

Figure 3.13 Total emission spectra of *Λ*-**[EuL^2]** in $CHCl_3$ and with additions of (*S*)-hexahydromandelic acid (295 K, λ_{exc} 340 nm).

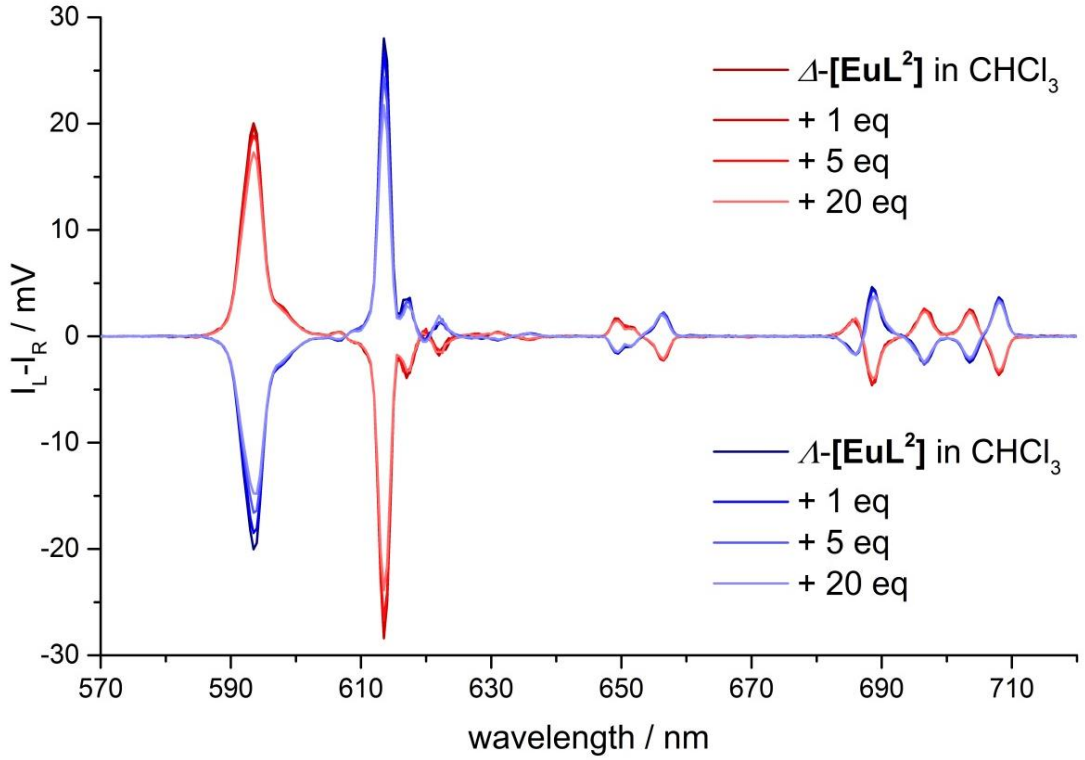

Figure 3.14 CPL spectra of *Δ*- and *Λ*-**[EuL^2]** in $CHCl_3$ and with additions of (*S*)-hexahydromandelic acid (295 K, λ_{exc} 340 nm).

The lack of observable change in total emission or CPL spectral form for **[EuL^2]** on addition of 1-phenylethanol and hexahydromandelic acid, even in large excess, suggests that the complex is sufficiently rigid such that addition of chiral additives does not disrupt the structure of the lowest energy molecular conformation sufficiently to modulate the emission. Similarly, addition of polar protic solvents does not appear to overcome the solvation by the bulk non polar aprotic solvents. It is possible that this is due to the low concentrations of the chiral additives, even at 50 equivalents. If the molecules of chiral additive preferentially interact with each other rather than hydrogen bonding to the complex, then the complex will remain effectively solvated by the bulk solvent, and so no modulation of emission would occur.

3.3 Solvent effects in the total emission and CPL of [EuL^6]

Since the work on **[EuL^2]** had provided clear evidence of solvent dependent emission, it was decided to investigate whether the same behaviour is observed in the parent system **[EuL^6]**. Since this complex does not possess an extended chromophore, it does not sensitise the metal through an internal charge transfer transition, and excitation occurs via the traditional triplet-mediated pathway. If similar behaviour was observed in a system without the extended chromophore, it would suggest that the effect of the solvent polarity can be attributed to perturbations on the donor ability and/or polarisability of the pyridine nitrogen atoms and phosphinate oxygen atoms rather than effects associated with dipolar coupling involving the large extended chromophore dipole.

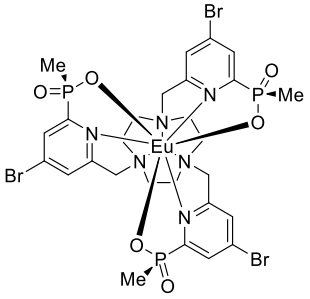

[EuL^6]

3.3.1 Solvent effects in the total emission of [EuL^6]

Unlike **[EuL^2]**, the complex **[EuL^6]** did not display significant variation in the position and intensity of the absorption maximum upon changing solvent, consistent with the absence of an internal charge transfer transition. However, **[EuL^6]** did display solvent dependent emission behaviour (Fig. 3.15). In the total emission spectra, it is immediately evident that variation is observed beyond the electric dipole allowed manifolds, ΔJ = 2 and 4. In the case of **[EuL^6]**, significant differences were observed in ΔJ = 1, 2 and 4.

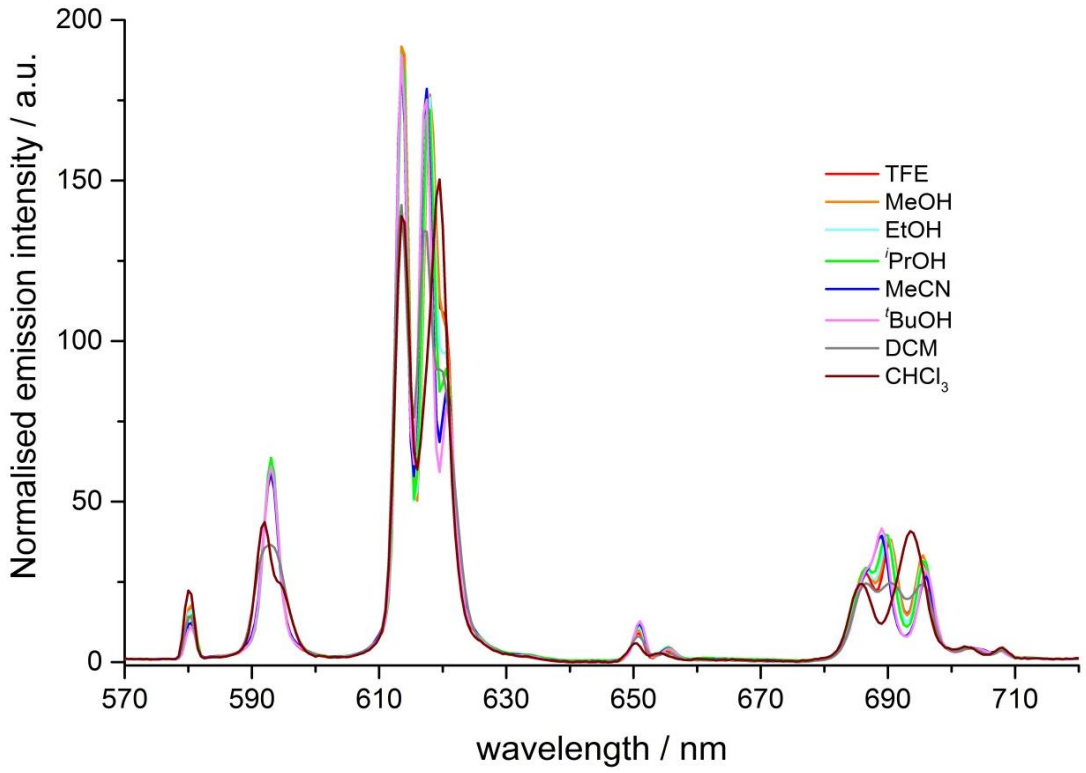

Figure 3.15 The total emission spectra of **[EuL^6]** in various solvents (295 K, λ_{exc} 268 nm). Spectra are normalised to the integrated emission intensity of the ΔJ = 1 manifold.

Inspection of the ΔJ = 1 manifold (585-600 nm) shows a consistent profile for the series of alcohols and acetonitrile, but broadening was evident in dichloromethane, separating into a major and minor peak in chloroform (see Fig. 3.16). The fine structure of the ΔJ = 1 manifold is controlled by the crystal field splitting in the $^7F_1$ level caused by the set of donor atoms in the ligand.[2] As such, the structure of this manifold varies considerably with changing donor atoms, and in systems of different symmetry. Indeed, the number of expected transitions can be predicted from the symmetry of the complex. In C_3 symmetric systems, the ΔJ = 1 manifold

exists as a non-degenerate singlet and a twofold degenerate pair of crystal field states. The order and separation of these levels is dependent on the size of the crystal field parameter (*vide infra* Section 3.4). It is likely that the crystal field parameter is sufficiently small in this complex that multiple bands cannot normally be resolved in this manifold. However, the appearance of the shoulder in the $\Delta J = 1$ manifold of **[EuL^6]** in chloroform suggests that there is a specific interaction present in this solvent that increases the magnitude of the crystal field splitting.

In the $\Delta J = 2$ manifold, dichloromethane and chloroform also exhibit behaviour that cannot be accounted for simply by their solvent polarity. In the alcohol series, as polarity decreases, the longest wavelength transition reduced in intensity and became a more pronounced shoulder on the neighbouring transition. Meanwhile, the intensity of the shortest wavelength transition (at 613 nm) showed very little variation. In contrast, for dichloromethane and chloroform, the transition at 613 nm was significantly weaker and the two transitions at longer wavelength were not resolved, as would be expected if the spectra followed a simple solvent polarity trend (i.e. the spectra for chloroform and dichloromethane might be expected to resemble that of ^{t}BuOH). In fact, in chloroform, the manifold appeared simply as two broad bands of approximately equal intensity.

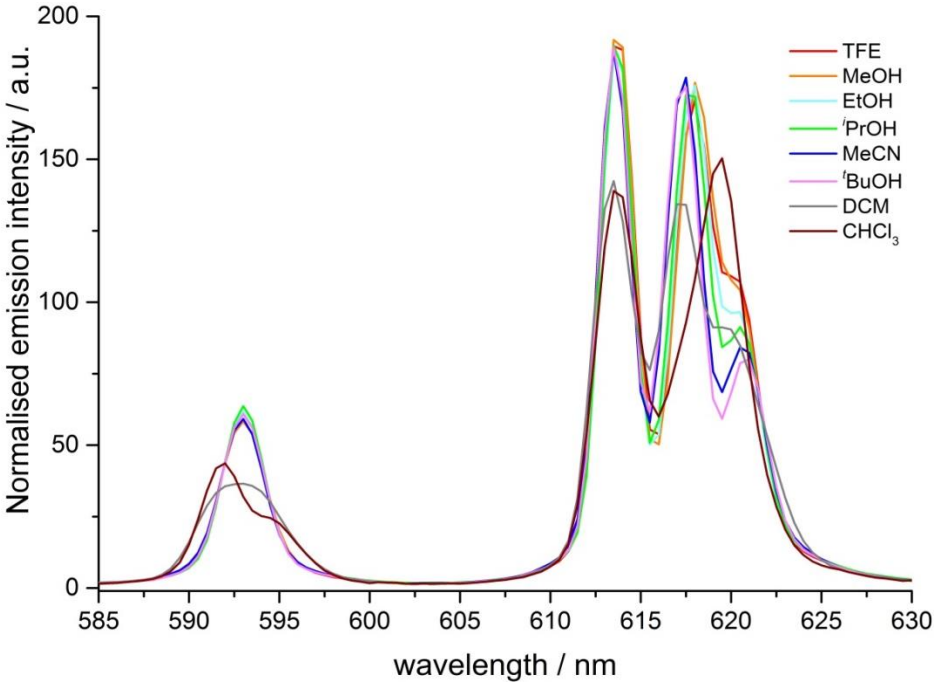

Figure 3.16 Expanded emission spectra of **[EuL^6]** in various solvents in the $\Delta J = 1$ and 2 manifolds.

The Δ*J* = 4 manifold also displays specific solvent effects for dichloromethane and chloroform (see Fig. 3.17). Ignoring these two solvents, the general behaviour is similar to that displayed by **[EuL^2]** (Fig. 3.5), with the longest wavelength transition moving to lower energy with decreasing solvent polarity and the lower wavelength and central transitions coalescing. However, anomalous behaviour is clearly exhibited in chloroform and dichloromethane, which does not fit with the general trend shown in other solvents.

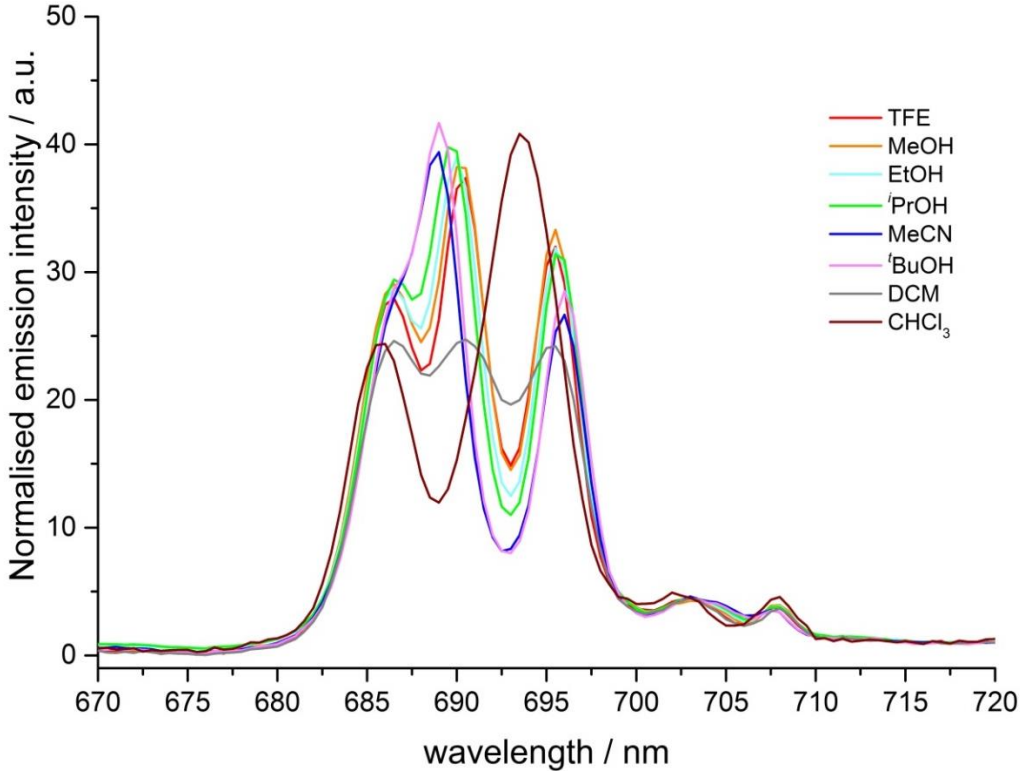

Figure 3.17 Expanded emission spectra of **[EuL^6]** in various solvents in the Δ*J* = 4 manifold.

3.3.2 Solvent effects in the CPL of [EuL^6]

Since **[EuL^6]** is inherently less bright than **[EuL^2]**, its CPL spectra appear more noisy. However, they are sufficiently intense to observe some general trends (see Fig. 3.18.). Of particular interest in the CPL spectra is the behaviour of the Δ*J* = 1 and 2 manifolds, which show significant changes as solvent is varied.

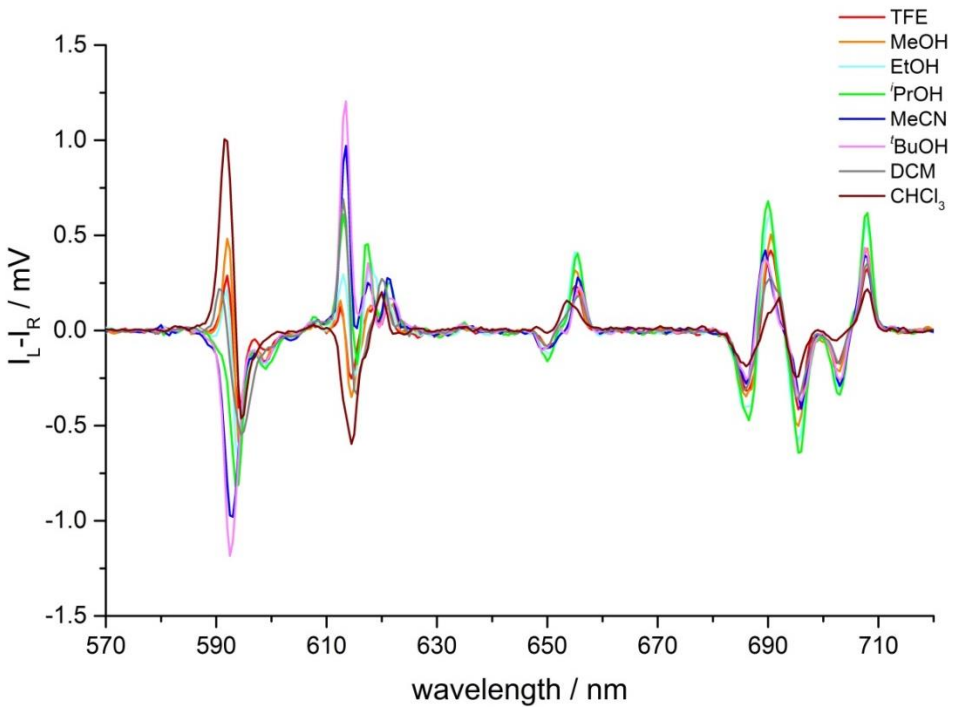

Figure 3.18 Circularly polarised emission spectra of *Λ*-**[EuL^6]** in various solvents (295 K, λ_{exc} 268 nm). Spectra are not normalised.

In the Δ*J* = 1 manifold of *Λ*-**[EuL^6]** in polar solvents, the CPL spectrum showed a transition of positive sign at 592 nm, followed by a negative transition at 594 nm (see Fig. 3.19). This pattern is consistent with the behaviour of other methyl phosphinate complexes recorded in polar solvents such as water and methanol.[39,133,134] As solvent polarity is decreased, the positive transition appears to invert sign and coalesce with the negative transition, resulting in a single negative transition centred at 593 nm in ^{t}BuOH. In ^{t}BuOH, the pattern in the Δ*J* = 1 manifold more closely resembles the profile of the same transition in the phenyl phosphinate series of complexes (see Fig. 3.8). However, in dichloromethane and to a greater extent chloroform, a positive and negative transition are observed, which does not fit the overall solvent polarity trend. Additionally, the transitions move slightly further apart, which may explain the appearance of the shoulder in the same manifold in the total emission spectrum, i.e. the transitions are sufficiently different in energy for two transitions to be observed in total emission.

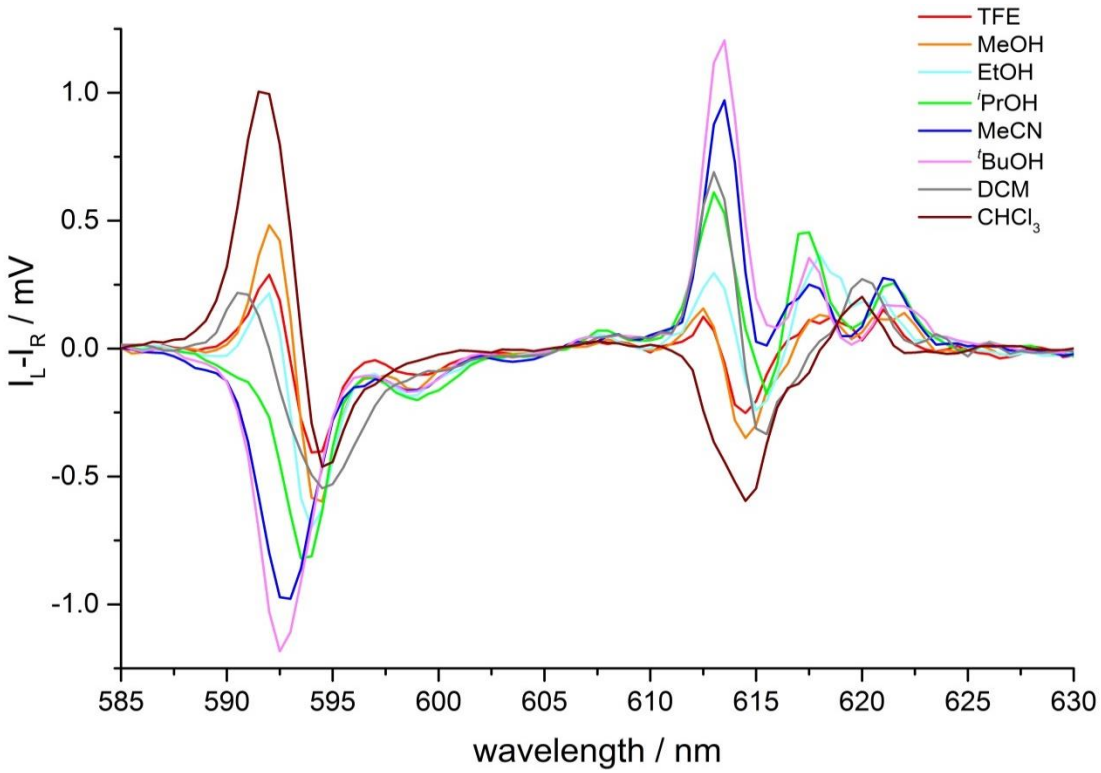

Figure 3.19 Expanded circularly polarised emission spectra of *Λ*-**[EuL^6]** in various solvents in the Δ*J* = 1 and 2 manifolds.

The form of the Δ*J* = 2 manifold of the CPL spectrum is also very different in chloroform and dichloromethane. There is a clear trend following solvent polarity, with the exception of dichloromethane and chloroform (Fig. 3.19). In polar solvents there is a positive transition followed by a negative transition around 614 nm. As solvent polarity is decreased, the negative transition becomes weaker and the positive transition increases in intensity. However, in dichloromethane, the profile resembles that of isopropanol in this region, and in chloroform, there is no positive transition, just a single broad negative transition at 614.5 nm. The two longer wavelength transitions also appear as a single transition in the chlorinated solvents.

In contrast to the behaviour of **[EuL^2]**, the changes of the Δ*J* = 4 manifold for **[EuL^6]** were less clear (see Fig. 3.20). No coalescence of peaks in the CPL spectra was observed in total emission, although the transition around 690 nm does appear to move to slightly longer wavelength in chloroform. Neither is any significant change observed in the relative intensities of transitions within the manifold, as the solvent is varied.

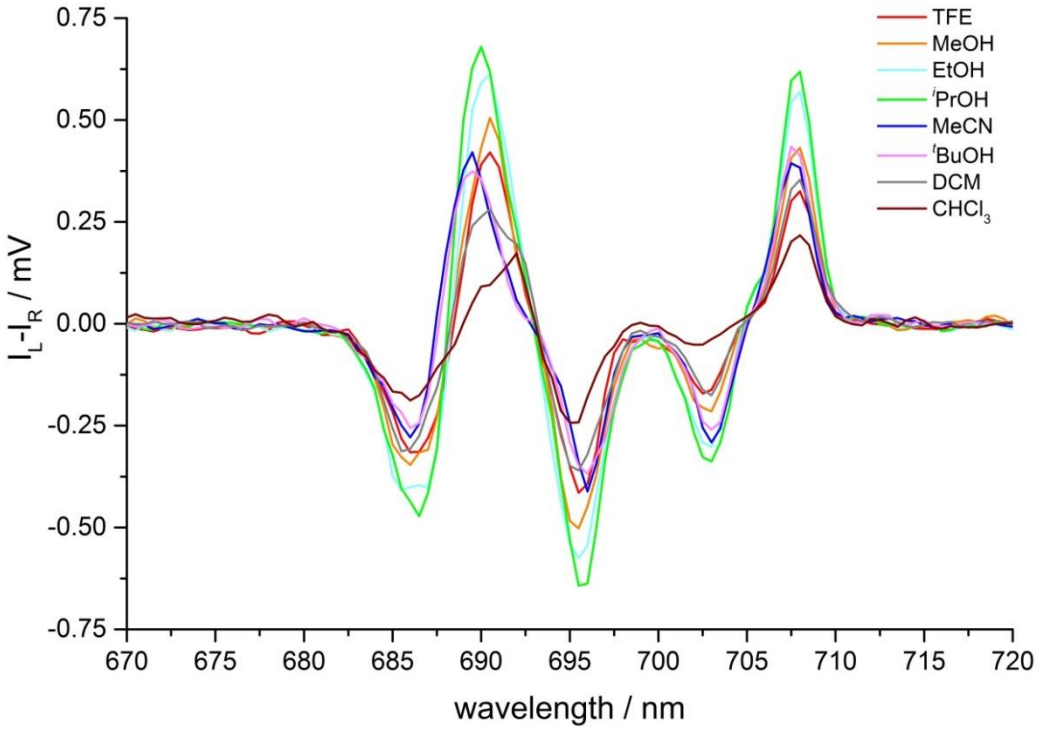

Figure 3.20 Expanded circularly polarised emission spectra of *Λ*-**[EuL^6]** in various solvents in the Δ*J* = 4 manifold.

3.3.3 Specific solvent effect of chlorinated solvents

The results above show a clear indication that there is a specific solvent interaction occurring between **[EuL^6]** and chloroform, and to a lesser extent, dichloromethane, which cannot be attributed simply to modulation of solvent polarity. Chloroform can be considered a C-H acid, due to the electron withdrawing nature of the three chlorine atoms. As such it is capable of interacting with lone pairs of electrons on solutes. In the structure of **[EuL^6]** obtained by X-ray crystallography,[39] water molecules are observed to hydrogen bond to the lone pairs on the phosphinate oxygen atoms (see Fig. 3.21). This observation is consistent with other crystal structures of complexes with phosphinate donors, where polar protic solvents are seen to interact in the same manner.[30,133] However, the appearance of the emission spectrum of **[EuL^6]** in chloroform is very different to those obtained in polar protic solvents, suggesting that chloroform is not behaving as a hydrogen bond donor in an interaction with the ligand phosphinate oxygen.

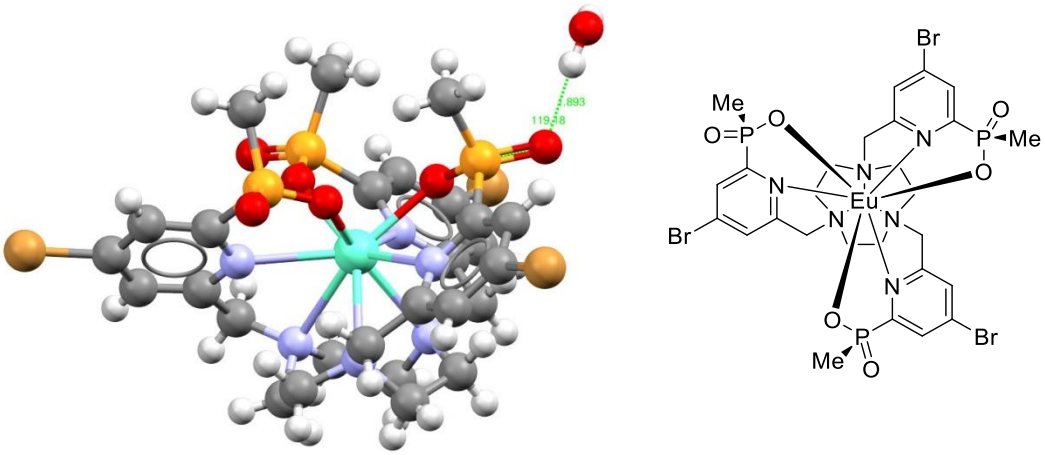

Figure 3.21 X-ray crystal structure of **[EuL^6]** showing a water molecule hydrogen bonded to the phosphinate oxygen atom; r = 1.893 Å, θ = 119.18°.[39] Atom colours are as follows: grey, carbon; white, hydrogen; blue, nitrogen; red, oxygen; orange, phosphorus; brown, bromine; turquoise, europium. CCDC identifier: 948247/GINCEN.

Alternatively, it is possible that there is a C-H···Br interaction with the bromine atom in the 4-position of the pyridine ring. There are several literature examples of chloroform interactions with aromatic bromides, including some in metal complexes. A selection obtained by screening the CCDC database is shown in Fig. 3.22. Only short contact interactions with chloroform are shown. Some of the structures crystallise with additional chloroform molecules in the unit cell, but they do not exhibit short contact interactions.

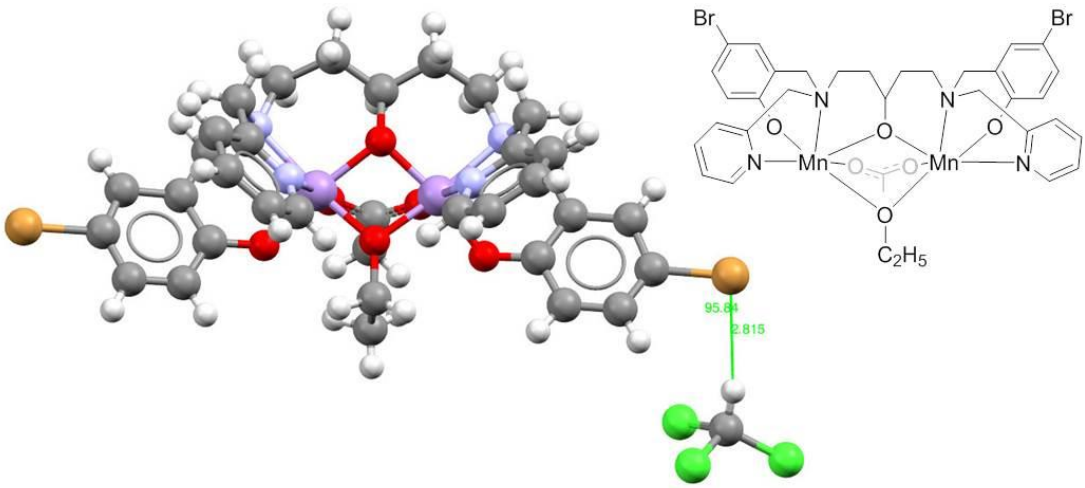

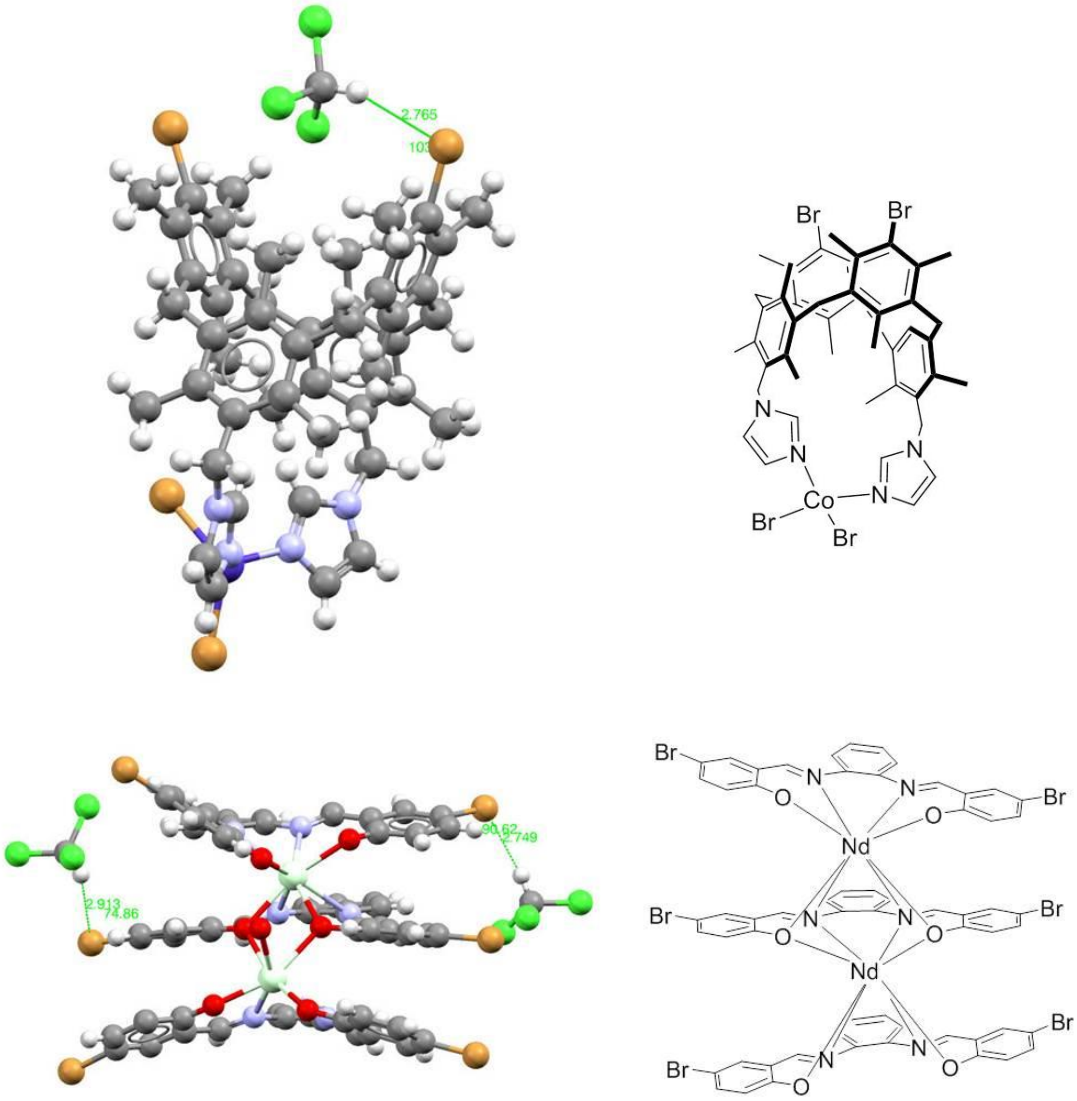

Figure 3.22 Examples from the Crystal Structure Database of Cl_3C-H···Br interactions. *Top*: a bimetallic manganese chelate,[169] r = 2.815 Å, θ = 95.84°, CCDC identifier: 729555/GUXXON, $[BPh_4]^-$ counter-ion omitted for clarity. *Middle*: a 1,3-alternate calixarene capped with a cobalt ion,[170] r = 2.765 Å, θ = 103.32°, CCDC identifier: 744813/PURVOO. *Bottom*: A triple decker dinuclear neodymium sandwich complex,[171] r_1 = 2.749 Å, θ_1 = 90.62°, r_2 = 2.913 Å, θ_2 = 74.86°, CCDC identifier: 91969/VILWIY. Atom colours: grey, carbon; white, hydrogen; blue, nitrogen; red, oxygen; brown, bromine; green, chlorine; purple, manganese; dark blue, cobalt; pale green, neodymium.

In each case, the Cl_3C-H···Br distance is less than the sum of the van der Waals radii of the atoms, i.e. a 'short contact'. Additionally, the interactions are all 'side-on', i.e. the C-H bond points towards the equator of the bromine atoms, rather than along the C-Br bond. Such an interaction is to be expected, as electron deficient aromatic bromides do display anisotropic electron density, with an electron rich equator and an electron deficient pole (see Fig. 3.23).[172] In **[EuL^6]**, the pyridine ring is electron deficient due to the electron withdrawing nature of the central metal ion.

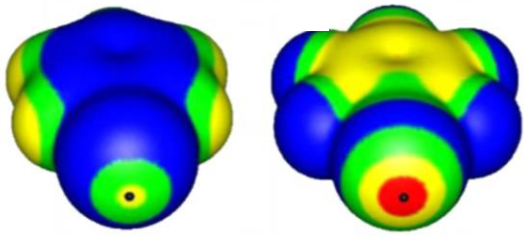

Figure 3.23 Computed electrostatic potentials of bromobenzene (*left*) and pentafluorobromobenzene (*right*), showing the developing electron deficient pole and electron rich equator as electron withdrawing groups are added. Colour ranges in kcal mol^{-1} are: red, greater than 20; yellow, between 20 and 10; green, between 10 and 0; blue, negative. Adapted from Ref. [172] with permission of Springer. Copyright Springer-Verlag 2011.

It ought to be noted that this interaction is distinct from halogen bonding, where a halogen bond acceptor donates electron density into the electron deficient hole, along the axis of the C-X bond. Here, an electron deficient hydrogen atom is receiving electron density *from* the halogen.[173]

If such an interaction is occurring between chloroform and **[EuL^6]**, it would be expected that varying the nature of the halogenated solvent might provide more information regarding the nature of the contact. The emission from **[EuL^6]** in dichloromethane has already suggested that there is a specific solvation effect, and that it is weaker than in chloroform. Therefore, attempts were made to record total emission and CPL spectra of **[EuL^6]** in carbon tetrachloride. If a C-H acid interaction was occurring in chloroform and dichloromethane, this anomalous behaviour would not be expected to occur in carbon tetrachloride as there is no hydrogen atom. Unfortunately, **[EuL^6]** was not sufficiently soluble in carbon tetrachloride for good spectra to be obtained. Similar attempts were made in dibromomethane and bromoform which would be expected to produce weaker C-H acid interactions than chloroform and dichloromethane, respectively, but the complex was not soluble in these solvents either. As such, it has not been possible to confirm a specific C-H acid interaction with **[EuL^6]** in chlorinated solvents. Very recent work in the related system **[EuL^{15}]** has also indicated that specific solvent interactions occur with chlorinated solvents.[148] In this example, the complex contained two extended chromophore arms and one 4-hydroxypyridine arm. The unusual emission

behaviour was attributed to chloroform acting as a C-H hydrogen bond donor to the oxygen lone pair of the 4-hydroxypyridine moiety.

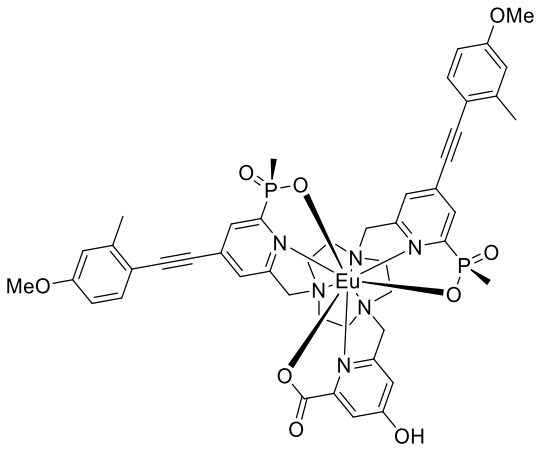

[Eu.L^{15}]

Another recent example of solvent dependent CPL emission involved mixing achiral Eu(hfac)$_3$ with the enantiomers of the planar chiral paracyclophane Phanephos, which is used as a chiral ligand in catalysis.[174] The resulting complexes exhibited CPL emission, in which some transitions in the ΔJ = 1 and 2 manifolds inverted sign on changing the solvent from acetone to chloroform. However, there appears to be some variation in complex speciation in the two solvents, so it is difficult to determine to what extent the change in solvent affects the emission, or whether it is due to a change in molecular structure. Additionally, no further solvents were investigated, so it is impossible to ascertain whether any real trend was present.

Whilst the observations described above are not conclusive evidence of a C-H···Br interaction between chloroform and **[EuL^6]**, the unusual emission behaviour does point towards a specific interaction which differs from that observed in non-chlorinated solvent. There is a precedent in the literature for such interactions, although only a few have been observed in the solid state in metal coordinated aromatic bromides. However, since these are X-ray crystal structure records, it is very likely that these interactions occur in systems which do not crystallise from chloroform.

3.4 A combined emission and NMR study into solvent effects in the [LnL^7] series

In parallel to the investigations into solvent dependent emission described above, an in-depth study of the unusual paramagnetic NMR shift behaviour of several series of lanthanide complexes has been carried out (Dr. Kevin Mason, Durham). Of particular interest has been the unexpected behaviour of the chemical shifts of the pyridine resonances in the **[LnL^7]** series of complexes.[175]

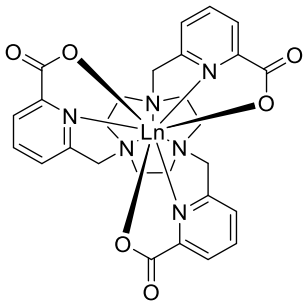

[LnL^7]

The chemical shift behaviour in paramagnetic lanthanide complexes has, for many years, been interpreted using Bleaney's theory of magnetic anisotropy.[176,177] Briefly, the observed chemical shift of a proton resonance is the sum of the diamagnetic shift and the paramagnetic shift. The paramagnetic contribution can be further split into the Fermi contact shift (a very short range, through bond transfer of spin polarisation) and the pseudocontact shift (a through space dipolar effect caused by the magnetic anisotropy of unpaired electrons). Bleaney's theory states that for nuclei where the Fermi contact shift is negligible (usually considered for nuclei more than 4 bonds away from the paramagnetic centre), the paramagnetic chemical shift is dominated by the pseudocontact shift, which can simply be related to the complex geometry, the crystal field splitting, and a term relating to the nature of the lanthanide ion. In the case of **[LnL^7]**, it has been shown that the contact shift is negligible for the pyridine proton resonances.[178] For axially symmetric complexes such as **[LnL^7]**, the pseudocontact shift, δ_{pc}, can be approximated by Eqn. 3.2.

$$\delta_{pc} = -\frac{C_J {\mu_B}^2}{60(kT)^2}\left[\frac{(3\cos^2\theta - 1)}{r^3} B_0^2\right] \quad \textbf{(3.2)}$$

where C_J is Bleaney's constant, μ_B is the Bohr magneton, k is the Boltzmann constant, T is the temperature, r and θ are polar coordinates of the nucleus with respect to the principal axis of the magnetic susceptibility tensor χ, and B_0^2 is the second rank axial crystal field parameter.[**] In turn, Bleaney's constant can be expressed as a function of the total angular momentum quantum number, J, the Landé factor, g_J, and a numerical coefficient $\langle J||k||J\rangle$ which is specific to a particular f^n configuration.

$$C_J = g^2 J(J+1)(2J-1)(2J+3)\langle J||k||J\rangle \quad \textbf{(3.3)}$$

As Bleaney's constant is dependent only on the total angular momentum and the Landé factor, the electronic configuration determines Bleaney's constant for a given lanthanide ion.

There are two critical assumptions made in this theory. The first is that the total crystal field splitting is much less than kT (205 cm^{-1} at 298 K), and the second is that J is a good quantum number. The crystal field splitting in **[LnL^7]** is small, so the first assumption is expected to hold in this example.

As a result of this theory, in a series of lanthanide complexes of the same ligand, assuming that the crystal field and the complex geometry are constant across the series, there should be a linear relationship between the pseudocontact shift for a proton resonance and Bleaney's constant for a given lanthanide ion. In recent work on **[LnL^7]** (and other complexes) the experimental data do not support a linear relationship with Bleaney's constants.[178,179] Indeed, in some examples, even the ordering of the pseudocontact shift contributions cannot be predicted.

[**] There are various formalisms used to describe crystal field. In this thesis, spherical tensor formalism is used, in contrast to the Stevens' operator formalism originally used by Bleaney, and used for calculations in Ref. [175]. Conversion between the systems can be achieved using the following relationship taken from Table 6 in Ref. [142]: $2B_2^0[\text{Stevens}'\,\text{operator}] = B_0^2[\text{Spherical tensors}]$.

In the case of **[LnL^7]** (where Ln = Eu, Tb, Dy, Ho, Er, Tm and Yb), the magnitude and order of the pseudocontact shifts of the three pyridyl proton resonances do not correlate with Bleaney's constant (see Fig. 3.24). Assuming a constant crystal field across the series, the expected order is Dy < Tb < Ho < Eu < Yb < Er < Tm, whist the experimentally observed pseudocontact shifts follow the order Tb < Ho < Eu < Er < Yb < Dy < Tm. Of particular note here, is that **[DyL^1]** exhibits pseudocontact shifts of positive sign, despite having the most negative Bleaney constant.[175]

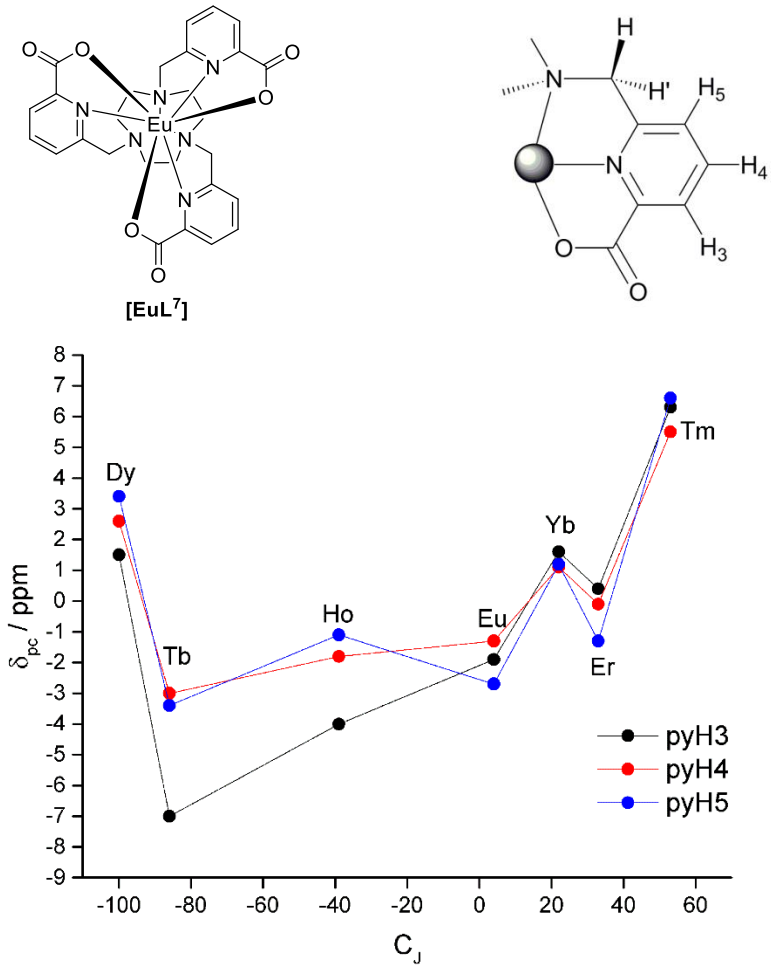

Figure 3.24 *Top*: structure of **[LnL^7]** and assignment of the three pyridyl (py) H atoms. *Bottom*: pseudo-contact shift (δ_p) as a function of the Bleaney constant, C_J for the three pyridyl H atoms (pyH3-5) for **[LnL^7]** (in D_2O, 298 K). Reprinted with permission from Ref. [175]. Copyright (2017) American Chemical Society.

Additionally, a significant solvent dependence was observed on changing between D_2O, MeOD and d_6-DMSO, with the three pyridyl proton resonances swapping order with changing solvent for some metals (see Fig. 3.25). It is important to note that this solvent dependence cannot be attributed simply to the diamagnetic shifts

varying with solvent, as the solvent dependence of the chemical shifts of the diamagnetic complex **[YL^7]** is negligible (<0.2 ppm variation). Indeed, in some examples a change in sign is observed, which cannot be accounted for by changes in diamagnetic shift.

In order to rationalise these observations computational methods have been developed by collaborators (Prof. Eric J. L. McInnes and Dr. Nicholas F. Chilton, Manchester; Dr. Ilya Kuprov, Southampton).[175] Whilst a detailed description of the computations will not be given here, a summary of the methods and results will be presented in order to explain the unusual NMR and emission behaviour of the **[LnL^7]** series.

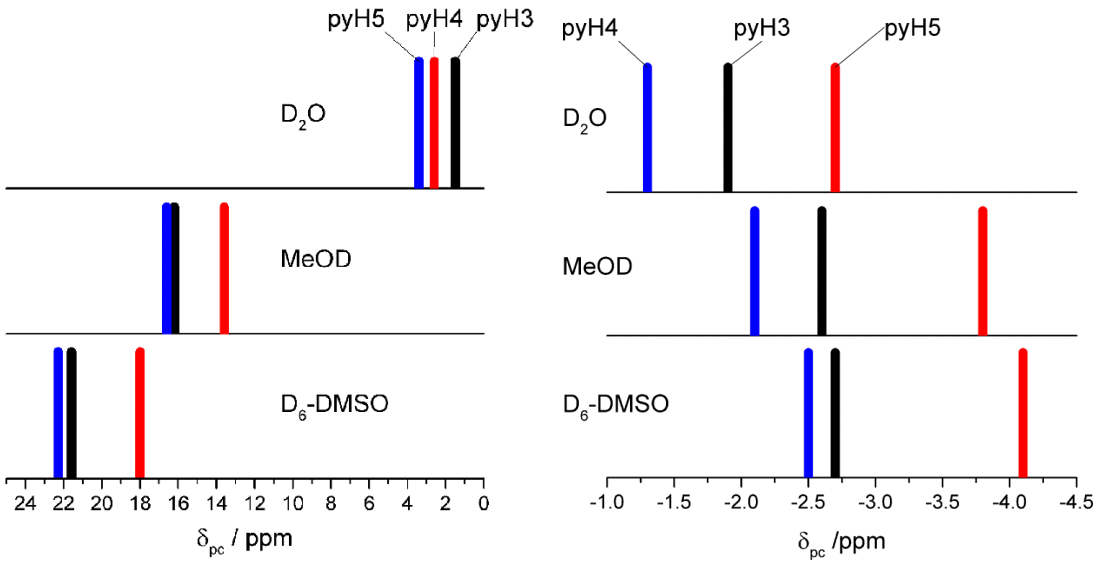

Figure 3.25 Solvent dependence of the pseudocontact shift, δ_{pc} of pyH3-5 for **[DyL^7]** (*left*) and **[EuL^7]** (*right*) in D_2O, MeOD, and d_6-DMSO (solution at 298 K). Reprinted with permission from Ref. [175]. Copyright (2017) American Chemical Society.

Various attempts to calculate pseudocontact shifts using existing computational models could not successfully predict the pseudocontact shifts in **[DyL^1]**. In fact, the predictions from the different methods varied by up to 40 ppm and were of various signs. Comparisons of the computed optimised structures showed that the various methods predicted identical macrocycle structures and very minor differences in the pyridine orientations. Since the pseudocontact shift is dependent on both a structural component and on the magnetic anisotropy, this raises an important point. Since the structural variation in the calculated structures was minimal (<10

%), the large variation in the calculated pseudocontact shifts must be attributed to the magnetic anisotropy term. Therefore, seemingly trivial structural change must cause large changes in the magnetic anisotropy, which in turn result in unexpected experimental pseudocontact shifts.

The tricapped trigonal prismatic donor atom set in the **[LnL^7]** series comprises three axial nitrogen atoms (from the 9-N_3 macrocycle), three equatorial nitrogen atoms (in the pyridine rings), and three axial oxygen atoms (from the carboxylate groups) (see Fig. 3.26). Treating the donor atoms as point charges, crystal field theory predicts that a donor atom switches from being axial to equatorial at an angle of approximately 55° (or 125°) from the C_3 axis.[180] As a donor atom switches from being axial to equatorial (or *vice versa*), it can be expected that the magnetic anisotropy will be affected. In **[LnL^7]** both sets of nitrogen donors sit far enough away from the so-called 'magic angle' of 55°, such that small variations in their position do not affect the magnetic susceptibility anisotropy significantly. However, the three oxygen atoms sit sufficiently close to the magic angle that small variations in their position lead to significant variation in the calculated magnetic anisotropy. Indeed, a variation of just 2° in the angle of the oxygen donors is sufficient to change the sign of the magnetic anisotropy.[175] DFT calculations show that the energy required for a 2° change in polar angle of the oxygen atoms is within *kT* at 298 K.

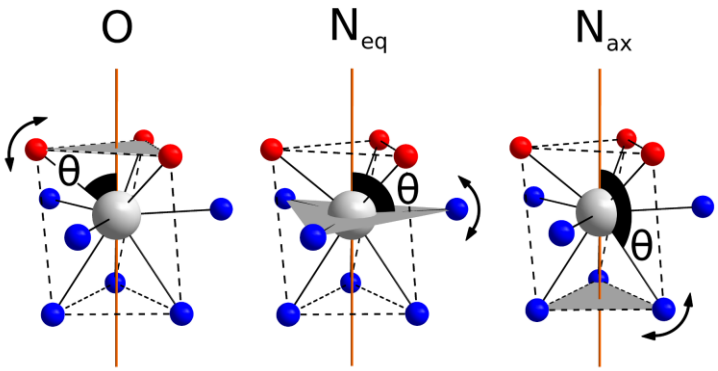

Figure 3.26 *Top:* schematic of the variation of polar angles (θ) for O, N_{eq}, and N_{ax} donor atoms in **[DyL^7]**. The orange line represents the C_3 symmetry axis. Reprinted with permission from Ref. [175]. Copyright (2017) American Chemical Society.

In the Russell-Saunders coupling scheme, Dy(III) has a $^6H_{15/2}$ ground state comprising sixteen m_J levels which exist as eight Kramers doublets (the Dy(III) ground state has non-integer spin). In the optimised geometry, the two lowest-lying Kramers doublets are separated by only 11 cm^{-1} in energy. Importantly, the lowest energy doublet has 'easy axis' magnetic anisotropy while the first excited doublet is 'easy plane', and a change of only 1° in the angle of the three oxygen donor atoms can swap the order of these doublets (see Fig. 3.27).[175] The implication here is that very small variations in molecular geometry are sufficient to change the sense of the anisotropy of the magnetic susceptibility and hence the sign of the crystal field parameter, B_0^2. Thus, the crystal field cannot be assumed to be constant across the series of lanthanides, which explains the apparent breakdown of Bleaney's theory in predicting pseudocontact shifts in these complexes.

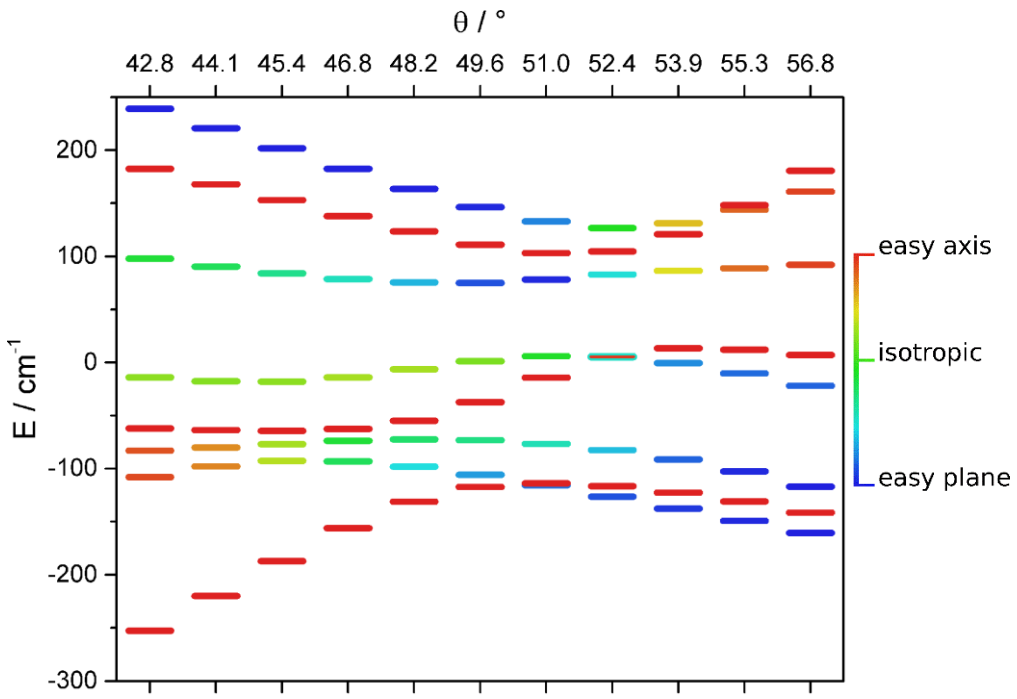

Figure 3.27 CASSCF-SO calculated energy levels of the J = 15/2 ground state of Dy(III) in **[DyL^7]** as a function of O-donor polar angle θ). The barycentre of each multiplet is set to zero. The magnetic anisotropy of the Kramers doublets is visualised as red for easy axis ($g_{||} > g_{\perp}$), green for isotropic ($g_{||} = g_{\perp}$) and blue for easy plane ($g_{||} < g_{\perp}$). Kramers doublets between perfectly easy axis and isotropic appear orange/yellow, and those between fully easy plane and isotropic appear light blue/green. Reprinted with permission from Ref. [175]. Copyright (2017) American Chemical Society.

With a detailed understanding of the behaviour of the anisotropy of the magnetic susceptibility in hand, the solvent dependent behaviour in **[DyL^7]** was assessed. The experimental data showed that on moving from D_2O to MeOD to d_6-DMSO the

pseudocontact shifts of the pyridyl protons in **[DyL^7]** became more positive and have a larger spread. Using the model developed in D_2O, it was confirmed that the dependence of the magnetic anisotropy on the polar angle of the oxygen donors is conserved on changing solvent. The position of the pyridyl protons is very similar in all three solvents, meaning the structural factor in the pseudocontact shift equation (Eqn. 3.2) does not vary significantly. Therefore, the observed solvent dependence must be due to changes to the magnetic anisotropy. Using the experimental results for pseudocontact shift in the three solvents, the polar angles of the oxygen donor atoms in each solvent were calculated to be 52.0, 53.3 and 53.8° for D_2O, MeOD and d_6-DMSO, respectively.[175] This suggests that as the solvent becomes more polar and increases in hydrogen bonding ability, the oxygen donor atoms become more axial.

In order to confirm this behaviour by an independent method, luminescence spectra were recorded for **[DyL^7]** in H_2O, MeOH and DMSO (emission profiles were observed to be identical in deuterated solvent). The emissive level in Dy(III) is a $^4F_{9/2}$ state and emission (see Fig. 3.28) is observed between 450 and 770 nm into the $^6H_{15/2}$, $^6H_{13/2}$, $^6H_{11/2}$ and $^6H_{9/2}$ states. The latter transition overlaps with $^4F_{9/2} \longrightarrow {}^6F_{11/2}$.

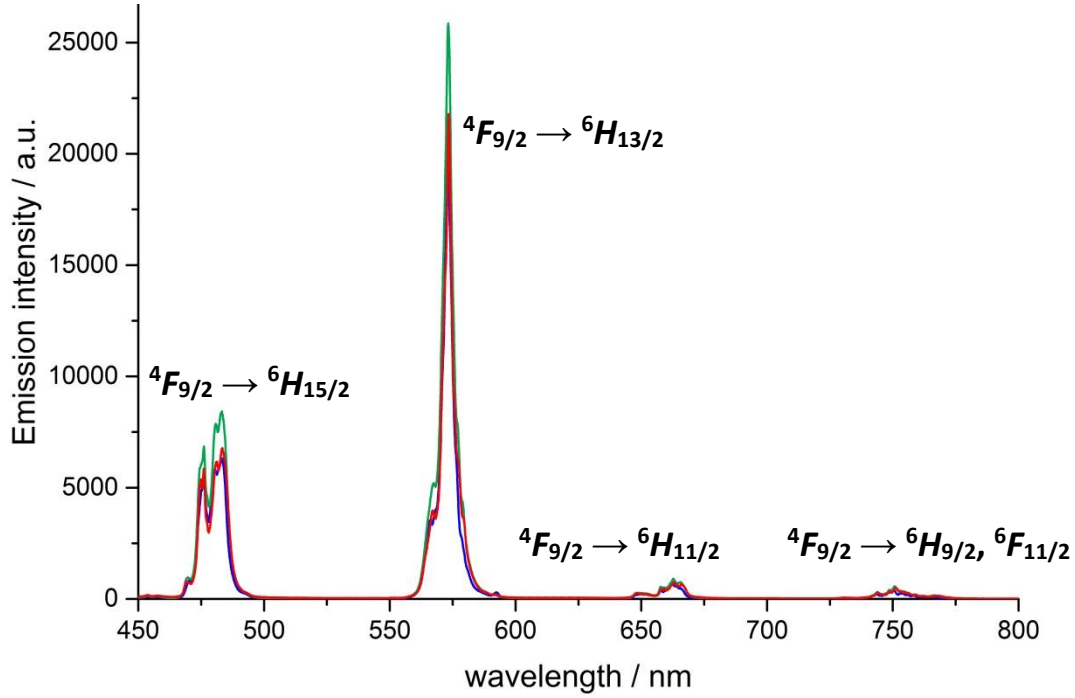

Figure 3.28 The emission spectra of **[DyL^7]** in H_2O (*blue*), MeOH (*green*) and DMSO (*red*) (295 K, λ_{exc} 272 nm).

In terms of determining the ordering of the ground state Kramers doublets, the highest energy transition into the ground state $^6H_{15/2}$ ground state is of most interest. Assuming that emission occurs only from the lowest m_J level of the $^4F_{9/2}$ state, one might expect to see a maximum of eight components in this manifold, corresponding to transitions into each of the Kramers doublets in the $^6H_{15/2}$ ground state. However, the crystal field splitting is not sufficiently large to resolve eight transitions in this manifold, and only six transitions were apparent in the emission spectra (see Fig. 3.29). The shoulder at 470 nm appears to become more distinct on moving from H_2O to MeOH to DMSO, whilst the lower energy transitions exhibit a small bathochromic shift on reducing solvent polarity. This behaviour correlates with the change in the calculated structures, where the polar angle of the oxygen donor atoms increased with decreasing solvent polarity. As this angle increases, the energy levels of the $^6H_{15/2}$ state become more separated (Fig. 3.27), which is reflected in the experimental emission data, where the components of the $^4F_{9/2} \rightarrow {}^6H_{15/2}$ manifold become more separated as solvent polarity is decreased. Unfortunately, because the eight transitions cannot be resolved in this spectrum, it is impossible to assign each transition reliably.

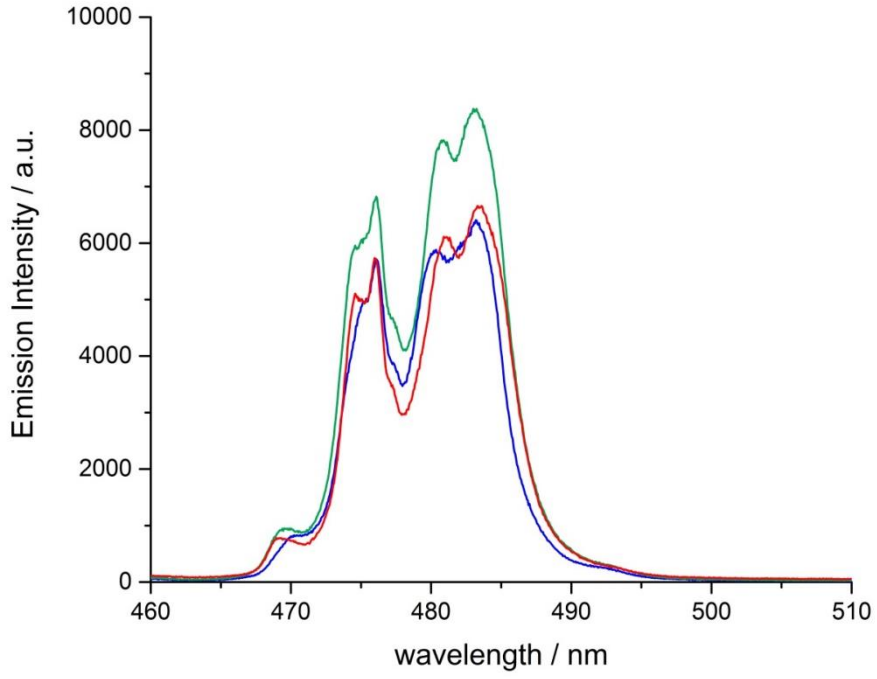

Figure 3.29 The expanded emission spectra of **[DyL^7]** in the $^4F_{9/2} \rightarrow {}^6H_{15/2}$ manifold in H_2O (*blue*), MeOH (*green*) and DMSO (*red*) (295 K, λ_{exc} 272 nm).

In an attempt to increase resolution, low temperature emission spectra were obtained for **[DyL^7]**. By reducing vibrations, transitions at low temperature should be sharper, and appear better resolved in the spectra. Since this would involve cooling the sample to 80 K, a suitable solvent mixture was required that produces a transparent glass at room temperature. A commonly used glass is a mixture of methanol:ethanol (1:4 v/v).[181] Comparison of the spectrum recorded at room temperature in methanol to that recorded in the methanol:ethanol mixture showed that they were very similar, meaning any assignments made at low temperature could be used reliably in methanol.

As the temperature was reduced, resolution was enhanced. In fact, at 80 K it appears that more than eight transitions are visible. The high energy shoulder at 470 nm that was visible at room temperature gradually disappears, suggesting that it might originate from a higher energy m_J level of the $^4F_{9/2}$ emissive state. The complex appearance of the manifold still does not allow reliable assignments to be made, as it is impossible to rule out the contributions from higher energy crystal field levels of the emissive state. Indeed, literature examples of studies of Dy(III) emission suggest that the next m_J level of the $^4F_{9/2}$ state is approximately 45 cm^{-1} higher in energy than the lowest emissive level,[182,183] which is within kT even at 80 K ($kT \approx 55$ cm^{-1} at 80 K).

Several examples in the literature have fitted very complex, poorly resolved emission manifolds with multiple Gaussian components to calculate the energies of the various transitions and to aid in their assignment.[182–185] However, this method is somewhat dubious, and attempts to utilise this procedure on the emission of **[DyL^7]** could not produce repeatable deconvolutions of the bands.

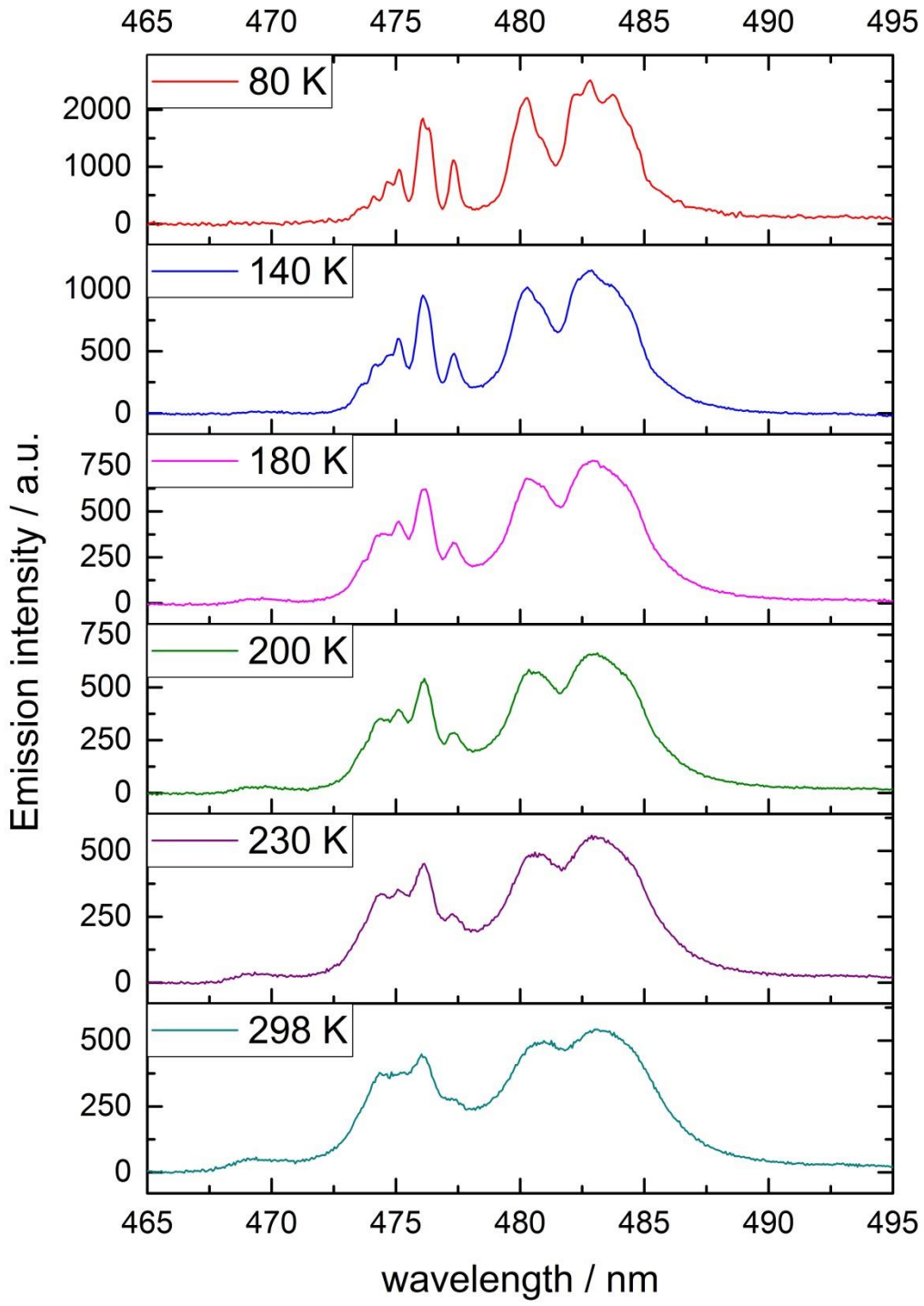

Figure 3.30 Variable temperature emission spectra of **[DyL^7]** in the $^4F_{9/2} \rightarrow {}^6H_{15/2}$ manifold showing increased resolution as temperature is decreased (1:4 v/v methanol:ethanol, λ_{exc} 272 nm).

The enantiomers of **[DyL^7]** were resolved by chiral HPLC and their CPL spectra were recorded in D_2O, CD_3OD and d_6-DMSO. It was hoped that the CPL spectra could provide increased resolution, if neighbouring transitions possessed opposite CPL sign. Despite the CPL signals being very weak, due to inefficient emission from dysprosium(III) compared to europium(III), variation in the relative intensities of

some transitions was evident (see Figs. 3.31 and 3.32). Of particular note is the size of the CPL signal in the $^4F_{9/2} \rightarrow {}^6H_{11/2}$ (650-670 nm) and the overlapping $^4F_{9/2} \rightarrow {}^6H_{9/2}$ and $^4F_{9/2} \rightarrow {}^6F_{11/2}$ manifolds (730-770 nm). However, the $^4F_{9/2} \rightarrow {}^6H_{11/2}$ and $^4F_{9/2} \rightarrow {}^6F_{11/2}$ are magnetic dipole allowed transitions which may account for their large CPL signals relative to the total emission intensity.

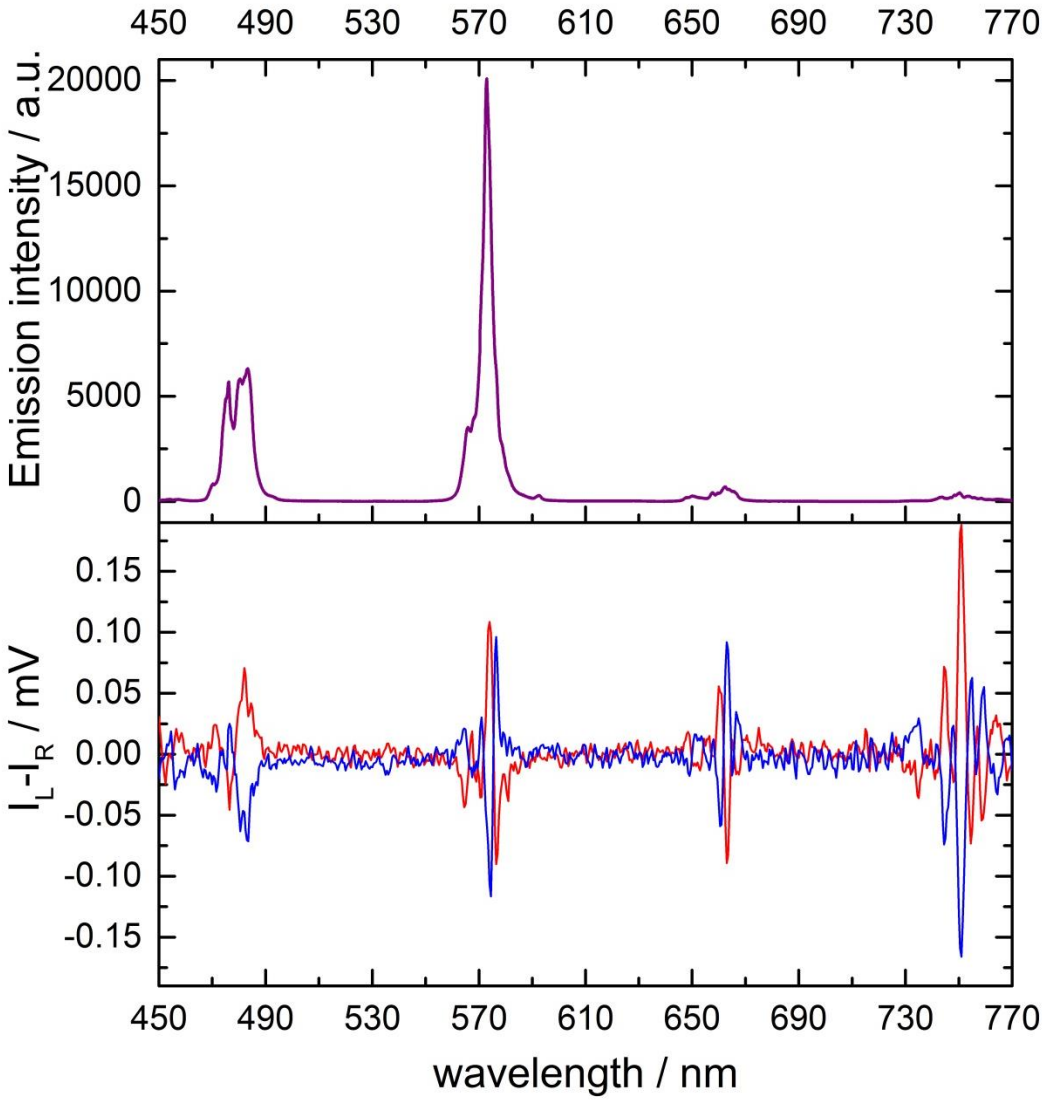

Figure 3.31 Total emission (*top*) and CPL (*bottom*) of **[DyL^7]** in D_2O showing the $^4F_{9/2} \rightarrow {}^6H_{15/2}$, $^4F_{9/2} \rightarrow {}^6H_{13/2}$, $^4F_{9/2} \rightarrow {}^6H_{11/2}$ and the overlapping $^4F_{9/2} \rightarrow {}^6H_{9/2}$ and $^4F_{9/2} \rightarrow {}^6F_{11/2}$ manifolds (*Δ*-(*red*) and *Λ*-(*blue*), 295 K, λ_{exc} 272 nm).

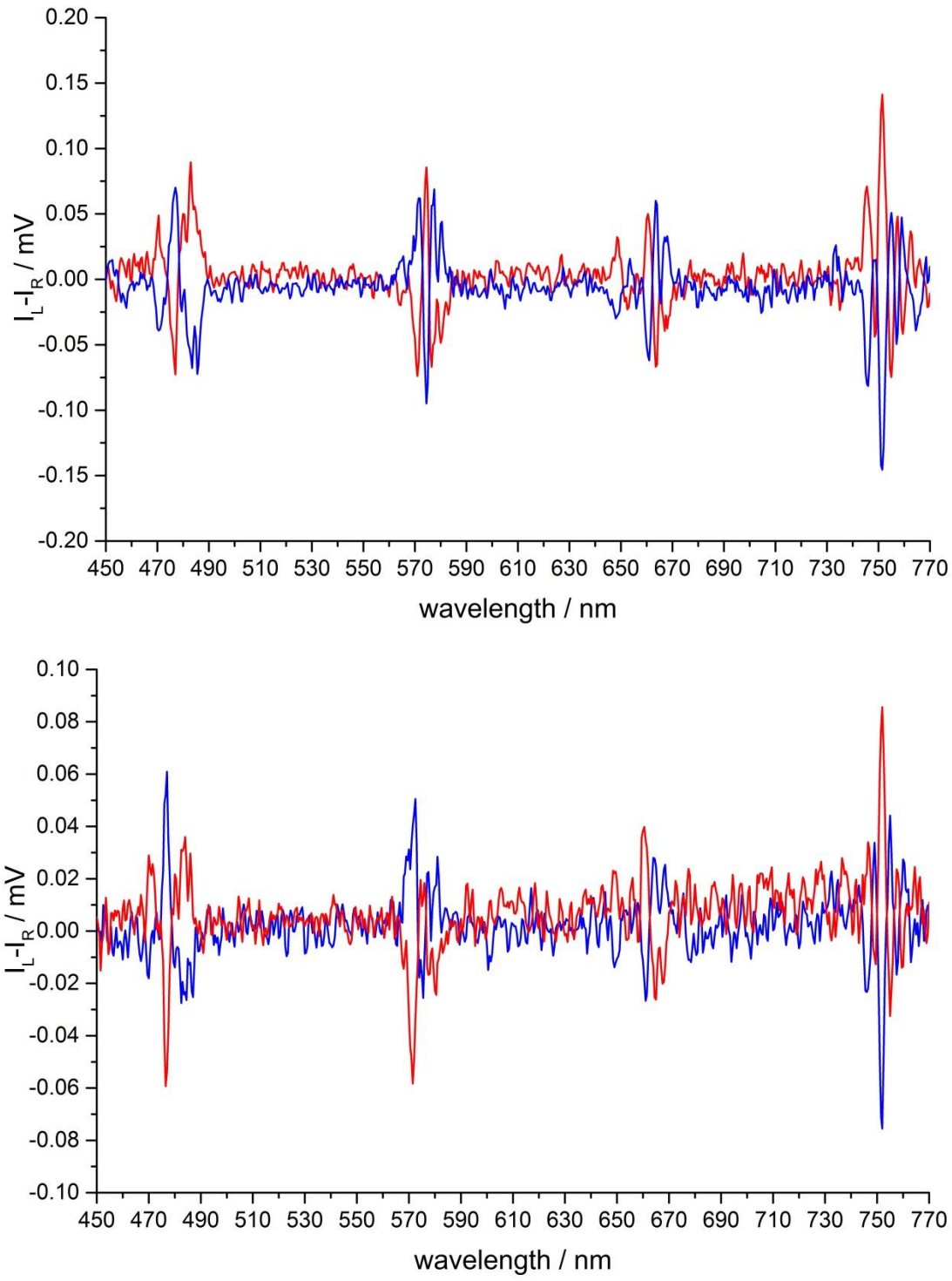

Figure 3.32 CPL spectra of *Δ*- (*red*) and Λ- (*blue*) **[DyL^7]** in CD_3OD (*top*) and d_6-DMSO (*bottom*) showing the $^4F_{9/2} \rightarrow {}^6H_{15/2}$, $^4F_{9/2} \rightarrow {}^6H_{13/2}$, $^4F_{9/2} \rightarrow {}^6H_{11/2}$ and the overlapping $^4F_{9/2} \rightarrow {}^6H_{9/2}$ and $^4F_{9/2} \rightarrow {}^6F_{11/2}$ manifolds (295 K, λ_{exc} 272 nm).

The emission from **[DyL^7]** was too complex to assign reliably. In contrast, the emission spectrum of **[EuL^7]** was much more informative. The emission spectra in water, methanol and DMSO are shown in Figure 3.33. It is evident that solvatochromic behaviour is observed in multiple manifolds, notably in water where

a different pattern in the Δ*J* = 4 manifold was observed compared to the other solvents.

However, it is the nature of the Δ*J* = 1 manifold that is diagnostic here. In trigonal symmetry, the $^7F_1$ state is split into a degenerate doublet (m_J = ±1) and a singlet (m_J = 0). The ordering and degree of separation of these levels in axially symmetric environments are dependent only on the axial crystal field parameter, B_0^2. For positive values of B_0^2, the singlet is higher in energy than the doublet, and *vice versa*.[186]

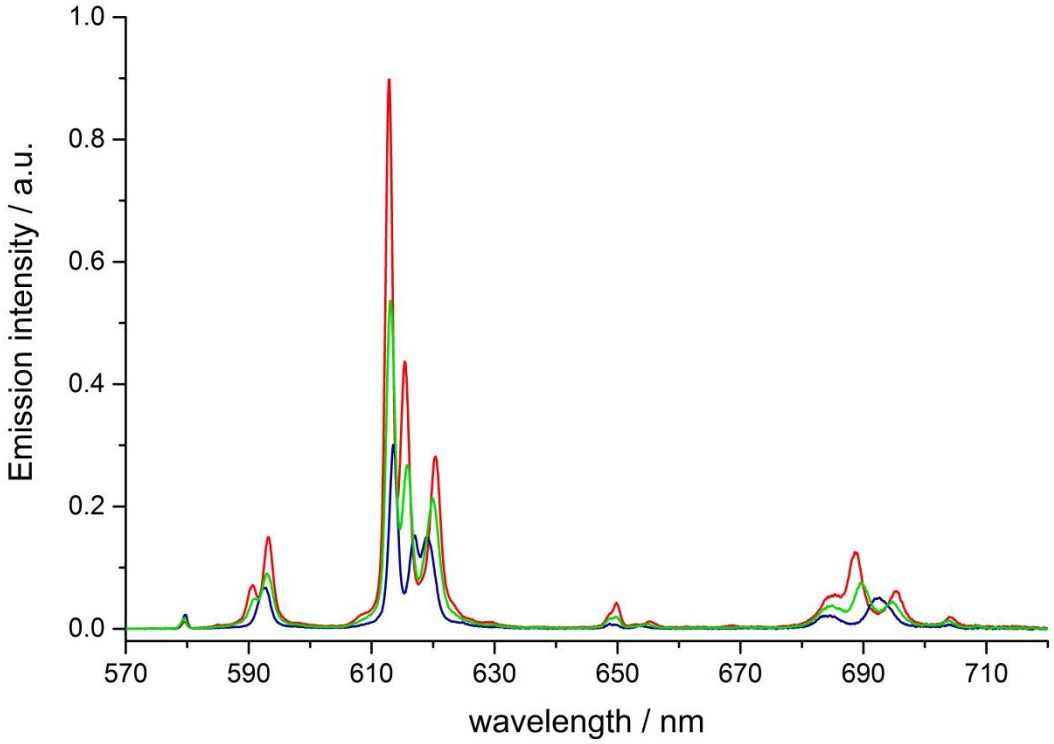

Figure 3.33 The total emission spectra of **[EuL^7]** in water (*blue*), methanol (*green*) and DMSO (*red*) (295 K, λ_{exc} 272 nm).

It is evident that the $^7F_1$ splitting increases on changing from water to methanol to DMSO, and this is observed experimentally as the resolution of two transitions in the Δ*J* = 1 manifold (see Fig. 3.34). Fitting the emission lines with Gaussian curves for all three solvents results in the expected 1:2 integrated area ratio, and demonstrates that B_0^2 is negative in all three cases. The $^7F_1$ splitting energies, *Δ*, for water, methanol and DMSO were found to be -33, -67 and -78 cm^{-1}, respectively.

The $^7F_1$ splitting energy, Δ, can be related to B_0^2 in the spherical tensor formalism as follows[187]:

$$\Delta = E_{singlet} - E_{doublet} = 0.3B_0^2 \quad \textbf{(3.4)}$$

As such, the B_0^2 values for **[EuL^7]** in water, methanol and DMSO were found to be -110, -223 and -260 cm^{-1}, respectively. In water, this value is approximately half the value of kT at 298 K, and in methanol and DMSO, the crystal field parameter is greater than kT. Therefore, Bleaney's assumption that $B_0^2 << kT$ does not hold true in this system.

Using the same methods employed for **[DyL^7]**, it was shown that the polar angle of the oxygen donor atoms in **[EuL^7]** increases on going from water to methanol to DMSO, with values calculated to be 52.7, 54.1 and 54.5°, respectively.[175] These values are slightly larger than observed for **[DyL^7]** which can be tentatively ascribed to the slightly larger size of the Eu(III) ion requiring a more open molecular structure.

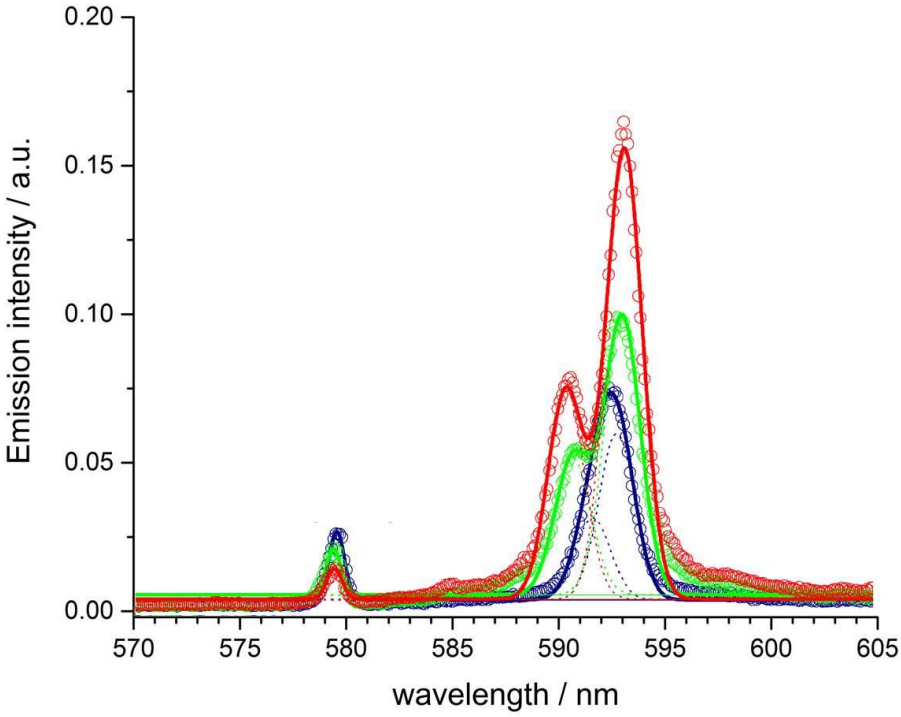

Figure 3.34 Expanded emission spectra of **[EuL^7]** in the ΔJ = 0 and 1 regions in water (*blue*), methanol (*green*) and DMSO (*red*) (295 K, λ_{exc} 272 nm); raw data is shown as open circles, fitted spectra as solid lines and deconvoluted Gaussians as dotted lines.

CPL spectra of *Δ*-**[EuL^7]** were also acquired in water, methanol and DMSO (see Fig. 3.35). Again, solvent dependent profiles were observed in the Δ*J* = 1 manifold, with the intensity ratio of the two components varying with solvent. Unfortunately, the resolution of the CPL spectrometer was not sufficiently high to allow the energies of the transitions to be extracted accurately.

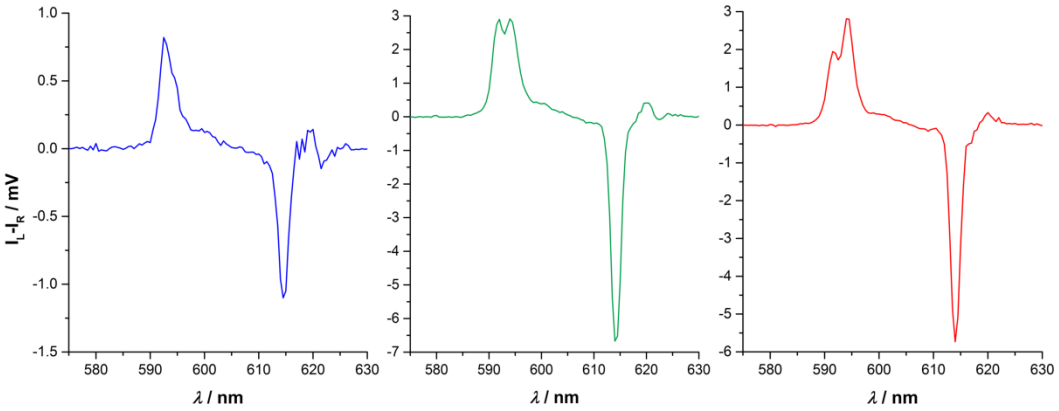

Figure 3.35 Circularly polarised luminescence spectra of the Δ*J* = 1 and 2 region for *Δ*-**[EuL^7]** in H_2O (*blue*), MeOH (*green*) and DMSO (*red*) (λ_{exc} 272 nm, 295 K). The maximum g_{em} values in the Δ*J* = 1 manifold are +0.07 in water, and +0.18 in DMSO and MeOH.

The difference in g_{em} between water (+0.07), methanol and DMSO (both +0.18) is unlikely to be accounted for by a change in the angle between the magnetic and electric dipole transition moments, as a small change in angle cannot account for a factor of more than 2 in the g_{em} values. It more likely that the difference is due to the variation in the relative magnitudes of the magnetic and electric dipole transition moments; variation in the latter may be more likely here.

In summary, experimental data from two independent techniques have demonstrated that the crystal field in the **[LnL^7]** series of complexes is extremely sensitive to geometric and electronic changes in the complex. In particular, calculations have shown that seemingly insignificant variations in the position of the three oxygen donor atoms are capable of changing the magnitude and, in some cases, the sign of the crystal field parameter, B_0^2. Whilst the total emission and CPL spectra of **[DyL^7]** obtained in water, methanol, DMSO and in a methanol:ethanol mixture were not sufficiently resolved to assign individual transitions, solvent dependence was observed. However, the emission from **[EuL^7]** allowed the

energies of the $^7F_1$ states to be measured, showing complementary solvent dependent behaviour to that observed in the rest of the **[LnL^7]** series.

3.5 Conclusions and Future Work

In addition to the known solvatochromism in the internal charge transfer absorption in complexes with extended pyridylarylalkynyl chromophores, significant solvatochromism has been observed in the emission behaviour of **[EuL^2]** in both total emission and CPL. In total emission, the most significant variations were observed in the ΔJ = 2 and 4 manifolds, which are known to be particularly sensitive to the environment. It is important to note that this behaviour is not due to a change in inner sphere donor atoms; there is no coordinated solvent molecule in these complexes. Instead, it is due to outer sphere effects, likely due to changes in ligand polarisability caused by the chromophore dipole coupling with the solvent dipole. In the CPL spectra, variation was observed in the ΔJ = 1 manifold. Since this manifold is generally regarded as being relatively insensitive to the environment, any change here is likely due to changes in the crystal field. However, the changes are probably too small to be observed in the total emission spectrum. Addition of polar chiral solvents to solutions of **[EuL^2]** in non-polar solvents did not result in a change in the spectral form in either total emission or CPL.

Similar results were observed for **[EuL^6]**, although anomalous behaviour was exhibited in chloroform and dichloromethane, suggesting a specific interaction in these solvents, possibly due to the C-H acid nature of the protons. Since the appearance of the spectra were considerably different to those recorded in polar protic solvents, it was assumed that this interaction was distinct from the hydrogen bonding interaction with the phosphinate oxygen observed in the X-ray crystal structure. A literature search for short range interactions between aromatic bromides and chloroform yielded several examples of ‘side-on’ C-H···Br interactions, where the electron rich equator of the bromine atom was interacting with the partial positive charge on the chloroform proton. The unusual emission behaviour in chloroform and dichloromethane has been tentatively attributed to such an interaction, although further evidence using other chlorinated solvents

could not be obtained due to lack of solubility. Future work should include similar analyses of the 4-chloro, 4-iodo and unsubstituted analogues of **[EuL^6]** in order to more confidently ascertain the nature of the interaction with chloroform.

In parallel to a wide-ranging study into the behaviour of several paramagnetic complexes by NMR spectroscopy, the solvent dependent emission behaviour of **[DyL^7]** and **[EuL^7]** has been investigated. Combined with extensive computational modelling and calculations carried out by collaborators,[175] the results show that the crystal field in the **[LnL^7]** series cannot be assumed to be constant, and is very sensitive to minor changes in electronic and geometric structure.

It is possible that the same processes observed in the **[LnL^7]** series are responsible for the variation in the Δ*J* = 1 manifolds of **[EuL^2]** and **[EuL^6]** with changing solvent. However, in contrast to **[LnL^7]**, the Δ*J* = 1 manifold of **[EuL^6]** suggests that the value of B_0^2 is positive in chloroform. Without further investigation, it is difficult to say whether this is indicative of a change in sign of B_0^2 in chlorinated solvents, or whether B_0^2 is positive in all solvents for this complex, because the transitions in the Δ*J* = 1 manifold are not well resolved in other solvents.

The outcome of these investigations has implications in the design of responsive probes based both on optical properties and magnetic resonance, and also demonstrates the scope and potential of this class of complex in environment-dependent sensing.

Future investigation into the solvent dependent emission behaviour of these complexes should include detailed studies of the changing crystal field in derivatives of **[LnL^7]**. Addition of pyridyl substituents could allow solubility in a wider range of solvents than possible for **[LnL^7]**. Additionally, if the substituents were capable of intermolecular interactions with chiral solvents, subtle changes in the crystal field may be observed in CPL. Varying pyridyl substituents would also affect the ligand polarisability which may help to elicit the relationship between modulation of the ligand dipole by solvent, and the corresponding total emission and CPL spectral form.

CHAPTER FOUR : CELL UPTAKE OF CHIRAL Eu(III) COMPLEXES

4.1 Introduction

Europium(III) complexes have been used extensively as stains for live cell fluorescence microscopy (Section 1.5). The development of responsive probes has allowed emissive europium(III) complexes to be used to measure the intracellular concentrations of a number of biologically relevant molecules, in addition to pH and pO_2. Of critical importance for intracellular stains and probes, is the mechanism of uptake. In order for a complex to be used *in cellulo*, a comprehensive understanding of cell uptake and sub-cellular localisation is required, and can aid in the design of new probes to target particular organelles. Whilst the cell uptake mechanism of a wide range of 12-N_4 based systems has been studied,[22] a thorough investigation of the mechanism of internalisation of the EuroTracker 9-N_3 based systems with pyridylarylalkynyl chromophores has not been undertaken. A preliminary investigation suggested that macropinocytosis was involved in the uptake of these complexes, but the presence of other competing mechanisms was not ruled out.[100] Additionally, the complexes tested in the preliminary study either possessed multiple anionic groups or contained conjugated polycationic nuclear localisation peptides. The highly charged nature of these complexes is likely to affect their uptake mechanism.

Of particular interest is the effect of probe chirality in the uptake process. Since biological recognition is achieved using chiral sugars and proteins, any uptake of chiral species might be expected to display some chiral discrimination due to differential diastereomeric interactions. Indeed, chiral discrimination of such complexes by sugars has already been demonstrated in the resolution of the enantiomers by chiral HPLC using sugar-based chiral stationary phases. Similarly, if the sub-cellular transport of the complexes is regulated by proteins, then variation in the localisation of the enantiomers and their rate of transfer inside the cell may also be affected.

Initially, a cell uptake study was carried out using racemic **[EuL^4]**, which has already been demonstrated to be taken into cells, in order to confirm that macropinocytosis is the mechanism by which internalisation occurs. Secondly, the uptake and sub-cellular localisation of **[EuL^3]** and **[EuL^4]** were investigated. Cell work was carried out by Holly Linford and Dr. Robert Pal.

The synthesis of each complex was achieved via previously reported routes (see Scheme 4.1 for **[EuL^4]**),[29,188] analogous to those used for the synthesis of the phenylphosphinate derivatives **[EuL^1]** and **[EuL^2]** (see Section 2.2). Full synthetic details and characterisation can be found in Chapter 5.

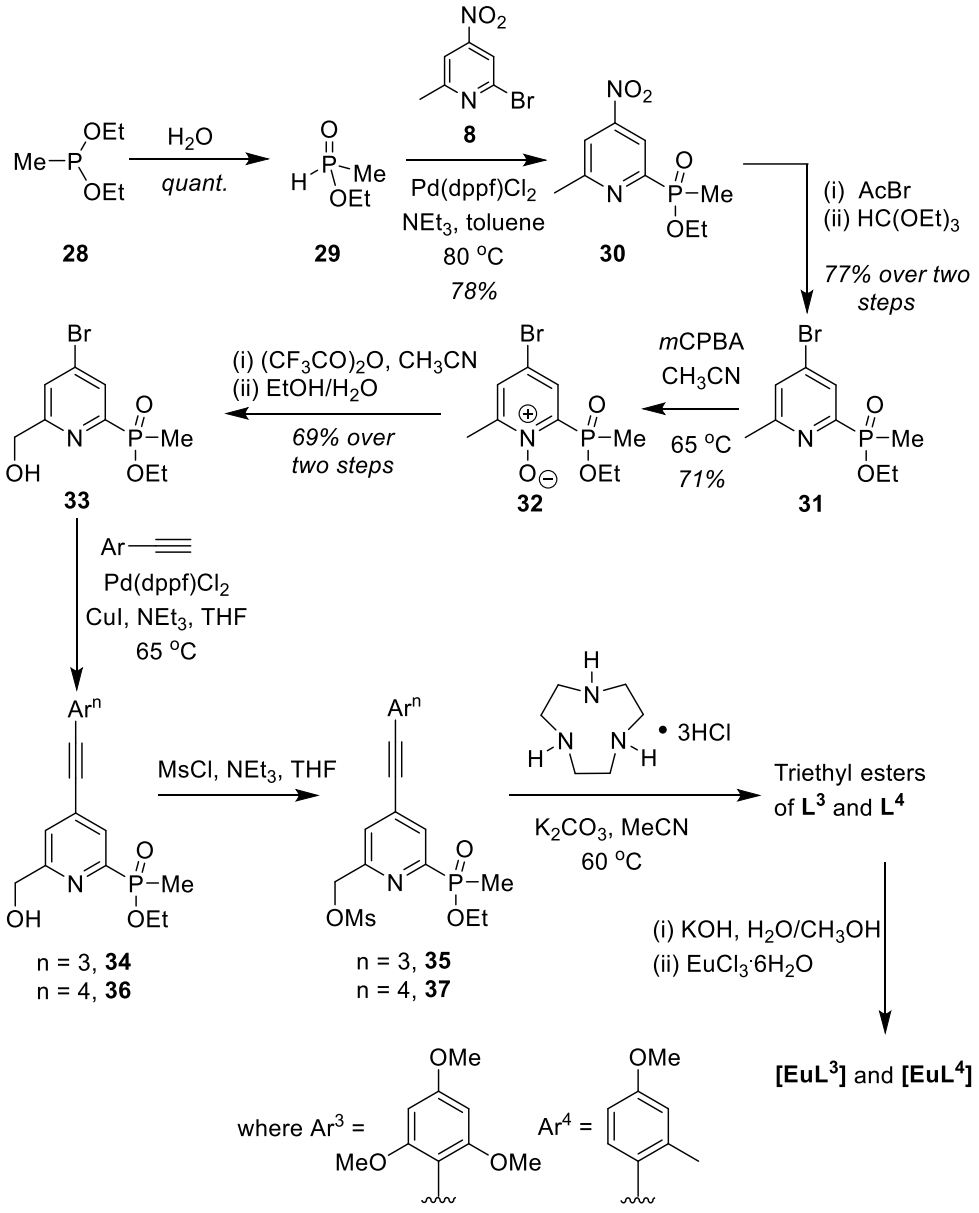

Scheme 4.1 Synthetic route to **[EuL^3]** and **[EuL^4]**.

4.2 Cell uptake mechanism of [EuL^4]

The cell uptake behaviour of **[EuL^4]** was investigated in NIH-3T3 cells (mouse skin fibroblast) in the presence of various promoters and inhibitors of macropinocytosis, clathrin-mediated endocytosis and caveolae-mediated endocytosis (see Fig. 4.1).

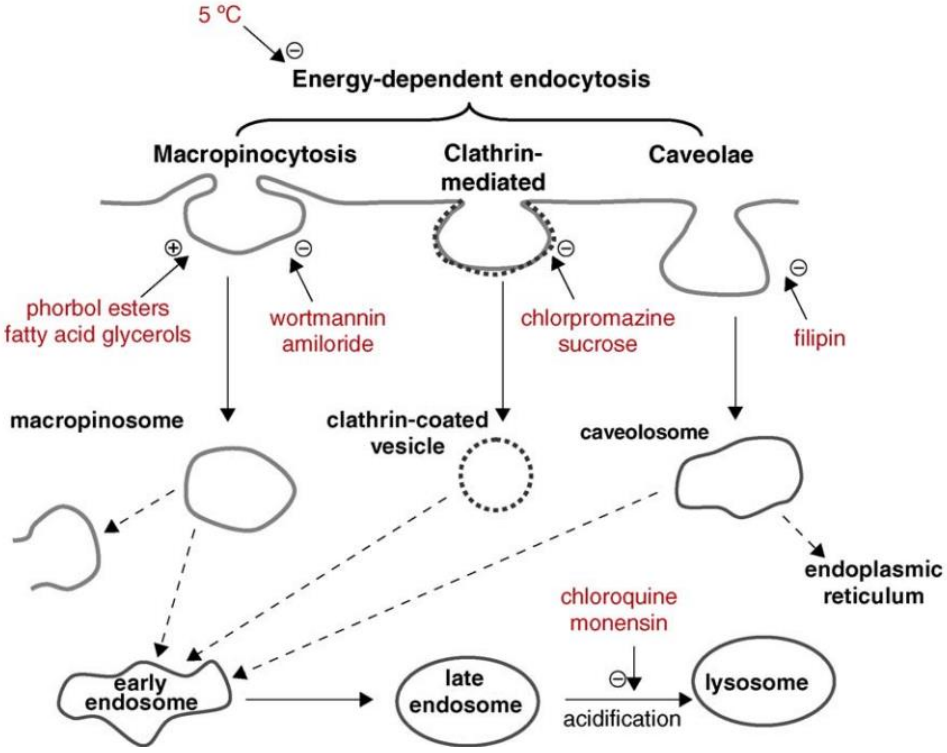

Figure 4.1 A schematic illustration of three possible endocytotic pathways for the uptake of lanthanide complexes, and the maturation of endosome to lysosomes. In red are known activators (denoted with a +) and inhibitors (-) of each process. Reprinted from Ref. [116] with permission Copyright (2009) Elsevier.

In each case, the cells were grown on coverslips using standard methods (see Chapter 5). For the cell uptake experiments, the cells were incubated for 30 minutes in growth medium containing the promoters and inhibitors shown in Figure 4.1 (the concentrations used are reported in Chapter 5). The cells were then washed and incubated with growth medium containing **[EuL^4]** (30 μM) and the promoters/inhibitors. After 4 hours, the coverslips were removed, washed with growth medium and mounted on glass slides. A control sample was produced using identical procedures, without the addition of promoters or inhibitors. Microscopy images were recorded using a Leica SP5 II laser scanning confocal microscope, with pulsed excitation at 355 nm. The extent of complex internalisation was measured

by analysis of the brightness of the acquired images. In each case, the image brightness in the 605-720 nm emission range of several perinuclear sample areas from each cell was recorded. This was repeated for multiple cells. Overall, at least 45 sample areas from multiple cells were recorded per treatment. The mean value was taken for each result and compared to the image brightness recorded using the same method for the control sample (see Fig. 4.2). Earlier work has shown that comparative image brightness measurements in such experiments were similar to independent measurement of intracellular europium concentration by ICP-MS.[189]

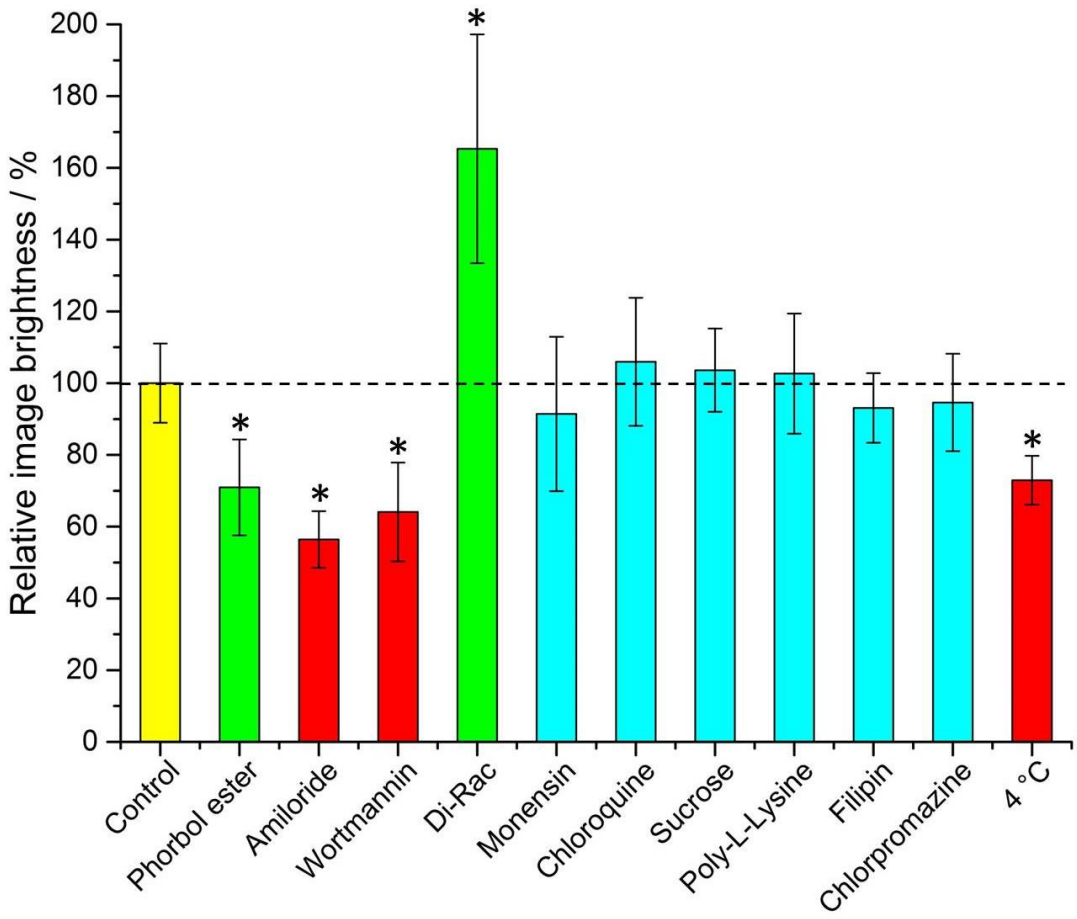

Figure 4.2 Mean relative brightness of europium(III) emission from cells incubated with **[EuL^4]** after treatment with promoters and inhibitors of various cell uptake mechanisms. Inhibitors (*red*) and promoters (*green*) of macropinocytosis are highlighted. Results which have statistical significance (two-tailed student's t-test at 95% confidence) are marked with an asterisk. Error bars represent one standard deviation from the mean.

It is immediately evident that 1,2-dipalmitoyl-*rac*-diacylglycerol (Di-Rac), a fatty acid glycerol and known promoter of macropinocytosis, significantly enhances the uptake of **[EuL^4]**. After treatment of the cells with amiloride and wortmannin, both

inhibitors of macropinocytosis, the internalisation of **[EuL^4]** is reduced by almost 50%. Similarly, for cells incubated at low temperature, the uptake of complexes is reduced, although low temperature is expected to inhibit all three endocytotic pathways. Such behaviour does, however, confirm that uptake is via an active process. The promoters and inhibitors of other pathways do not have significant effects on the internalisation of the complex. Such behaviour is consistent with that observed previously for 12-N_4 based complexes.[22]

The error bars for some treatments are quite large, which is to be expected when dealing with live cell imaging, where variation between cells is natural. However, variation in microscope performance can be discounted in this experiment as the acquisition of control samples was repeated between each measurement of treated cells.

Conspicuously, on treatment of the cells with a phorbol ester (phorbol 12-myristate 13-acetate) which is known to stimulate macropinocytosis, the brightness of the complex in the cells is reduced by approximately 30% relative to the control. In order to check whether the phorbol ester was quenching the **[EuL^4]** emission and causing this anomalous result, emission spectra were recorded in cell lysate in the presence and absence of phorbol ester. In the presence of phorbol ester, the emission intensity was quenched by approximately 35% (see Fig. 4.3), without a significant change in emission lifetime (1.11 vs. 1.06 ms). Such behaviour is consistent with reduced absorption efficiency or energy transfer to the metal, rather than quenching of the metal excited state. Whilst a 35% quenching effect may initially appear to account for the 30% reduced brightness in microscopy, one cannot assume that the relative concentrations of the complex and the phorbol ester is the same *in cellulo* as it is *in vitro*. However, it does provide evidence that such a quenching process may account, at least in part, for the lower than expected emission observed for this complex by microscopy.

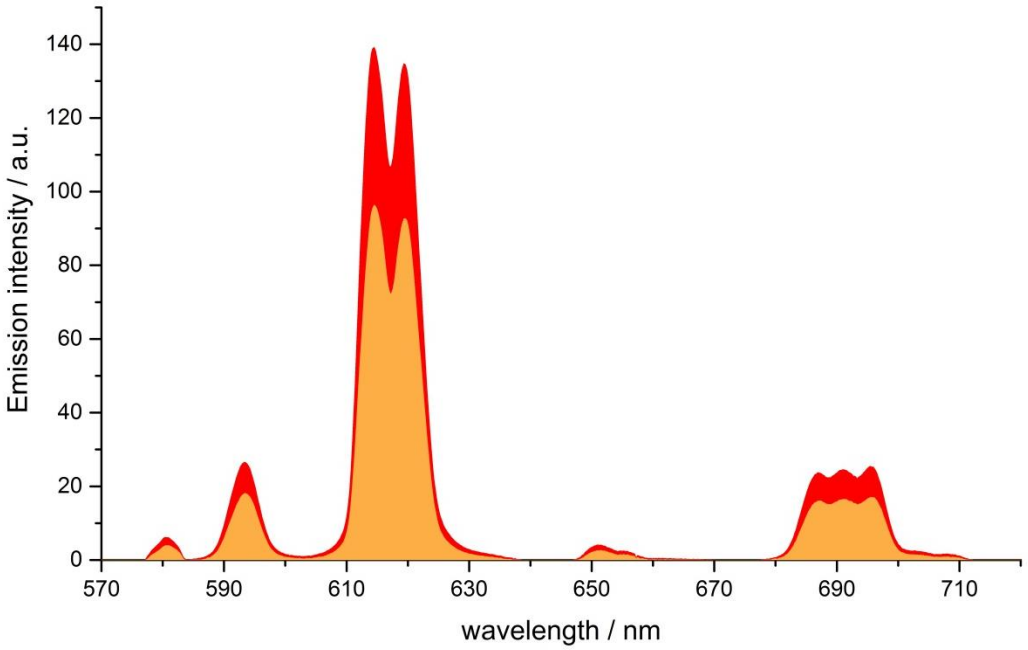

Figure 4.3 Spectral imaging of **[EuL^4]** in cell lysate (*red*) and cell lysate containing phorbol 12-myristate 13-acetate (*yellow*) (λ_{exc} 355 nm).

Taking into account all the data, it seems highly likely that macropinocytosis is the primary route of uptake of **[EuL^4],** although confirmation using a method independent of brightness would be beneficial. The use of ICP-MS would allow the concentration of Eu(III) in the cell to be measured, which would be independent of any quenching of sensitised europium(III) emission. Co-staining at early time points with a fluorescein isothiocyanate-dextran conjugate (which localises in macropinosomes),[190] would also allow confirmation that **[EuL^4]** is internalised via macropinocytosis.

Since macropinocytosis is a non-selective pathway, these results combined with those acquired in the preliminary study for complexes with similar structures, suggest that macropinocytosis is the primary route of uptake for this class of compounds. Previous work on 12-N_4 complexes concluded that simultaneous passive uptake was unlikely, as complexes of different hydrophilicity (by comparison of octanol-water partition coefficients) did not show any variation in cell uptake.[22] Since the uptake of anionic, cationic and neutral complexes appear to be affected to a similar extent by promoters and inhibitors of macropinocytosis, it is reasonable to assume that variations in charge and hydrophilicity do not affect the uptake mechanism, across a series of otherwise structurally similar complexes.

However, it should be noted that anionic complexes bearing sulfonate groups in various positions on the complexes are not internalised by cells, even after long incubation times, and instead localise on the plasma membrane.[81,191]

Unlike receptor-mediated endocytosis which is activated by binding of a specific substrate to a specific cell surface receptor, macropinocytosis is a non-selective uptake mechanism. It occurs in response to stimulation of receptor tyrosine kinases,[192] which are trans-membrane proteins capable of up-regulating actin polymerisation. It is the increase of actin polymerisation that is responsible for the formation of membrane ruffling. Occasionally, the membrane ruffles fold back on themselves, forming macropinosomes. These macropinosomes are large (>0.2 µm diameter and up to 5 µm in some examples)[111,193] compared to other endocytotic vesicles (e.g. clathrin-coated vesicles are approximately 100 nm in diameter),[194] meaning a large volume of extracellular fluid is internalised (see Fig. 4.4).

It has been observed that the fate of macropinosomes varies in different cell types. In epithelial and fibroblast cells (such as A431 and NIH-3T3) which are growth factor stimulated, macropinosomes remain relatively isolated from the endolysosomal system and eventually fuse back with the cell membrane.[193] Such an observation is consistent with the need for these types of cells to constantly reorganise the plasma membrane in response to external stimuli. In contrast, in cells where degradation of extracellular material is key (such as renal cells and macrophages), macropinosomes fuse with late endosomes and lysosomes.[195]

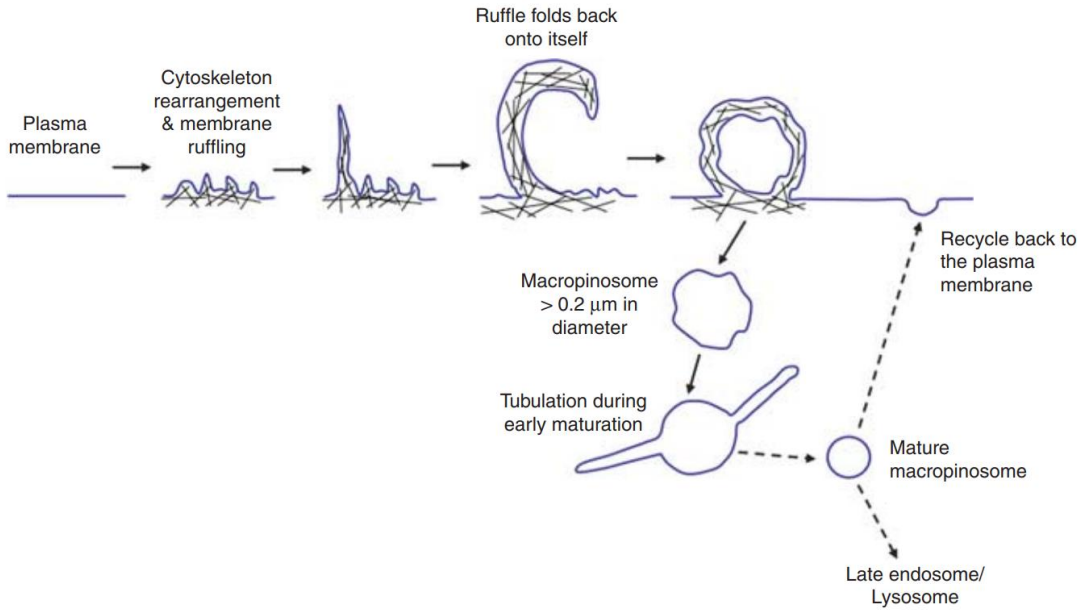

Figure 4.4 Schematic diagram describing the process of macropinocytosis. The plasma membrane is represented by a blue line, while black lines represent actin filaments. Reprinted from Ref. [196] with permission from Macmillan Publishers Ltd. Copyright 2011.

4.3 Effect of chirality on cell uptake and sub-cellular localisation

Although macropinocytosis is a non-specific mechanism of internalisation, the possibility of chirality dependent cell uptake and sub-cellular localisation is not precluded. For instance, favourable interaction of one enantiomer of complex with a protein or other substrate in the extracellular environment which can stimulate membrane ruffling, may result in one enantiomer being internalised more than the other. The fate of the complex once internalised may also involve transport by protein. Since proteins possess chiral binding pockets, it is possible that different sub-cellular localisations may be observed for different enantiomers.

An understanding of such behaviour is crucial in the use of emissive stains and probes in live cell imaging, both for chiral complexes and achiral complexes which may exhibit induced chirality on binding. Since complex **[EuL^4]** has already been reported as a stain for live cell imaging,[100] and it is simple to resolve the enantiomers by chiral HPLC (see Section 2.4), it was a logical choice for such an investigation. Additionally, experiments were carried out on **[EuL^3]** to ascertain whether the nature of the chromophore would affect its uptake or localisation profile.

Initially, NIH-3T3 cells were treated with racemic **[EuL^4]** and studied by microscopy. The complex was readily internalised by the cells and co-staining with MitoTracker Green confirmed a predominant mitochondrial localisation after 4 hours (see Fig. 4.5), consistent with the behaviour observed previously for this complex.[100] Although mitochondria are often illustrated as 'bean-shaped' organelles (and often appear as such in electron micrographs where cells are fixed with heavy metals), in live cells they are dynamic, with the ability to change their shape as well as fuse and divide.[197] As such, in live cell imaging they appear as a tubular network rather than as distinct organelles.

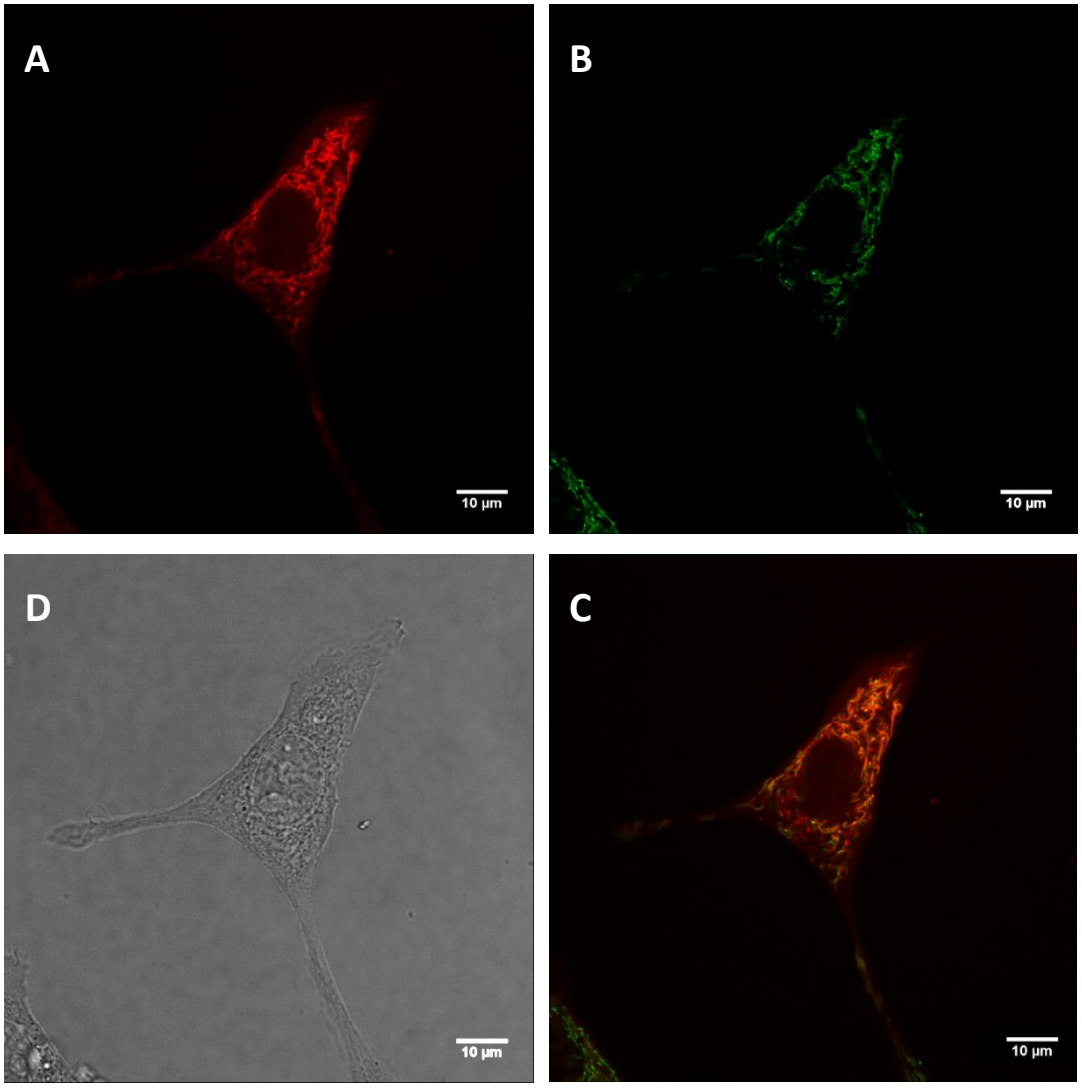

Figure 4.5 LSCM images of NIH-3T3 cells treated with **[EuL^4]** and MitoTracker Green showing (A) mitochondrial localisation of **[EuL^4]** (4 h, 30 µM, λ_{exc} 355 nm, λ_{em} 605-720 nm); (B) MitoTracker Green (0.2 µM, λ_{exc} 488 nm, λ_{em} 500-530 nm); (C) RGB merged image showing co-localisation (P = 0.92); (D) A transmission image of the cell of interest.

4.3.1 Cell uptake of enantiopure complexes

Cell uptake experiments were repeated with enantiopure *Δ*- and *Λ*-**[EuL^4]**. NIH-3T3 cells were treated with complex (30 μM) and examined by microscopy after 24 hours incubation. Comparison of the europium(III) emission brightness showed that emission from the cells treated with *Λ*-**[EuL^4]** was brighter than from the cells treated with *Δ*-**[EuL^4]** by a factor of two. In order to confirm that uptake of the two enantiomers was different, cells were also prepared for inductively coupled plasma mass spectrometry (ICP-MS) measurements. In this technique, samples are ionised using an argon plasma and analysed using a mass spectrometer, which can detect metal ions at very low concentrations (as low as 1 in 10^{15} in some cases). Cells dosed with complex were washed with phosphate buffered saline to remove any complex that was not internalised, before being trypsinated and harvested from the cover slip. Following digestion of the sample overnight in concentrated nitric acid, ICP-MS was used to measure the concentration of europium in the sample. This value can then be used to calculate the concentration of europium that was in the cell sample. In the case of cells treated with **[EuL^4]**, ICP-MS analysis of a number of cell samples showed that on average there was 1.6 times more *Λ*-**[EuL^4]** than *Δ*-**[EuL^4]** internalised. Whilst the difference in uptake measured by ICP-MS is not as pronounced as that observed by microscopy, it is further evidence that the *Λ*-enantiomer is selectively internalised by NIH-3T3 cells.

Initial attempts to carry out the same experiments using *Δ*- and *Λ*-**[EuL^3]** resulted in cell images that were significantly less bright that those observed for **[EuL^4]**, when cells were treated with the same concentration of complex. However, it was possible to estimate that the emission from the cells treated with *Δ*-**[EuL^3]** was more intense by approximately 30%. ICP-MS analysis of these cell samples revealed that 1.7 times more of the *Δ*-enantiomer was internalised than the *Λ*-enantiomer

The reduced brightness in cells can be attributed to self-aggregation leading to quenching of the europium(III) emission. In water, a reduction in emission lifetime is observed for **[EuL^3]** at concentrations above 15 μM. Whilst ICP-MS data suggests that the overall concentration in the cells is not this high, it is possible that local

concentrations in areas where the complex localises may be similar to this. Additionally, both enantiomers of **[EuL^3]** were more emissive and possessed longer-lived excited states in cell growth medium than in water, suggesting that complex aggregation is suppressed in the growth medium.

Repeating the cell experiments with a lower dosing of complex **[EuL^3]** (3 μM) resulted in significantly brighter images for both enantiomers than were originally acquired, confirming that self-quenching was indeed occurring at higher concentration. In agreement with the more concentrated treatments, and the ICP-MS data, the cells treated with *Δ*-**[EuL^3]** were brighter than those treated with *Λ*-**[EuL^3]**.

Spectral imaging of the complexes *in cellulo* revealed emission profiles and lifetimes that are consistent with those observed *in vitro*, confirming that the europium(III) ion is still held within the intact ligand framework (see Fig. 4.6).

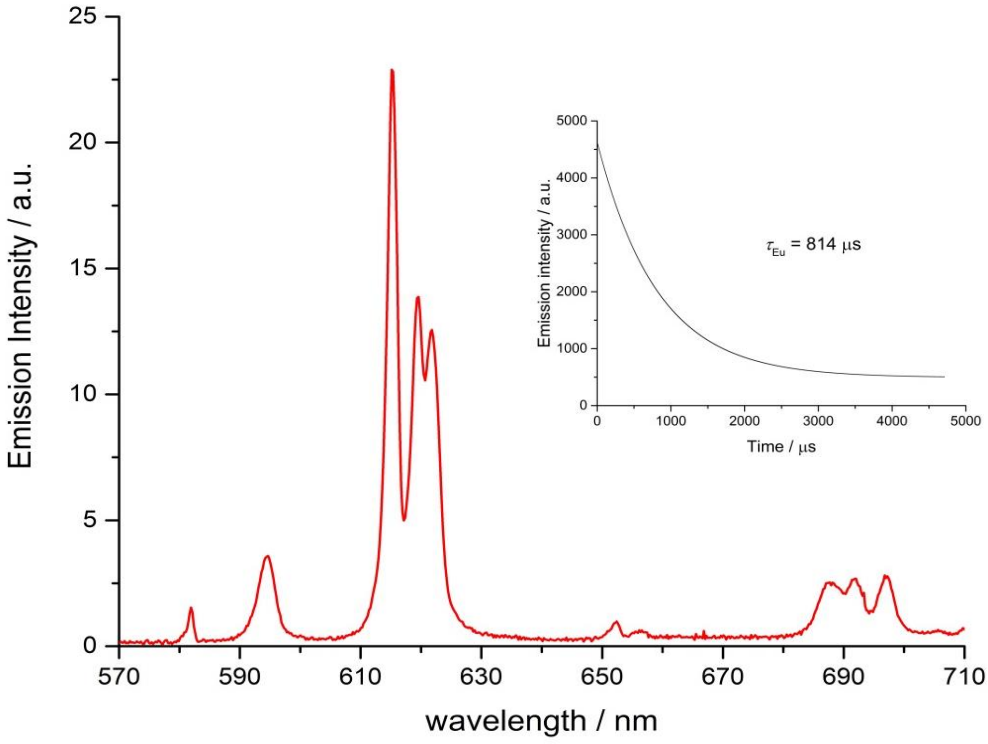

Figure 4.6 Spectral imaging of **[EuL^3]** *in cellulo* showing an emission profile consistent with that obtained *in vitro,* and an emission lifetime of 0.81 ms.

It is evident that in each case, one enantiomer is favourably internalised. Such behaviour might be explained if one of the enantiomers is interacting more strongly

with a protein and being internalised whilst bound to protein. In order to test this hypothesis, each enantiomer of **[EuL^4]** was titrated with bovine serum albumin (BSA, the most abundant protein in the cell growth medium). The absorption and emission spectra, as well as emission lifetimes, were monitored as a function of added BSA for each enantiomer.

In the absorption spectra, the extinction coefficient of the chromophore internal charge transfer band of both enantiomers increased as BSA was added, and for *Λ*-**[EuL^4]** a small hypsochromic shift (5 nm) of the absorption maximum was observed. Such behaviour is consistent with the chromophore experiencing a less polar environment.

The total emission intensity for each enantiomer increased as a function of added BSA, although a more significant change was observed for the *Λ*-enantiomer (see Fig. 4.7).

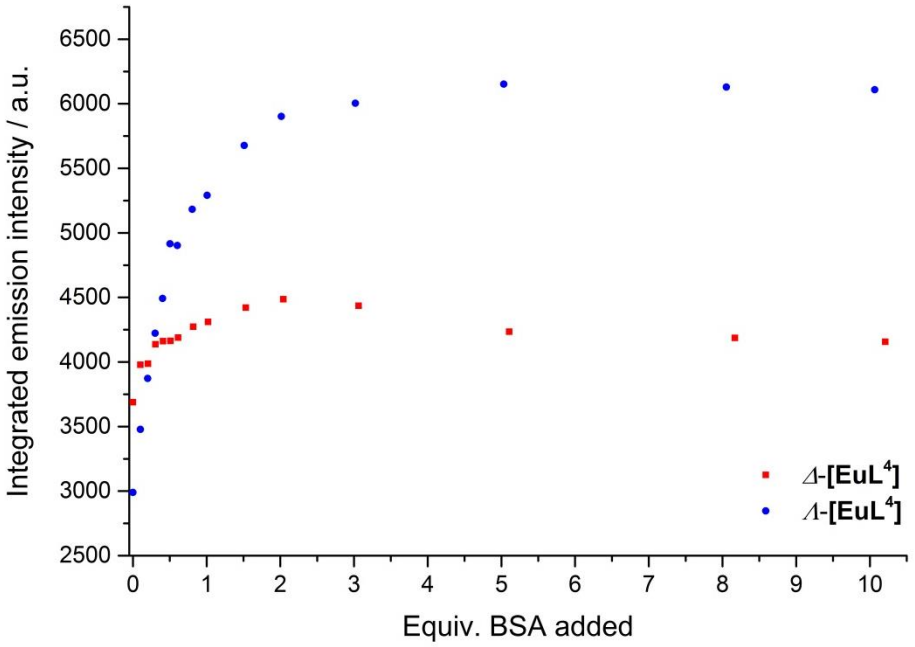

Figure 4.7 Total integrated emission intensity for *Δ*- and *Λ*-**[EuL^4]** as a function of added BSA (4 µM complex, 0.1 M HEPES, 0.1 M NaCl, pH 7.40, 295 K, λ_{exc} 340 nm).

The emission lifetime of *Λ*-**[EuL^4]** also increased by approximately 20% as the protein concentration increased, while the lifetime of the *Δ*-enantiomer showed little variation. The CPL spectra of the enantiomers were also recorded as protein was added (Fig. 4.8). The CPL spectrum of *Λ*-**[EuL^4]** increased in intensity as protein

was added, consistent with the increased intensity observed in total emission. The behaviour of *Δ*-**[EuL^4]** was more complicated. In the Δ*J* = 4 manifold, a small decrease in CPL intensity is observed, whilst a significant decrease in CPL intensity is evident in the Δ*J* = 1 and 2 manifolds. The Δ*J* = 3 manifold is largely unaffected by protein. If the complex was experiencing protein-catalysed racemisation, all manifolds would be expected to lose CPL intensity together.

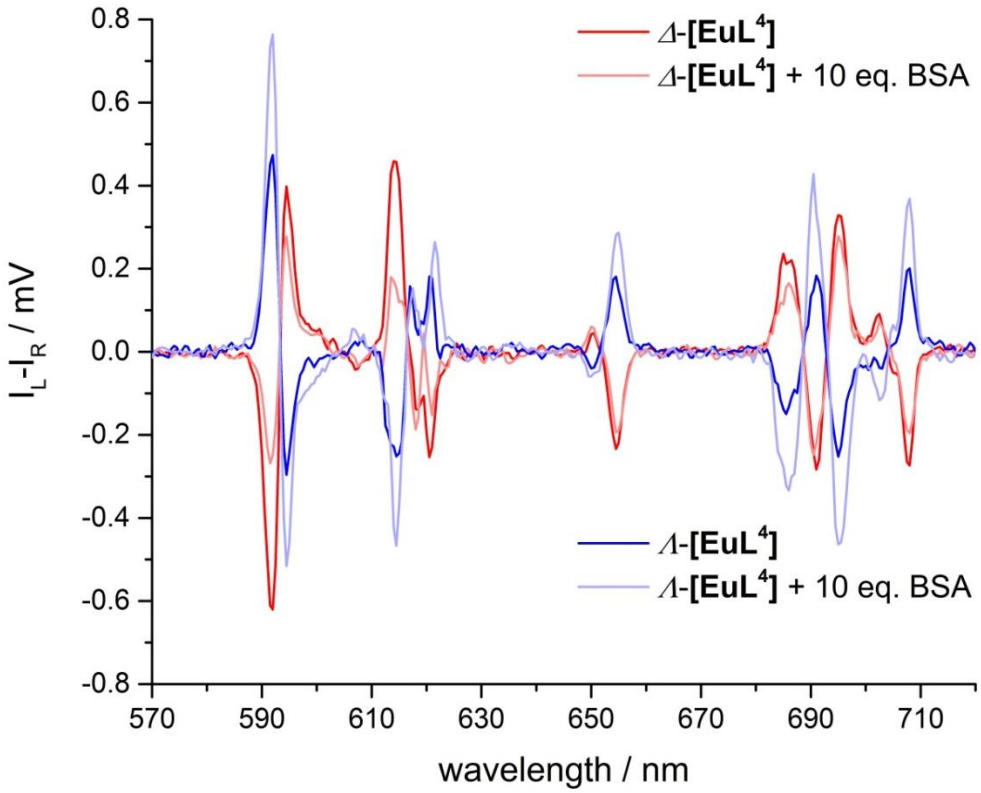

Figure 4.8 CPL spectra of *Δ*- and *Λ*-**[EuL^4]** in the presence and absence of 10 equivalents of BSA (4 μM complex, 0.1 M HEPES, 0.1 M NaCl, pH 7.40, 295 K, λ_{exc} 340 nm).

The increase in emission intensity and lifetime exhibited by *Λ*-**[EuL^4]** with added protein is consistent with the complex experiencing a less polar environment, which reduces the extent of quenching by water, and may enhance the efficiency of energy transfer from the ICT excited state to the europium(III) ion, as the energy of the ICT state is changed. Although *Δ*-**[EuL^4]** does exhibit a small increase in emission intensity, the effect is clearly not as significant as that observed for the *Λ*-enantiomer. Such behaviour suggests that the two enantiomers do not experience the same interaction with BSA as each other. Given the more significant response displayed by *Λ*-**[EuL^4]**, it conceivable that it is experiencing a stronger interaction with BSA, which might tentatively explain why it is internalised more than *Δ*-**[EuL^4]**.

Serum albumin possesses a number of distinct binding pockets of varying structure,[198,199] and is known to bind to a variety of endogenous and exogenous species, including fatty acids, metal ions, steroids, amino acids and many drugs.[200–203] It is also known to bind to a variety of chelating and macrocyclic metal complexes used as contrast agents.[204–207] Indeed, recent work within the Parker group has shown that complexes bearing pyridylarylalkynyl chromophores bind to serum albumin, perturbing the energy of the ICT excited state, signalled by a switching on of europium(III) emission.[208]

It has been proposed that serum albumin proteins exhibit non-specific adsorption to cell surface membranes, acting to protect the cell membrane from physical stress, although this behaviour seems to originate from physicochemical interactions as opposed to any biological response.[209] Studies of the interaction between BSA and lipid bilayers suggest that BSA adsorbs to the membrane at low concentrations, but causes disruption and membrane leakage at higher concentration.[210] However, serum albumins also bind to a number of cell surface receptors, which vary depending on cell type.[211] Binding to cell membranes allows serum albumins to deliver their cargo directly to target cells.

If *Λ*-**[EuL^4]** interacts more strongly with serum albumin, then it may increase the local concentration of the complex at the cell membrane, hence increasing the probability of internalisation of this enantiomer over the *Δ*-enantiomer.

Chiral lanthanide(III) complexes have previously been shown to exhibit differential binding to BSA.[87] The enantiomers of complexes with tetraazatriphenylene chromophores were shown to have very different behaviour in the presence of BSA, with the *Δ* enantiomer binding to BSA with a 1:1 binding constant of log *K*= 5.1, while the *Λ*-enantiomer formed various low affinity adducts. Indeed, for the *Δ*-enantiomer, there was a significant change in CPL spectral form, consistent with a change in complex helicity upon binding.[88] Whilst such significant variation in behaviour is not exhibited by **[EuL^4]**, there is a precedent for enantioselective protein binding in emissive europium(III) complexes.

4.3.2 Sub-cellular localisation of enantiopure complexes

In addition to studying the relative uptake of the enantiomers of **[EuL^3]** and **[EuL^4]**, the sub-cellular localisation of the enantiomers was also investigated. As before, the cells were incubated with enantiopure complex and imaged by laser scanning confocal microscopy. Complex **[EuL^4]** clearly demonstrated differential localisation after 24 hours, with the *Λ*-enantiomer predominantly exhibiting mitochondrial localisation (revealed by the appearance of tubular networks, Fig. 4.9) while the *Δ*-enantiomer exhibited a more lysosomal profile (appearing as circular dots, especially in the perinuclear region, Fig. 4.10). Both enantiomers also produced weak emission from the cytosol.

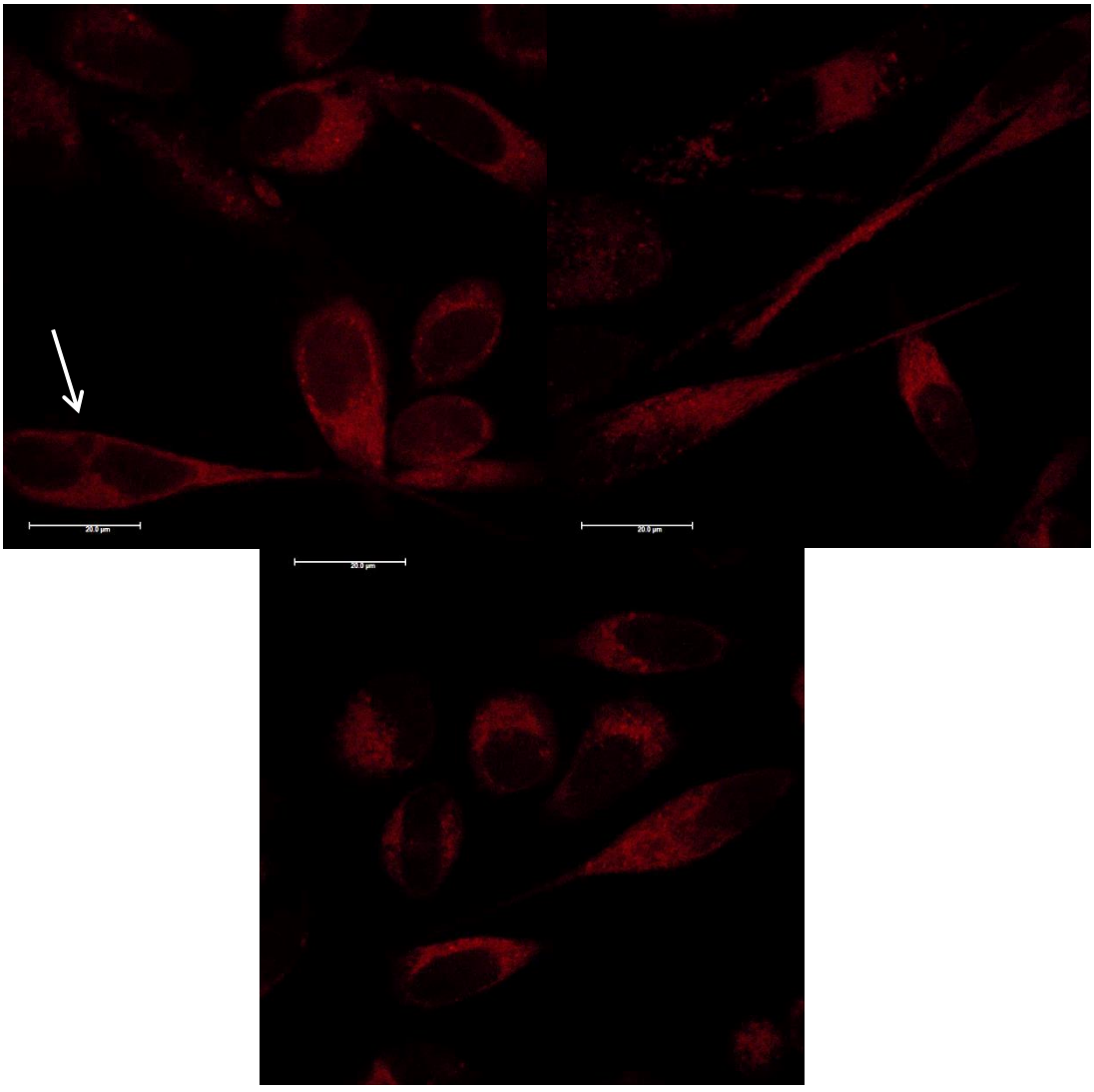

Figure 4.9 LSCM images of NIH-3T3 cells treated with *Λ*-**[EuL^4]** showing a predominant mitochondrial localisation profile (24 h, 20 µM, λ_{exc} 355 nm, λ_{em} 605-720 nm). Scale bars denote 20 µm.

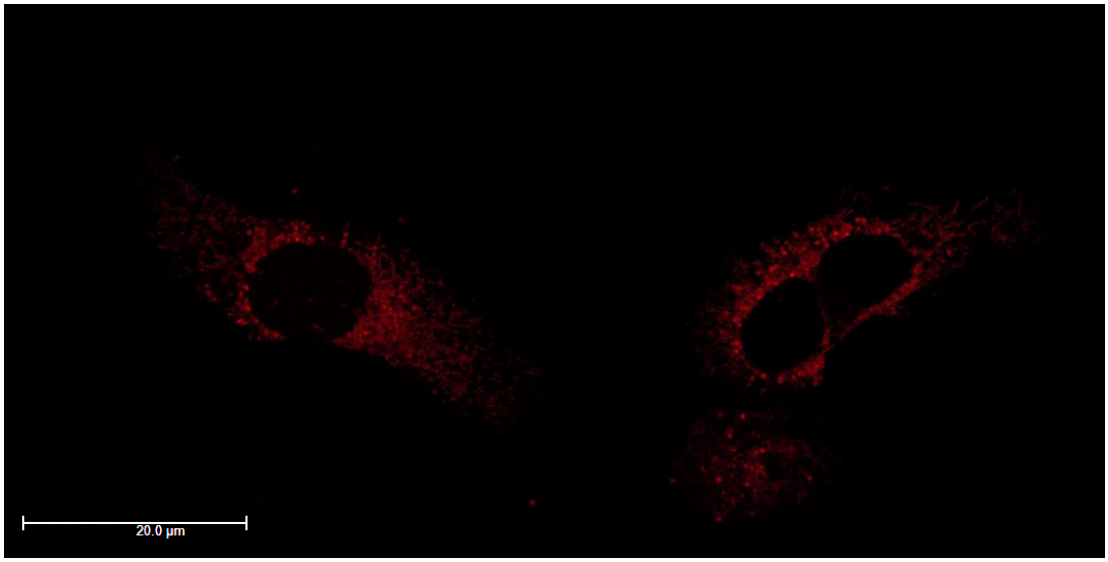

Figure 4.10 LSCM images of NIH-3T3 cells treated with *Δ*-**[EuL^4]** showing predominant lysosomal localisation (24 h, 20 µM, λ_{exc} 355 nm, λ_{em} 605-720 nm). Scale bar denotes 20 µm.

After 24 hours incubation, the cells were still alive and exhibiting normal cell cycles. Indeed, in Figure 4.9, it is possible to see a cell in the telophase state of mitosis (indicated with an arrow), where the nuclear membranes have reformed, and the cell is about to undergo cytokinesis, where the cell membrane separates to form two distinct cells.

Similar behaviour was observed for **[EuL^3]**, with the *Λ*-enantiomer exhibiting predominantly localisation in the mitochondrial network after 24 hours, in contrast to the lysosomal localisation shown by the *Δ*-enantiomer (Figures 4.11 and 4.12, respectively).

As discussed in Section 4.3.1, at the initial complex loading concentration of 30 µM, the images of **[EuL^3]** were not particularly bright due to a self-quenching effect. Therefore, the experiments were repeated using lower concentrations of complex (3 µM). Additionally, co-staining with LysoTracker Green allowed comparison of the localisation profiles of both enantiomers of **[EuL^3]** to a species known to localise to the lysosomes (see Fig. 4.13).

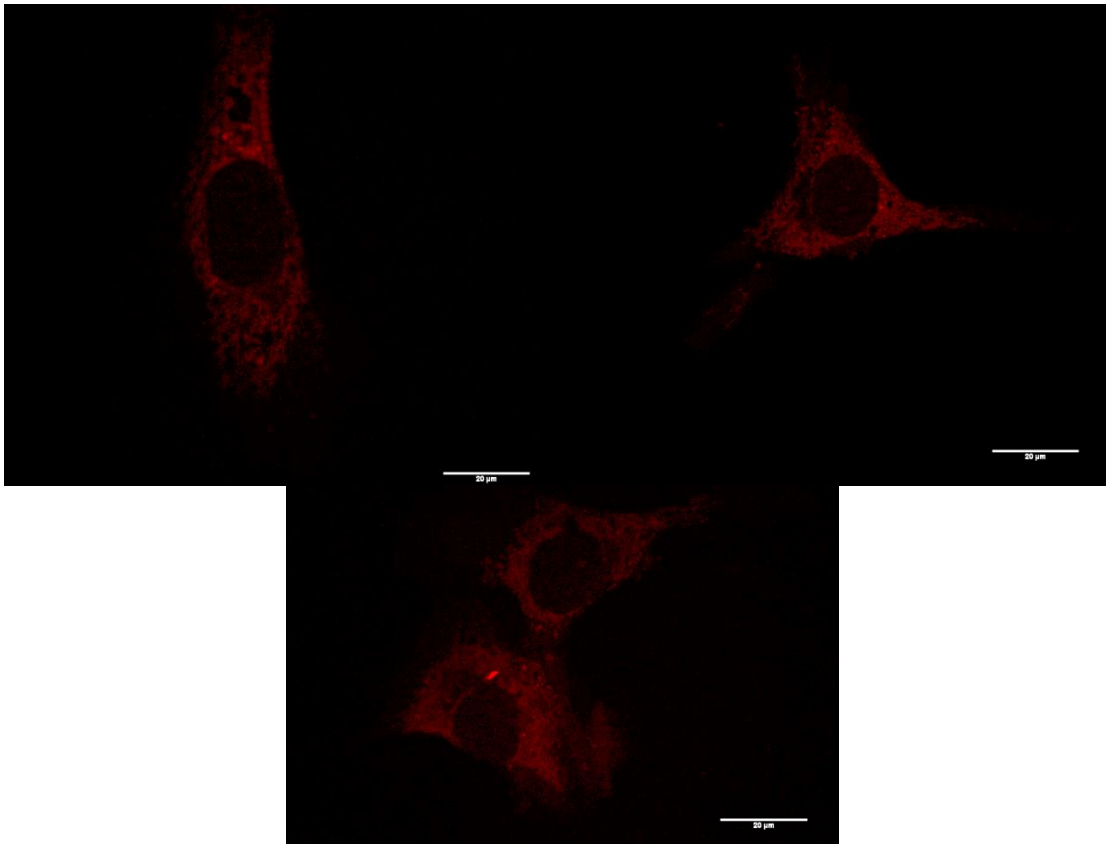

Figure 4.11 LSCM images of NIH-3T3 cells treated with *Λ*-**[EuL^3]** showing mitochondrial localisation (24 h, 30 µM, λ_{exc} 355 nm, λ_{em} 605-720 nm). Scale bars denote 20 µm.

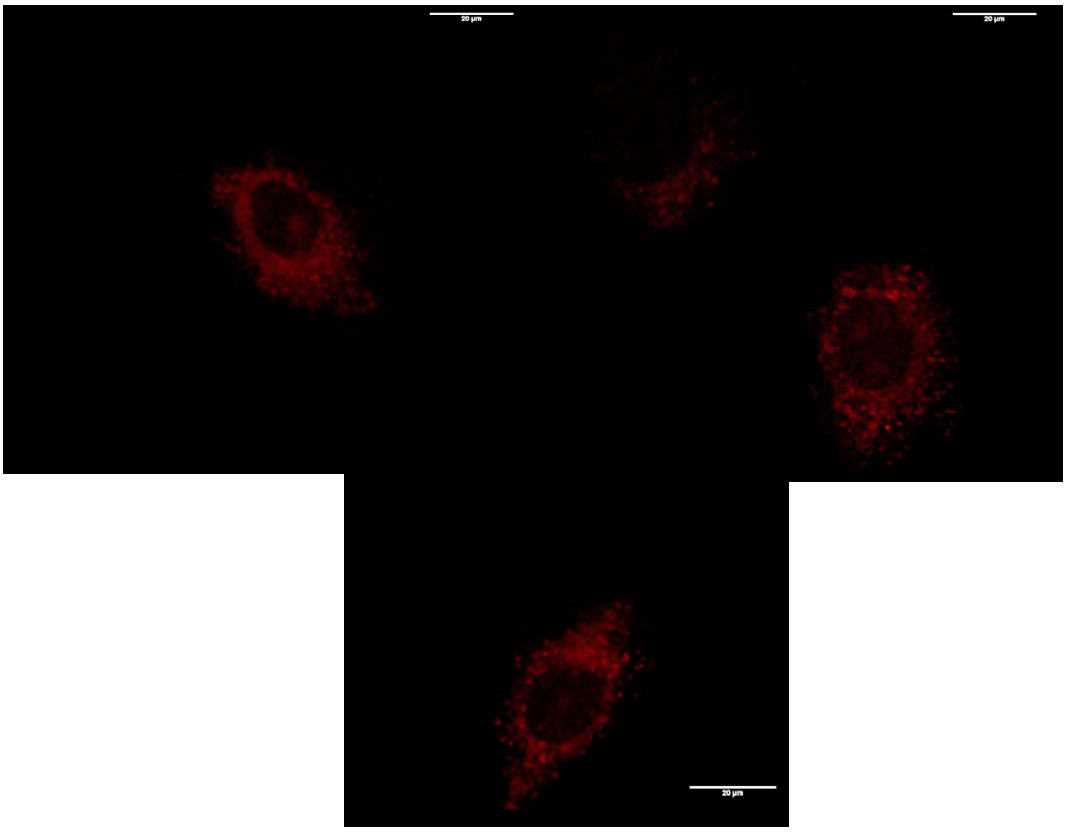

Figure 4.12 LSCM images of NIH-3T3 cells treated with *Δ*-**[EuL^3]** showing predominant lysosomal localisation (24 h, 30 µM, λ_{exc} 355 nm, λ_{em} 605-720 nm). Scale bars denote 20 µm.

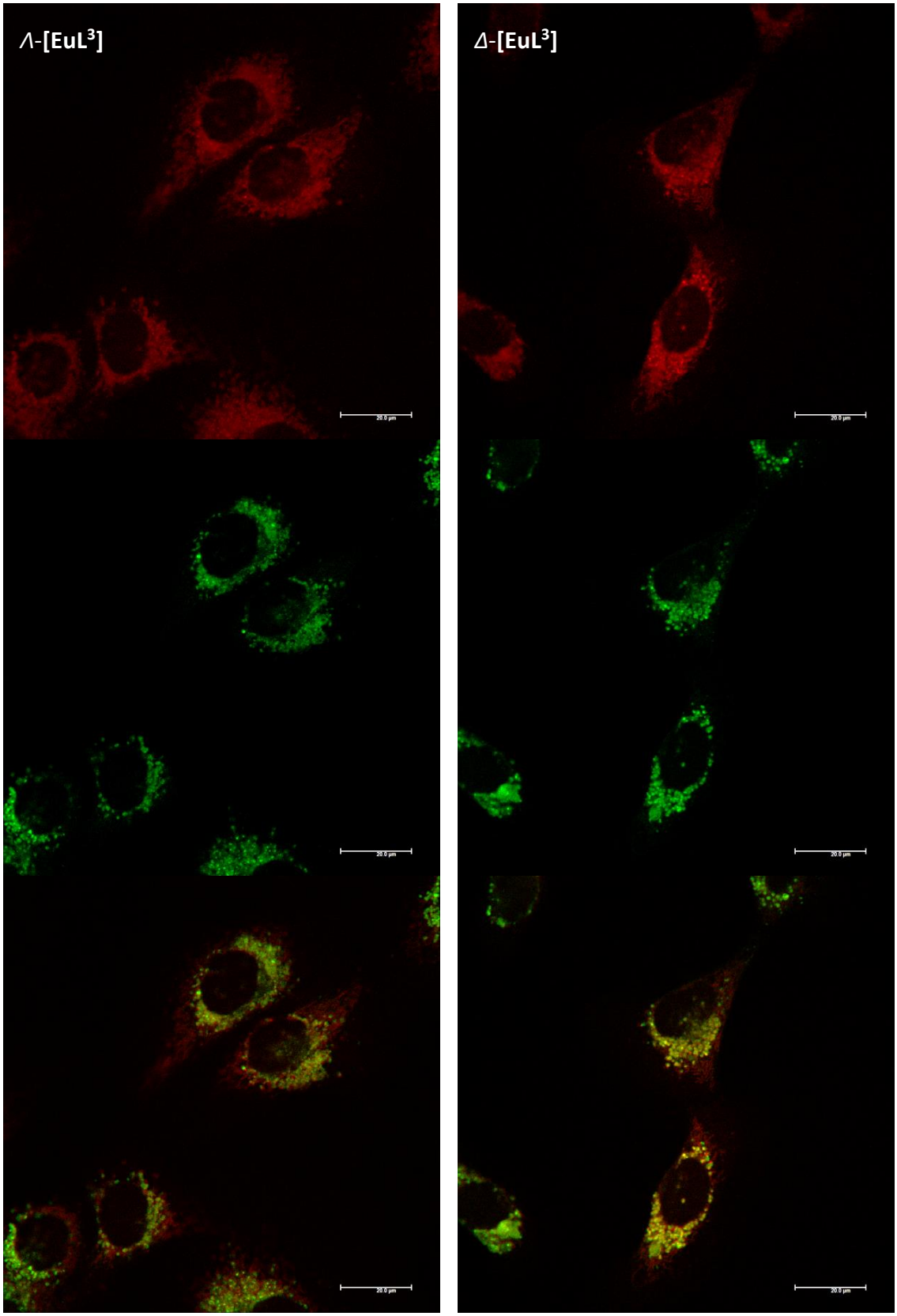

Figure 4.13 LSCM images of NIH-3T3 cells treated with *Λ*-(*left*) and *Δ*-(*right*) **[EuL^3]** (*top,* 24 h, 3 μM, λ_{exc} 355 nm, λ_{em} 605-720 nm)**;** LysoTracker Green (0.2 μM, *middle,* λ_{exc} 514 nm, λ_{em} 530-550 nm); and RGB merged image (*bottom*) (P_{Λ} = 0.65, P_{Δ} = 0.79). Scale bars denote 20 μm.

From the images in Figure 4.13, it is evident that the localisation profiles of the enantiomers of **[EuL^3]** are retained, even at much lower dosing concentrations. Again, the *Λ*-enantiomer appeared to be predominantly mitochondrial while the *Δ*-enantiomer was predominantly lysosomal. These profiles were confirmed by co-staining with LysoTracker Green. The localisation of *Δ*-**[EuL^3]** very closely matched that of LysoTracker Green, with the RGB colour merge showing almost exact co-localisation in spherical organelles concentrated around the nucleus. In contrast, the profiles for LysoTracker Green and *Λ*-**[EuL^3]** show weaker correlation, with the complex emission appearing much more diffuse than the lysosomal localisation of the BODIPY-based stain.

Given that the different enantiomers of **[EuL^3]** and **[EuL^4]** localise in both the mitochondrial network and the lysosomes, it is perhaps surprising that this cannot be observed in the images acquired of cells treated with racemic complex. For example, in Figure 4.5, the localisation of the racemic **[EuL^4]** appears distinctly mitochondrial. However, it should be noted that those images were recorded after 4 hours incubation with complex, rather than after 24 hours. It is possible, therefore, that both enantiomers initially localise in the mitochondria, but that the *Δ*-enantiomer moves to the lysosomes faster than the *Λ*-enantiomer. Such time-dependent localisation behaviour has been observed previously for racemic complexes bearing both pyridylarylalkynyl chromophores and azaxanthones.[22,100]

The sub-cellular localisation behaviour of the closely-related complex **[EuL^9]** is consistent with this hypothesis.[148] Complex **[EuL^9]** is structurally similar to **[EuL^4]**, with one extended chromophore arm replaced by a 4-methoxy substituted pyridine moiety.

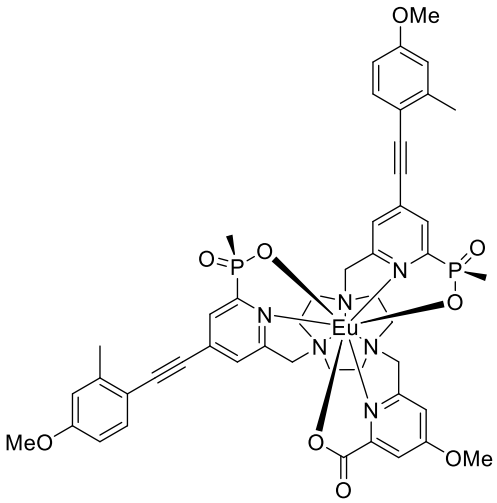

[Eu.L^9]

At early time points, *Λ*-**[EuL^9]** exhibited localisation predominantly in the mitochondrial network, which was confirmed by co-staining with MitoTracker Green (Fig. 4.14). In contrast, europium(III) emission from both the tubular networks of the mitochondria and the circular perinuclear lysosomes was evident in cells treated with *Δ*-**[EuL^9]**, suggesting both mitochondrial and lysosomal localisation (Fig. 4.15).[148]

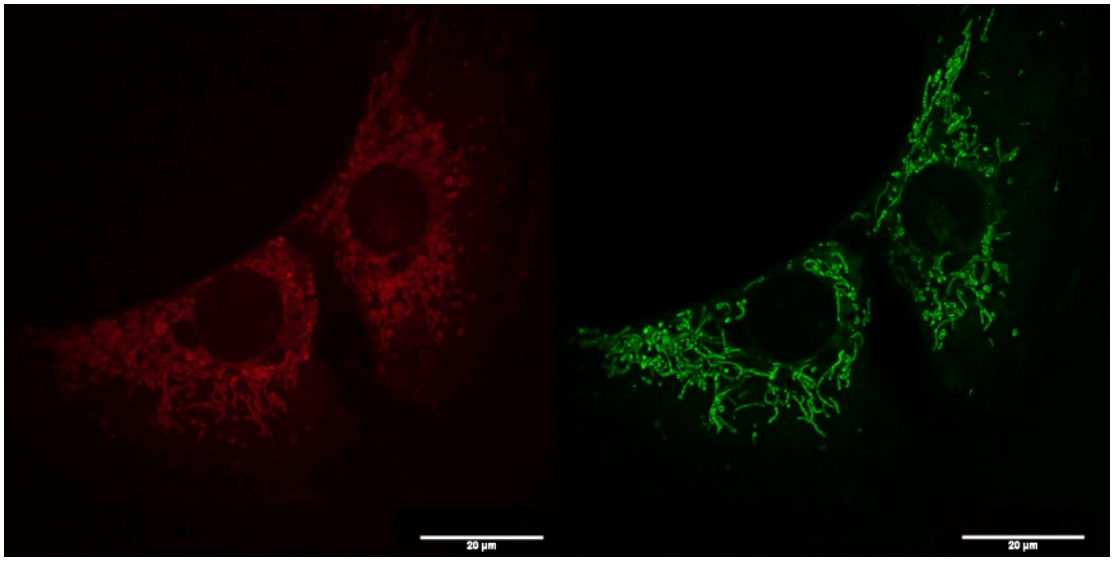

Figure 4.14 LSCM images of NIH-3T3 cells treated with *Λ*-**[EuL^9]** and MitoTracker Green showing predominant mitochondrial localisation of *Λ*-**[EuL^9]** (*left*, 8 h, 26 µM, λ_{exc} 355 nm, λ_{em} 605-720 nm) and MitoTracker Green (*right*, 0.2 µM, λ_{exc} 488 nm, λ_{em} 500-530 nm). Scale bars denote 20 µm.

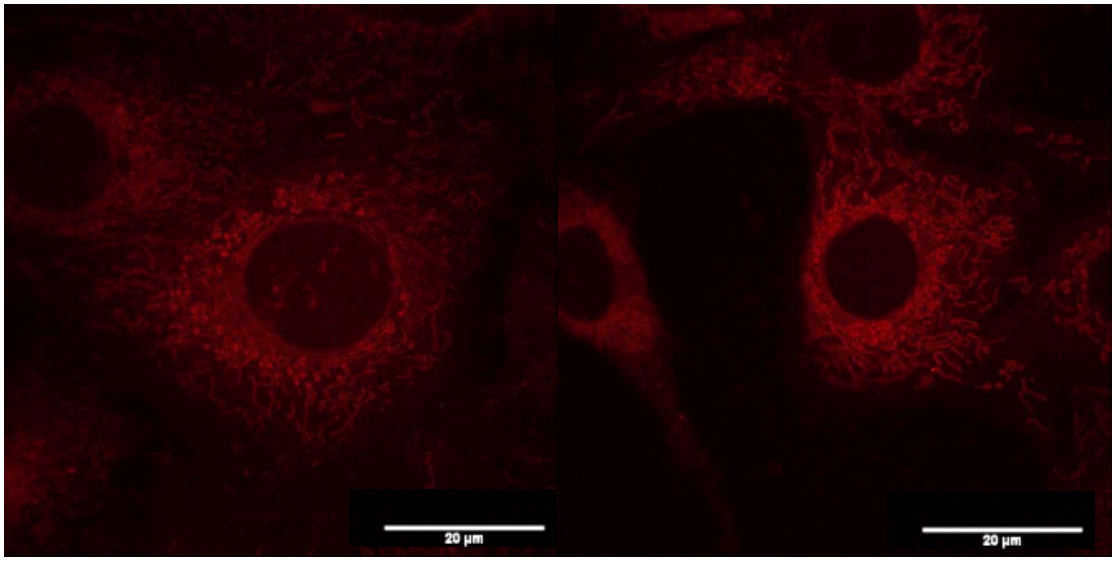

Figure 4.15 LSCM images of NIH-3T3 cells treated with *Δ*-**[EuL^9]** showing both mitochondrial and lysosomal localisation (4 h, 26 µM, λ_{exc} 355 nm, λ_{em} 605-720 nm). Scale bars denote 20 µm.

Such behaviour is consistent with a time-dependent process. The complexes are internalised in macropinosomes which, in fibroblast cells such as NIH-3T3, are isolated from the endosomal-lysosomal pathways.[193] Therefore, direct trafficking of the *Δ*-enantiomers to the lysosomes is unlikely. A more likely hypothesis is that both enantiomers are transported to the mitochondria and the *Δ*-enantiomer is subsequently removed from the mitochondria and trafficked to the lysosomes, while the *Λ*-enantiomer remains in the mitochondria.

Due to their irregular structure and lack of coating compared to endocytotic vesicles regulated by clathrin or caveolae, macropinosomes are more prone to leakage of their contents. Leakage of macropinosome content has been observed in A431 epithelial cells, where fluorescent dyes used to label macropinosomes were found to be distributed throughout the cytosol.[212] The cells were confirmed to be viable as they excluded Trypan Blue, a dye which stains only necrotic or apoptotic cells.[213] Indeed, the complexes described above do exhibit weak emission from the cytosol, suggesting that some of the complex leaks from the macropinosomes.

Whilst extensive research into transport of biological molecules has been carried out, the mechanisms of intracellular transport of exogenous molecules are largely unknown. It is likely that trafficking of the complexes to their sub-cellular

destinations is via vesicular transport, but the processes that govern the destinations of different complexes are still unknown.

Mitochondria are comprised of two membranes. The inner membrane is permeable only to small neutral molecules (oxygen, carbon dioxide and water) and contains sophisticated transport proteins to facilitate entry of specific molecules required for aerobic respiration, which occurs inside the mitochondria.[214] The proteins responsible for ATP synthesis are embedded in the inner membrane. The outer membrane is similar in composition to the cell surface membrane. Between the two membranes is the intermembrane space which is broadly similar in composition to the cytosol. The outer membrane also contains porins, which are a family of barrel-shaped proteins through which large molecules (in some cases up to 5000 Da) can diffuse into the intermembrane space.[215] It is possible that the europium(III) complexes diffuse through these porins and localise in the intermembrane space, or that they localise to the outside of the outer mitochondrial membrane.

From here, the observed localisation profiles suggest that the *Δ*-enantiomer is more quickly trafficked to the lysosomes than the *Λ*-enantiomer. Since the function of the lysosomes is to chemically degrade unwanted species using enzymes operating at acidic pH,[216] it is possible that the *Δ*-enantiomer is less well tolerated by the cell, hence is removed to the lysosomes for degradation faster than the *Λ*-enantiomer. Alternatively, it is possible that the *Λ*-enantiomer preferentially interacts with a species in the mitochondria, which reduces its rate of transport to the lysosomes.

4.4 Conclusions and Future Work

The primary mechanism of cell uptake of **[EuL^4]** in mouse skin fibroblast cells has been confirmed to be macropinocytosis, determined by measuring complex uptake in the presence of inhibitors and promoters of various endocytotic pathways. In order to confirm these findings, similar experiments on other structurally similar complexes should be carried out. Additionally, quantitative measurements by ICP-MS could be used to confirm the observations made by LSCM.

Using both microscopy and ICP-MS, differential uptake of the enantiomers of **[EuL^3]** and **[EuL^4]** has been observed. In the case of **[EuL^3]**, the *Δ*-enantiomer is internalised to a greater extent than the *Λ*-enantiomer, whilst for **[EuL^4]** the reverse behaviour was observed. Titrations of the enantiomers of **[EuL^4]** with BSA showed varied interactions, with the *Λ*-enantiomer appearing to interact more strongly with BSA. This behaviour might explain why this enantiomer is internalised to a greater extent.

The self-quenching behaviour of **[EuL^3]** has been explored, both *in vitro* and *in cellulo*. In cells dosed with 30 μM solutions of complex, emission was significantly quenched. Cells dosed with diluted solutions appeared much brighter, suggesting that at high concentration, the **[EuL^3]** complex aggregates, resulting in a quenching of europium(III) emission.

Comparison of the sub-cellular localisation profiles of enantiopure complexes shows that for both **[EuL^3]** and **[EuL^4]**, the *Λ*-enantiomer predominantly localises in the mitochondrial network, while the *Δ*-enantiomer exhibits a predominantly lysosomal localisation after 24 hours. Similar behaviour has also been reported for the related complex **[EuL^9]**. The *Δ*-enantiomer exhibits both mitochondrial and lysosomal localisation at early time points, consistent with a time-dependent localisation process.

A proposed pathway involves leakage of the complexes from the macropinosomes into the cytosol, followed by trafficking to the mitochondria. Subsequent removal to the lysosomes for degradation may occur more quickly for the *Δ*-enantiomer. Whilst the mechanisms by which the complexes are trafficked between various sub-cellular locations remain unknown, it is evident that there is chiral selectivity in the process.

Whilst it has long been known that different enantiomers of drugs can exhibit different biological activity, to the best of our knowledge, there has been only one other report of enantioselective localisation of emissive metal complexes. The two enantiomers of a chiral ruthenium(II) complex exhibited slightly different

localisation patterns with the *Δ*-enantiomer appearing in the cytosol, while the *Λ*-enantiomer seemed to concentrate around the nucleus of HepG2 cells (human liver cancer cells).[217] The difference in localisation behaviour was ascribed to each enantiomer having a different mechanism of internalisation, although no attempt to identify the uptake mechanisms was reported.

Further work regarding the cell uptake mechanism of complexes such as **[EuL^3]** and **[EuL^4]** might include confirming macropinocytosis as the primary mechanism in alternative cell types. Since the fate of macropinosomes varies between different types of cell, it is possible that the fate of the complexes internalised in them may also be affected.

In order to elucidate the sub-cellular trafficking mechanisms of complexes such as **[EuL^3]** and **[EuL^4]**, a detailed understanding of the transport of exogenous molecules would be required. Genetic modifications of cells to 'knock out' proteins known to be involved in trafficking might allow certain routes to be identified, although this is likely to affect normal cell function.

An understanding of the sub-cellular localisation mechanisms of these complexes is key to fully understanding their biological behaviour. Their time-dependent localisation means that their use as organelle stains (especially in the racemic form) requires very careful consideration. Similarly, responsive probes designed to measure the concentration of various analytes *in cellulo* may also exhibit time-dependent localisation. Since the concentration of the target analytes may vary between organelles, judicious interpretation of the results is required.

CHAPTER FIVE : EXPERIMENTAL METHODS

5.1 General Procedures

Commercially available reagents were used as received. Solvents were laboratory grade and were dried over appropriate drying agents when required. Where appropriate, solvents were degassed using freeze-pump-thaw cycles.

Thin layer chromatography (TLC) was carried out on aluminium-backed silica gel plates with 0.2 mm thick silica gel 60 F_{254} (Merck), and visualised by UV irradiation at 254 nm or 366 nm. Preparative flash column chromatography was performed using flash silica gel 60 (230-400 mesh) from Merck or Fluorochem.

^{1}H, ^{13}C and ^{31}P NMR spectra were recorded in commercially available deuterated solvents on a Bruker Avance-400 (^{1}H at 400.06 MHz, ^{13}C at 100.61 MHz and ^{31}P at 161.95 MHz), a Mercury 400 (^{1}H at 399.95 MHz), a Varian VNMRS-600 (^{1}H at 599.67 MHz, ^{13}C at 150.79 MHz and ^{31}P at 242.75 MHz), or a Varian VNMRS-700 (^{1}H at 699.73 MHz, ^{13}C at 175.95 MHz and ^{31}P at 283.26 MHz). All chemical shifts are in ppm and coupling constants are in Hz.

Electrospray mass spectra were obtained on a TQD mass spectrometer equipped with an Acquity UPLC system, an electrospray ion source and an Acquity photodiode array detector (Waters Ltd., UK). Accurate masses were recorded on an LCT Premier XE mass spectrometer or a QToF Premier Mass spectrometer, both equipped with an Acquity UPLC, a lock-mass electrospray ion source and an Acquity photodiode array detector (Waters Ltd., UK). Methanol or acetonitrile were used as the carrier solvents.

Gas chromatography mass spectra were obtained using a Shimadzu QP2010-Ultra spectrometer equipped with an Rxi-5Sil-MS column, operating in EI mode at 70 eV using helium as the carrier gas (0.41 mL/min).

Melting points were determined using a Sanyo Gallenkamp Melting Point Apparatus at atmospheric pressure and are uncorrected.

X-ray crystal structure images were produced using Mercury CSD 3.7 software using data from the Cambridge Structural Database. Original publications of the crystal structures, along with their CCDC identifiers, are cited in the text.

5.2 HPLC analysis

Reverse phase HPLC was performed at 295 K using a Shimadzu system comprising a Degassing Unit (DGU-20A_{5R}), a Prominence Preparative Liquid Chromatography pump (LC-20AP), a Prominence UV-Vis Detector (SPD-20A) and Communications Bus Module (CBM-20A). For preparative HPLC an XBridge C18 OBD column was used (19 x 100 mm, 5 µm) with a flow rate of 17 mL/min. For analytical HPLC a Shimadzu Shim-Pack VP-ODS column was used (4.6 x 150 mm, 5 µm) with a flow rate of 2.0 mL/min. Fraction collection was performed manually. A solvent system of H_2O / CH_3OH (Methods A-C and E) or H_2O / CH_3CN (Method D) was used with gradient elution as follows:

Method A

Step	Time / min	% H_2O	% CH_3OH
0	0	90	10
1	3	90	10
2	13	0	100
3	17	0	100
4	18	90	10

Method B

Step	Time / min	% H_2O	% CH_3OH
0	0	90	10
1	10	90	10
2	25	0	100
3	30	0	100
4	31	90	10

Method C

Step	Time / min	% H_2O	% CH_3OH
0	0	90	10
1	7	90	10
2	22	0	100
3	27	0	100
4	28	90	10

Method D

Step	Time / min	% H_2O	% CH_3CN
0	0	90	10
1	7	90	10
2	22	0	100
3	27	0	100
4	28	90	10

Method E

Step	Time / min	% H_2O	% CH_3OH
0	0	90	10
1	3	90	10
2	23	0	100
3	26	0	100
4	27	90	10

Chiral HPLC analysis was carried out on a Perkin Elmer Series 200 system comprising a Perkin Elmer Series 200 pump, autosampler, and UV/Vis detector, using either Daicel CHIRALPAK-IC or ID columns (4.6 x 250 mm for analytical with a flow rate of 1.0 mL/min, 10 x 250 mm for preparative with a flow rate of 4.4 mL/min, all 5 µm particle size). Isocratic methanol was used as the mobile phase. Fraction collection was performed manually. Data was analysed using TotalChrom 6.3.1 software.

5.3 Optical measurements

All solution state optical analyses were carried out in quartz cuvettes with a path length of 1 cm. UV/Vis absorbance spectra were measured on an ATI Unicam UV/Vis spectrometer (Model UV2) using Vision software (version 3.33). Emission spectra were recorded using either an ISA Jobin-Yvon Spex Fluorolog-3 luminescence spectrometer using DataMax software (version 2.2.10) or a HORIBA Jobin-Yvon Fluorolog-3 luminescence spectrometer equipped with an iHR320 module, which selects either a HORIBA FL-1073 (Hammatsu R928P) photomultiplier tube or a HORIBA Synapse BIDD CCD for detection of emitted light, using FluorEssence software (based on Origin® software). Quantum yields were recorded using a HORIBA Quanta-Φ integrating sphere. Lifetime measurements were carried out using a Perkin Elmer LS55 spectrometer using FL Winlab software. Low temperature emission spectra were recorded in the above instruments using a Janis VNF-100 cryostat coupled to a LakeShore 332 temperature controller, and cooled with liquid nitrogen.

CPL spectra were recorded on a custom-built spectrometer consisting of a laser driven light source (Energetiq EQ-99 LDLS, spectral range 170 – 2100 nm) coupled to an Acton SP2150 monochromator (600 g/nm, 300 nm Blaze) that allows excitation wavelengths to be selected with a 6 nm FWHM band-pass. The collection of the emitted light was facilitated (90° angle setup) by a Lock-In Amplifier (Hinds Instruments Signaloc 2100) and Photoelastic Modulator (Hinds Instruments Series II/FS2AA). The differentiated light was focused onto an Acton SP2150 monochromator (1200 g/nm, 500 nm Blaze) equipped with a high sensitivity cooled Photo Multiplier Tube (Hamamatsu H10723-20 PhotoSensor). Red correction is

embedded in the detection algorithm and was constructed using a calibrated Ocean Optics lamp. Spectra were recorded with 0.5 nm spectral intervals and 500 µs integration time, using a 5 spectral average sequence for europium(III) complexes and between 10 and 12 spectral averages for dysprosium(III) complexes. The monochromators, PEM control unit and lock-in amplifier were interfaced with a desktop PC and controlled by LabView code.

5.4 Time-gated photography

Time-gated photography was achieved using an off-the-shelf DSLR camera (Nikon D5300) equipped with an i-TTL flash unit (Nikon SB910) paired with a wireless flash trigger and receiver (YN-622N). Test samples were prepared using Canson Infinity Rag Photographique 2010 g/m^2 paper. Emissive species were deposited as solutions in methanol using a small volume pipette (Gilson, Inc.) and allowed to dry in air. Time-gating was introduced by placing the camera and sample 1.8 m apart, giving a 6 ns delay (light travels at 0.3 m ns^{-1}).

5.5 Circularly polarised microscopy

Chiroptical contrast based imaging was facilitated via modification of a time-resolved Zeiss Axiovert 200M epifluorescence microscope set-up.[218] Areas of the two enantiopure **[EuL^2]** spots with similar brightness were selected (contrast values: *Λ*-**[EuL^2]** 222/255 and *Δ*-**[EuL^2]** 231/255) and using a dye punch (0.3 x 150 mm), two well-defined line-shaped blotted pieces of paper were mounted parallel to each other on a SuperFrost microscope slide capped with a 170 µm coverslip for imaging. The microscope is equipped with a variable pulse sequence generator, allowing both CW and time-resolved operation. Images were acquired using an EO-M (monochrome, Thor Labs.) 0.7 megapixel rolling shutter camera with an acquisition time set at 7.2 ms per frame. A typical value for time gating was 6-10 µs, after pulsed excitation with a 365 nm UV LED (Nichia, 24 V, 1.2 W, collimated and scrambled to 1” diameter, focused to the back focal plane of a Zeiss x10/0.25NA A-Plan air objective). Chiroptical selection was achieved by converting right- and left-handed CPL into vertical and horizontal linearly polarised light, respectively, using a

10 mm aperture quarter-wave plate (400-800 nm, Thor Labs.). Light of the correct linear polarisation was selected using a pair of linear polarisers (1”; 40000:1 extinction ratio, Thor Labs.) orientated at 90° to each other. This light was focused onto a CCD detector (EO-1312M, Edmund Optics). The imaging sequence can be programmed for any number of frame averages or in the case of low light collection, an accumulation sequence, controlled manually or by an average FOV pixel contrast saturation-limiting algorithm. The image is accumulated until the maximum contrast value of 255 is achieved in a 20 pixel cluster, at which point any further acquisition saturates the image; in digital image acquisition there are 254 possible shades of grey, in addition to black and white. The accumulations are averaged until the difference in contrast between the two regions is 5x the signal to noise ratio.

5.6 Preparation of PMMA films

A 100 µL aliquot of a 1 mg mL^{-1} solution of europium(III) complex in DMF was added to 1 mL of a 10 mg mL^{-1} solution of PMMA (average $M_w \approx 15\ 000$) in DMF. The resulting solution was stirred at room temperature for approximately 30 min, after which the solution was drop-cast in 20 µL portions using a Gilson pipette onto a quartz disc (20 × 1 mm, UQG Optics, UK) and dried in air. After the final deposition, the disc was heated to 35 °C overnight before photophysical properties were measured.

5.7 Cell culture protocols

Cells used for simple microscopy studies were cultured as follows. Cells were grown in a 12-well plate on a sterilised (autoclaved at 121 °C for 45 min) glass coverslip in phenol red 3-containing DMEM/F12 cell growth medium (pH 7.6) supplemented with sodium pyruvate, glucose, 0.25 mM HEPES buffer and 10% fetal bovine serum. The cells were allowed to grow to 70-80% confluence at which point the medium was removed and replaced with medium containing complex. The cells were incubated at 37 °C at 5% CO_2 and 10% humidity. For co-staining experiments, MitoTracker Green (0.2 µM) was added to the medium 30 min before imaging,

while LysoTracker Green (0.2 μM) was added 5 min before imaging. Prior to imaging, the coverslips were washed with fresh medium three times and fixed to glass slides for imaging.

Cell uptake mechanism experiments using promoters and inhibitors of various uptake pathways were carried out as follows. Cells were pre-incubated with medium containing the treatment (concentrations below) for 30 min, before being incubated at 37 °C for a further 4 h in complex-containing medium (30 μM). In the case of the low temperature samples, the cells were incubated at 4 °C. The control samples were prepared in an identical fashion without promoter/inhibitor treatment. Prior to imaging, the coverslips were removed, washed with fresh medium four times and fixed to glass slides.

Treatment	**Dose**
Phorbol 12-myristate-13-acetate	8 nM
Amiloride	30 μM
Wortmannin	3 nM
1,2,-Dipalmitoyl-*rac*-diacylglycerol	90 nM
Monensin	0.2 nM
Chloroquine	1 μM
Sucrose	0.5 mM
Poly-L-lysine	0.001% w/v
Filipin	1.5 μM
Chlorpromazine	5 μM

In all cases, the following experimental parameters were used for imaging. For europium complexes: λ_{exc} = 355 nm, λ_{em} 605-720 nm; for MitoTracker Green: λ_{exc} = 488 nm, λ_{em} 500-530 nm; for LysoTracker Green: λ_{exc} = 514 nm, λ_{em} 530-550 nm.

Cells used for ICP-MS studies were prepared as follows. Cells were cultured in a 6-well plate to 90% confluence. Cells were then counted (10^7 cells based on a cell volume of 4000 μm^3) and incubated with medium containing the complex before

being washed three times with phosphate-buffered saline (PBS). The cells were then trypsinated and harvested and diluted to 1 mL with PBS. Concentrated nitric acid (0.6 mL) was added and the samples were digested for 24 h at 37 °C. These digested samples were submitted for ICP-MS measurements (Dr. Chris Ottley, Department of Earth Sciences, Durham University). The samples were run against a series of Eu standards, and the measured concentration was back calculated to find the total Eu concentration present in the original counted cells.

5.8 Confocal microscopy and cell imaging

Cell images and co-localisation experiments were obtained using a Leica SP5 II microscope equipped with PhMoNa.[219] In order to achieve excitation with maximal probe emission, the microscope was coupled by an optical fibre to a coherent 355 nm CW (Nd:YAG) laser (3rd harmonic), operating at 8 mW power. A HeNe or Ar ion laser was used when commercially available organelle-specific stains (e.g. MitoTracker Green and LysoTracker Green) were used to corroborate cellular compartmentalisation. The microscope was equipped with a triple channel imaging detector, comprising two conventional PMT systems and a HyD hybrid avalanche photodiode detector. The latter part of the detection system, when operated in the BrightRed mode, is capable of improving imaging sensitivity above 550 nm by 25%, reducing signal to noise by a factor of 5. The pinhole was determined by the Airy disc size, calculated from the objective in use (HCX PL APO 63x/1.40 NA Lbd Blue), using the lowest excitation wavelength (355 nm) and was set to 0.6 Airy unit. Scanning speed was adjusted to 200 Hz in a unidirectional mode, to ensure both sufficient light exposure and enough time to collect the emitted light from the lanthanide based optical probes (1024 x 1024 frame size, a pixel size of 120 x 120 nm and depth of 0.772 μm) but sufficiently fast to prevent movement of cellular compartments due to natural homeostasis. Spectral imaging in cells was achieved using a custom built microscope (modified Zeiss Axiovert 200M), using a Zeiss APOCHROMAT 63x/1.40 NA objective combined with a low voltage (24 V) 365 nm pulsed UV LED focused, collimated excitation source (1.2 W). For rapid spectral acquisition the microscope was equipped at the X1 port with a Peltier cooled 2D-

CCD detector (Maya Pro, Ocean Optics) used in an inverse 100 Hz time gated sequence. Spectra were recorded from 400-800 nm with a resolution of 0.24 nm and averaged using a 10,000 scan duty cycle. Probe lifetimes were measured on the same microscope platform using a novel cooled PMT detector (Hamamatsu H7155) interchangeable on the X1 port, with the application of pre-selected interference filters. Both the control and detection algorithm were written in LabView2014, where probe lifetime was determined by using a single exponential fitting algorithm to the monitored signal intensity decay.

5.9 Synthetic procedures

2-(2,2-Dibromovinyl)-1,3,5-trimethoxybenzene,[220] 2

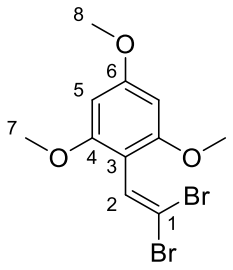

2,4,6-Trimethoxybenzaldehyde **1** (0.50 g, 2.5 mmol) and triphenylphosphine (1.34 g, 5.10 mmol) were dissolved in anhydrous dichloromethane (2 mL) and the solution was cooled in ice. A solution of tetrabromomethane (1.69 g, 5.10 mmol) in anhydrous dichloromethane (3 mL) was added dropwise. The reaction was allowed to warm to room temperature and was stirred for 22 h, at which time further triphenylphosphine (1.34 g, 5.10 mmol) was added. The reaction was stirred for a further 6 h, before the solvent was removed under reduced pressure. The residue was purified by silica gel column chromatography (neat hexane to 7:3 v/v hexane:ethyl acetate) to give a white solid (0.205 g, 23%); m.p. 126-129 °C (lit.[220] 128-130 °C); ^{1}H NMR (700 MHz, $CDCl_3$) δ 7.19 (1 H, s, H^2), 6.11 (2 H, s, H^5), 3.82 (3 H, s, H^8), 3.81 (6 H, s, H^7); ^{13}C NMR (176 MHz, $CDCl_3$) δ 161.9 (C^6), 158.2 (C^4), 131.1 (C^2), 107.0 (C^3), 92.9 (C^1), 90.6 (C^5), 55.8 (C^7), 55.5 (C^8); LCMS (ESI^+) *m/z* 353 $[M+H]^+$; HRMS (ESI^+) *m/z* 350.9220 $[M+H]^+$ ($C_{11}H_{13}O_3{}^{79}Br_2$ requires 350.9231).

2-Ethynyl-1,3,5-trimethoxybenzene,[220] 3

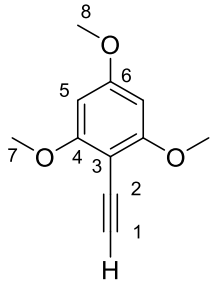

2-(2,2-Dibromovinyl)-1,3,5-trimethoxybenzene **2** (0.300 g, 0.85 mmol) was dissolved in anhydrous tetrahydrofuran (8 mL) and the solution was cooled

to -78 °C. *n*-Butyllithium (1.13 mL of a 1.6 M solution in hexane) was added dropwise and the pale yellow solution was stirred for 20 min. Water (3 mL) was added slowly and the solution was stirred for 30 min. The organic solvents were removed under reduced pressure and the remaining aqueous solution was extracted with ethyl acetate (2 x 10 mL). The organic layers were combined and washed with brine (20 mL), then dried with $MgSO_4$, filtered and concentrated under reduced pressure to yield a yellow solid (0.162 g, 99%) which was used without further purification; m.p. 120-123 °C (lit.[220] 119-122 °C); ^{1}H NMR (700 MHz, $CDCl_3$) δ 6.11 (2 H, s, H^5), 3.88 (6 H, s, H^7), 3.83 (3 H, s, H^8), 3.49 (1 H, s, H^1); ^{13}C NMR (176 MHz, $CDCl_3$) δ 163.2 (C^4), 162.1 (C^6), 93.2 (C^3), 90.5 (C^5), 83.9 (C^1), 76.7 (C^2), 56.2 (C^7), 55.6 (C^8). LCMS (ESI$^+$) *m/z* 192 $[M+H]^+$; HRMS (ESI$^+$) *m/z* 193.0853 $[M+H]^+$ ($C_{11}H_{13}O_3$ requires 193.0865).

2-Bromo-6-methylpyridine-1-oxide,[30] 6

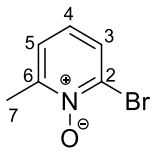

2-Bromo-6-methylpyridine (4.95 mL, 7.48 g, 43.5 mmol) and *m*-chloroperbenzoic acid (15 g, 86.9 mmol) were dissolved in chloroform (110 mL). The resulting colourless solution was stirred at 65 °C under argon for 17 h, at which time TLC showed complete consumption of starting material. The solution was cooled and the solvent was removed under reduced pressure. The resulting residue was dissolved in dichloromethane (50 mL) and washed with saturated aqueous sodium bicarbonate (3 x 50 mL). The aqueous solution was extracted with dichloromethane (3 x 50 mL). The organic layers were combined, dried over $MgSO_4$, filtered and concentrated to yield a yellow oil (7.69 g, 94%); ^{1}H NMR (400 MHz, $CDCl_3$) δ 7.55 (1 H, d, $^3J_{H\text{-}H}$ 7.5, H^3), 7.22 (1 H, d, $^3J_{H\text{-}H}$ 7.5, H^5), 7.00 (1 H, t, $^3J_{H\text{-}H}$ 7.5, H^4), 2.57 (3 H, s, H^7); ^{13}C NMR (101 MHz, $CDCl_3$) δ 150.7 (C^6), 133.1 (C^2), 128.4 (C^3), 125.0 (C^5), 124.8 (C^4), 18.9 (C^7); LCMS (ESI$^+$) *m/z* 188 $[M+H]^+$; HRMS (ESI$^+$) *m/z* 187.9702 $[M+H]^+$ ($C_6H_7O^{79}Br$ requires 187.9711).

2-Bromo-6-methyl-4-nitropyridine-1-oxide,[30] 7

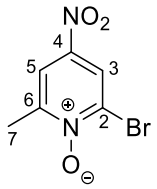

2-Bromo-6-methylpyridine-1-oxide **6** (19.65 g, 0.101 mol) was dissolved in concentrated sulfuric acid (98%, 37 mL) and the resulting solution was cooled in an ice bath. Concentrated nitric acid (70%, 34 mL) was added dropwise, and the resulting brown solution was stirred at 100 °C for 19 h. The solution was poured cautiously onto 200 mL of ice water, with immediate precipitation of a pale yellow solid. This solid was collected by filtration and dissolved in dichloromethane (100 mL). The solution was dried over $MgSO_4$, filtered and concentrated to yield the product as a pale yellow solid (16.00 g, 66%); m.p. 138-141 °C (lit.[30] 138-139 °C); ^{1}H NMR (600 MHz, $CDCl_3$) δ 8.42 (1 H, d, $^4J_{H\text{-}H}$ 3.0, H^3), 8.10 (1 H, d, $^4J_{H\text{-}H}$ 3.0, H^5), 2.63 (3 H, s, H^7); ^{13}C NMR (151 MHz, $CDCl_3$) δ 151.7 (C^6), 140.6 (C^4), 133.9 (C^2), 122.8 (C^3), 118.8 (C^5), 19.5 (C^7); LCMS (ESI^+) *m/z* 233 $[M+H]^+$; HRMS (ESI^+) *m/z* 232.9564 $[M+H]^+$ ($C_6H_6N_2O_3{}^{79}Br$ requires 232.9562).

2-Bromo-6-methyl-4-nitropyridine,[30] 8

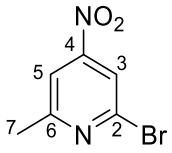

2-Bromo-6-methyl-4-nitropyridine-1-oxide **7** (3.94 g, 16.91 mmol) was dissolved in chloroform (150 mL). Phosphorus tribromide (4.8 mL, 51 mmol) was added dropwise and the resulting yellow solution was stirred at 60 °C for 17 h. The solution was cooled and the solvent removed under reduced pressure. The residue was dissolved in dichloromethane (100 mL) and washed with saturated aqueous sodium bicarbonate (2 x 50 mL). The aqueous layer was extracted with dichloromethane (3 x 100 mL). The organic extracts were combined, dried over $MgSO_4$, filtered and concentrated to give a bright yellow oil which solidified on

standing (2.72 g, 74%); m.p. 56-58 °C (lit.[221] 51-52 °C); ^{1}H NMR (400 MHz, $CDCl_3$) δ 8.03 (1 H, d, $^{4}J_{H\text{-}H}$ 1.5, H^3), 7.84 (1 H, d, $^{4}J_{H\text{-}H}$ 1.5, H^5), 2.71 (3 H, s, H^7); ^{13}C NMR (101 MHz, $CDCl_3$) δ 163.1 (C^6), 155.0 (C^4), 142.5 (C^2), 118.6 (C^3), 115.2 (C^5), 24.7 (C^7); GCMS-EI *m/z* 217 $[M(^{79}Br)]^+$.

Ethyl (6-methyl-4-nitropyridin-2-yl)(phenyl)phosphinate,[30] 9

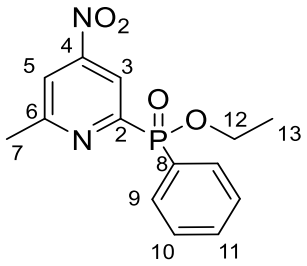

2-Bromo-6-methyl-4-nitropyridine, **8** (1.00 g, 4.61 mmol) was dissolved in anhydrous toluene (10 mL) and the solution was degassed (freeze-pump-thaw x 3). Ethyl phenylphosphinate (830 µL, 5.53 mmol) and trimethylamine (2.25 mL, 16.1 mmol) were added. Argon was bubbled through the solution for 45 min. [1,1'-Bis(diphenylphosphino)ferrocene]dichloropalladium (II) (188 mg, 0.231 mmol) was added and the resulting red solution was stirred at 120 °C under argon for 16 h. The solvent was removed under reduced pressure and the resulting black residue was purified by column chromatography (silica, 3:1 hexane:ethyl acetate to 1:2 hexane:ethyl acetate) to yield the desired product as a yellow oil (380 mg, 27%); ^{1}H NMR (600 MHz, $CDCl_3$) δ 8.56 (1 H, dd, $^{3}J_{H\text{-}P}$ 6.5, $^{4}J_{H\text{-}H}$ 2.5, H^3), 7.98 (2 H, ddd, $^{3}J_{H\text{-}P}$ 12.5, $^{3}J_{H\text{-}H}$ 8.0, $^{4}J_{H\text{-}H}$ 1.5, H^9), 7.91 (1 H, br s, H^5), 7.56 (1 H, tq, $^{3}J_{H\text{-}H}$ 7.0, $^{4}J_{H\text{-}H}$, 1.5, $^{5}J_{H\text{-}P}$ 1.5, H^{11}), 7.47 (2 H, td, $^{3}J_{H\text{-}H}$ 8.0, $^{4}J_{H\text{-}P}$ 3.5, H^{10}), 4.19-4.15 (2 H, m, H^{12}), 2.73 (3 H, s, H^7), 1.39 (3 H, t, $^{3}J_{H\text{-}H}$ 7.0, H^{13}); ^{13}C NMR (151 MHz, $CDCl_3$) δ 163.2 (d, $^{3}J_{C\text{-}P}$ 21, C^6), 158.3 (d, $^{1}J_{C\text{-}P}$ 168, C^2), 154.2 (d, $^{3}J_{C\text{-}P}$ 14, C^4), 133.0 (d, $^{4}J_{C\text{-}P}$ 3, C^{11}), 132.6 (d, $^{2}J_{C\text{-}P}$ 10, C^9), 129.2 (d, $^{1}J_{C\text{-}P}$ 141, C^8), 128.6 (d, $^{3}J_{C\text{-}P}$ 13, C^{10}), 117.6 (d, $^{2}J_{C\text{-}P}$ 24, C^3), 117.5 (d, $^{4}J_{C\text{-}P}$ 3, C^5), 62.3 (d, $^{2}J_{C\text{-}P}$ 6, C^{12}), 25.0 (C^7), 16.6 (d, $^{3}J_{C\text{-}P}$ 6, C^{13}); ^{31}P NMR (162 MHz, $CDCl_3$) δ +23.6; LCMS (ESI^+) *m/z* 307 $[M+H]^+$; HRMS (ESI^+) *m/z* 307.0850 $[M+H]^+$ ($C_{14}H_{16}NO_4P$ requires 307.0848).

(6-Methyl-4-nitropyridin-2-yl)(phenyl)phosphinic acid[30]

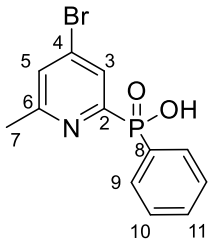

Ethyl (6-methyl-4-nitropyridin-2-yl)(phenyl)phosphinate **9** (380 mg, 1.24 mmol) was dissolved in acetyl bromide (2.75 mL, 37.2 mmol) and the solution as stirred at 70 °C for 16 h. The solution was cooled and added dropwise to ice cold stirring methanol (20 mL). This solution was stirred at room temperature for 1 h, after which time the solvent was removed under reduced pressure to yield a dark red oil (348 mg, 90%) which was used without further purification; ^{1}H NMR (600 MHz, CD_3OD) δ 8.39 (1 H, dd, $^{3}J_{H\text{-}P}$ 7.0, $^{4}J_{H\text{-}H}$ 2.5, H^{3}), 8.30 (1 H, d, $^{4}J_{H\text{-}H}$ 2.5, H^{5}), 7.97 (2 H, dd, $^{3}J_{H\text{-}P}$ 11.5, $^{3}J_{H\text{-}H}$ 7.0, H^{9}), 7.67 (1 H, t, $^{3}J_{H\text{-}H}$ 7.0, H^{11}), 7.58 (2 H, t, $^{3}J_{H\text{-}H}$ 7.0, H^{10}), 2.79 (3 H, s, H^{7}); ^{13}C NMR (151 MHz, CD_3OD) δ 159.5 (d, $^{3}J_{C\text{-}P}$ 8, C^{6}), 152.8 (d, $^{1}J_{C\text{-}P}$ 132, C^{2}), 144.6 (d, $^{3}J_{C\text{-}P}$ 11, C^{4}), 134.7 (d, $^{4}J_{C\text{-}P}$ 1, C^{11}), 134.5 (s, C^{5}), 133.3 (d, $^{2}J_{C\text{-}P}$ 11, C^{9}), 132.4 (d, $^{2}J_{C\text{-}P}$ 12, C^{3}), 131.8 (d, $^{1}J_{C\text{-}P}$ 147, C^{8}), 130.2 (d, $^{3}J_{C\text{-}P}$ 14, C^{10}), 20.3 (C^{7}); ^{31}P NMR (162 MHz, CD_3OD) δ +13.6; LCMS (ESI^{+}) *m/z* 312 $[M+H]^{+}$; HRMS (ESI^{+}) *m/z* 311.9794 $[M+H]^{+}$ ($C_{12}H_{12}{}^{79}BrNO_2P$ requires 311.9789).

Ethyl (6-methyl-4-nitropyridin-2-yl)(phenyl)phosphinate,[30] **10**

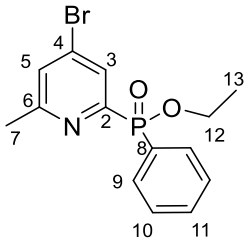

(6-Methyl-4-nitropyridin-2-yl)(phenyl)phosphinic acid (348 mg, 1.12 mmol) was dissolved in triethyl orthoformate (11 mL, 66.1 mmol) and the solution was stirred 140 °C for 65 h under argon. The solvent was removed under reduced pressure to give a brown oil. The crude product was purified by column chromatography (silica,

CH_2Cl_2 to 1% CH_3OH in CH_2Cl_2) yielding a pale yellow oil (282 mg, 75%); ^{1}H NMR (600 MHz, $CDCl_3$) δ 8.06 (1 H, dd, $^3J_{H\text{-}P}$ 6.5, $^4J_{H\text{-}H}$ 2.0, H^3), 7.97 (2 H, ddd, $^3J_{H\text{-}P}$ 12.0, $^3J_{H\text{-}H}$ 7.0, $^2J_{H\text{-}H}$ 1.5, H^9), 7.53 (1 H, td, $^3J_{H\text{-}H}$ 7.0, $^4J_{H\text{-}P}$ 1.5, H^{11}), 7.45 (2 H, td, $^3J_{H\text{-}H}$ 7.0, $^4J_{H\text{-}P}$ 3.5, H^{10}), 7.40 (1 H, br s, H^5), 4.18-4.08 (2 H, m, H^{12}), 2.54 (3 H, s, H^7), 1.36 (3 H, t, $^3J_{H\text{-}H}$ 7.0, H^{13}); ^{13}C NMR (151 MHz, $CHCl_3$) δ 161.1 (d, $^3J_{C\text{-}P}$ 21, C^6), 155.5 (d, $^1J_{C\text{-}P}$ 166, C^2), 133.5 (d, $^3J_{C\text{-}P}$ 15, C^4), 132.6 (d, $^4J_{C\text{-}P}$ 3, C^{11}), 132.5 (d, $^2J_{C\text{-}P}$ 10, C^9), 129.9 (d, $^1J_{C\text{-}P}$ 140, C^8), 128.7 (d, $^4J_{C\text{-}P}$, 3, C^5), 128.6 (d, $^2J_{C\text{-}P}$ 24, C^3), 128.5 (d, $^3J_{C\text{-}P}$ 13, C^{10}), 62.0 (d, $^2J_{C\text{-}P}$ 6, C^{12}), 24.5 (s, C^7), 16.6 (d, $^3J_{C\text{-}P}$ 6, C^{13}); ^{31}P NMR (162 MHz, $CHCl_3$) δ +24.3; LCMS (ESI^+) *m/z* 340 $[M+H]^+$; HRMS (ESI^+) *m/z* 340.0114 $[M+H]^+$ ($C_{14}H_{16}{}^{79}BrNO_2P$ requires 340.0102).

Ethyl (4-nitro-6-methyl-1-oxo-yridin-2-yl)(phenyl)phosphinate,[30] 11

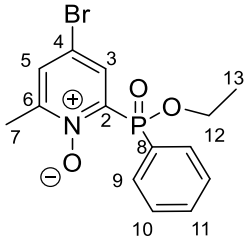

Ethyl (6-methyl-4-nitropyridin-2-yl)(phenyl)phosphinate **10** (282 mg, 0.829 mmol) and *m*-chloroperbenzoic acid (300 mg, 1.74 mmol) were dissolved in anhydrous $CHCl_3$ (5 mL) and the solution was heated at 65 °C for 42 h, after which time the solvent was removed under reduced pressure. The pale yellow residue was dissolved in CH_2Cl_2 (15 mL) and washed with 0.5 M $NaHCO_3$ solution (15 mL). The aqueous layer was extracted with CH_2Cl_2 (3 x 15 mL). The organic layers were combined, dried over $MgSO_4$, filtered and concentrated. The crude product was purified by column chromatography (silica, CH_2Cl_2 to 3% CH_3OH in CH_2Cl_2) to yield a pale yellow oil (224 mg, 76%); ^{1}H NMR (700 MHz, $CDCl_3$) δ 8.04 (1 H, dd, $^3J_{H\text{-}P}$ 8.0, $^4J_{H\text{-}H}$ 2.5, H^3), 7.98 (2 H, dd, $^3J_{H\text{-}P}$ 12.5, $^3J_{H\text{-}H}$ 7.5, H^9), 7.51 (1 H, td, $^3J_{H\text{-}H}$ 7.5, $^4J_{H\text{-}H}$ 1.5, H^{11}), 7.46 (1 H, d, $^4J_{H\text{-}H}$ 2.5, H^5), 7.42 (2 H, td, $^3J_{H\text{-}H}$ 7.5, $^4J_{H\text{-}P}$ 3.5, H^{10}), 2.45 (3 H, s, H^7), 4.16-4.08 (2 H, m, H^{12}), 1.34 (3 H, t, $^3J_{H\text{-}H}$ 6.5, H^{13}); ^{13}C NMR (176 MHz, $CDCl_3$) δ 151.0 (d, $^3J_{C\text{-}P}$ 3, C^6), 144.3 (d, $^1J_{C\text{-}P}$ 146, C^2), 133.3 (d, $^2J_{C\text{-}P}$ 10, C^9), 133.1 (d, $^4J_{C\text{-}P}$ 4,

C^{11}), 133.0 (d, $^{2}J_{C\text{-}P}$ 11, C^{3}), 132.2 (d, $^{4}J_{C\text{-}P}$ 3, C^{5}), 129.1 (d, $^{1}J_{C\text{-}P}$ 148, C^{8}), 128.4 (d, $^{3}J_{C\text{-}P}$ 14, C^{10}), 117.6 (d, $^{3}J_{C\text{-}P}$, 12, C^{4}), 62.3 (d, $^{2}J_{C\text{-}P}$ 5, C^{12}), 17.5 (d, $^{4}J_{C\text{-}P}$ 2, C^{7}), 16.6 (d, $^{3}J_{C\text{-}P}$ 7, C^{13}); ^{31}P NMR (283 MHz, $CDCl_3$) δ +21.4; LCMS (ESI^+) *m/z* 356 $[M+H]^+$; HRMS (ESI^+) 356.0064 $[M+H]^+$ ($C_{14}H_{16}NO_3P^{79}Br$ requires 356.0051).

Ethyl [4-bromo-6-(hydroxymethyl)pyridine-2-yl](phenyl) phosphinate,[188] 4

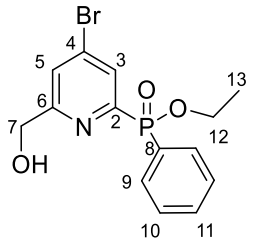

Ethyl (4-bromo-6-methylpyridin-1-oxide-2-yl)phenylphosphinate **11** (224 mg, 0.63 mmol) was dissolved in anhydrous acetonitrile (5 mL). Trifluoroacetic anhydride (1.77 mL, 2.64 g, 12.6 mmol) was added and the resulting green solution was heated to 60 °C under argon. After 3 h, the formation of the trifluoroacetate ester was complete (confirmed by ^{1}H NMR). The solvent was removed under reduced pressure, and the residue dissolved in a 1:1 mixture of ethanol:water (10 mL). This solution was stirred at room temperature for 21 h, at which time the organic solvent was removed under reduced pressure and the aqueous solution was extracted with dichloromethane (3 x 20 mL). The organic layers were combined, dried over $MgSO_4$, filtered and concentrated to give a brown oil which was purified by silica gel column chromatography (CH_2Cl_2 to 3% CH_3OH in CH_2Cl_2) to yield a yellow oil (164 mg, 73%); ^{1}H NMR (700 MHz, $CDCl_3$) δ 8.14 (1 H, d, $^{3}J_{H\text{-}P}$ 6.5, H^{3}), 7.93 (2 H, dd, $^{3}J_{H\text{-}P}$ 12.0, $^{3}J_{H\text{-}H}$ 7.5, H^{9}), 7.58 (1 H, s, H^{5}), 7.55 (1 H, t, $^{3}J_{H\text{-}H}$ 7.5, H^{11}), 7.47 (2 H, td, $^{3}J_{H\text{-}H}$ 7.5, $^{4}J_{H\text{-}P}$ 3.5, H^{10}), 4.75 (2 H, s, H^{7}), 4.19-4.09 (2 H, m, H^{12}), 1.37 (3 H, t, $^{3}J_{H\text{-}H}$ 7.0, H^{13}); ^{13}C NMR (176 MHz, $CDCl_3$) δ 162.2 (d, $^{3}J_{C\text{-}P}$ 20, C^{6}), 155.0 (d, $^{1}J_{C\text{-}P}$ 165, C^{2}), 134.3 (d, $^{3}J_{C\text{-}P}$ 14, C^{4}), 133.0 (d, $^{4}J_{C\text{-}P}$ 3, C^{11}), 132.4 (d, $^{2}J_{C\text{-}P}$ 10, H^{9}), 130.0 (d, $^{3}J_{C\text{-}P}$ 23, C^{3}), 129.4 (d, $^{1}J_{C\text{-}P}$ 141, C^{8}), 128.7 (d, $^{3}J_{C\text{-}P}$ 13, C^{10}), 126.0 (d, $^{4}J_{C\text{-}P}$ 3, C^{5}), 64.0 (s, C^{7}), 62.2 (d, $^{2}J_{C\text{-}P}$ 6, C^{12}), 16.7 (d, $^{3}J_{C\text{-}P}$ 6, C^{13}); ^{31}P NMR (283 MHz, $CDCl_3$) δ +24.4; LCMS (ESI^+) *m/z* 356 $[M(^{79}Br)+H]^+$; HRMS (ESI^+) *m/z* 356.0047 $[M+H]^+$ ($C_{14}H_{16}NO_3P^{79}Br$ requires 356.0051).

Ethyl [6-(hydroxymethyl)-4-[2-(2,4,6-trimethoxyphenyl)ethynyl] pyridin-2-yl](phenyl)phosphinate, 13

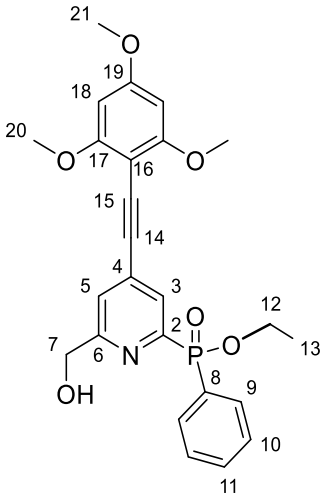

2-Ethynyl-1,3,5-trimethoxybenzene **3** (30 mg, 0.15 mmol) and ethyl [4-bromo-6-(hydroxymethyl)pyridine-2-yl](phenyl) phosphinate **4** (50 mg, 0.14 mmol) were dissolved in anhydrous tetrahydrofuran (1 mL) and the solution was degassed (freeze-pump-thaw cycle x 3). Triethylamine (96 µL, 70 mg, 0.7 mmol) was added and the solution degassed again (freeze-pump-thaw x 1). [1,1'-Bis(diphenylphosphino)ferrocene]dichloropalladium(II) (11.4 mg, 0.0140 mmol) and CuI (5.3 mg, 0.0280 mmol) were added and the solution stirred at 65 °C under argon for 4 h. The solvent was removed under reduced pressure and the residue was purified by silica gel column chromatography (neat CH_2Cl_2 to 3% CH_3OH in CH_2Cl_2). The product was still contaminated with catalyst residue so the mixture was subjected to a second purification by silica gel column chromatography (1:1 to 4:1 v/v ethyl acetate:hexane) which gave a yellow oil (41 mg, 62%); ^{1}H NMR (700 MHz, $CDCl_3$) δ 8.12 (1 H, d, $^3J_{H\text{-}P}$ 6.5, H^3), 7.95 (2 H, dd, $^3J_{H\text{-}P}$ 12.0, $^3J_{H\text{-}H}$ 7.0, H^9), 7.53 (1 H, t, $^3J_{H\text{-}H}$ 7.0, H^{11}), 7.45 (2 H, dt, $^3J_{H\text{-}H}$ 7.0, $^4J_{H\text{-}P}$ 3.5, H^{10}), 7.41 (1 H, s, H^5), 6.10 (2 H, s, H^{18}), 4.73 (2 H, d, $^5J_{H\text{-}P}$ 5.0, H^7), 4.19-4.08 (2 H, m, H^{12}), 3.88 (6 H, s, H^{20}), 3.84 (3 H, s, H^{21}), 1.36 (3 H, t, $^3J_{H\text{-}H}$ 7.0, H^{13}); ^{13}C NMR (176 MHz, $CDCl_3$) δ 163.0 (C^{19}), 162.9 (C^{17}), 160.0 (d, $^3J_{C\text{-}P}$ 19, C^6), 152.8 (d, $^1J_{C\text{-}P}$ 167, C^2), 133.9 (d, $^3J_{C\text{-}P}$ 12, C^4), 132.7 (d, $^4J_{C\text{-}P}$ 3, C^{11}), 132.4 (d, $^2J_{C\text{-}P}$ 10, C^9), 129.9 (d, $^1J_{C\text{-}P}$ 140, C^8), 128.8 (d, $^2J_{C\text{-}P}$ 23, C^3), 128.5 (d, $^3J_{C\text{-}P}$ 13, C^{10}), 123.9 (d, $^4J_{C\text{-}P}$ 3, C^5), 93.5 (d, $^4J_{C\text{-}P}$ 2, C^{14}), 93.2 (C^{16}), 90.6 (C^{18}), 89.9 (C^{15}), 63.9 (C^7), 62.0 (d, $^2J_{C\text{-}P}$ 6, C^{12}), 56.2 (C^{20}), 55.6 (C^{21}), 16.6 (d, $^3J_{C\text{-}P}$ 6, C^{13}); ^{31}P

NMR (162 MHz, $CDCl_3$) δ +25.8; LCMS (ESI^+) *m/z* 468 $[M+H]^+$; HRMS (ESI^+) *m/z* 468.1568 $[M+H]^+$ ($C_{25}H_{27}NO_6P$ requires 468.1576).

{4-[2-(2,4,6-Trimethoxyphenyl)ethynyl]-6-[ethoxy(phenyl)phosphoryl]pyridin-2-yl}methyl methanesulfonate, 14

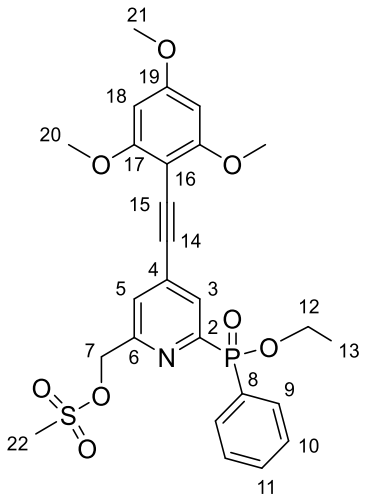

Ethyl [6-(hydroxymethyl)-4-[2-(2,4,6-trimethoxyphenyl)ethynyl] pyridin-2-yl](phenyl)phosphinate **13** (41 mg, 0.088 mmol) was dissolved in anhydrous tetrahydrofuran (2 mL) and the solution was cooled in an ice bath. Triethylamine (25 µL, 0.18 mmol) was added followed by dropwise addition of methanesulfonyl chloride (10 µL, 0.13 mmol), which resulted in the formation of a precipitate. The reaction was stirred under argon for 45 min and the solvent was removed under reduced pressure. The residue was redissolved in dichloromethane (20 mL) and washed with saturated brine solution (20 mL). The aqueous solution was re-extracted with dichloromethane (3 x 20 mL) and the organic layers combined, dried with $MgSO_4$, filtered and concentrated under reduced pressure to give a pale yellow oil (48 mg, quant.) which was used without further purification; ^1H NMR (400 MHz, $CDCl_3$) δ 8.14 (1 H, d, $^3J_{H\text{-}P}$ 6.0, H^3), 7.98-7.89 (2 H, m, H^9), 7.55 (1 H, s, H^{11}), 7.45 (2 H, d, $^4J_{H\text{-}P}$ 4.0, H^{10}), 7.43 (1 H, s, H^5), 6.08 (2 H, s, H^{18}), 5.28 (2 H, s, H^7), 4.11 (2 H, q, $^3J_{H\text{-}H}$ 7.0, H^{12}), 3.87 (6 H, s, H^{20}), 3.82 (3 H, s, H^{21}), 2.94 (3 H, s, H^{22}), 1.36 (3 H, t, $^3J_{H\text{-}H}$ 7.0, H^{13}); LCMS (ESI^+) *m/z* 546 $[M+H]^+$; HRMS (ESI^+) *m/z* 546.1345 $[M+H]^+$ ($C_{26}H_{29}NO_8PS$ requires 546.1352).

1,4,7-Tris({4-[2-(2,4,6-trimethoxyphenyl)ethynyl]-6-[ethoxy(phenyl)phosphoryl]pyridin-2-yl}methyl)-1,4,7-triazacyclononane (tri-ethyl ester of L^1)

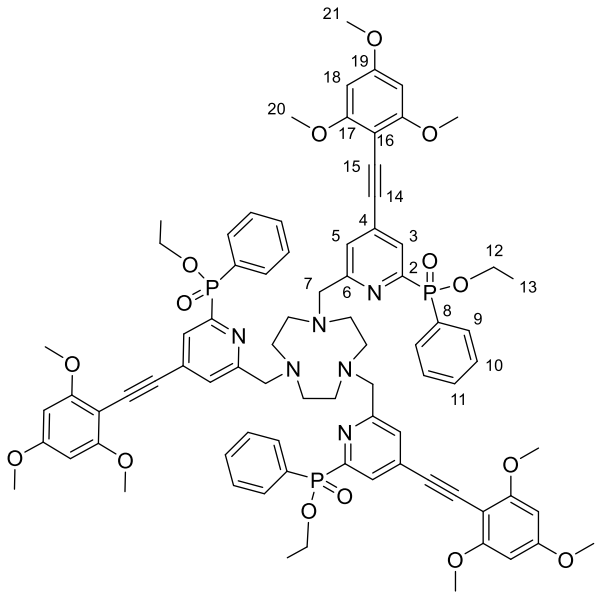

1,4,7-Triazacyclononane trihydrochloride (6.5 mg, 0.027 mmol) and potassium carbonate (15.0 mg, 0.109 mmol) were dissolved in anhydrous acetonitrile (1 mL). {4-[2-(2,4,6-Trimethoxyphenyl)ethynyl]-6-[ethoxy(phenyl)phosphoryl]pyridin-2-yl} methyl methanesulfonate **(6)** (48 mg, 0.088 mmol) was added as a solution in anhydrous acetonitrile (1 mL). The solution was stirred at 65 °C under argon for 16 h, at which time the solution was cooled to room temperature, and the solution decanted from excess potassium salts and concentrated under reduced pressure. The residue was purified by silica gel column chromatography (neat CH_2Cl_2 to 10% CH_3OH in CH_2Cl_2) to give a yellow film (7.1 mg, 18%); ^{1}H NMR (600 MHz, $CDCl_3$) δ 8.12 (3 H, d, $^3J_{H\text{-}P}$ 6.5, H^3), 7.85 (6 H, dd, $^3J_{H\text{-}P}$ 12.0, $^3J_{H\text{-}H}$ 7.0, H^9), 7.50 (3 H, t, $^3J_{H\text{-}H}$ 7.0, H^{11}), 7.44-7.40 (9 H , m, H^5 + H^{10}, peaks overlap), 6.11 (6 H, s, H^{18}), 4.14-4.09 (6 H, m, H^{12}), 3.90-3.89 (24 H, two overlapping singlets, H^7 + H^{20}), 3.85 (9 H, s, H^{21}), 3.03-2.65 (12 H, m, ring CH_2), 1.34 (9 H, t, $^3J_{H\text{-}H}$ 7.0, H^{13}); ^{13}C NMR (151 MHz, $CDCl_3$) δ 163.2 (C^{19}), 163.1 (C^{17}), 159.9 (C^6), 154.4 (d, $^1J_{C\text{-}P}$ 168, C^2), 134.2 (d, $^3J_{C\text{-}P}$ 15, C^4), 132.8 (C^{11}), 132.4 (d, $^2J_{C\text{-}P}$ 10, C^9), 130.5 (C^8), 129.5 (C^{10}), 128.6 (d, $^2J_{C\text{-}P}$ 12, C^3), 127.3 (C^5), 93.3 (C^{14}), 93.2 (C^{16}), 90.7 (C^{15}), 90.6 (C^{18}), 61.9 (d, $^2J_{C\text{-}P}$ 6, C^{12}), 59.6 (C^7), 56.2 (C^{20}), 55.7 (C^{21}), 51.5-45.4 (ring CH_2), 16.7 (d, $^3J_{C\text{-}P}$ 6, C^{13}); ^{31}P NMR (243 MHz, $CDCl_3$)

δ +25.7; LCMS (ESI$^+$) *m/z* 1478 [M+H]$^+$; HRMS (ESI$^+$) *m/z* 1477.551 [M+H]$^+$ ($C_{81}H_{88}N_6O_{15}P_3$ requires 1477.552).

[EuL^1]

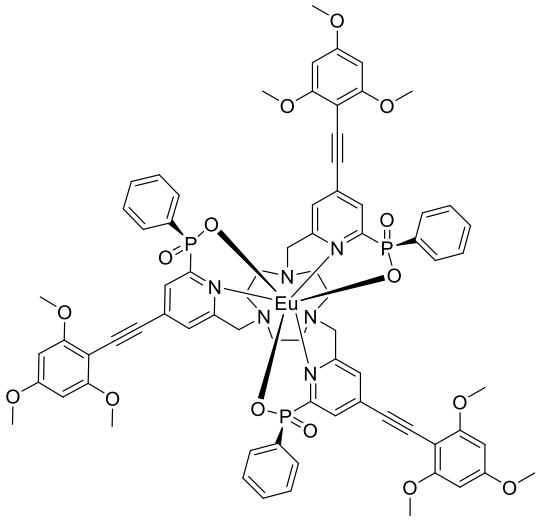

1,4,7-Tris({4-[2-(2,4,6-trimethoxyphenyl)ethynyl]-6-[ethoxy(phenyl)phosphoryl]pyridin-2-yl}methyl)-1,4,7-triazacyclononane (7 mg, 4.8 µmol) was dissolved in CD_3OD (0.5 mL) and a solution (0.3 mL) of 0.05 M potassium hydroxide in D_2O was added. The solution was stirred at 60 °C under argon for 4 days at which point further potassium hydroxide (1 mg) was added. The solution was stirred for a further 4 days. Hydrolysis of the phosphinate esters was monitored by ^{31}P NMR (starting material: +25.7 ppm, product: +16.5 ppm). After hydrolysis was complete, $EuCl_3{\cdot}6H_2O$ (1.8 mg, 4.9 µmol) was added and the reaction stirred at 60 °C for 18 h. The solution was then neutralised with dilute HCl and the solvent removed under reduced pressure. The crude product was purified by RP-HPLC (Method A, t_R = 13.5 min) to give the product (2.3 mg, 30%); LCMS (ESI$^+$) *m/z* 1548 [M($^2H_5$)+H]$^+$; λ_{max} (MeOH) = 356 nm; τ_{Eu} (MeOH) = 1.18 ms; Φ^{em}_{MeOH} = 39 (±5)%. Accurate mass analysis could not be obtained due to multiple deuteration of the complex during phosphinate ester hydrolysis. This resulted in many overlapping signals which obscured the monoisotopic mass. A base-catalysed mechanism for H/D exchange has been proposed for the acidic protons in the pyridyl-CH_2 linker:

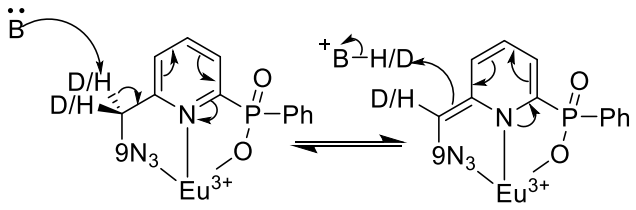

Because Eu^{3+} is relatively easy to reduce compared to other Ln^{3+} ions (forms a favourable $4f^7$ configuration), it can act as a charge sink to favour the reaction, via stabilisation of the non-aromatic vinylidene structure.

[2-(4-Methoxyphenyl)ethynyl]trimethylsilane,[80] 16

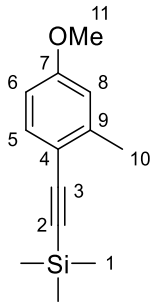

4-Bromo-3-methylanisole **15** (0.500 g, 2.49 mmol) was dissolved in anhydrous tetrahydrofuran (18 mL) and the solution was degassed (freeze-pump-thaw cycle x 3). Triethylamine (1.73 mL, 12.5 mmol) and ethynyltrimethylsilane (1.05 mL, 7.47 mmol) were added and the solution was degassed again (freeze-pump-thaw x 3). [1,1'-Bis(diphenylphosphino)ferrocene] dichloropalladium(II) (108 mg, 0.25 mmol) and copper (I) iodide (48 mg, 0.25 mmol) were added and the solution was stirred at 65 °C under argon for 90 h. The solvent was removed under reduced pressure and the brown residue was purified by silica gel column chromatography (neat hexane to 12% dichloromethane in hexane) to yield the desired product as a yellow oil (0.54 g, quant.); ^{1}H NMR (700 MHz, $CDCl_3$) δ 7.36 (1 H, d, $^3J_{H\text{-}H}$ 8.5, H^5), 6.72 (1 H, d, $^4J_{H\text{-}H}$ 2.0, H^8), 6.65 (1 H, dd, $^3J_{H\text{-}H}$ 8.5, $^4J_{H\text{-}H}$ 2.0, H^6), 3.79 (3 H, s, H^{11}), 2.41 (3 H, s, H^{10}), 0.25 (9 H, s, H^1); ^{13}C NMR (176 MHz, $CDCl_3$) δ 159.8 (C^7), 142.6 (C^9), 133.6 (C^5), 115.4 (C^4), 115.1 (C^8), 111.2 (C^6), 104.3 (C^3), 96.5 (C^2), 55.3 (C^{11}), 21.1 (C^{10}), 0.3 (C^1); GCMS-EI *m/z* 218 $[M]^+$.

1-Ethynyl-4-methoxy-2-methylbenzene,[80] 17

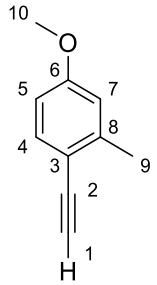

[2-(4-Methoxyphenyl)ethynyl]trimethylsilane **16** (0.542 g, 2.49 mmol) was dissolved in anhydrous tetrahydrofuran (9 mL) and triethylamine trihydrofluoride (4.1 mL, 25 mmol) was added. The resulting orange solution was stirred at 35 °C for 140 h after which the solvent was removed under reduced pressure. The residue was redissolved in water (20 mL) and this solution was extracted with toluene (3 x 20 mL). The organic layers were combined, dried with $MgSO_4$, filtered, combined and concentrated to give the product as a red oil (0.260 g, 71%); ^{1}H NMR (700 MHz, $CDCl_3$) δ 7.39 (1 H, d, $^3J_{H\text{-}H}$ 8.5, H^4), 6.74 (1 H, d, $^4J_{H\text{-}H}$ 3.0, H^7), 6.68 (1 H, dd, $^3J_{H\text{-}H}$ 8.5, $^4J_{H\text{-}H}$ 3.0, H^5), 3.80 (3 H, s, H^{10}), 3.19 (1 H, s, H^1), 2.43 (3 H, s, H^9); ^{13}C NMR (176 MHz, $CDCl_3$) δ 160.0 (C^6), 142.7 (C^8), 134.0 (C^4), 115.2 (C^7), 114.3 (C^3), 111.4 (C^5), 82.7 (C^2), 79.6 (C^1), 53.4 (C^{10}), 21.0 (C^9); GCMS-EI *m/z* 146 $[M]^+$.

Ethyl [6-(hydroxymethyl)-4-[2-(4-methoxy-2-methylphenyl)ethynyl] pyridin-2-yl](phenyl)phosphinate, 18

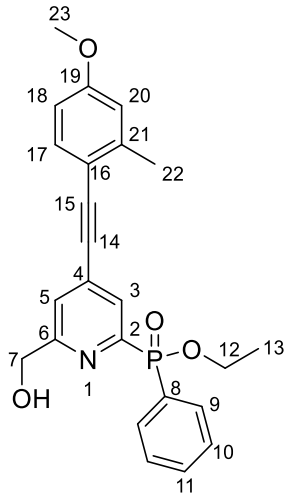

1-Ethynyl-4-methoxy-2-methylbenzene **17** (100 mg, 0.684 mmol) and ethyl [4-bromo-6-(hydroxymethyl)] pyridin-2-yl](phenyl)phosphinate (221 mg, 0.622 mmol) were dissolved in anhydrous tetrahydrofuran (4.5 mL) and the solution was degassed (freeze-pump-thaw cycle x 3). Triethylamine (435 µL, 316 mg, 3.12 mmol) was added and the solution was further degassed (freeze-pump-thaw x 3). [1,1'-Bis(diphenylphosphino)ferrocene]dichloropalladium(II) (51 mg, 0.062 mmol) and copper (I) iodide (24 mg, 0.12 mmol) were added and the solution was stirred at 65 °C under argon for 24 h. The solvent was removed under reduced pressure and the brown residue was purified by silica gel column chromatography (neat CH_2Cl_2 to 3% CH_3OH in CH_2Cl_2) to yield a brown oil. This was further purified by silica gel column chromatography (50:50 ethyl acetate:hexane to 80:20 ethyl acetate:hexane) to yield the desired product as a yellow oil (192 mg, 73%); ^{1}H NMR (600 MHz, $CDCl_3$) δ 8.07 (1 H, br s, H^3), 7.97 (2 H, dd, $^3J_{H\text{-}P}$ 11.5, $^3J_{H\text{-}H}$ 8.5, H^9), 7.54 (1 H, t, $^3J_{H\text{-}H}$ 7.0, H^{11}), 7.45-7.48 (2 H, m, H^{10}), 7.42 (1 H, d, $^3J_{H\text{-}H}$ 8.5, H^{17}), 7.40 (1 H, s, H^5), 6.77 (1 H, d, $^4J_{H\text{-}H}$ 2.5, H^{20}), 6.73 (1 H, dd, $^3J_{H\text{-}H}$ 8.5, $^4J_{H\text{-}H}$ 2.5, H^{18}), 4.76 (2 H, s, H^7), 4.09-4.19 (2 H, m, H^{12}), 3.81 (3 H, s, H^{23}), 2.47 (3 H, s, H^{22}), 1.38 (3 H, t, $^3J_{H\text{-}H}$ 7.0, H^{13}); ^{13}C NMR (151 MHz, $CDCl_3$) δ 160.7 (C^{19}), 160.4 (d, $^3J_{C\text{-}P}$ 19, C^6), 153.3 (d, $^1J_{C\text{-}P}$ 165, C^2), 143.0 (C^{21}), 134.1 (C^{17}), 133.3 (d, $^3J_{C\text{-}P}$ 12, C^4), 132.7 (C^{11}), 132.4 (d, $^2J_{C\text{-}P}$ 10, C^9), 129.8 (d, $^1J_{C\text{-}P}$ 141, C^8), 128.7 (C^3), 128.6 (d, $^3J_{C\text{-}P}$ 13, C^{10}), 123.9 (C^5), 115.4 (C^{20}), 113.8 (C^{16}), 111.7 (C^{16}), 95.3 (C^{15}), 89.1 (C^{14}), 64.0 (C^7), 62.0 (C^{12}), 55.4 (C^{23}), 21.1

(C^{22}), 16.7 (C^{13}); ^{31}P (243 MHz, $CDCl_3$) δ +25.5; LCMS (ESI^+) *m/z* 422 $[M+H]^+$; HRMS (ESI^+) *m/z* 422.1528 $[M+H]^+$ ($C_{24}H_{25}NO_4P$ requires 422.1521).

{4-[2-(4-Methoxy-2-methylphenyl)ethynyl]-6-[ethoxy(phenyl)phosphoryl]pyridin-2-yl}methyl methanesulfonate, 19

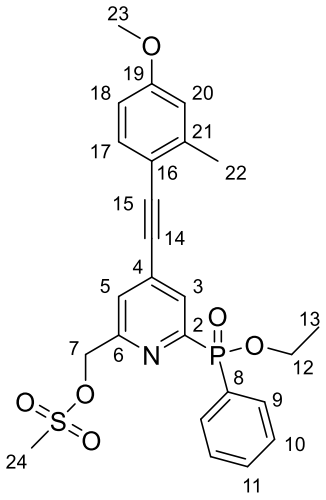

Ethyl [6-(hydroxymethyl)-4-[2-(4-methoxy-2-methylphenyl)ethynyl] pyridin-2-yl](phenyl)phosphinate **18** (96 mg, 0.23 mmol) was dissolved in anhydrous tetrahydrofuran (3 mL) and the solution was cooled in an ice bath. Triethylamine (64 µL, 0.46 mmol) was added followed by dropwise addition of methanesulfonyl chloride (27 µL, 0.34 mmol), which resulted in the formation of a precipitate. The reaction was stirred under argon for 45 min and the solvent was removed under reduced pressure. The residue was redissolved in dichloromethane (20 mL) and washed with saturated brine solution (30 mL). The aqueous solution was re-extracted with dichloromethane (3 x 20 mL) and the organic layers combined, dried with $MgSO_4$, filtered and concentrated under reduced pressure to give the product as a pale yellow oil (115 mg, quant.) which was used without further purification; ^1H NMR (400 MHz, $CDCl_3$) δ 8.13 (1 H, d, $^3J_{H\text{-}P}$ 6.0, H^3), 7.96 (2 H, dd, $^3J_{H\text{-}P}$ 12.0, $^3J_{H\text{-}H}$ 7.0, H^9), 7.54 (1 H, br s, H^{11}), 7.49-7.46 (2 H, m, H^{10}), 7.45 (1 H, br s, H^{17}), 7.42 (1 H, s, H^5), 6.77 (1 H, d, $^4J_{H\text{-}H}$ 2.0, H^{20}), 6.73 (1 H, dd, $^3J_{H\text{-}H}$ 8.5, $^4J_{H\text{-}H}$ 2.0, H^{18}), 5.32 (2 H, s, H^7), 4.14 (2 H, q, $^3J_{C\text{-}P}$ 7.0, H^{12}), 3.81 (3 H, s, H^{23}), 2.99 (3 H, s, H^{24}), 2.48 (3 H, s, H^{22}),

1.37 (3 H, t, $^{3}J_{H\text{-}H}$ 7.0, H^{13}); ^{31}P NMR (162 MHz, $CDCl_3$) δ +24.9; LCMS (ESI^+) *m/z* 500$[M+H]^+$; HRMS (ESI^+) *m/z* 500.1286 $[M+H]^+$ ($C_{25}H_{27}NO_6PS$ requires 500.1297).

1,4,7-Tris({4-[2-(4-methoxy-2-methylphenyl)ethynyl]-6-[ethoxy(phenyl)phosphoryl]pyridin-2-yl}methyl)-1,4,7-triazacyclononane (tri-ethyl ester of L^2)

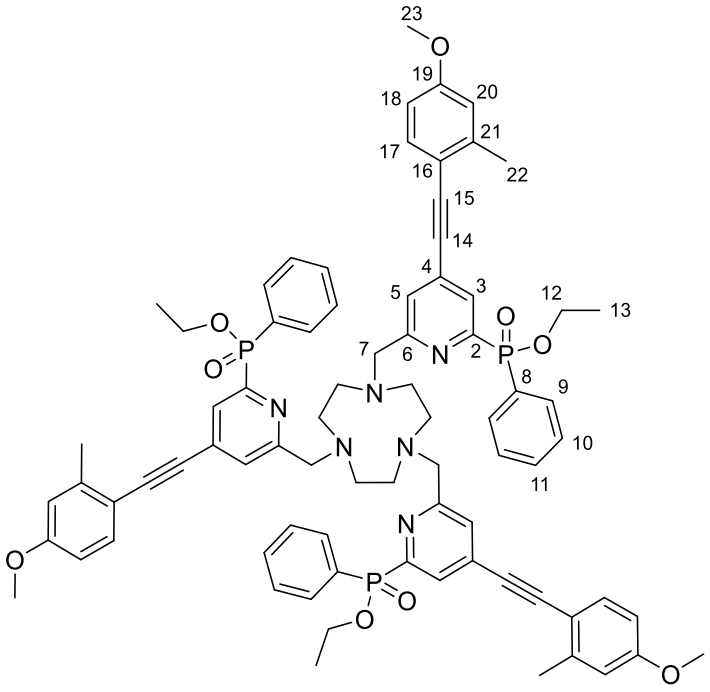

{4-[2-(4-Methoxy-2-methylphenyl)ethynyl]-6-[ethoxy(phenyl)phosphoryl]pyridin-2-yl}methyl methanesulfonate (114 mg, 0.228 mmol), 1,4,7-triazacyclononane trihydrochloride (16.5 mg, 0.0691 mmol) and potassium carbonate (189 mg, 1.37 mmol) were dissolved in anhydrous acetonitrile (5 mL). The solution was stirred at 65 °C under argon for 66 h, at which time the solution was cooled to room temperature, and the solution decanted from excess potassium salts and concentrated under reduced pressure. Attempts to find a suitable solvent system for column chromatography were unsuccessful so the crude product (66 mg) was taken on without further purification; ^{1}H NMR (700 MHz, $CDCl_3$) δ 8.03 (3 H, d, $^{3}J_{H\text{-}P}$ 5.5, H^3), 7.95 (6 H, dd, $^{3}J_{H\text{-}P}$ 12.0, $^{3}J_{H\text{-}H}$ 7.5, H^9), 7.56 (3 H, s, H^5), 7.44-7.41 (3 H, m, H^{11}), 7.39 (3 H, d, $^{3}J_{H\text{-}H}$ 7.5, H^{17}), 7.37-7.36 (6 H, m, H^{10}), 6.74 (3 H, d, $^{4}J_{H\text{-}H}$ 2.0, H^{20}),

6.70 (3 H, dd, $^{3}J_{H\text{-}H}$ 7.5, $^{4}J_{H\text{-}H}$ 2.0, H^{18}), 4.13-4.06 (6 H, m, H^{12}), 3.83 (6 H, s, H^{7}), 3.79 (9 H, s, H^{23}), 2.75 (12 H, br s, ring CH_2), 2.43 (9 H, s, H^{22}), 1.32 (9 H, t, $^{3}J_{H\text{-}H}$ 7.0, H^{13}); ^{13}C NMR (176 MHz, $CDCl_3$) δ 161.5 (d, $^{3}J_{C\text{-}P}$ 20, C^{6}), 160.4 (C^{19}), 153.8 (d, $^{1}J_{C\text{-}P}$ 167, C^{2}), 142.8 (C^{21}), 133.8 (C^{17}), 132.5 (d, $^{3}J_{C\text{-}P}$ 12, C^{4}), 132.4 (d, $^{2}J_{C\text{-}P}$ 10, C^{9}), 132.3 (d, $^{4}J_{C\text{-}P}$ 2, C^{11}), 130.1 (d, $^{1}J_{C\text{-}P}$ 139, C^{8}), 128.2 (d, $^{3}J_{C\text{-}P}$ 13, C^{10}), 127.9 (d, $^{2}J_{C\text{-}P}$ 24, C^{3}), 126.3 (C^{5}), 115.2 (C^{20}), 114.0 (C^{16}), 111.5 (C^{18}), 94.5 (C^{15}), 89.5 (C^{14}), 63.7 (C^{7}), 61.6 (d, $^{2}J_{C\text{-}P}$ 6, C^{12}), 55.6 (br s, ring CH_2), 55.3 (C^{23}), 21.0 (C^{22}), 16.5 (d, $^{3}J_{C\text{-}P}$ 6, C^{13}); ^{31}P NMR (283 MHz, $CDCl_3$) δ +25.5; LCMS (ESI^+) *m/z* 1340 $[M+H]^+$; HRMS (ESI^+) *m/z* 1339.538 $[M+H]^+$ ($C_{78}H_{82}N_6O_9P_3$ requires 1339.536).

The ^{1}H NMR spectrum (700 MHz, $CDCl_3$) of the crude mixture is shown to establish the extent of purity of the ligand used in the next step.

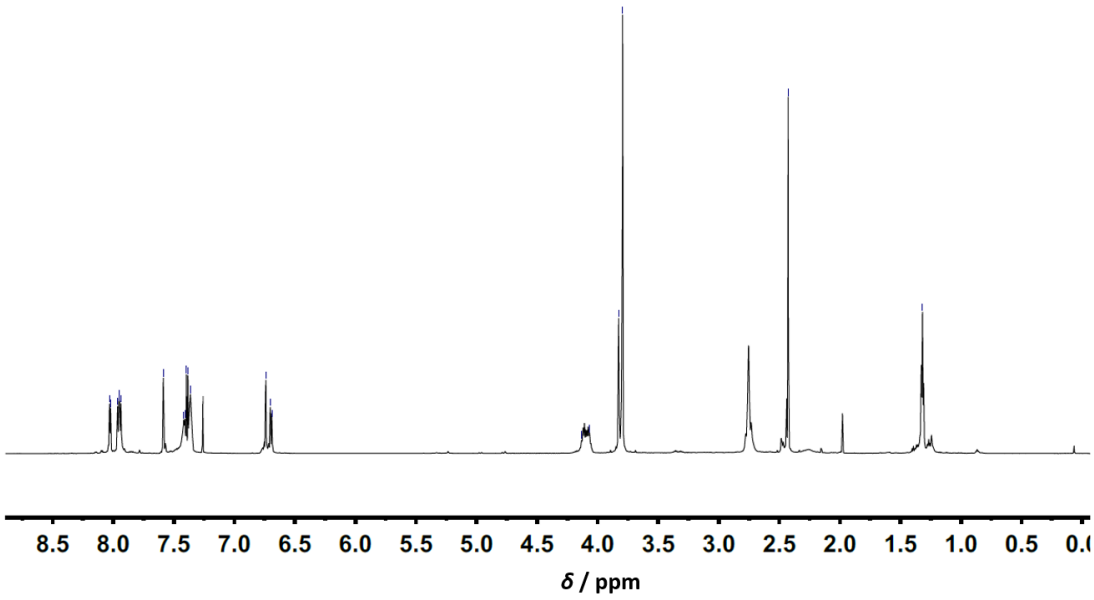

[EuL^2]

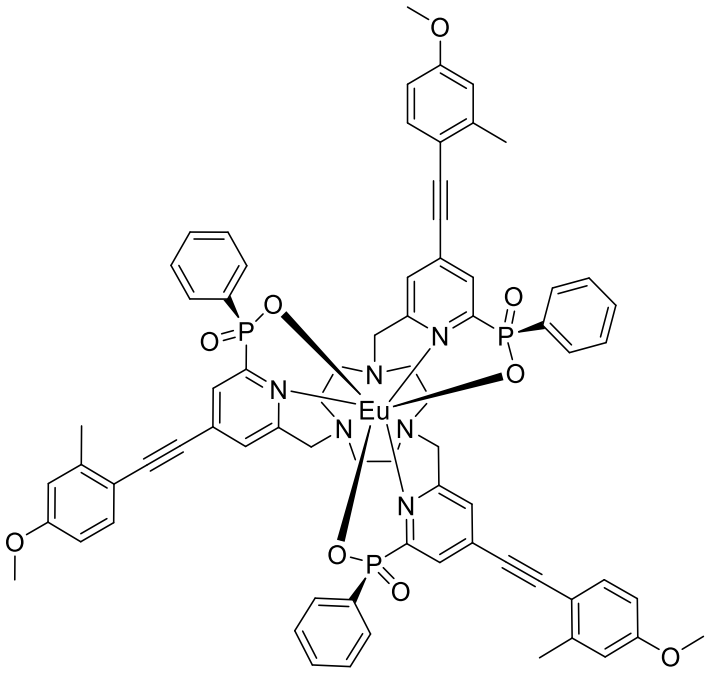

1,4,7-Tris({4-[2-(4-methoxy-2-methylphenyl)ethynyl]-6-[ethoxy(phenyl)phosphoryl]pyridin-2-yl}methyl)-1,4,7-triazacyclononane (18.4 mg, 0.0137 mmol) and potassium hydroxide (6 mg, 0.1 mmol) were dissolved in a H_2O/CH_3OH mixture (2 mL, v/v 3:1) and stirred at 60 °C under argon for 20 days. Phosphinate ester hydrolysis was confirmed by ^{31}P NMR (starting material: +25.5 ppm, product: +15.5 ppm). $EuCl_3{\cdot}6H_2O$ (6 mg, 0.0164 mmol) was added and the reaction stirred at 60 °C for 19 h. The solution was neutralised with dilute HCl and the solvent removed under reduced pressure. The crude product was purified by RP-HPLC (Method A, t_R = 14.5 min) to give the product as a white solid (5.2 mg, 29%); LCMS (ESI$^+$) *m/z* 1403 $[M+H]^+$; HRMS (ESI$^+$) *m/z* 1403.341 $[M(^{151}Eu)+H]^+$ ($C_{72}H_{67}N_6O_9P_3{}^{151}Eu$ requires 1403.338); λ_{max} (MeOH) = 343 nm; τ_{Eu} (MeOH) = 1.22 ms; Φ^{em}_{MeOH} = 50 (±5)%.

Dimethyl 4-chloropyridine-2,6-dicarboxylate,[150] 21

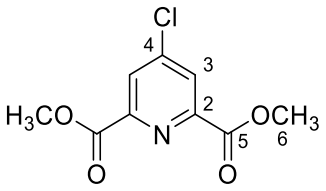

Chelidamic acid **20** (949 mg, 5.18 mmol) was dissolved in thionyl chloride (6 mL) and 5 drops of dimethylformamide were added to aid solubility. The mixture was stirred at 100 °C for 48 h, after which the solvent was removed by vacuum distillation. The residue was redissolved in anhydrous dichloromethane (5 mL) and cooled to 0 °C. Anhydrous methanol (5 mL) was added dropwise over 10 min the solution was allowed to warm to room temperature. The solvent was removed under reduced pressure. The residue was washed with a saturated sodium bicarbonate solution (10 mL) and extracted into dichloromethane (3 x 40 mL). The organic layers were combined and washed successively with water (40 mL) and brine (40 mL), dried over $MgSO_4$, filtered and the solvent removed under reduced pressure to yield the title product as an orange solid (855 mg, 72%) which was used without further purification; m.p. 139-141 °C (lit.[222] 139-140 °C); ^{1}H NMR (400 MHz; $CDCl_3$) δ 8.29 (2 H, s, H^3), 4.03 (6 H, s, H^6); ^{13}C NMR (101 MHz, $CDCl_3$) δ 163.7 (C^5), 149.1 (C^2), 146.3(C^4), 127.9 (C^3), 53.1 (C^6); LCMS (ESI^+) *m/z* 230 [M(^{35}Cl)+H]$^+$; HRMS (ESI^+) *m/z* 230.0222 [M(^{35}Cl)+H]$^+$ ($C_9H_9NO_4Cl$ requires 230.0220).

Dimethyl 4-iodopyridine-2,6-dicarboxylate,[150] 22

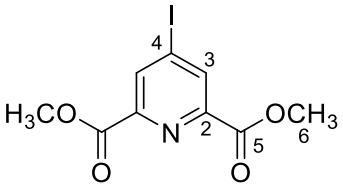

Dimethyl 4-chloropyridine-2,6-dicarboxylate **21** (353 mg, 1.54 mmol) and sodium iodide (2.30 g, 15.4 mmol) were dissolved in anhydrous acetonitrile (20 mL) and the solution was sonicated (in a bath sonicator) for 30 min under argon. Acetyl chloride

(0.33 mL, 4.62 mmol) was added resulting in an orange suspension, which was sonicated for a further 1 h. The solvent was removed under reduced pressure and the residue was redissolved in dichloromethane (40 mL), washed with sat. sodium carbonate solution (25 mL). The aqueous layer was then extracted into dichloromethane (3 x 20 mL). The organic layers were then combined, washed successively with sat. sodium thiosulfate solution (30 mL) and water (30 mL), dried over $MgSO_4$, filtered and concentrated. The crude mixture was purified by silica gel column chromatography (neat CH_2Cl_2 to 1% CH_3OH in CH_2Cl_2) to yield the title product as an off-white solid (352 mg, 72%); m.p. 180-182 °C (lit.[223] 179-180 °C); ^{1}H NMR (400 MHz, $CDCl_3$) δ 8.63 (2 H, s, H^3), 4.00 (6 H, s, H^6); ^{13}C NMR (101 MHz, $CDCl_3$) δ 163.9 (C^5), 148.4 (C^2), 137.2 (C^3), 107.1 (C^4), 53.5 (C^6); LCMS (ESI^+) *m/z* 322 $[M+H]^+$; HRMS (ESI^+) *m/z* 321.9584 $[M+H]^+$ ($C_9H_9NO_4I$ requires 321.9576).

Methyl 6-(hydroxymethyl)-4-iodopicolinate,[150] 23

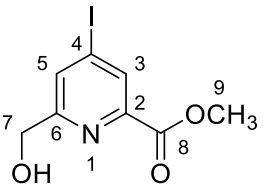

Dimethyl 4-iodopyridine-2,6-dicarboxlyate **22** (353 mg, 1.10 mmol) was dissolved in a mixture of anhydrous dichloromethane (3 mL) and anhydrous methanol (2 mL) and cooled in ice under argon. Sodium borohydride (46 mg, 1.21 mmol) was added and the reaction was stirred at 0 °C and monitored by TLC. After 30 min, 1 M HCl (2 mL) was added. The volatile solvents were removed under reduced pressure and the aqueous solution was extracted with ethyl acetate (3 x 25 mL). The organic layers were combined, dried over $MgSO_4$, filtered and concentrated. The crude mixture was purified by silica gel column chromatography (neat CH_2Cl_2 to 1.5% CH_3OH in CH_2Cl_2) to yield the title product as a white solid (212 mg, 66%); m.p. 138-139 °C (lit.[223] 140-141 °C); ^{1}H NMR (700 MHz, $CDCl_3$) δ 8.36 (1 H, s, H^3), 7.98 (1 H, s, H^5), 4.81 (2 H, s, H^7), 3.97 (3 H, s, H^9); ^{13}C NMR (176 MHz, $CDCl_3$) δ 164.4 (C^8), 161.4

(C^6), 147.3 (C^2), 133.4 (C^5), 133.1 (C^3), 107.1 (C^4), 64.3 (C^7), 53.3 (C^9); LCMS (ESI^+) *m/z* 294 $[M+H]^+$; HRMS (ESI^+) *m/z* 293.9633 $[M+H]^+$ ($C_8H_9NO_3I$ requires 293.9627).

Methyl 4-iodo-6-[(methanesulfonyloxy)methyl]pyridine-2-carboxylate, 24

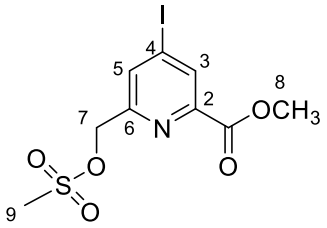

Methyl 6-(hydroxymethyl)-4-iodopicolinate **23** (212 mg, 0.72 mmol) was dissolved in anhydrous tetrahydrofuran (8 mL) and cooled to 0 °C under argon. Triethylamine (84 µL, 124 mg, 1.09 mmol) was added, followed by dropwise addition of methanesulfonyl chloride (200 µL, 146 mg, 1.44 mmol). The mixture was stirred under argon for 30 min at which point TLC showed all starting material had been consumed. The solvent was removed under reduced pressure and residue redissolved in dichloromethane (60 mL), washed with water (50 mL) and the aqueous layer was extracted with dichloromethane (3 x 50 mL). The organic layers were combined, dried over $MgSO_4$, filtered and concentrated to give a pale yellow solid (268 mg, 97%) which was used immediately without further purification; ^1H NMR (400 MHz, $CDCl_3$) δ 8.46 (1 H, s, H^3), 8.04 (1 H, s, H^5), 5.36 (2 H, s, H^7), 4.00 (3 H, s, H^8), 3.16 (3 H, s, H^9); LCMS (ESI^+) *m/z* 372 $[M+H]^+$; HRMS (ESI^+) *m/z* 371.9396 $[M+H]^+$ ($C_9H_{11}NO_5SI$ requires 371.9403).

1,4,7-Tris({4-iodo-6-[methoxycarbonyl]-pyridin-2-yl}methyl)-1,4,7-triazacyclononane (trimethyl ester of L^{11})

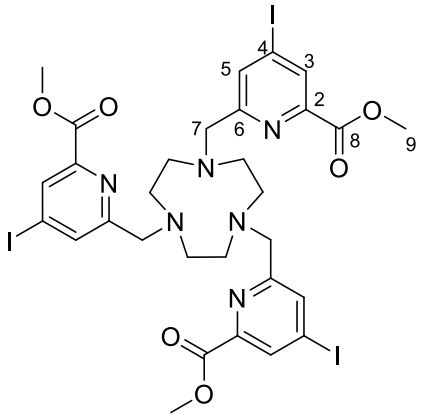

Methyl 4-iodo-6-[(methanesulfonyloxy)methyl]pyridine-2-carboxylate **24** (260 mg, 0.70 mmol) and 1,4,7-triazacyclononane trihydrochloride (54 mg, 0.23 mmol) and potassium carbonate (194 mg, 1.40 mmol) were dissolved in anhydrous acetonitrile (15 mL) and stirred under argon at 60 °C for 19 h, at which point the mixture was allowed to cool to room temperature. The yellow solution was decanted from insoluble salts and concentrated to yield a yellow oil (202 mg, 94%); ^{1}H NMR (700 MHz, $CDCl_3$) δ 8.31 (3 H, s, H^3), 8.18 (3 H, s, H^5), 3.94 (9 H, s, H^9), 3.91 (6 H, s, H^7), 2.88 (12 H, br s, ring CH_2); ^{13}C NMR (176 MHz, $CDCl_3$) δ 164.6 (C^8), 161.9 (C^6), 147.6 (C^2), 135.6 (C^5), 132.8 (C^3), 106.7 (C^4), 63.9 (br, C^7), 56.0 (br, ring CH_2), 53.2 (C^9); LCMS (ESI^+) *m/z* 955 $[M+H]^+$; HRMS (ESI^+) 954.9659 $[M+H]^+$ ($C_{30}H_{34}N_6O_6I_3$ requires 954.9674).

[EuL^{11}]

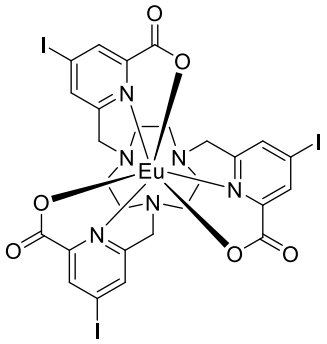

The trimethyl ester of **L^{11}** (55 mg, 0.058 mmol) was suspended in 0.1 M aqueous sodium hydroxide and acetonitrile was added dropwise until the solid dissolved. The solution was stirred at room temperature for 19 h until complete ester hydrolysis was observed by mass spectrometry. The solution was neutralised using dilute hydrochloric acid and the solvent was removed under reduced pressure. The resulting solid was redissolved in water (3 mL) and $EuCl_3 \cdot 6H_2O$ (24 mg, 0.064 mmol) was added. The pH was adjusted to 6 with dilute HCl and the solution was stirred at 70 °C for 20 h during which time a white precipitate formed. The solution was cooled and the solid was isolated by centrifugation. The solution that was removed showed no evidence of containing europium complex by either mass spectrometry or photophysical analysis. The solid could not be dissolved in any common laboratory solvents. The solid was suspended in DMSO and stirred at 70 °C for 48 h after which time enough solid had dissolved for crude photophysical characterisation that established that a Eu(III) complex had been formed; λ_{max} (DMSO) = 277 nm; τ_{Eu} (DMSO) = 1.18 ms.

[EuL^{12}] and [EuL^{13}]

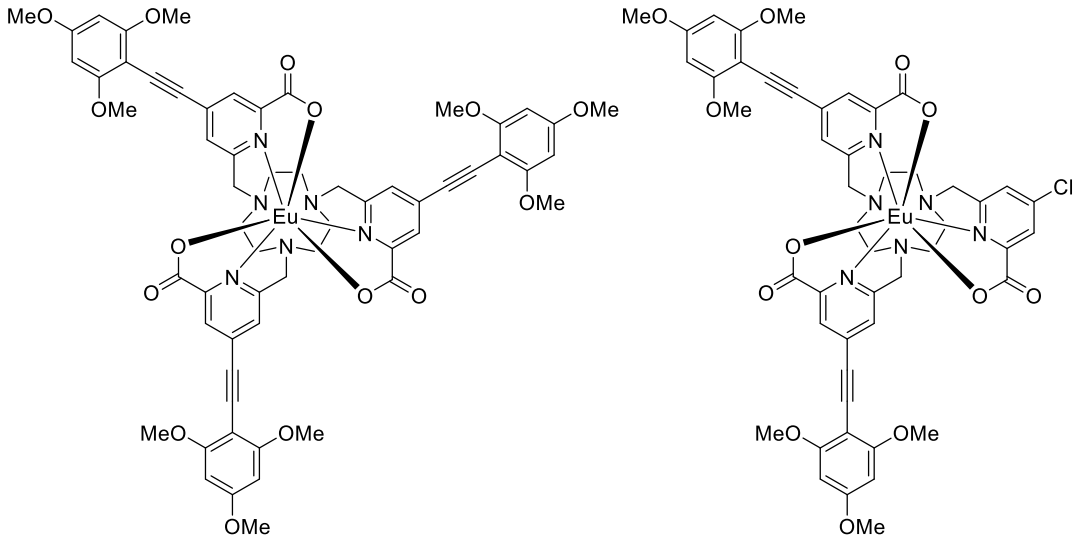

Complex **[EuL^{11}]** (50 mg, 0.047 mmol) and 2-ethynyl-1,3,5-trimethoxybenzene (29 mg, 0.15 mmol) were suspended in dimethylsulfoxide (5 mL). The suspension was degassed using freeze-pump-thaw cycles (x 3). Triethylamine (80 µL, 58 mg, 0.57 mmol) was added and the suspension was degassed again (freeze-pump-thaw x 1). [1,1'-Bis(diphenylphosphino)ferrocene]dichloropalladium(II) (14 mg, 0.017 mmol) and copper (I) iodide (7 mg, 0.034 mmol) were added and the solution was stirred at 65 °C under argon for 19 h. The reaction was cooled to room temperature and added dropwise to 400 mL of ice cold stirring diethyl ether. The solution was decanted and the brown precipitate collected. This crude product was subjected to column chromatography (alumina, CH_2Cl_2 to 2% CH_3OH in CH_2Cl_2) to remove the catalysts. Mass spectrometry revealed the presence of a second species in the product-containing fractions. This mixture was further purified by RP-HPLC (Method B) to give **[EuL^{12}]** as a white solid (t_R = 22.1 min, 4.3 mg) and **[EuL^{13}]** as a white solid (t_R = 21.0, 1.3 mg); **[EuL^{12}]**: HRMS (ESI$^+$) *m/z* 1253.315 [M(^{151}Eu)+H]$^+$ ($C_{60}H_{58}N_6O_{15}{}^{151}$Eu requires 1253.316); λ_{max} (MeOH) = 363 nm; τ_{Eu} (MeOH) = 0.55 ms; Φ_{MeOH}^{em} = 24 (±5)%; **[EuL^{13}]**: HRMS (ESI$^+$) *m/z* 1097.213 [M(^{151}Eu)+H]$^+$ ($C_{49}H_{47}N_6O_{12}Cl^{151}$Eu requires 1097.214); λ_{max} (MeOH) = 362 nm; τ_{Eu} (MeOH) = 0.58 ms; Φ_{MeOH}^{em} = 20 (±5)%.

The chlorine substitution to form **[EuL^{13}]** could have occurred in a number of steps. No trace of the chlorine substituted species was observed in the alkylation reaction to form the trimethyl ester of L^{10}. However, the complexation reaction is carried out with europium(III) chloride so it is possible that a chloride ion displaces an iodide during the reaction which is carried out at increased temperature. Additionally, the Sonogashira coupling reaction to form **[EuL^{12}]** uses a precatalyst with coordinated chlorides which could displace the iodide in this step. The 4-chloropyridine will not participate in a Sonogashira reaction under the conditions used above, hence a chloropyridine arm is preserved in the by-product **[EuL^{13}]**.

Dimethyl 4-bromopyridine-2,6-dicarboxylate,[191] **25**

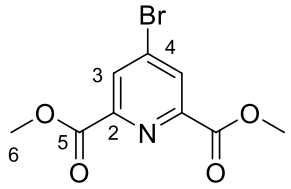

Chelidamic acid **20** (1.00 g, 5.48 mmol) and phosphorus pentabromide (7.31 g, 16.9 mmol) were heated to 90 °C and stirred for 3 h (CAUTION: HBr produced). The reaction mixture was cooled and the residue dissolved in anhydrous chloroform (30 mL). The resulting deep red solution was cooled in an ice bath and anhydrous methanol (20 mL) was added dropwise with stirring. The solvents were removed under reduced pressure. Cold water (100 mL) was added and the suspension left to stand in an ice bath for 1 h. The precipitate was isolated and dried under vacuum, to yield an orange solid (1.05 g, 70%); m.p. 164-166 °C (lit.[224] 166-167 °C); ^{1}H NMR (700 MHz, $CDCl_3$) δ 8.40 (2 H, s, H^3), 3.98 (6 H, s, H^6); ^{13}C NMR (176 MHz, $CDCl_3$) δ 164.0 (C^5), 149.1 (C^2), 135.1 (C^4), 131.3 (C^3), 53.5 (C^6); LCMS (ESI$^+$) *m/z* 274 [M(^{79}Br)+H]$^+$; HRMS (ESI$^+$) 273.9713 [M(^{79}Br)+H]$^+$ ($C_9H_9NO_4{}^{79}Br$ requires 273.9715).

Methyl 6-(hydroxymethyl)-4-bromopicolinate,[191] 26

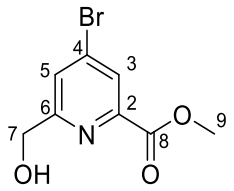

Dimethyl 4-bromopyridine-2,6-dicarboxylate **25** (1.05 g, 3.83 mmol) was dissolved in a mixture of anhydrous dichloromethane and anhydrous methanol (15 mL, 3:2). The solution was cooled in ice. Sodium borohydride (160 mg, 4.22 mmol) was added and the reaction was stirred and monitored by thin layer chromatography (silica, CH_2Cl_2:MeOH, 95:5, R_f (starting material) 0.81, R_f (product) 0.31, R_f (diol) 0.1). After 30 min 1 M aqueous HCl (10 mL) was added and the mixture stirred for 30 min. The organic solvents were removed under reduced pressure and the aqueous solution was extracted with ethyl acetate (3 x 100 mL). The organic layers were combined, dried over $MgSO_4$, filtered and concentrated to give a pale yellow oil, which was purified by silica gel column chromatography (neat CH_2Cl_2 to 3% CH_3OH in CH_2Cl_2) to yield the product as a white solid (652 mg, 69%); m.p. 128-130 °C (lit.[191] 131-132 °C); ^{1}H NMR (600 MHz, $CDCl_3$) δ 8.20 (1 H, d, $^4J_{H\text{-}H}$ 1.0, H^3), 7.78 (1 H, d, $^4J_{H\text{-}H}$ 1.0, H^5), 4.86 (2 H, s, H^7), 4.01 (3 H, s, H^9); ^{13}C NMR (151 MHz, $CDCl_3$) δ 164.3 (C^8), 161.8 (C^6), 147.9 (C^2),135.1 (C^4), 127.5 (C^3), 127.4 (C^5), 64.4 (C^7), 53.4 (C^9); LCMS (ESI^+) *m/z* 246 $[M(^{79}Br)+H]^+$; HRMS (ESI^+) 245.9785 $[M(^{79}Br)+H]^+$ ($C_8H_9NO_3{}^{79}Br$ requires 245.9766).

Methyl 4-bromo-6-[(methanesulfonyloxy)methyl]pyridine-2-carboxylate, 27

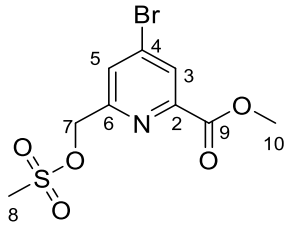

Methyl 6-(hydroxymethyl)-4-bromopicolinate **26** (100 mg, 0.407 mmol) was dissolved in anhydrous tetrahydrofuran (4 mL). Triethylamine (110 µL, 0.814 mmol) was added and the solution was cooled in ice. Methanesulfonyl chloride (50 µL,

0.61 mmol) was added dropwise and the resulting suspension stirred in an ice bath under argon. Monitoring by TLC (silica, 5% CH_3OH in CH_2Cl_2) showed complete consumption of starting material after 30 min. The solvents were removed under reduced pressure and the residue dissolved in dichloromethane (30 mL). This solution was washed with water (20 mL) and the aqueous solution was extracted with dichloromethane (3 x 20 mL). The organic extracts were combined, dried over $MgSO_4$, filtered and concentrated to yield a pale yellow solid (130 mg, 99%) which was used immediately without further purification; ^{1}H NMR (400 MHz, $CDCl_3$) δ 8.24 (1 H, d, $^4J_{H\text{-}H}$ 1.5, H^3), 7.84 (1 H, d, $^4J_{H\text{-}H}$ 1.5, H^5), 5.38 (2 H, s, H^7), 3.99 (3 H, s, H^{10}), 3.16 (3 H, s, H^8); LCMS (ESI^+) *m/z* 324 $[M+H]^+$; HRMS 323.9547 $[M+H]^+$ ($C_9H_{11}NO_5S^{79}Br$ requires 323.9541).

1,4,7-Tris({4-bromo-6-[methoxycarbonyl]-pyridin-2-yl}methyl)-1,4,7-triazacyclononane (trimethyl ester of L^{14})

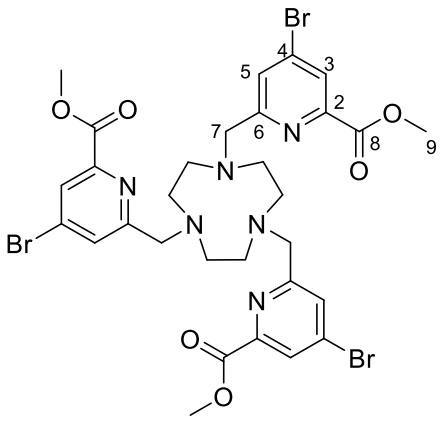

Methyl 4-bromo-6-[(methanesulfonyloxy)methyl]pyridine-2-carboxylate **27** (131 mg, 0.407 mmol) and 1,4,7-triazacyclononane trihydrochloride (31 mg, 0.13 mmol) and potassium carbonate (110 mg, 0.800 mmol) were dissolved in anhydrous acetonitrile (7 mL) and stirred under argon at 60 °C for 24 h, at which point the mixture was allowed to cool to room temperature. The yellow solution was decanted from insoluble salts and concentrated. The crude residue was purified by column chromatography (alumina, neat CH_2Cl_2 to 1% CH_3OH in CH_2Cl_2) to yield a yellow oil (61 mg, 58%) ; ^{1}H NMR (700 MHz, $CDCl_3$) δ 8.12 (3 H, dd, $^4J_{H\text{-}H}$ 2.0, H^3), 7.97 (3 H, dd, $^4J_{H\text{-}H}$ 2.0, H^5), 4.07 (6 H, br s, H^7), 3.93 (9 H, s, H^9), 3.03 (12 H,

br s, ring CH_2); ^{13}C NMR (176 MHz, $CDCl_3$) δ 164.6 (C^8), 160.8 (C^6), 148.4 (C^2), 134.5 (C^4), 129.8 (C^5), 127.4 (C^3), 63.0 (br, C^7), 55.1 (br, ring CH_2), 53.2 (C^9); LCMS (ESI^+) *m/z* 811 $[M+H]^+$; HRMS (ESI^+) 811.0101 $[M+H]^+$ ($C_{33}H_{34}N_6O_6{}^{79}Br_3$ requires 811.0090).

[EuL^{13}]

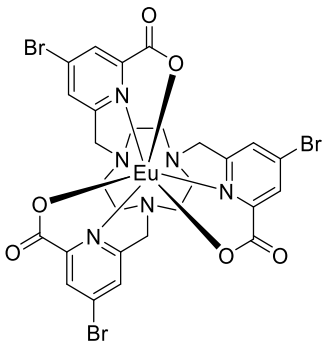

The trimethyl ester of **L^{14}** (61 mg, 0.066 mmol) was dissolved in methanol (3 mL) and sodium hydroxide (0.1 M, 3 mL) was added. The resulting solution was stirred at 50 °C for 3 days after which the organic solvent was removed under reduced pressure. The remaining aqueous solution was neutralised using dilute HCl and $EuCl_3{\cdot}6H_2O$ (30 mg, 0.082 mmol) was added. This solution was stirred at 50 °C for 48 h during which time a precipitate formed. The solid was isolated from the solution by centrifugation, but could not be dissolved in any common laboratory solvents for analysis.

Ethyl methylphosphinate,[188] 29

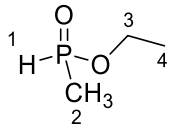

Water (0.2 mL, 11.1 mmol) was added to neat diethyl methylphosphonite **28** (1.66 mL, 1.51 g, 11.1 mmol) and the mixture was stirred under argon at room temperature for 18 h. Conversion to ethyl methylphosphinate was confirmed by ^1H and ^{31}P NMR and the product was used directly without further purification, containing one equivalent of ethanol; ^1H NMR (400 MHz, $CDCl_3$) δ 7.14 (1 H, d, $^1J_{H\text{-}P}$

78539, H^1), 4.05 (2 H, dq, $^3J_{H\text{-}P}$ 41, $^3J_{H\text{-}H}$ 7.0, H^3), 1.47 (3 H, d, $^2J_{H\text{-}P}$ 15.0, H^2), 1.29 (3 H, 78t, $^3J_{H\text{-}H}$ 7.0, H^4); ^{31}P NMR (162 MHz, $CDCl_3$) δ +33.7.

Ethyl (6-methyl-4-nitropyridin-2-yl)methylphosphinate,[188] **30**

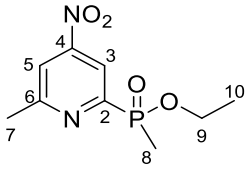

2-Bromo-6-methyl-4-nitropyridine **8** (2.0 g, 9.2 mmol), ethyl methylphosphinate **29** (containing 1 equivalent of ethanol) (1.2 g, 11.1 mmol) and triethylamine (4.5 mL, 3.3 g, 32.3 mmol), were added to degassed (3 x freeze-pump-thaw) anhydrous toluene (20 mL). Argon was bubbled through the solution for 45 min. Under positive flow of argon, [1,1'-bis(diphenylphosphino)ferrocene]dichloropalladium(II) (0.380 g, 0.47 mmol) was added. The resulting red solution was stirred at 80 °C under argon for 20 h. The solvent was removed under reduced pressure and the resulting black oil was purified by silica gel column chromatography (1:1 hexane:ethyl acetate to 1:3 hexane:ethyl acetate) to yield an off-white solid (1.75 g, 78%); m.p. 78-80 °C; ^{1}H NMR (600 MHz, $CDCl_3$) δ 8.49 (1 H, dd, $^3J_{H\text{-}P}$ 6.0, $^4J_{H\text{-}H}$ 1.5, H^3), 7.94 (1 H, d, $^3J_{H\text{-}H}$ 1.5, H^5), 4.15-3.84 (2 H, m, H^9), 2.75 (3 H, s, H^7), 1.78 (3 H, d, $^2J_{H\text{-}P}$ 15.0, H^8), 1.25 (3 H, t, $^3J_{H\text{-}H}$ 7.0, H^{10}); ^{13}C NMR (151 MHz, $CDCl_3$) δ 163.1 (d, $^3J_{C\text{-}P}$ 21, C^6), 158.0 (d, $^1J_{C\text{-}P}$ 157, C^2), 154.2 (d, $^3J_{C\text{-}P}$ 12, C^4), 117.8 (d, $^4J_{C\text{-}P}$ 3, C^5), 117.1 (d, $^2J_{C\text{-}P}$ 23, C^3), 61.5 (d, $^2J_{C\text{-}P}$ 6, C^9), 24.9 (s, C^7), 16.5 (d, $^3J_{C\text{-}P}$ 6, C^{10}), 13.5 (d, $^1J_{C\text{-}P}$ 106, C^8); ^{31}P NMR (243 MHz, $CDCl_3$) δ +38.0; LCMS (ESI^+) *m/z* 245 $[M+H]^+$; HRMS (ESI^+) 245.0703 $[M+H]^+$ ($C_9H_{14}N_2O_4P$ requires 245.0691).

(4-Bromo-6-methylpyridin-2-yl)methylphosphinic acid,[188]

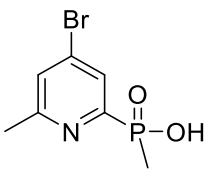

Ethyl (6-methyl-4-nitropyridin-2-yl)methylphosphinate **30** (1.38 g, 5.65 mmol) was dissolved in acetyl bromide (21 mL, 170 mmol) and the mixture was stirred at 70 °C.

The reaction was monitored by LCMS and after 48 h all starting material had been consumed. The solution was cooled in an ice bath and methanol (60 mL) was added dropwise with stirring [CAUTION: HBr fumes produced]. The solvent was removed under reduced pressure and the resulting thick brown oil was used in the next step without further purification, assuming complete conversion to the bromophosphinic acid; ^{31}P NMR (162 MHz, CD_3OD) δ +27.6; LCMS (ESI$^+$) *m/z* 250 $[M+H]^+$; HRMS (ESI$^+$) 249.9646 $[M+H]^+$ ($C_7H_{10}NO_2P^{79}Br$ requires 249.9633); ^{1}H NMR spectra showed extremely broad peaks that were impossible to assign. This could be attributed to the presence of radical species formed from the reaction being present in the crude product.

Ethyl (4-bromo-6-methylpyridin-2-yl)methylphosphinate,[188] 31

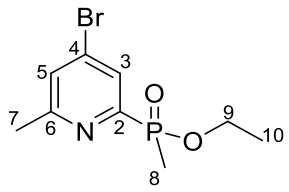

(4-Bromo-6-methylpyridin-2-yl)methylphosphinic acid (1.41 g, 5.65 mmol, assuming complete conversion in previous step) was dissolved in triethyl orthoformate (50 mL) and the solution was stirred at 140 °C under argon for 3 days. The solution was cooled to room temperature and solvent was removed under reduced pressure to yield a brown solid. This was purified by silica gel column chromatography (CH_2Cl_2 to 2% CH_3OH in CH_2Cl_2) to yield a white solid (1.21 g, 77% over two steps); m.p. 69-71 °C; Elem. Anal. Found: C, 38.7; H, 4.7; N, 5.1. $C_9H_{13}NO_2BrP$ requires C, 38.9; H, 4.7; N, 5.0%; ^{1}H NMR (700 MHz, $CDCl_3$) δ 8.01 (1 H, dd, $^3J_{H\text{-}P}$ 6.0, $^4J_{H\text{-}H}$ 1.5, H^3), 7.43 (1 H, t, $^3J_{H\text{-}H}$ 1.5, H^5), 4.11-3.81 (2 H, m, H^9), 2.56 (3 H, s, H^7), 1.74 (3 H, d, $^2J_{H\text{-}P}$ 15.0, H^8), 1.25 (3 H, t, $^3J_{H\text{-}H}$ 7.0, H^{10}); ^{13}C NMR (176 MHz, $CDCl_3$) δ 161.0 (d, $^3J_{C\text{-}P}$, 21, C^6), 155.4 (d, $^1J_{C\text{-}P}$ 155, C^2), 133.6 (d, $^3J_{C\text{-}P}$ 14, C^4), 128.9 (d, $^4J_{C\text{-}P}$ 4, C^5), 128.1 (d, $^2J_{C\text{-}P}$ 21, C^3), 61.3 (d, $^2J_{C\text{-}P}$ 7, C^9), 24.4 (C^7), 16.5 (d, $^3J_{C\text{-}P}$ 5, C^{10}), 13.5 (d, $^1J_{C\text{-}P}$ 106, C^8) ; ^{31}P NMR (283 MHz, $CDCl_3$) δ +38.9; LCMS (ESI$^+$) *m/z* 278 $[M+H]^+$; HRMS (ESI$^+$) 277.9945 $[M+H]^+$ ($C_9H_{14}NO_2P^{79}Br$ requires 277.9946).

Ethyl (4-bromo-6-methylpyridin-1-oxide-2-yl)methylphosphinate,[188] 32

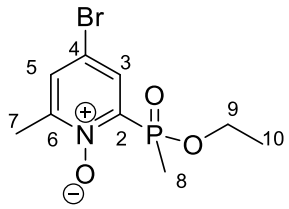

Ethyl (4-bromo-6-methylpyridin-2-yl)methylphosphinate **31** (100 mg, 0.36 mmol) was dissolved in anhydrous acetonitrile (2 mL). *m*-Chloroperbenzoic acid (190 mg, 1.10 mmol) was added and the solution stirred at 65 °C for 21 h. The solvent was removed under reduced pressure and the resulting oil was redissolved in dichloromethane (5 mL). This solution was washed with aqueous $NaHCO_3$ (0.5 M, 5 mL), and the aqueous layer was re-extracted with dichloromethane (3 x 5 mL). The organic extracts were combined, dried over $MgSO_4$, filtered and concentrated to yield a pale yellow oil, that was purified by silica gel column chromatography (CH_2Cl_2 to 3% CH_3OH in CH_2Cl_2) to afford a colourless oil (75 mg, 71%); ^{1}H NMR (700 MHz, $CDCl_3$) δ 8.02 (1 H, dd, $^3J_{H\text{-}P}$ 8.0, $^4J_{H\text{-}H}$ 3.0, H^3), 7.54 (1 H, d, $^4J_{H\text{-}H}$ 3.0, H^5), 4.19-3.91 (2 H, m, H^9), 2.47 (3 H, s, H^7), 1.95 (3 H, d, $^2J_{H\text{-}P}$ 16.0, H^8), 1.30 (3 H, t, $^3J_{H\text{-}H}$ 7.0, H^{10}); ^{13}C NMR (176 MHz, $CDCl_3$) δ 151.1 (d, $^3J_{C\text{-}P}$ 3, C^6), 143.8 (d, $^1J_{C\text{-}P}$ 136, C^2), 133.3 (d, $^2J_{C\text{-}P}$ 11, C^3), 132.2 (d, $^4J_{C\text{-}P}$ 2, C^5), 117.9 (d, $^3J_{C\text{-}P}$, 12, C^4), 62.1 (d, $^2J_{C\text{-}P}$ 5, C^9), 17.5 (d, $^4J_{C\text{-}P}$ 2, C^7), 16.5 (d, $^3J_{C\text{-}P}$ 7, C^{10}), 14.5 (d, $^1J_{C\text{-}P}$ 111, C^8); ^{31}P NMR (283 MHz, $CDCl_3$) δ +32.9; LCMS (ESI$^+$) *m/z* 294 [M+]$^+$; HRMS (ESI$^+$) 293.9902 [M+H]$^+$ ($C_9H_{14}NO_3P^{79}Br$ requires 293.9895).

Ethyl (4-bromo-6-hydroxymethylpyridin-2-yl)methylphosphinate,[188] 33

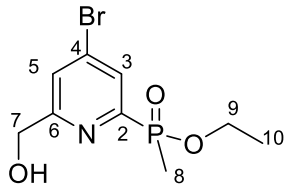

Ethyl (4-bromo-6-methylpyridin-1-oxide-2-yl)methylphosphinate **32** (781 mg, 2.66 mmol) was dissolved in anhydrous acetonitrile (20 mL). Trifluoroacetic anhydride (7.4 mL, 11.2 g, 53.1 mmol) was added and the resulting green solution

was heated to 60 °C under argon. After 3 h, the formation of the trifluoroacetate ester was complete (monitored by ^{1}H NMR). The solvent was removed under reduced pressure, and the residue dissolved in a 1:1 mixture of ethanol:water (50 mL). This solution was stirred at room temperature for 18 h, at which time the organic solvent was removed under reduced pressure and the aqueous solution was extracted with dichloromethane (3 x 100 mL). The organic layers were combined, dried over $MgSO_4$, filtered and concentrated to give a brown oil which was purified by silica gel column chromatography (CH_2Cl_2 to 5% CH_3OH in CH_2Cl_2) to yield a yellow oil (540 mg, 69%); ^{1}H NMR (700 MHz, $CDCl_3$) δ 8.05 (1 H, d, $^{3}J_{H\text{-}P}$ 5.5, H^{3}), 7.72 (1 H, s, H^{5}), 4.79 (2 H, s, H^{7}), 4.36 (1 H, br s, -OH), 4.11-3.82 (2 H, m, H^{9}), 1.74 (3 H, s, $^{2}J_{H\text{-}P}$ 15.5, H^{8}), 1.25 (3 H, t, $^{3}J_{H\text{-}H}$ 7.0, H^{10}); ^{13}C NMR (176 MHz, $CDCl_3$) δ 163.1 (d, $^{3}J_{C\text{-}P}$ 20, C^{6}), 154.7 (d, $^{1}J_{C\text{-}P}$ 155, C^{2}), 134.4 (d, $^{3}J_{C\text{-}P}$ 13, C^{4}), 129.4 (d, $^{3}J_{C\text{-}P}$ 22, C^{3}), 126.3 (d, $^{4}J_{C\text{-}P}$ 3, C^{5}), 64.2 (C^{7}), 61.5 (d, $^{2}J_{C\text{-}P}$ 7, C^{9}), 16.5 (d, $^{3}J_{C\text{-}P}$ 6, C^{10}), 13.5 (d, $^{1}J_{C\text{-}P}$ 105, C^{8}); ^{31}P NMR (162 MHz, $CDCl_3$) δ +38.9; LCMS (ESI^{+}) *m/z* 294 $[M(^{79}Br)+H]^{+}$; HRMS (ESI^{+}) *m/z* 293.9896 $[M+H]^{+}$ ($C_9H_{14}NO_3P^{79}Br$ requires 293.9895).

Ethyl [6-(hydroxymethyl)-4-[2-(2,4,6-trimethoxyphenyl)ethynyl]pyridine-2-yl](methyl)phosphinate,[29] 34

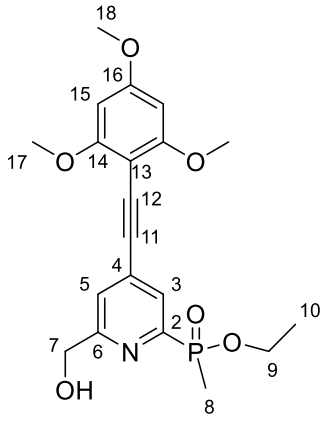

Ethyl (4-bromo-6-hydroxymethylpyridin-2-yl)methylphosphinate **33** (169 mg, 0.58 mmol) and 2-ethynyl-1,3,5-trimethoxybenzene **3** (124 mg, 0.64 mmol) were dissolved in anhydrous tetrahydrofuran (4 mL) and the solution was degassed (freeze-pump-thaw cycle x 3). Triethylamine (404 µL, 293 mg, 2.9 mmol) was added and the solution was further degassed (freeze-pump-thaw x 1). [1,1'-

Bis(diphenylphosphino)ferrocene]dichloropalladium (II) (47 mg, 0.058 mmol) and copper (I) iodide (11 mg, 0.058 mmol) were added and the solution was stirred at 65 °C under argon for 26 h. The solvent was removed under reduced pressure and the brown residue was taken into dichloromethane. This solution was washed with water (5 mL) and brine (5 mL). The organic layer was dried over $MgSO_4$, filtered and concentrated. The crude product was purified by silica gel column chromatography (CH_2Cl_2 to 5% CH_3OH in CH_2Cl_2) to yield a brown oil (123 mg, 53%); ^{1}H NMR (700 MHz, $CDCl_3$) δ 8.08 (1 H, br s, H^3), 7.48 (1 H, br s, H^5), 6.10 (2 H, s, H^{15}), 4.79 (2 H, br s, H^7), 4.10-3.92 (2 H, m, H^9), 3.88 (6 H, s, H^{17}), 3.84 (3 H, s, H^{18}), 1.77 (3 H, d, $^2J_{H\text{-}P}$ 12.0, H^8), 1.26 (3 H, t, $^3J_{H\text{-}H}$ 6.5, H^{10}); ^{13}C NMR (176 MHz, $CDCl_3$) δ 162.9 (C^{16}), 162.8 (C^{14}), 160.8 (d, $^3J_{C\text{-}P}$ 20, C^6), 152.7 (d, $^1J_{C\text{-}P}$ 156, C^2), 133.7 (C^4), 127.9 (d, $^2J_{C\text{-}P}$ 24, C^3), 124.1 (C^5), 93.4 (C^{11}), 93.1 (C^{13}), 90.5 (C^{15}), 89.8 (C^{12}), 64.2 (C^7), 61.2 (C^9), 56.0 (C^{17}), 55.5 (C^{18}), 16.4 (s, C^{10}), 13.5 (d, $^1J_{C\text{-}P}$ 103, C^8); ^{31}P NMR (162 MHz, $CDCl_3$) δ +39.6; LCMS (ESI^+) *m/z* 406 $[M+H]^+$; HRMS (ESI^+) *m/z* 406.1411 $[M+H]^+$ ($C_{20}H_{25}NO_6P$ requires 406.1420).

{4-[2-(2,4,6-Trimethoxyphenyl)ethynyl]-6-[ethoxy(methyl)phosphoryl]pyridin-2-yl}methyl methanesulfonate,[29] 35

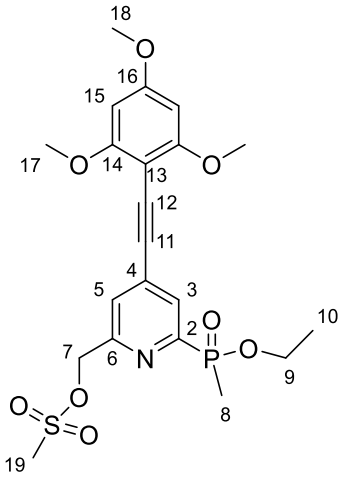

Ethyl [6-(hydroxymethyl)-4-[2-(2,4,6-trimethoxyphenyl)ethynyl]pyridine-2-yl](methyl)phosphinate **34** (123 mg, 0.304 mmol) was dissolved in anhydrous tetrahydrofuran (4 mL) and the solution was cooled in an ice bath. Triethylamine (85 µL, 0.608 mmol) was added, followed by dropwise addition of methanesulfonyl

chloride (35 µL, 0.456 mmol), which resulted in the formation of a precipitate. The reaction was stirred under argon for 90 min after which the solvent was removed under reduced pressure. The residue was redissolved in dichloromethane (20 mL) and washed with water (10 mL). The aqueous solution was re-extracted with dichloromethane (3 x 20 mL) and the organic layers combined, dried with $MgSO_4$, filtered and concentrated under reduced pressure to give a brown oil (112 mg, 76%) which was used without further purification; ^{1}H NMR (400 MHz, $CDCl_3$) δ 8.15 (1 H, br s, H^3), 7.57 (1 H, br s, H^5), 6.11 (2 H, s, H^{15}), 5.35 (2 H, s, H^7), 4.16-3.94 (2 H, m, H^9), 3.90 (6 H, s, H^{17}), 3.85 (3 H, s, H^{18}), 3.12 (3 H, s, H^{19}), 1.77 (3 H, d, $^2J_{H\text{-}P}$ 15.0, H^8), 1.27 (3 H, t, $^3J_{H\text{-}H}$ 7.0, H^{10}); ^{31}P NMR (162 MHz, $CDCl_3$) δ +39.4; LCMS (ESI^+) *m/z* 484 $[M+H]^+$; HRMS (ESI^+) *m/z* 484.1198 $[M+H]^+$ ($C_{21}H_{27}NO_8PS$ requires 484.1195).

1,4,7-Tris({4-[2-(2,4,6-trimethoxyphenyl)ethynyl]-6-[ethoxy(methyl)phosphoryl]pyridin-2-yl}methyl)-1,4,7-triazacyclononane (triethyl ester of L^3)[29]

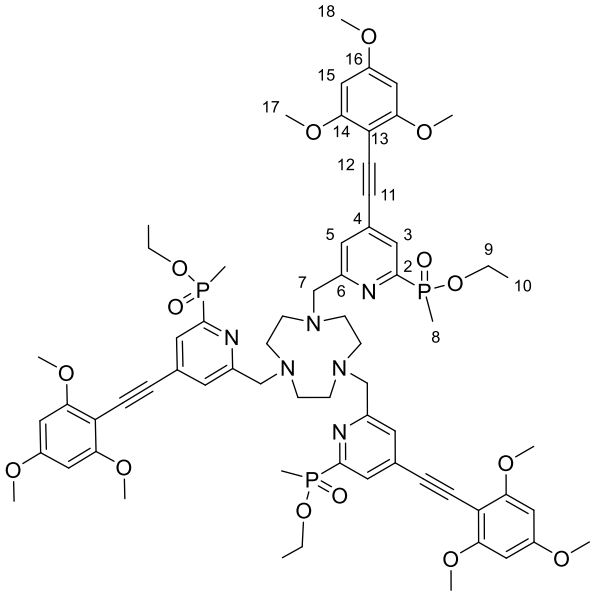

{4-[2-(2,4,6-Trimethoxyphenyl)ethynyl]-6-[ethoxy(methyl)phosphoryl]pyridin-2-yl}methyl methanesulfonate **35** (112 mg, 0.232 mmol), 1,4,7-triazacyclononane trihydrochloride (17 mg, 0.070 mmol) and potassium carbonate (58 mg, 0.422 mmol) were dissolved in anhydrous acetonitrile (5 mL) and stirred under argon at 80 °C for 40 h, at which point the mixture was allowed to cool to room

temperature. The brown solution was isolated from insoluble salts by centrifugation and concentrated. The crude residue was purified by column chromatography (alumina, neat CH_2Cl_2 to 8% CH_3OH in CH_2Cl_2) to yield a pale yellow oil (67 mg, 22%); ^{1}H NMR (600 MHz, $CDCl_3$) δ 8.04 (3 H, br s, H^3), 7.44 (3 H, br s, H^5), 6.09 (6 H, s, H^{15}), 4.12-3.96 (6 H, m, H^9), 3.90 (6 H, s, H^7), 3.85 (18 H, s, H^{17}), 3.81 (9 H, s, H^{18}), 3.00-2.76 (12 H, m, ring CH_2), 1.75 (9 H, d, $^2J_{H\text{-}P}$ 14.0, H^8), 1.28 (9 H, t, $^3J_{H\text{-}H}$ 7.0, H^{10}); ^{13}C NMR (151 MHz, $CDCl_3$) δ 162.9 (C^{16}), 162.8 (C^{14}), 161.2 (d, $^3J_{C\text{-}P}$ 21, C^6), 153.4 (d, $^1J_{C\text{-}P}$ 159, C^2), 133.7 (C^4), 127.7 (d, $^2J_{C\text{-}P}$ 20, C^3), 126.9 (C^5), 93.6 (C^{11}), 93.2 (C^{13}), 89.7 (C^{12}), 90.5 (C^{15}), 64.0 (C^7), 61.1 (C^9), 56.2 (C^{17}), 55.6 (C^{18}), 55.2 (ring CH_2), 16.4 (s, C^{10}), 13.5 (d, $^1J_{C\text{-}P}$ 106, C^8); ^{31}P NMR (162 MHz, $CDCl_3$) δ +40.1; LCMS (ESI^+) *m/z* 1291 $[M+H]^+$; HRMS (ESI^+) *m/z* 1291.504 $[M+H]^+$ ($C_{66}H_{82}N_6O_{15}P_3$ requires 1291.505).

[EuL^3][29]

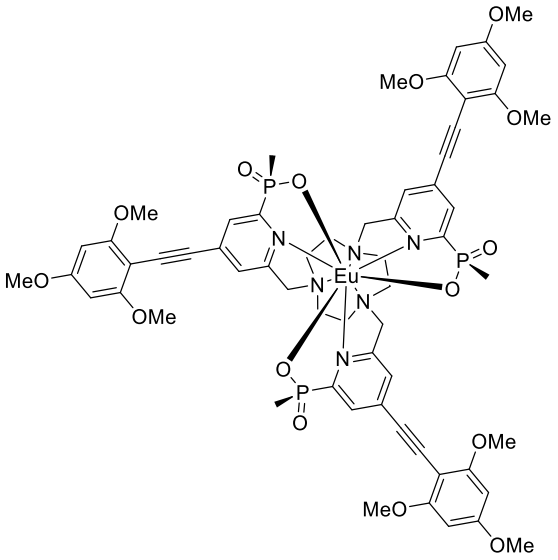

The triethyl ester of **L^3** (67 mg, 0.052 mmol) was dissolved in a mixture of 0.1 M NaOH (2.5 mL) and methanol (2.5 mL). The cloudy solution was stirred at 60 °C for 72 h at which point ^{31}P NMR showed that no phosphinate ester was present. The solution was cooled and the organic solvent removed under reduced pressure. The remaining aqueous solution was adjusted to pH 7 with dilute HCl. $EuCl_3{\cdot}6H_2O$ (24 mg, 0.066 mmol) was added and the solution was heated at 60 °C for 24 h. The solution was cooled to room temperature and concentrated. The crude product

was purified by reverse phase HPLC (Method E, t_R= 19.0 min) to give **[EuL^3]** as an off-white solid (12.4 mg, 18%); LCMS (ESI$^+$) *m/z* 1355 [M(^{151}Eu)+H]$^+$; HRMS (ESI$^+$) *m/z* 1355.310 [M+H]$^+$ ($C_{60}H_{67}N_6O_{15}P_3{}^{151}Eu$ requires 1355.308). λ_{max} (MeOH) = 355 nm; τ_{Eu} (MeOH) = 1.10 ms; Φ_{MeOH}^{em} = 28 (±5)%.

Ethyl [6-(hydroxymethyl)-4-[2-(4-methoxy-2-methylphenyl)ethynyl]pyridine-2-yl](methyl)phosphinate,[29] 36

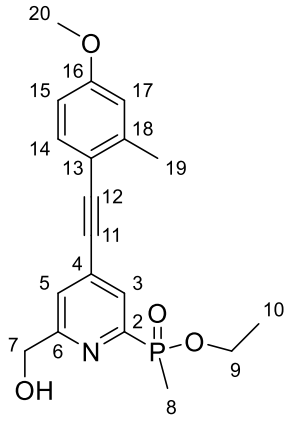

Ethyl (4-bromo-6-hydroxymethylpyridin-2-yl)methylphosphinate **33** (169 mg, 0.58 mmol) and 1-ethynyl-4-methoxy-2-methylbenzene **17** (93 mg, 0.64 mmol) were dissolved in anhydrous tetrahydrofuran (4 mL) and the solution was degassed (freeze-pump-thaw cycle x 3). Triethylamine (404 µL, 293 mg, 2.9 mmol) was added and the solution was further degassed (freeze-pump-thaw x 1). [1,1'-Bis(diphenylphosphino)ferrocene]dichloropalladium (II) (47 mg, 0.058 mmol) and copper (I) iodide (11 mg, 0.058 mmol) were added and the solution was stirred at 65 °C under argon for 20 h. The solvent was removed under reduced pressure and the brown residue was purified by silica gel column chromatography (CH_2Cl_2 to 10% CH_3OH in CH_2Cl_2) to yield a brown oil (141 mg, 68%); ^{1}H NMR (600 MHz, $CDCl_3$) δ 8.04 (1 H, br s, H^3), 7.45 (1 H, s, H^5), 7.43 (1 H, d, $^3J_{H\text{-}H}$ 8.5, H^{14}), 6.79 (1 H, d, $^3J_{H\text{-}H}$ 2.0, H^{17}), 6.74 (1 H, dd, $^3J_{H\text{-}H}$ 8.5, $^4J_{H\text{-}H}$ 2.0, H^{15}), 4.82 (2 H, s, H^7), 4.17-4.09 (1 H, m, H^9), 3.92-3.85 (1 H, m, H^9), 3.83 (3 H, s, H^{20}), 3.56 (1 H, br s, CH_2*OH*), 2.49 (3 H, s, H^{19}), 1.80 (3 H, d, $^2J_{H\text{-}P}$ 14.5, H^8), 1.29 (3 H, t, $^3J_{H\text{-}H}$ 6.5, H^{10}); ^{13}C NMR (176 MHz, $CDCl_3$) δ 161.3 (C^6), 160.8 (C^{16}), 153.0 (d, $^1J_{C\text{-}P}$ 153, C^2), 142.8 (C^{18}), 133.9 (C^{14}), 133.3 (C^4), 127.8 (C^3), 124.2 (C^5), 115.3 (C^{17}), 113.7 (C^{13}), 111.6 (C^{15}), 95.2 (C^{12}), 89.1 (C^{11}), 64.1

(C^7), 61.3 (C^9), 55.3 (C^{20}), 21.0 (C^{19}), 16.5 (d, $^3J_{C\text{-}P}$ 3, C^{10}), 13.5 (d, $^1J_{C\text{-}P}$ 107, C^8); ^{31}P NMR (162 MHz, $CDCl_3$) δ +39.4; LCMS (ESI^+) *m/z* 360 $[M+H]^+$; HRMS (ESI^+) *m/z* 360.1372 $[M+H]^+$ ($C_{19}H_{23}NO_4P$ requires 360.1365).

{4-[2-(4-Methoxy-2-methylphenyl)ethynyl]-6-[ethoxy(methyl)phosphoryl]pyridin-2-yl}methyl methanesulfonate,[29] 37

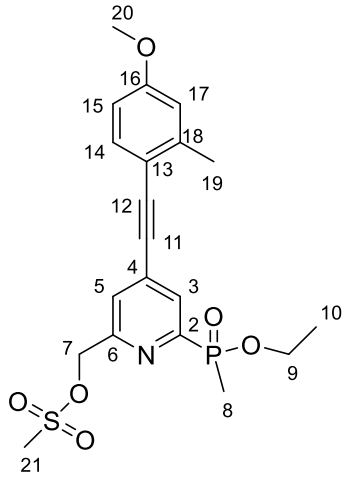

Ethyl [6-(hydroxymethyl)-4-[2-(4-methoxy-2-methylphenyl)ethynyl] pyridin-2-yl](methyl)phosphinate **36** (71 mg, 0.19 mmol) was dissolved in anhydrous tetrahydrofuran (2 mL) and the solution was cooled in an ice bath. Triethylamine (54 µL, 0.40 mmol) was added followed by dropwise addition of methanesulfonyl chloride (22 µL, 0.29 mmol), which resulted in the formation of a precipitate. The reaction was stirred under argon for 30 min and the solvent was then removed under reduced pressure. The residue was redissolved in dichloromethane (20 mL) and washed with water (10 mL). The aqueous solution was re-extracted with dichloromethane (3 x 20 mL) and the organic layers were combined, dried with $MgSO_4$, filtered and concentrated under reduced pressure to give the product as a yellow oil (83 mg, 98%) which was used immediately without further purification; ^1H NMR (400 MHz, $CDCl_3$) δ 8.08 (1 H, br s, H^3), 7.62 (1 H, br s, H^5), 7.45 (1 H, d, $^3J_{H\text{-}H}$ 8.5, H^{14}), 6.78 (1 H, s, H^{17}), 6.74 (1 H, d, $^3J_{H\text{-}H}$ 8.5, H^{15}), 5.36 (2 H, s, H^7), 4.14-4.10 (1 H, m, H^9), 3.91-3.85 (1 H, m, H^9), 3.82 (3 H, s, H^{20}), 3.14 (3 H, s, H^{21}), 2.49 (3 H, s, H^{19}), 1.78 (3 H, d, $^2J_{H\text{-}P}$ 15.0, H^8), 1.28 (3 H, t, $^3J_{H\text{-}H}$ 7.0, H^{10}); ^{31}P NMR (162 MHz,

$CDCl_3$) δ +39.2; LCMS (ESI^+) *m/z* 438 $[M+H]^+$; HRMS (ESI^+) *m/z* 438.1143 $[M+H]^+$ ($C_{20}H_{25}NO_6PS$ requires 438.1140).

1,4,7-Tris({4-[2-(4-Methoxy-2-methylphenyl)ethynyl]-6-[ethoxy(methyl)phosphoryl]pyridin-2-yl}methyl)-1,4,7-triazacyclononane (triethyl ester of L^4)[29]

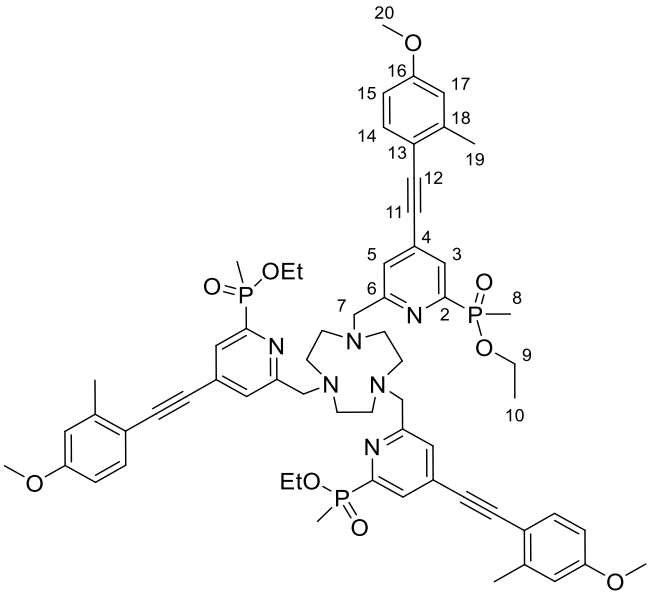

{4-[2-(4-Methoxy-2-methylphenyl)ethynyl]-6-[ethoxy(methyl)phosphoryl]pyridin-2-yl}methyl methanesulfonate **37** (85 mg, 0.195 mmol), 1,4,7-triazacyclononane trihydrochloride (14 mg, 0.059 mmol) and potassium carbonate (49 mg, 0.353 mmol) were dissolved in anhydrous acetonitrile (4 mL) and stirred under argon at 80 °C for 21 h, at which point the mixture was allowed to cool to room temperature. The yellow solution was decanted from insoluble salts and concentrated. The crude residue was purified by column chromatography (alumina, neat CH_2Cl_2 to 1% CH_3OH in CH_2Cl_2) to yield a yellow oil (18 mg, 26%); ^1H NMR (700 MHz, $CDCl_3$) δ 7.98 (3 H, d, $^3J_{H\text{-}P}$ 5.5, H^3), 7.68 (3 H, s, H^5), 7.41 (3 H, d, $^3J_{H\text{-}H}$ 8.5, H^{14}), 6.76 (3 H, d, $^4J_{H\text{-}H}$ 2.0, H^{17}), 6.72 (3 H, dd, $^3J_{H\text{-}H}$ 8.5, $^4J_{H\text{-}H}$ 2.0, H^{15}), 4.12-4.07 (3 H, m, H^9), 3.89-3.84 (3 H, m, H^9), 3.82 (6 H, s, H^7), 3.81 (9 H, s, H^{19}), 3.03 (12 H, br s, ring CH_2), 2.46 (9 H, s, H^{19}), 1.75 (9 H, d, $^2J_{H\text{-}P}$ 15.5, H^8), 1.25 (9 H, t, $^3J_{H\text{-}H}$ 7.0, H^{10}); ^{13}C NMR (176 MHz, $CDCl_3$) δ 161.1 (d, $^3J_{C\text{-}P}$ 18, C^6), 160.7 (C^{16}), 153.9 (d, $^1J_{C\text{-}P}$ 164, C^2), 142.9 (C^{18}), 134.0 (C^{14}), 133.1 (C^4), 127.7 (d, $^2J_{C\text{-}P}$ 23, C^3), 126.9 (C^5), 115.4 (C^{17}),

113.8 (C^{13}), 111.7 (C^{15}) 97.2 (C^{12}), 89.3 (C^{11}), 61.2 (d, $^{2}J_{C\text{-}P}$ 6, C^{9}), 55.4 (C^{20}), 54.4 (ring CH_2), 21.1 (C^{19}), 16.6 (d, $^{3}J_{C\text{-}P}$ 6, C^{10}), 13.5 (d, $^{1}J_{C\text{-}P}$ 105, C^{8}); ^{31}P NMR (283 MHz, $CDCl_3$) δ +39.9; LCMS (ESI$^+$) *m/z* 1153 $[M+H]^+$; HRMS (ESI$^+$) *m/z* 1153.490 $[M+H]^+$ ($C_{63}H_{76}N_6O_9P_3$ requires 1153.489).

[EuL^4][29]

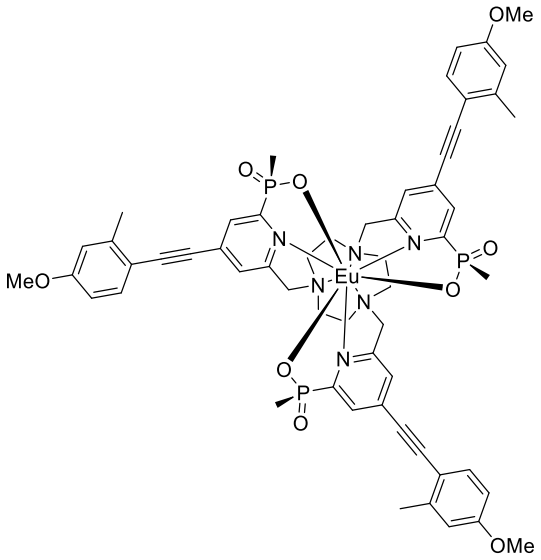

The triethyl ester of **L^4** (18 mg, 0.016 mmol) and potassium hydroxide (3 mg, 0.053 mmol) was dissolved in a mixture of water (1 mL) and methanol (1 mL). The cloudy solution was stirred at 60 °C under argon for 18 h, at which point ^{31}P NMR showed no phosphinate ester was present. The solution was cooled and the organic solvent removed under reduced pressure. The remaining aqueous solution was adjusted to pH 7 with dilute HCl. $EuCl_3{\cdot}6H_2O$ (7 mg, 0.019 mmol) was added and the solution was heated at 60 °C for 48 hours. The solution was cooled to room temperature and concentrated. The crude product was purified by reverse phase HPLC (Method C, t_R= 21.9 min; or Method D, t_R = 16.4 min) to give **[EuL^4]** as an off-white solid (4.9 mg, 25%); LCMS (ESI$^+$) *m/z* 1217 $[M[^{151}Eu+H]^+$; HRMS (ESI$^+$) *m/z* 1217.295 $[M+H]^+$ ($C_{57}H_{61}N_6O_9P_3{}^{151}Eu$ requires 1217.291). λ_{max} (MeOH) = 342 nm; τ_{Eu} (MeOH) = 1.14 ms; Φ^{em}_{MeOH} = 42 (±5)%.

REFERENCES

1 M. Kasha, *Discuss. Faraday Soc.*, 1950, **9**, 14–19.

2 K. Binnemans, *Coord. Chem. Rev.*, 2015, **295**, 1–45.

3 T. Förster, *Discuss. Faraday Soc.*, 1959, **27**, 7–17.

4 D. L. Dexter, *J. Chem. Phys.*, 1953, **21**, 836–850.

5 D. Parker, *Coord. Chem. Rev.*, 2000, **205**, 109–130.

6 A. D'Aléo, F. Pointillart, L. Ouahab, C. Andraud and O. Maury, *Coord. Chem. Rev.*, 2012, **256**, 1604–1620.

7 D. Parker, *Chem. Soc. Rev.*, 2004, **33**, 156–165.

8 J. M. Idée, M. Port, C. Robic, C. Medina, M. Sabatou and C. Corot, *J. Magn. Reson. Imaging*, 2009, **30**, 1249–1258.

9 W. P. Cacheris, S. K. Nickle and A. D. Sherry, *Inorg. Chem.*, 1987, **26**, 958–960.

10 E. T. Clarke and A. E. Martell, *Inorganica Chim. Acta*, 1991, **181**, 273–280.

11 E. Cole, R. C. B. Copley, J. A. K. Howard, D. Parker, G. Ferguson, J. F. Gallagher, B. Kaitner, A. Harrison and L. Royle, *J. Chem. Soc., Dalton Trans.,* 1994, 1619–1629.

12 B. Alpha, R. Ballardini, V. Balzani, J.-M. Lehn, S. Perathoner and N. Sabbatini, *Photochem. Photobiol.*, 1990, **52**, 299–306.

13 S. J. A. Pope, *Polyhedron*, 2007, **26**, 4818–4824.

14 S. Comby, D. Imbert, C. Vandevyver and J. C. G. Bünzli, *Chem. Eur. J.*, 2007, **13**, 936–944.

15 E. G. Moore, C. J. Jocher, J. Xu, E. J. Werner and K. N. Raymond, *Inorg. Chem.*, 2007, **46**, 5468–5470.

16 A. P. S. Samuel, E. G. Moore, M. Melchior, J. Xu and K. N. Raymond, *Inorg. Chem.*, 2008, **47**, 7535–7544.

17 R. A. Poole, G. Bobba, M. J. Cann, J.-C. Frias, D. Parker and R. D. Peacock, *Org. Biomol. Chem.*, 2005, **3**, 1013–24.

18 Y. Bretonnière, M. J. Cann, D. Parker and R. Slater, *Org. Biomol. Chem.*, 2004, **2**, 1624–1632.

19 A. Dadabhoy, S. Faulkner and P. G. Sammes, *J. Chem. Soc. Perkin Trans. 2*, 2002, 348–357.

20 P. Atkinson, K. S. Findlay, F. Kielar, R. Pal, D. Parker, R. A. Poole, H. Puschmann, S. L. Richardson, P. A. Stenson, A. L. Thompson and J. Yu, *Org. Biomol. Chem.*, 2006, **4**, 1707–1722.

21 B. S. Murray, E. J. New, R. Pal and D. Parker, *Org. Biomol. Chem.*, 2008, **6**, 2085–2094.

22 E. J. New, A. Congreve and D. Parker, *Chem. Sci.*, 2010, **1**, 111–118.

23 D. G. Smith, G. Law, B. S. Murray, R. Pal, D. Parker and K.-L. Wong, *Chem. Commun.*, 2011, **47**, 7347–7349.

24 R. Pal, D. Parker and L. C. Costello, *Org. Biomol. Chem.*, 2009, **7**, 1525–1528.

25 R. Pal and D. Parker, *Org. Biomol. Chem.*, 2008, **6**, 1020–1033.

26 L. Seveus, M. Väisälä, S. Syrjänen, M. Sandberg, A. Kuusisto, R. Harju, J. Salo, I. Hemmilä, H. Kojola and E. Soini, *Cytometry*, 1992, **13**, 329–338.

27 H. Takalo, I. Hemmilä, T. Sutela and M. Latva, *Helv. Chim. Acta*, 1996, **79**, 789–802.

28 M. Latva, H. Takalo, V.-M. Mukkala, C. Matachescu, J. C. Rodríguez-Ubis and J. Kankare, *J. Lumin.*, 1997, **75**, 149–169.

29 M. Soulié, F. Latzko, E. Bourrier, V. Placide, S. J. Butler, R. Pal, J. W. Walton, P. L. Baldeck, B. Le Guennic, C. Andraud, J. M. Zwier, L. Lamarque, D. Parker and O. Maury, *Chem. Eur. J.*, 2014, **20**, 8636–8646.

30 J. W. Walton, A. Bourdolle, S. J. Butler, M. Soulié, M. Delbianco, B. K. McMahon, R. Pal, H. Puschmann, J. M. Zwier, L. Lamarque, O. Maury, C. Andraud and D. Parker, *Chem. Commun.*, 2013, **49**, 1600–1602.

31 B. N. Samojlov, *J. Exp. Theor. Phys.*, 1948, **18**, 1030–1039.

32 C. A. Emeis and L. J. Oosterhoff, *Chem. Phys. Lett.*, 1967, **1**, 129–132.

33 C. A. Emeis and L. J. Oosterhoff, *J. Chem. Phys.*, 1971, **54**, 4809–4819.

34 C. K. Luk and F. S. Richardson, *Chem. Phys. Lett.*, 1974, **25**, 215–220.

35 F. S. Richardson and J. P. Riehl, *Chem. Rev.*, 1977, **77**, 773–792.

36 J. P. Riehl and F. S. Richardson, *Chem. Rev.*, 1986, **86**, 1–16.

37 I. Z. Steinberg and A. Gafni, *Rev. Sci. Instrum.*, 1972, **43**, 409–413.

38 P. H. Schippers, A. van den Beukel and H. P. J. M. Dekkers, *J. Phys. E Sci. Instrum.*, 1982, **15**, 945–950.

39 N. H. Evans, R. Carr, M. Delbianco, R. Pal, D. S. Yufit and D. Parker, *Dalton Trans.*, 2013, **42**, 15610–15616.

40 G. Longhi, E. Castiglioni, S. Abbate, F. Lebon and D. A. Lightner, *Chirality*, 2013, **25**, 589–599.

41 N. Steinberg, A. Gafni and I. Z. Steinberg, *J. Am. Chem. Soc.*, 1981, **103**, 1636–1640.

42 P. H. Schippers, J. P. M. Van der Ploeg and H. P. J. M. Dekkers, *J. Am. Chem. Soc.*, 1983, **105**, 84–89.

43 N. Boens, V. Leen and W. Dehaen, *Chem. Soc. Rev.*, 2012, **41**, 1130–1172.

44 A. Gossauer, F. Fehr, F. Nydegger and H. Stöckli-Evans, *J. Am. Chem. Soc.*, 1997, **119**, 1599–1608.

45 E. M. Sánchez-Carnerero, F. Moreno, B. L. Maroto, A. R. Agarrabeitia, M. J. Ortiz, B. G. Vo, G. Muller and S. D. La Moya, *J. Am. Chem. Soc.*, 2014, **136**, 3346–3349.

46 T. Bruhn, G. Pescitelli, S. Jurinovich, A. Schaumlöffel, F. Witterauf, J. Ahrens, M. Bröring and G. Bringmann, *Angew. Chem. Int. Ed.*, 2014, **53**, 14592–14595.

47 F. Zinna, T. Bruhn, C. A. Guido, J. Ahrens, M. Bröring, L. Di Bari and G. Pescitelli, *Chem. Eur. J.*, 2016, **22**, 16089–16098.

48 Y. Sawada, S. Furumi, A. Takai, M. Takeuchi, K. Noguchi and K. Tanaka, *J. Am. Chem. Soc.*, 2012, **134**, 4080–4083.

49 K. Nakamura, S. Furumi, M. Takeuchi, T. Shibuya and K. Tanaka, *J. Am. Chem. Soc.*, 2014, **136**, 5555–5558.

50 A. Ushiyama, S. Hiroto, J. Yuasa, T. Kawai and H. Shinokubo, *Org. Chem. Front.*, 2017, **4**, 664–667.

51 H. Oyama, K. Nakano, T. Harada, R. Kuroda, M. Naito, K. Nobusawa and K. Nozaki, *Org. Lett.*, 2013, **15**, 2104–2107.

52 C. Shen, M. Srebro-Hooper, M. Jean, N. Vanthuyne, L. Toupet, J. A. G. Williams, A. R. Torres, A. J. Riives, G. Muller, J. Autschbach and J. Crassous, *Chem. Eur. J.*, 2017, **23**, 407–418.

53 J. R. Brandt, X. Wang, Y. Yang, A. J. Campbell and M. J. Fuchter, *J. Am. Chem. Soc.*, 2016, **138**, 9743–9746.

54 J. Kumar, T. Nakashima, H. Tsumatori, M. Mori, M. Naito and T. Kawai, *Chem. Eur. J.*, 2013, **19**, 14090–14097.

55 J. Kumar, T. Nakashima and T. Kawai, *J. Phys. Chem. Lett.*, 2015, **6**, 3445–3452.

56 S. T. Spees and A. W. Adamson,.

57 F. P. Dwyer and F. L. Garvan, *J. Am. Chem. Soc.*, 1960, **82**, 4823–4826.

58 F. P. Dwyer and F. L. Garvan, *J. Am. Chem. Soc.*, 1961, **83**, 2610–2615.

59 F. P. Dwyer, I. K. Reid and F. L. Garvan, *J. Am. Chem. Soc.*, 1961, **83**, 1285–1287.

60 N. A. P. Kane-Maguire and C. H. Langford, *Inorg. Chem.*, 1976, **15**, 464–466.

61 J. Coughlin, M. Westrol, K. Oyler, N. Byrne, C. Kraml, E. Zysman-Colman, M. Lowry and S. Bernhard, *Inorg. Chem.*, 2008, **47**, 2039–2048.

62 T.-Y. Li, Y.-M. Jing, X. Liu, Y. Zhao, L. Shi, Z. Tang, Y.-X. Zheng and J.-L. Zuo, *Sci. Rep.*, 2015, **5**, 14912.

63 K. D. Oyler, F. J. Coughlin and S. Bernhard, *J. Am. Chem. Soc.*, 2007, **129**, 210–217.

64 X. P. Zhang, V. Y. Chang, J. Liu, X.-L. Yang, W. Huang, Y. Li, C.-H. Li, G. Muller and X.-Z. You, *Inorg. Chem.*, 2015, **54**, 143–152.

65 F. Zinna and L. Di Bari, *Chirality*, 2015, **27**, 1–13.

66 T. Harada, Y. Nakano, M. Fujiki, M. Naito, T. Kawai and Y. Hasegawa, *Inorg. Chem.*, 2009, **48**, 11242–11250.

67 T. Harada, H. Tsumatori, K. Nishiyama, J. Yuasa, Y. Hasegawa and T. Kawai, *Inorg. Chem.*, 2012, **51**, 6476–6485.

68 J. Yuasa, T. Ohno, K. Miyata, H. Tsumatori, Y. Hasegawa and T. Kawai, *J. Am. Chem. Soc.*, 2011, **133**, 9892–9902.

69 J. L. Lunkley, D. Shirotani, K. Yamanari, S. Kaizaki and G. Muller, *J. Am. Chem. Soc.*, 2008, **130**, 13814–13815.

70 J. L. Lunkley, D. Shirotani, K. Yamanari, S. Kaizaki and G. Muller, *Inorg. Chem.*, 2011, **50**, 12724–12732.

71 S. Di Pietro and L. Di Bari, *Inorg. Chem.*, 2012, **51**, 12007–12014.

72 J. I. Bruce, D. Parker, S. Lopinski and R. D. Peacock, *Chirality*, 2002, **14**, 562–567.

73 S. D. Bonsall, M. Houcheime, D. A. Straus and G. Muller, *Chem. Commun.*, 2007, 3676–3678.

74 K. T. Hua, J. Xu, E. E. Quiroz, S. Lopez, A. J. Ingram, V. A. Johnson, A. R. Tisch, A. De Bettencourt-Dias, D. A. Straus and G. Muller, *Inorg. Chem.*, 2012, **51**, 647–660.

75 E. R. Neil, A. M. Funk, D. S. Yufit and D. Parker, *Dalton Trans.*, 2014, **43**, 5490–5504.

76 R. S. Dickins, J. A. K. Howard, C. L. Maupin, J. M. Moloney, D. Parker, J. P. Riehl, G. Siligardi and J. A. G. Williams, *Chem. Eur. J.*, 1999, **5**, 1095–1105.

77 M. Woods, S. Aime, M. Botta, J. A. K. Howard, J. M. Moloney, M. Navet, D. Parker, M. Port and O. Rousseaux, *J. Am. Chem. Soc.*, 2000, **122**, 9781–9792.

78 R. S. Ranganathan, R. K. Pillai, N. Raju, H. Fan, H. Nguyen, M. F. Tweedle, J. F. Desreux and V. Jacques, *Inorg. Chem.*, 2002, **41**, 6846–6855.

79 R. S. Ranganathan, N. Raju, H. Fan, X. Zhang, M. F. Tweedle, J. F. Desreux and V. Jacques, *Inorg. Chem.*, 2002, **41**, 6856–6866.

80 M. Delbianco, L. Lamarque and D. Parker, *Org. Biomol. Chem.*, 2014, **12**, 8061–8071.

81 M. Delbianco, V. Sadovnikova, E. Bourrier, G. Mathis, L. Lamarque, J. M. Zwier and D. Parker, *Angew. Chem. Int. Ed.*, 2014, **53**, 10718–10722.

82 P. Pfeiffer and K. Quehl, *Ber. Dtsch. Chem. Ges. A/B*, 1931, **64**, 2667–2671.

83 G. Muller and J. P. Riehl, *J. Fluoresc.*, 2005, **15**, 553–558.

84 H. G. Brittain, *J. Chem. Soc., Dalton Trans.*, 1984, 1367–1370.

85 F. Yan, R. A. Copeland and H. G. Brittain, *Inorg. Chem.*, 1982, **21**, 1180–1185.

86 A. Moussa, C. Pham, S. Bommireddy and G. Muller, *Chirality*, 2009, **21**, 497–506.

87 C. P. Montgomery, E. J. New, D. Parker and R. D. Peacock, *Chem. Commun.*, 2008, 4261–4263.

88 D. M. Dias, J. M. Teixeira, I. Kuprov, E. J. New, D. Parker and C. F. G. C. Geraldes, *Org. Biomol. Chem.*, 2011, **9**, 5047–5050.

89 D. G. Smith, R. Pal and D. Parker, *Chem. Eur. J.*, 2012, **18**, 11604–11613.

90 D. G. Smith, B. K. McMahon, R. Pal and D. Parker, *Chem. Commun.*, 2012, **48**, 8520–8522.

91 P. Atkinson, Y. Bretonnière, D. Parker and G. Muller, *Helv. Chim. Acta*, 2005, **88**, 391–405.

92 R. Carr, L. Di Bari, S. Lo Piano, D. Parker, R. D. Peacock and J. M. Sanderson, *Dalton Trans.*, 2012, **41**, 13154.

93 E. R. Neil, M. A. Fox, R. Pal and D. Parker, *Dalton Trans.*, 2016, **45**, 8355–8366.

94 E. R. Neil and D. Parker, *RSC Adv.*, 2017, **7**, 4531–4540.

95 T. D. James, K. R. A. S. Sandanayake and S. Shinkai, *Angew. Chem. Int. Ed.*, 1996, **35**, 1910–1922.

96 G. Wulff, *Pure Appl. Chem.*, 1982, **54**, 2093–2102.

97 R. Nishiyabu, Y. Kubo, T. D. James and J. S. Fossey, *Chem. Commun.*, 2011, **47**, 1124–1150.

98 M. Iwamura, Y. Kimura, R. Miyamoto and K. Nozaki, *Inorg. Chem.*, 2012, **51**, 4094–4098.

99 K. Okutani, K. Nozaki and M. Iwamura, *Inorg. Chem.*, 2014, **53**, 5527–5537.

100 S. J. Butler, L. Lamarque, R. Pal and D. Parker, *Chem. Sci.*, 2014, **5**, 1750–1756.

101 J. Goldstein, R. Anderson and M. Brown, *Nature*, 1979, **279**, 679–684.

102 I. A. Khalil, K. Kogure, H. Akita and H. Harashima, *Pharmacol. Rev.*, 2006, **58**, 32–45.

103 S. Veldhoen, S. D. Laufer, A. Trampe and T. Restle, *Nucleic Acids Res.*, 2006, **34**, 6561–6573.

104 L. H. Wang, K. G. Rothberg and R. G. W. Anderson, *J. Cell Biol.*, 1993, **123**, 1107–1117.

105 J. E. Schnitzer, P. Oh, E. Pinney and J. Allard, *J. Cell Biol.*, 1994, **127**, 1217–1232.

106 P. A. Orlandi and P. H. Fishman, *J. Cell Biol.*, 1998, **141**, 905–915.

107 N. Araki, M. T. Johnson and J. A. Swanson, *J. Cell Biol.*, 1996, **135**, 1249–1260.

108 M. A. West, M. S. Bretscher and C. Watts, *J. Cell Biol.*, 1989, **109**, 2731–2739.

109 P. Dowrick, P. Kenworthy, B. McCann and R. Warn, *Eur. J. Cell Biol.*, 1993, **61**, 44–53.

110 H. U. Keller, *J. Cell. Physiol.*, 1990, **145**, 465–471.

111 J. A. Swanson, *J. Cell Sci.*, 1989, **94**, 135–142.

112 H. H. Mollenhauer, D. J. Morre and L. D. Rowe, *Biochim. Biophys. Acta*, 1990, **1031**, 225–246.

113 D. D. Pless and R. B. Wellner, *J. Cell. Biochem.*, 1996, **62**, 27–39.

114 W. A. Dunn, A. L. Hubbard and N. N. Aronson, *J. Biol. Chem.*, 1980, **255**, 5971–5978.

115 G. Drin, S. Cottin, E. Blanc, A. R. Rees and J. Temsamani, *J. Biol. Chem.*, 2003, **278**, 31192–31201.

116 E. J. New, D. Parker, D. G. Smith and J. W. Walton, *Curr. Opin. Chem. Biol.*, 2010, **14**, 238–246.

117 E. J. New and D. Parker, *Org. Biomol. Chem.*, 2009, **7**, 851–855.

118 B. Hardwick, W. Jackson, G. Wilson and A. W. H. Mau, *Adv. Mater.*, 2001, **13**, 980–984.

119 Bank of England, Polymer banknotes Q & A library, http://www.bankofengland.co.uk/banknotes/polymer/Documents/QALibrar

y.pdf, (accessed 19 September 2017).

120 F. Suyver and A. Meijerink, *Chemisch2Weekblad*, 2002, **98**, 12–13.

121 J.-C. G. Bünzli and S. V Eliseeva, *Chem. Sci.*, 2013, **4**, 1939–1949.

122 J. Andres, R. D. Hersch, J. E. Moser and A. S. Chauvin, *Adv. Funct. Mater.*, 2014, **24**, 5029–5036.

123 B. W. Ennis, S. Muzzioli, B. L. Reid, D. M. D'Alessio, S. Stagni, D. H. Brown, M. I. Ogden and M. Massi, *Dalton Trans.*, 2013, **42**, 6894–6901.

124 O. A. Blackburn, M. Tropiano, T. J. Sørensen, J. Thom, A. Beeby, L. M. Bushby, D. Parker, L. S. Natrajan and S. Faulkner, *Phys. Chem. Chem. Phys.*, 2012, **14**, 13378–13384.

125 P. Kumar, K. Nagpal and B. K. Gupta, *ACS Appl. Mater. Interfaces*, 2017, **9**, 14301–14308.

126 S. Cotton, *Lanthanide and Actinide Chemistry*, John Wiley & Sons, Ltd., Chichester, UK, 2006.

127 US Pat., 2008, 2008/0305243 A1.

128 US Pat., 2012, 8167989 B2.

129 J. F. Suyver, J. Grimm, M. K. Van Veen, D. Biner, K. W. Krämer and H. U. Güdel, *J. Lumin.*, 2006, **117**, 1–12.

130 J. M. Meruga, W. M. Cross, P. Stanley May, Q. Luu, G. A. Crawford and J. J. Kellar, *Nanotechnology*, 2012, **23**, 395201.

131 What is a QR code?, www.qrcode.com/en/about, (accessed 20 May 2015).

132 P. Hwang, How Often Does a Banknote Change Hands?, https://www.onstride.co.uk/blog/often-banknote-change-hands/, (accessed 24 August 2017).

133 S. J. Butler, M. Delbianco, N. H. Evans, A. T. Frawley, R. Pal, D. Parker, R. S. Puckrin and D. S. Yufit, *Dalton Trans.*, 2014, **43**, 5721–5730.

134 A. T. Frawley, R. Pal and D. Parker, *Chem. Commun.*, 2016, **52**, 13349–13352.

135 E. J. Corey and P. L. Fuchs, *Tetrahedron Lett.*, 1972, **13**, 3769–3772.

136 S. Oae, T. Kitao and Y. Kitaoka, *J. Am. Chem. Soc.*, 1962, **84**, 3359–3362.

137 A. T. Frawley, MChem Thesis, Durham University, 2014.

138 T. M. Wannier, M. M. Moore, Y. Mou and S. L. Mayo, *PLoS One*, 2015, **10**, e0130582.

139 L. Porrès, A. Holland, L. O. Pålsson, A. P. Monkman, C. Kemp and A. Beeby, *J. Fluoresc.*, 2006, **16**, 267–272.

140 J. W. Walton, R. Carr, N. H. Evans, A. M. Funk, A. M. Kenwright, D. Parker, D. S. Yufit, M. Botta, S. De Pinto and K. L. Wong, *Inorg. Chem.*, 2012, **51**, 8042–8056.

141 J. W. Walton, PhD Thesis, Durham University, 2012.

142 C. Görller-Walrand and K. Binnemans, *Handb. Phys. Chem. Rare Earths 23*, 1996, 121–283.

143 F. S. Richardson, *Inorg. Chem.*, 1980, **19**, 2806–2812.

144 M. Kasperczyk, S. Person, D. Ananias, L. D. Carlos and L. Novotny, *Phys. Rev. Lett.*, 2015, **114**, 163903.

145 M. D. Chambers, P. A. Rousseve and D. R. Clarke, *J. Lumin.*, 2009, **129**, 263–269.

146 R. Brennetot and J. Georges, *Spectrochim. Acta - Part A Mol. Biomol. Spectrosc.*, 2000, **56**, 703–715.

147 T. Yamase, T. Kobayashi, M. Sugeta and H. Naruke, *J. Phys. Chem. A*, 1997, **101**, 5046–5053.

148 H. S. Blandon, MChem Thesis, Durham University, 2017.

149 R. Chinchilla and C. Nájera, *Chem. Rev.*, 2007, **107**, 874–922.

150 A. Bourdolle, M. Allali, J. C. Mulatier, B. Le Guennic, J. M. Zwier, P. L. Baldeck, J.-C. G. Bünzli, C. Andraud, L. Lamarque and O. Maury, *Inorg. Chem.*, 2011, **50**, 4987–4999.

151 T. Hofbeck and H. Yersin, *Inorg. Chem.*, 2010, **49**, 9290–9299.

152 P. Brulatti, R. J. Gildea, J. A. K. Howard, V. Fattori, M. Cocchi and J. A. G. Williams, *Inorg. Chem.*, 2012, **51**, 3813–3826.

153 S. Culham, P. H. Lanoë, V. L. Whittle, M. C. Durrant, J. A. G. Williams and V. N. Kozhevnikov, *Inorg. Chem.*, 2013, **52**, 10992–11003.

154 E. Slyusareva, A. Sizykh, A. Tyagi and A. Penzkofer, *J. Photochem. Photobiol. A Chem.*, 2009, **208**, 131–140.

155 D. M. Walba, F. Stevens, N. A. Clark and D. C. Parks, *Acc. Chem. Res.*, 1996, **29**, 591–597.

156 H. Fang, L. C. Giancarlo and G. W. Flynn, *J. Phys. Chem. B*, 1999, **102**, 7311–7315.

157 R. Mckendry, M. Theoclitou, T. Rayment and C. Abell, *Nature*, 1998, **391**, 566–568.

158 S. Blair, M. P. Lowe, C. E. Mathieu, D. Parker, P. K. Senanayake and R. Kataky, *Inorg. Chem.*, 2001, **40**, 5860–5867.

159 E. R. Neil, PhD Thesis, Durham University, 2015.

160 M. Tropiano, O. A. Blackburn, J. A. Tilney, L. R. Hill, T. Just Sørensen and S. Faulkner, *J. Lumin.*, 2015, **167**, 296–304.

161 C. Reichardt, *Solvents and Solvent Effects in Organic Chemistry*, VCH, Weinheim, 1988.

162 W. M. Haynes, Ed., *CRC Handbook of Chemistry and Physics*, CRC Press, Boca Raton, FL, 92nd edn., 2011.

163 J. Salgado, T. Regueira, L. Lugo, J. Vijande, J. Fernández and J. García, *J. Chem. Thermodyn.*, 2014, **70**, 101–110.

164 B. R. Judd, *Phys. Rev.*, 1962, **127**, 750–761.

165 G. S. Ofelt, *J. Chem. Phys.*, 1962, **37**, 511–520.

166 C. K. Jorgensen and B. R. Judd, *Mol. Phys.*, 1964, **8**, 281–290.

167 S. F. Mason, R. D. Peacock and B. Stewart, *Mol. Phys.*, 975, **30**, 1829–1841.

168 M. F. Reid and F. S. Richardson, *Chem. Phys. Lett.*, 1983, **95**, 501–506.

169 H. Biava, C. Palopoli, C. Duhayon, J.-P. Tuchagues and S. Signorella, *Inorg. Chem.*, 2009, **48**, 3205–3214.

170 J. Ehrhart, J.-M. Planeix, N. Kyritsakas-Gruber and M. W. Hosseini, *Dalton Trans.*, 2010, **39**, 2137–2146.

171 A. M. Abu-Dief, R. Díaz-Torres, E. C. Sañudo, L. H. Abdel-Rahman and N.

Aliaga-Alcalde, *Polyhedron*, 2013, **64**, 203–208.

172 K. E. Riley, J. S. Murray, J. Fanfrlík, J. Řezáč, R. J. Solá, M. C. Concha, F. M. Ramos and P. Politzer, *J. Mol. Model.*, 2011, **17**, 3309–3318.

173 G. Cavallo, P. Metrangolo, R. Milani, T. Pliati, A. Priimagi, G. Resnati and G. Terraneo, *Chem. Rev.*, 2016, **116**, 2478–2601.

174 Y. Kono, N. Hara, M. Shizuma, M. Fujiki and Y. Imai, *Dalton Trans.*, 2017, **46**, 5170–5174.

175 M. Vonci, K. Mason, E. A. Suturina, A. T. Frawley, S. G. Worswick, I. Kuprov, D. Parker, E. J. L. McInnes and N. F. Chilton, *J. Am. Chem. Soc.*, 2017, **Accepted**, jacs.7b07094.

176 B. Bleaney, *J. Magn. Reson.*, 1972, **8**, 91–100.

177 B. Bleaney, C. M. Dobson, B. A. Levine, R. B. Martin, R. J. P. Williams and A. V. Xavier, *J. Chem. Soc., Chem. Commun.*, 1972, 791–793.

178 A. M. Funk, K.-L. N. A. Finney, P. Harvey, A. M. Kenwright, E. R. Neil, N. J. Rogers, P. K. Senanayake and D. Parker, *Chem. Sci.*, 2015, **6**, 1655–1662.

179 G. Castro, M. Regueiro-Figueroa, D. Esteban-Gómez, P. Pérez-Lourido, C. Platas-Iglesias and L. Valencia, *Inorg. Chem.*, 2016, **55**, 3490–3497.

180 L. Sorace, C. Benelli and D. Gatteschi, *Chem. Soc. Rev.*, 2011, **40**, 3092–3104.

181 D. R. Scott and J. B. Allison, *J. Phys. Chem.*, 1962, **66**, 561–562.

182 J. Long, R. Vallat, R. A. S. Ferreira, L. D. Carlos, F. A. Almeida Paz, Y. Guari and J. Larionova, *Chem. Commun.*, 2012, **48**, 9974–9976.

183 E. Mamontova, J. Long, R. Ferreira, A. Botas, D. Luneau, Y. Guari, L. Carlos and J. Larionova, *Magnetochemistry*, 2016, **2**, 41.

184 G. Cucinotta, M. Perfetti, J. Luzon, M. Etienne, P. E. Car, A. Caneschi, G. Calvez, K. Bernot and R. Sessoli, *Angew. Chem. Int. Ed.*, 2012, **51**, 1606–1610.

185 S. Shintoyo, K. Murakami, T. Fujinami, N. Matsumoto, N. Mochida, T. Ishida, Y. Sunatsuki, M. Watanabe, M. Tsuchimoto, J. Mrozinski, C. Coletti and N. Re, *Inorg. Chem.*, 2014, **53**, 10359–10369.

186 K. Binnemans and C. Görller-Walrand, *Chem. Phys. Lett.*, 1995, **245**, 75–78.

187 C. Görller-Walrand, E. Huygen, K. Binnemans and L. Fluyt, *J. Phys. Condens.*

Matter, 1994, **6**, 7797–7812.

188 US Pat., US20150361116 A1, 2015.

189 E. J. New, PhD Thesis, Durham University, 2009.

190 C. Plank, B. Oberhauser, K. Mechtler, C. Koch and E. Wagner, *J. Biol. Chem.*, 1994, **269**, 12918–12924.

191 M. Starck, R. Pal and D. Parker, *Chem. Eur. J.*, 2016, **22**, 570–580.

192 M. C. Kerr and R. D. Teasdale, *Traffic*, 2009, **10**, 364–371.

193 L. J. Hewlett, A. R. Prescott and C. Watts, *J. Cell Biol.*, 1994, **124**, 689–703.

194 S. E. Miller, S. Mathiasen, N. A. Bright, F. Pierre, B. T. Kelly, N. Kladt, A. Schauss, C. J. Merrifield, D. Stamou, S. Höning and D. J. Owen, *Dev. Cell*, 2015, **33**, 163–175.

195 E. L. Racoosin and J. A. Swanson, *J. Cell Biol.*, 1993, **121**, 1011–1020.

196 J. P. Lim and P. A. Gleeson, *Immunol. Cell Biol.*, 2011, **89**, 836–843.

197 J. Bereiter-Hahn and M. Vöth, *Microsc. Res. Tech.*, 1994, **27**, 198–219.

198 S. Sugio, A. Kashima, S. Mochizuki, M. Noda and K. Kobayashi, *Protein Eng.*, 1999, **12**, 439–446.

199 P. Zunszain, J. Ghuman, T. Komatsu, E. Tsuchida and S. Curry, *BMC Struct. Biol.*, 2003, **3**, 6–14.

200 J. Ghuman, P. A. Zunszain, I. Petitpas, A. A. Bhattacharya, M. Otagiri and S. Curry, *J. Mol. Biol.*, 2005, **353**, 38–52.

201 K. Yamasaki, V. T. G. Chuang, T. Maruyama and M. Otagiri, *Biochim. Biophys. Acta - Gen. Subj.*, 2013, **1830**, 5435–5443.

202 W. Bal, M. Sokołowska, E. Kurowska and P. Faller, *Biochim. Biophys. Acta - Gen. Subj.*, 2013, **1830**, 5444–5455.

203 M. Fasano, S. Curry, E. Terreno, M. Galliano, G. Fanali, P. Narciso, S. Notari and P. Ascenzi, *IUBMB Life (International Union Biochem. Mol. Biol. Life)*, 2005, **57**, 787–796.

204 S. Aime, M. Botta, M. Fasano, S. G. Crich and E. Terreno, *J. Biol. Inorg. Chem.*, 1996, **1**, 312–319.

205 P. Caravan, N. J. Cloutier, M. T. Greenfield, S. A. McDermid, S. U. Dunham, J. W. M. Bulte, J. C. Amedio, R. J. Looby, R. M. Supkowski, W. D. W. Horrocks, T. J. McMurry and R. B. Lauffer, *J. Am. Chem. Soc.*, 2002, **124**, 3152–3162.

206 P. Caravan, M. T. Greenfield, X. Li and A. D. Sherry, *Inorg. Chem.*, 2001, **40**, 6580–6587.

207 S. Aime, E. Gianolio, D. Longo, R. Pagliarin, C. Lovazzano and M. Sisti, *ChemBioChem*, 2005, **6**, 818–820.

208 S. Shuvaev, R. Pal and D. Parker, *Chem. Commun.*, 2017, **53**, 6724–6727.

209 G. L. Francis, *Cytotechnology*, 2010, **62**, 1–16.

210 F. Ruggeri, F. Zhang, T. Lind, E. D. Bruce, B. L. T. Lau and M. Cárdenas, *Soft Matter*, 2013, **9**, 4219–4226.

211 A. M. Merlot, D. S. Kalinowski and D. R. Richardson, *Front. Physiol.*, 2014, **5**, 1–7.

212 C. C. Norbury, L. J. Hewlett, A. R. Prescott, N. Shastri and C. Watts, *Immunity*, 1995, **3**, 783–791.

213 J. R. Tennant, *Transplantation*, 1964, **2**, 685–694.

214 S. Krauss, *Mitochondria : Structure and Role in Respiration*, John Wiley & Sons, Ltd., 2001.

215 G. Banfalvi, *Permeability of Biological Membranes*, Springer International Publishing, Switzerland, 1st edn., 2016.

216 J. A. Mindell, *Annu. Rev. Physiol.*, 2012, **74**, 69–86.

217 Q. Yu, Y. Liu, C. Wang, D. Sun, X. Yang, Y. Liu and J. Liu, *PLoS One*, 2012, **7**, e50902.

218 GB Pat. Appl., GB1507296.0, 2015.

219 R. Pal, *Faraday Discuss.*, 2015, **177**, 507–515.

220 M. V. R. Reddy, P. Venkatapuram, M. R. Mallireddigari, V. R. Pallela, S. C. Cosenza, K. A. Robell, B. Akula, B. S. Hoffman and E. P. Reddy, *J. Med. Chem.*, 2011, **54**, 6254–6276.

221 US Pat., US2014/0336373 A1, 2014.

222 G. Chessa, L. Canovese, F. Visentin, C. Santo and R. Seraglia, *Tetrahedron*, 2005, **61**, 1755–1763.

223 E. R. Neil, M. A. Fox, R. Pal, L.-O. Pålsson, B. A. O'Sullivan and D. Parker, *Dalton Trans.*, 2015, **44**, 14937–14951.

224 US Pat., US20040029851 A1, 2004.

APPENDICES

Seminars attended

04/11/2014	Prof. Laurence M. Harwood University of Reading, UK	*The development of ligands for separating minor actinides from lanthanides for nuclear fuel reprocessing*
19/11/2014	Dr John Spencer University of Sussex, UK	*Development of chemical tools for cancer*
28/11/2014	Dr Sarah Trimpin Wayne State University, Detroit, MI, USA	*Novel ionisation process for use in mass spectrometry: a special focus on surface applications*
02/12/2014	Colin Banks Cheshire Science UK	*puriFlash – ultra-performance flash purification & interface*
02/12/2014	Guy Wilson Waters Ltd., UK	*The use of supercritical fluid chromatography for reaction monitoring and purification*
02/12/2014	Peter Ridgeway Reach Separations, UK	*Exploiting supercritical fluid chromatography in a purification environment*
27/01/2015	Prof. Stuart J. Conway Oxford University, UK	*Chemistry enabling biology: the synthesis of chemical probes for biological systems*
04/02/2015	Prof. Thorri Gunnlaugsson Trinity College, Dublin	*Surprising 'twists and turns' in supramolecular self-assembly formations*
10/02/2015	Dr Kai Hilpert St George's, University of London, UK	*Multiple biological functions of short antimicrobial peptides*
18/02/2015	Prof. Muriel Hissler University of Rennes, France	*Phosphorus chemistry for opto-electronic applications*
25/02/2015	Prof. Nicolas Willand University of Lille, France	*Boosting antibiotics using transcriptional regulators: how an old drug can become a new drug.*
04/03/2015	Prof. Robert M. J. Liskamp University of Glasgow, UK	*Peptide biomolecular constructs for chemical biology and beyond*
18/03/2015	Dr Neil Hunt University of Strathclyde, UK	*Ultrafast 2D-IR spectroscopy of biomolecular interactions*

15/04/2015	Prof. Jacques Mortier University du Maine, France	*Directed ortho & remote metalation of arenes – recent advances*
21/04/2015	Dr Jonathan K. Watts University of Southampton, UK	*Chemically modified oligonucleotides for therapeutic gene silencing*
22/04/2015	Prof. David R. Spring University of Cambridge, UK	*RSC Corday-Morgan Award Lecture: Enriching chemical space to drug undruggable targets*
29/04/2015	Dr Anna Peacock University of Birmingham, UK	*New peptide ligands for metal ions: from MRI contrast agents to DNA binding proteins*
21/05/2015	Prof. Jim Tour Rice University, Texas, USA	*Nanomedicine for stroke, traumatic brain injury, autoimmune diseases and drug delivery*
10/06/2015	Prof. F. R. Keene University of Adelaide, Australia	*Selective toxicity of ruthenium(II) complexes to drug-resistant pathogens: new paradigms for old molecules?*
04/09/2015	Dr Jeanne L. Bolliger University of Cambridge, UK	*Coordination cages: host guest chemistry and application in supramolecular catalysis*
27/10/2015	Prof. Mike Watkinson Queen Mary, University of London, UK	*Click to detect: bio- & chemo-sensing with triazole-containing macrocycles*
28/10/2015	Dr Andrew Marsh University of Warwick, UK	*Self-assembly and chemical virology*
09/12/2015	Prof G. J. Hutchings FRS Cardiff University, UK	*Catalysis on gold*
20/01/2016	Dr Rachel C. Evans Trinity College Dublin, Ireland	*Targeted design of photoactive organic-inorganic hybrid materials for energy and lighting applications*
27/01/2016	Dr Patrick C. McGowan	*Using organometallics as catalysts: from drug precursors to*

	University of Leeds, UK	*little black dresses*
03/02/2016	Dr Max Massi Curtin University, Perth, Australia	*Versatility of tetrazole ligands in luminescent metal complexes for applications in life science*
09/03/2061	Prof. Steve Liddle University of Manchester, UK	*Corday Morgan Award Lecture: Recent advances in uranium-ligand multiple bonding*
16/03/2016	Prof. Lesley Yellowlees University of Edinburgh, UK	*What has chemistry ever done for me?*
11/04/2016	Prof. Yi Lu University of Illinois, Urbana-Champaign, USA	*RSC Applied Inorganic Chemistry Award Lecture: Directed assembly of nanomaterials by functionalised DNA and their applications in environmental sensing, medical diagnostics and imaging*
20/04/2016	Dr Philip Kukura University of Oxford, UK	*Marlow Award Lecture: A new perspective on nanoscale structure dynamics with ultrasensitive optical microscopy*
10/05/2016	Dr Alison Hulme University of Edinburgh, UK	*Alkynes: a chemical swiss army knife*
17/06/2016	Dr Hendrik W. van Veen University of Cambridge	*Mechanisms and inhibition of multidrug transporters in health and disease*
21/06/2016	Prof. Sir Fraser Stoddart Northwestern University, Illinois, USA	*The nature of the mechanical bond: from molecules to machines (Durham Lecture 1)*
22/06/2016	Prof. Sir Fraser Stoddart Northwestern University, Illinois, USA	*Serendipity at work (Durham Lecture 2)*
23/06/2016	Prof. Sir Fraser Stoddart Northwestern University, Illinois, USA	*Cooperative capture in rotaxane synthesis (Durham Lecture 3)*
29/09/2016	Dr Elizabeth J. New	*Molecular imaging tools for the study of oxidative stress and metal*

	University of Sydney, Australia	*ions in biology*
19/10/2016	Dr Hugo Bronstein University College London	*Understanding and controlling triplet excited states in conjugated polymers*
02/11/2016	Prof. Angela Casini Cardiff University, UK	*Metal-based chemical entities for applications in chemical biology and medicine*
30/11/2016	Prof. Tatjana Parac-Vogt KU Leuven, Belgium	*Polyoxometalates as artificial proteases*
13/01/2017	Dr Michael J. G. Peach Lancaster University, UK	*An exciting future: rationalising photophysics and photochemistry with DFT*
25/01/2017	Prof. Richard Winpenny University of Manchester, UK	*Ludwig Mond Award Lecture: Nanoscale structures from supramolecular assembly of molecular magnets*
22/02/2017	Prof. Chris Schofield University of Oxford, UK	*Antibiotic resistance in beta-lactam drugs*
01/03/2017	Prof. Jane Clarke University of Cambridge, UK	*Intrinsically disordered protein: what is the role of disorder?*
19/06/2017	Prof. Marsha Lester University of Pennsylvania, USA	*The atmosphere's detergent (Durham Lecture 1)*
27/06/2017	Prof. Carlos F. G. C. Geraldes University of Coimbra, Portugal	*Ln(III) based MRI probes for the* $A\beta_{1\text{-}40}$ amyloid
05/07/2017	Prof. Munetaka Iwamura University of Toyama, Japan	*Chiral sensing for amino acids in water using induced CPL from Eu(III) complexes*
13/07/2017	Dr Kellie Tuck Monash University, Melbourne, Australia	*Strategies for the development of lanthanide-based chemosensors*

04/09/2017	Prof. Mike Ward University of Warwick, UK	*Guest binding and catalysed reactions in the cavity of a coordination cage*

Conferences Attended

- International Conference on the *f*-elements, Keble College, Oxford, September 2015 – oral presentation.

- RSC Macrocyclic and Supramolecular Chemistry Group Meeting, Durham, December 2015 – awarded the RSC poster prize.

- RSC Organic Division North Eastern Regional Meeting 2016, Newcastle University, April 2016 – presented poster.

- International Symposium on Macrocyclic and Supramolecular Chemistry, Seoul, S. Korea, July 2016 – presented poster.

- RSC Organic Division North Eastern Regional Meeting 2017, Durham University, March 2017.

Publications arising from PhD research

1. *Rationalisation of anomalous pseudo-contact shifts and their solvent dependence in a series of C_3-symmetric lanthanide complexes*, M. Vonci, K. Mason, E. A. Suturina, A. T. Frawley, S. G. Worswick, I. Kuprov, D. Parker, E. J. L. McInnes and N. F. Chilton, *J. Am. Chem. Soc.*, 2017, **139**, 14166-14172, DOI: 10.1021/jacs.7b07094.

2. *Very bright, enantiopure europium(III) complexes allow time-gated chiral contrast imaging*, A. T. Frawley, R. Pal, D. Parker, *Chem. Commun*., 2016, **52**, 13349-13352, DOI: 10.1039/c6cc07313a.

Future publications

1. *Enantioselective cellular localisation of europium(III) coordination complexes*, A. T. Frawley, H. V. Linford, M. Starck, R. Pal and D. Parker, *submitted*.

2. *Solution spectral evidence for a weak CH···Br interaction: specific solvation of a luminescent 9-coordinate europium(III) complex,* A. T. Frawley and D. Parker, *submitted.*

3. Solvent-dependent emission and CPL in pyridylphosphinate complexes, *manuscript in preparation*.